University of Liège - Belgium

# Fragmentation of a drop impacting near the edge of a solid substrate: a key to rain-induced foliar disease transmission

Sophie LEJEUNE

Thesis submitted in partial fulfilment of the requirements for the degree of Doctor of Philosophy in Engineering Sciences

Academic year 2017-2018

Advisor: Professor Tristan Gilet
Microfluidics Lab

This work has been done under the supervision of Prof. Tristan Gilet from the Microfluidics Lab at the University of Liège and in collaboration with Lydia Bourouiba from the Fluid dynamics of Disease Transmission Laboratory at the Massachusetts Institute of Technology.


**Microfluidics Lab**
Department of Aerospace and Mechanical engineering
Allée de la Découverte, 9
4000 Liège, Belgium

Members of the Examination Committee:

| | |
|---|---|
| Dr. Stéphane Dorbolo | University of Liège, Belgium |
| Prof. Tristan Gilet (Advisor) | University of Liège, Belgium |
| Prof. José Manuel Gordillo | University of Seville, Spain |
| Dr. Laurence Ramos | University of Montpellier, France |
| Dr. Sébastien Saint-Jean | AgroParisTech, INRA, France |
| Prof. Vincent Terrapon (Chair) | University of Liège, Belgium |

The research described in the present thesis was financially supported by the Belgian National Fund for Scientific Research-F.R.S.-FNRS through a research grant attributed by the Fund For Agriculture and Industrial Research (FRIA).

# Abstract

Plant diseases are still responsible for significant losses in crops despite the use of chemicals and genetically modified organisms. Moreover, these mitigation techniques present drawbacks in terms of cost and sustainability and their intensive use tends to reduce their effectiveness. There is thus a global call for alternative methods of crop protection and for the development of risk predicting models and decision aid tools to minimize the use of these techniques. One of the most promising of these global models rely on the physics behind the spreading of diseases. For example, the Septoria Leaf Blotch that affects wheat, is mainly dispersed through rainsplash. Modelling the rain dispersal of such disease requires information concerning the pathosystem, the raindrop size and speed distributions but also about the plant characteristics to only cite a few. The disease is known to propagate from one plant to the next when a raindrop hits a leaf on which contaminated fluid sits. The splash of contaminated droplets carries the pathogens to the next plant. The physics of such impacts remains poorly understood, both in terms of drop-leaf interactions and drop fragmentation upon impact. Such understanding could however improve the robustness and accuracy of the risk predicting models.

The aim of this experimental work was thus to investigate the fragmentation physics of drop impacts. The crescent moon is a particular impact configuration that was recently shown to be both frequent and efficient at ejecting droplets. It consists in the impact of a drop in the vicinity of a contaminated sessile drop. Upon impact the drop spreads on the substrate and pushes the sessile drop, which is stretched and develops into an asymmetric liquid sheet in the air that subsequently fragments into droplets. This phenomenon being fully three-dimensional, its investigation is challenging. We propose to study a simpler configuration that shares most of the features of the crescent moon: a single drop impacting close to the straight edge of a flat dry substrate. Upon impact, the drop spreads on the solid. The liquid, then, takes off at the edge and forms an asymmetric liquid sheet that presents similar characteristics to the three-dimensional crescent moon. However, the sheet now remains in the plane of the substrate, which facilitates its quantitative analysis.

Three parameters are systematically varied: (i) the impact speed, which modifies the kinetic energy of the impacting drop and thus its tendency to fragment into droplets, (ii) the offset, i.e., the distance between the impact point and the edge of the substrate, which modifies the asymmetry of the liquid sheet and the subsequent ejection pattern, and (iii) the inclination of the substrate and the corresponding addition of a tangential speed upon impact.

We quantified the liquid sheet kinematics by first looking at the spreading liquid on the solid. The maximum distance spread and the time to reach the edge are measured, as they represent the pre-history of the liquid sheet. The evolution of the sheet in the air is then quantified in directions normal and tangential to the edge. In particular, its maximum extension in both directions and corresponding time, are measured and scaling laws derived for

each. We identified three main retraction scenarios of the sheet based on its level of asymmetry. We related the occurrence of the scenarios to the entry parameters through, notably, maximal extension in both directions.

We finally focused on the ejected droplets and their link with the sheet asymmetry. Four ejection mechanisms were identified, among which one is directly related to the inclination of the substrate. We quantified the speed and mass of the droplets and derived general laws to describe them. We then used these relations to compute a maximum distance travelled by the ejected droplets. We showed that there was a direct link between sheet behaviour and droplet ejection pattern. Beyond a certain level, increasing the asymmetry of the liquid sheet through the offset does not significantly influence the maximum distance travelled by the ejected droplets. It however increases the size of the droplets travelling at a given distance. The inclination of the substrate should theoretically reduce the distance travelled by the droplets at given mass and speed. Yet, we showed that, through a complex interplay between the ejection mechanisms and effects on the mass and speed of the droplets, the distance travelled by the ejected droplets presents an optimum for intermediate values of substrate inclination.

The influence of the sheet asymmetry is then related to the ejected droplet characteristics and notably to the mass and distance travelled by the droplets as a function of the entry parameters. These results give insights into the physics of drop impacts on leaves and should help improving the robustness of disease propagation models. Increasing the accuracy and robustness of their predictions would make them a useful tool for the development of a more sustainable agriculture.

# Résumé

Les maladies des plantes sont, encore de nos jours, responsables d'une perte significative de rendement pour les agriculteurs et ce, malgré l'utilisation de fongicides et de variétés résistantes obtenue par mutation et sélection génétique. Ces méthodes de lutte contre les maladies sont courantes mais leur utilisation intensive présente un coût non négligeable et est de plus en plus critiquée pour son impact sur l'environnement. Les pathogènes possèdent également une capacité d'adaptation à ces produits, ce qui peut diminuer rapidement l'efficacité de ces derniers. L'agriculture de demain se tourne donc vers des méthodes de lutte alternatives et cherche également des moyens d'optimiser les techniques actuelles. Pour ce faire, des modèles capables de simuler et prédire les risques d'épidémies, voire de suggérer des stratégies d'épandage, sont de plus en plus étudiés.

Les plus prometteurs s'appuient sur la physique régissant la propagation des maladies. Par exemple, la Septoriose, un champignon affectant notamment le blé, est dispersée majoritairement par la pluie. La modélisation de sa propagation fait intervenir des informations de domaines variés telles que les interactions biologiques du pathosystème blé-Septoriose, la distribution en taille et vitesse des gouttes de pluie ou les caractéristiques des plantes. Ces modèles font l'objet de recherches intensives mais certains éléments, notamment liés à la physique de la fragmentation liquide, restent obscurs. Cette maladie est connue pour se propager d'une plante et d'une feuille à l'autre via des éjections de gouttelettes contaminées. Ces gouttelettes sont en général produites lors de l'impact d'une goutte sur une feuille malade sur laquelle de l'eau contaminée est déjà présente. La compréhension de la physique régissant la fragmentation et l'éjection de gouttelettes contaminées à l'échelle de la feuille et de la goutte pourrait améliorer la robustesse et la précision des modèles prédictifs de risque, ainsi que leur polyvalence.

L'objectif poursuivi dans ce travail de recherche expérimental est donc l'étude de la physique régissant la fragmentation lors d'un impact de goutte. Le scénario appelé crescent moon est une configuration d'impact récemment identifiée comme étant à la fois fréquente et efficace dans son mécanisme d'éjection de gouttelettes. Il consiste en l'impact d'une goutte à proximité d'une autre goutte contaminée déjà présente sur la feuille. Au moment de l'impact, la goutte impactant s'étale sur la surface et interagit avec celle au repos, la forçant à s'étirer dans l'air en un film liquide asymétrique qui se déstabilise ensuite en gouttelettes. Ce phénomène est tridimensionnel ce qui le rend complexe à caractériser quantitativement. Nous proposons donc d'étudier une configuration simplifiée mais qui reproduit les caractéristiques principales du crescent moon: l'impact d'une goutte unique à proximité du bord d'un substrat plat et sec. Au moment de l'impact, la goutte va s'étaler sur le solide puis dans l'air après avoir atteint le bord du substrat. Le film liquide qui se développe alors dans l'air présente une asymétrie et des caractéristiques similaires à celles observées dans le cas tridimensionnel. Cependant, le film liquide ici obtenu, reste dans

le plan du substrat, ce qui facilite l'étude quantitative de ses propriétés.

Trois paramètres de ce processus ont été variés systématiquement: (i) la vitesse d'impact, qui modifie l'énergie cinétique de la goutte impactant et donc sa propension à se fragmenter, (ii) l'offset, i.e., la distance entre le point d'impact et le bord du substrat, qui influence l'asymétrie du film liquide et l'éjection des gouttelettes et (iii) l'inclinaison du substrat et donc l'adjonction d'une vitesse tangentielle au moment de l'impact.

L'analyse de la cinématique du film liquide a commencé par le suivi de l'étalement du liquide sur le substrat. L'étalement maximal ainsi que le temps nécessaire au liquide pour atteindre le bord ont été mesurés. Ces deux valeurs sont en effet des paramètres clés décrivant l'historique du liquide sur le solide. L'évolution du film liquide dans l'air a ensuite été quantifiée en suivant les directions normale et tangentielle au bord. En particulier, nous avons mesuré l'extension maximale dans les deux directions ainsi que le temps nécessaire pour les atteindre et nous avons dérivé des lois d'échelles décrivant leurs liens aux paramètres d'entrée. Trois scénarios de rétraction du film liquide dans l'air ont été identifiés sur base du degré d'asymétrie observé. L'occurrence de ces scénarios a été mise en relation avec les paramètres d'entrée via, notamment, la comparaison des extensions du film liquide dans ses directions normale et tangentielle au bord.

Enfin, nous avons porté notre attention sur l'éjection des gouttelettes et sur leur lien avec l'asymétrie du film liquide. En tout, quatre mécanismes d'éjection de gouttelettes ont été identifiés dont un, en particulier, lié à l'inclinaison du substrat. La vitesse et la masse des gouttes a été quantifiée et des lois d'échelle décrivant leur dépendance aux différents paramètres d'entrée sont proposées. Nous avons mis en évidence un lien direct entre le comportement du film liquide et le schéma d'éjection des gouttes. Au-delà d'un certain seuil, nous avons également montré que le degré d'asymétrie, modifié via la distance entre le bord du substrat et le point d'impact, n'influait plus sur la distance maximale parcourue par les gouttelettes éjectées. La taille des gouttes éjectées pour une même distance, en revanche, augmente avec l'asymétrie du film liquide. L'inclinaison du substrat devrait, théoriquement, réduire la distance parcourue par ces gouttelettes à taille et vitesse données, au vu du régime aérodynamique dans lequel elles se trouvent. Cependant, nous avons pu montrer que, par des effets de l'inclinaison sur les masses et les vitesses, la distance maximale parcourue par les gouttelettes éjectées présente un optimum pour une inclinaison non-nulle du substrat.

Ces résultats nous offrent des informations sur la physique de la fragmentation en configuration asymétrique. Leur implémentation pourrait améliorer la robustesse des modèles de propagation des maladies transportées par la pluie. Des évaluations du risque d'épidémie plus précises et une robustesse accrue de ces modèles devraient encore promouvoir leur développement et augmenter leur utilisation dans le contexte d'une agriculture plus respectueuse de l'environnement.

# Acknowledgements

I want to begin this acknowledgement by thanking my advisor, Prof. Tristan Gilet who came up with this idea that I could become a scientist. I want to thank you for giving me this opportunity to wonder and ask questions about plants and droplets. I learned a lot and you were always patient and enthusiast, ready to push me toward the next question to be answered and helping me navigate through this journey. Your curiosity and scientific mind always amazed and inspired me. I want to thank you for your availability to all of your researchers throughout the years. It is, I believe, an invaluable quality. I wonder, after rainstorms and caves, where next you will bring the high-speed camera. It has been an amazing experience. Thank you.

I gratefully acknowledge the members of the examination committee, Dr. Stéphane Dorbolo, Prof. José Manuel Gordillo, Dr. Laurence Ramos, Dr. Sébastien Saint-Jean and Prof. Vincent Terrapon for agreeing to be part of my jury and to dedicate some of their time to the evaluation of this thesis.

Part of this work has been done in collaboration with Lydia Bourouiba from the Fluid Dynamics of Disease Transmission Laboratory at the Massachusetts Institute of Technology, which I want to acknowledge. She invited me to her lab and gave me this opportunity to uncover new ways of working. It was an experience full of learnings and discoveries.

This research was financially supported by the Belgian National Fund for Scientific Research-F.R.S.-FNRS through a research grant attributed by the Fund For Agriculture and Industrial Research (FRIA), which I thank. I also want to acknowledge the University of Liège and the Camille-Hela Foundation for their support as well as the Rotary Foundation that supported me through a District 1630 grant. I take this opportunity to address a special thank to Philippe Wittorski, Philippe Vanstalle and the members of the Rotary Club of Flémalle for their warm welcome, their coaching and their interest in my research. I also want to thank Willy Zorzi for his help as Rotary Coordinator for the University of Liège.

I want to thank Prof. Marteen Arnst, Dr. Stéphane Dorbolo and Dr. Davide Ruffoni for agreeing to be part of my annual thesis committee meeting and for their support and suggestions. I am also grateful to Dr. Sébastien Saint-Jean for welcoming me in the Ecosys Lab in Thierval-Grignon for some visualizations of impacts on wheat. Thank you for bringing my thesis closer to the field reality and for sharing your enthusiasm and experience.

In four years, many people cross your path. There are many which I will not be able to cite but I want to thank all these people that, each in its own way, has participated to make these four years a great experience.

From my stay at MIT, I want to thank my lab and office mates Maxime Inizan, Thimothée Jamin, Jesus Alvelo, Matthias Mayser, Youngsoo Joung, Stéphane Poulain, Julia Klinkert, Jia Su and Yongji Wang for the wonderful times, the scientific discussions, for your help in the lab with the drop tower,

the high speed camera or the autoclave among so many other things and for your support. Maxime and Thimothée, there is one Halloween in Salem that I will not forget! Thank you Jesus for showing me around with the bacteria but also for your support in times of need and of party and for your determination. I also met wonderful people from other labs such as Elise Ledieu and Estelle Clerc with which I had scientific discussions but that also made me feel at home far away from Belgium. In this, I do not forget Queralt Altés Buch either. I had a wonderful time with you in Boston and in Liège.

I am also grateful to all the people at the University of Liège who, by their everyday work made my life easier. I have a special thought for Pascal Harmeling and Antonio Martinez who punctually but very kindly, fixed urgently needed material or helped me in the design of some setup. I also want to thank my colleagues from the Microfluidics Lab: Matthias Mayser, Naresh Sampara, Julien Straat, Brice Begasse, Arnaud Peters, Antonio Iazzolino, Youness Tourtit, Justine Parmentier, Loïc Tadrist, Stéphanie van Loo and Sophie Gernay. To all of you, I want to say thank you for the great atmosphere in the lab, for the Funny Friday Experiments and the great discussions around tea breaks. Especially, thank you Loïc for your support on so many levels but also for bringing people together. Stéphanie, I also really enjoyed our trip in Boston. Your determination is inspiring and I am grateful to you for your coaching and your time in these last few weeks. Sophie, I miss our talks about science, books, sports and the way the world is. Thank you for the great times and the support at all times, thank you for the help in proofreading the manuscript too. I am looking forward to our next meeting.

Enfin, cette thèse n'aurait pas vu le jour sans le soutien de mes amis et ma famille que je tiens à remercier tout particulièrement. Merci donc à Céline Kluten pour la remotivation et à Antonio Sutera pour m'avoir coachée au FRIA et pour les discussions animées à propos de la vie académique et autres. Je tiens aussi à remercier Gilles Ghysens pour m'avoir épaulée comme il l'a fait. Merci à Nathalie Schnackers et à Stella Dederen pour tout, pour ces années d'amitié et ces moments partagés. Merci à mes parents, à mes soeurs et à mon frère qui ont vécu cette thèse en même temps que moi. Et finalement, merci à toi Joachim, qui m'a poussée vers la dernière ligne droite en connaissance de cause. Cette thèse, c'est aussi un peu la vôtre.

# List of variables and parameters

Table 1: List of variables and parameters

| Symbol | Meaning | Value/Range (room T° ≃ 20°C) |
|---|---|---|
| | **Physical properties and initial conditions** | |
| $d$ | offset | 2.4 - 12 mm |
| $R_0$ | initial drop radius | 2.4±0.03 mm |
| $V_0$ | initial drop speed | [1.6 - 6] ±0.1 m/s |
| $M_0$ | initial drop mass ($M_0 = 4\pi R_0^3/3$) | 57.9 ±2 mg |
| $\alpha$ | inclination of the substrate | -40°, -20°, 0°, 20°, 40°, 60° |
| $\rho$ | water density | 1000 kg/m$^3$ |
| $\nu$ | water kinematic viscosity | $10^{-6}$ m$^2$/s |
| $\sigma$ | water surface tension | 70±2 mN/m |
| | **Characteristic times and dimensionless numbers** | |
| $t_i$ | impact time - $t_i = 2R_0/V_0$ | [2.9 - 0.8] ms |
| $t_c$ | capillary time - $t_c = \sqrt{4\rho R_0^3/(3\sigma)}$ | 16.2 ms |
| $Oh$ | Ohnesorge number - $Oh = \sqrt{\nu^2\rho/(2R_0\sigma)}$ | 0.0017 |
| $Fr$ | Froude number - $Fr^2 = V_0^2/(2gR_0)$ | 50 - 800 |
| $We$ | Weber number - $We = 2\rho R_0 V_0^2/\sigma$ | 186 (◯), 367 (▷), 520 (▽), 700 (☆), 1340 (□), 2000 (△), 2435 (◇) |
| | **Sheet spreading on solid** | |
| $R_{sn}$ | spreading radius on solid, measured normally to the edge ($R_{st}$ for tangentially and $R_s$ for $\alpha = 0°$) | [mm] |
| $R_{snM}$ | maximum of $R_{sn}$ [$R_{stM}$ (resp. $R_{sM}$) for $R_{st}$ (resp. $R_s$)] | [mm] |
| $t_{snM}$ | time of $R_{snM}$ [$t_{stM}$ (resp. $t_{sM}$) for $R_{stM}$ (resp. $R_{sM}$)] | [s] |
| $\delta$ | dimensionless offset - $\delta = d/R_{snM}$ | [-] |
| $t_d$ | time at which the liquid reaches the edge of the substrate | [s] |
| | **Sheet expansion in the air** | |
| $l_n$ | extension of the air sheet normal to the edge | [mm] |
| $l_{nM}$ | maximum of $l_n$ | [mm] |
| $t_{nM}$ | time of $l_{nM}$ | [s] |
| $\tau_n$ | dimensionless normal time - $\tau_n = (t - t_d)/(t_{nM} - t_d)$ | [-] |
| $l_t$ | extension of the air sheet tangential to the edge | [mm] |
| $l_{tM}$ | maximum of $l_t$ | [mm] |
| $t_{tM}$ | time of $l_{tM}$ | [s] |
| $t_r$ | time of the sheet collapse along the edge | [s] |
| $\tau_r$ | dimensionless time of collapse along the edge - $\tau_r = (t_r - t_d) / (t_{nM} - t_d)$ | [-] |
| | **Droplet ejections** | |
| $v$ | horizontal ejection speed of a droplet | [mm/s] |
| $\theta_v$ | ejection angle of a droplet | [°] |
| $v_T$ | average speed of droplets ejected at a given $\tau_n$ | [mm/s] |
| $m$ | mass of a droplet | [mg] |
| $\Phi(X)$ | maximal value of a variable X taken as the cut-off of its CDF | [/] |
| $x$ | distance travelled horizontally from ejection by a droplet | [mm] |
| $\Psi$ | asymptotic value travelled by a droplet - $\Psi = \lim_{t\to\infty} x$ | [mm] |
| $\Psi_M$ | maximum value of $\Psi$ | [mm] |
| $Q_i(X)$ | quantile function of a variable X taken at i percent | [/] |

# Contents

# Chapter 1

# Introduction

## 1.1 Crop losses and foliar diseases

Crop diseases amount to around 10 percent of the world losses nowadays despite the use of mitigation techniques (Oerke, 2006). These losses cost billions of dollars each year and put pressure on fragilized communities (Strange & Scott, 2005). The still growing world population will require an increased food production (Chakraborty & Newton, 2011) and with a growing awareness of the population, this production should be performed in a sustainable way as to preserve our limited resources. Crop diseases are caused by pathogenic agents such as fungi, bacteria or viruses that propagate in the crops through dispersal agents and vectors such as wind, rain or insects (Strange & Scott, 2005). In the past decades, our agriculture practices have evolved towards global intensive monoculture which relies heavily on chemicals and resistant varieties to control diseases (Oerke, 2006). Yet the efficacy of fungicides, notably, has been shown to decrease due to the selection of resistant strains (Leroux *et al.*, 2008; Pangga *et al.*, 2011). For all these reasons, a change in our crop and disease management routines is required. For a more sustainable agriculture, integrated techniques could make use of a better understanding of the causes and propagation paths of diseases to prevent their physical spreading. Among these techniques, some can rely on mixed crop varieties (Wolfe, 2000) but also on disease outbreak prediction and decision support systems (Cook, 2000). Experiments on grapevines showed that a 30 to 70 percent reduction in pesticide use was achievable through the use of forecast models (Pertot *et al.*, 2017). In general, chemicals are sprayed at a dose higher than necessary and long term benefits in terms of savings and benefits for the environment could be drawn from the increased development and use of integrated farming (Jorgensen *et al.*, 2017).

Developing such techniques will require increased collaboration between the scientific and agricultural communities and increased awareness of the current challenges at a political level (Strange & Scott, 2005; Sherman & Gent, 2014; Pertot *et al.*, 2017). User friendly but also more accurate models are thus steps in implementing such disease management methods.

In this context, our research focuses on a better understanding of one of the major physical processes responsible for disease propagation in fields, namely rain-splash mechanisms. Pathogens can affect various parts of the plant such as the leaves, the stems or the fruits, causing losses in yields not only during growing season but also later on. We chose here to focus on foliar disease which are known to rely on rain-propagation as their main dispersal agent (Fitt *et al.*, 1989; Huber *et al.*, 2006).

Foliar diseases target the leaves of the plants. Currently in Europe, one of the most devastating is the Septoria leaf blotch (Fones & Gurr, 2015). It is caused by a fungus that affects wheat, the first cereal produced in the European Union and one of the top three worldwide. Septoria is present all over the world. It can cause a loss in yield up to 50% on susceptible varieties and is responsible in the European union for 70% percent of the

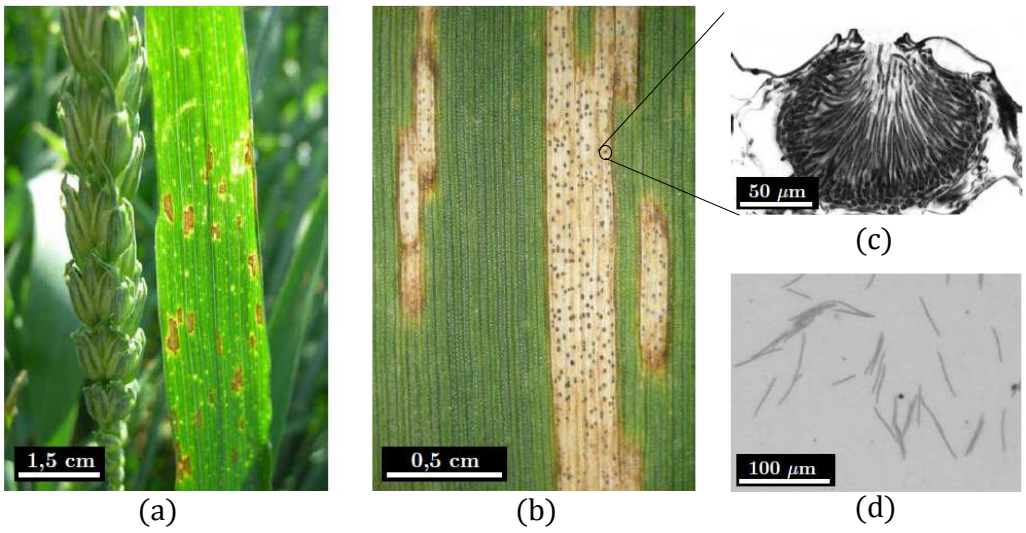


Figure 1.1: (a) Flag leaf beneath the grain showing septoria lesions (b) Sporulating lesions of septoria on a wheat leaf. (c) Pycnidium, the asexual fruiting body producing the asexual reproduction spores, the pycnidiospores (slice view) (d) Pycnidiospore under optical microscope. [Pictures from Gigot (2013), INRA-ARVALIS, with (c) adapted from Kema *et al.* (1996)]

fungicide use (Fones & Gurr, 2015). Beside fungicide application, the control of septoria is mainly performed through the use of resistant cultivars but both techniques have their limits. Septoria is a perfect example of the damage a pathogen can cause. It presents reproduction and dispersal cycles, representative of foliar diseases, which makes it highly adaptive to new chemicals and resistant varieties. Thus, despite continuous research on this pathogen, its control remains a challenge to be tackled by farmers every year thus the motivation to improve integrated and alternative techniques of disease management. These reasons make the Wheat-Septoria a representative example of a host-pathogen interaction, which we will use as model in this introduction to disease dispersal and management.

## 1.2 Wheat-Septoria pathosystem: Modes of propagations

The septoria leaf blotch is caused by a fungus that develops in the leaf tissues. It is characterized by necrotic tissues with a brownish colouration (Fig 1.1 - a) on which dark spots are visible (Fig 1.1 - b). These blotches are the fructification (Fig 1.1 - c) in which asexual (pycnidiospore - Fig 1.1 - d) and sexual (ascospores) spores develop. The necrotic lesions can cover an important area of the leaf. When situated on the flag leaf (the top one), this will hinder the ability of the wheat plant to harness nutrients in the ear, reducing yield.

The infection cycle of septoria is composed of an initial primary inoculum cycle and of a polycyclic secondary one, which occurs multiple times during the growing season as illustrated in Fig. 1.2a. The primary inoculum infects young leaves in autumn and is mainly composed of ascospores originating from infected residues on the ground, from infected seeds or through wind borne spores among other sources (Suffert *et al.*, 2011). These spores initiate the disease, which then enters multiple infectious cycles, illustrated in Fig. 1.2b. The infection cycle can be divided in four main phases (Robert *et al.*, 2008), which are here illustrated in terms of timing in the case of the asexual reproduction spores:

- Infection. The spores land on leaf tissue and infect it by penetrating into the stomata (breathing cells of the leaves) if they germinate. Germination requires certain temperatures as well as high humidity conditions or full wetting for a prolonged period

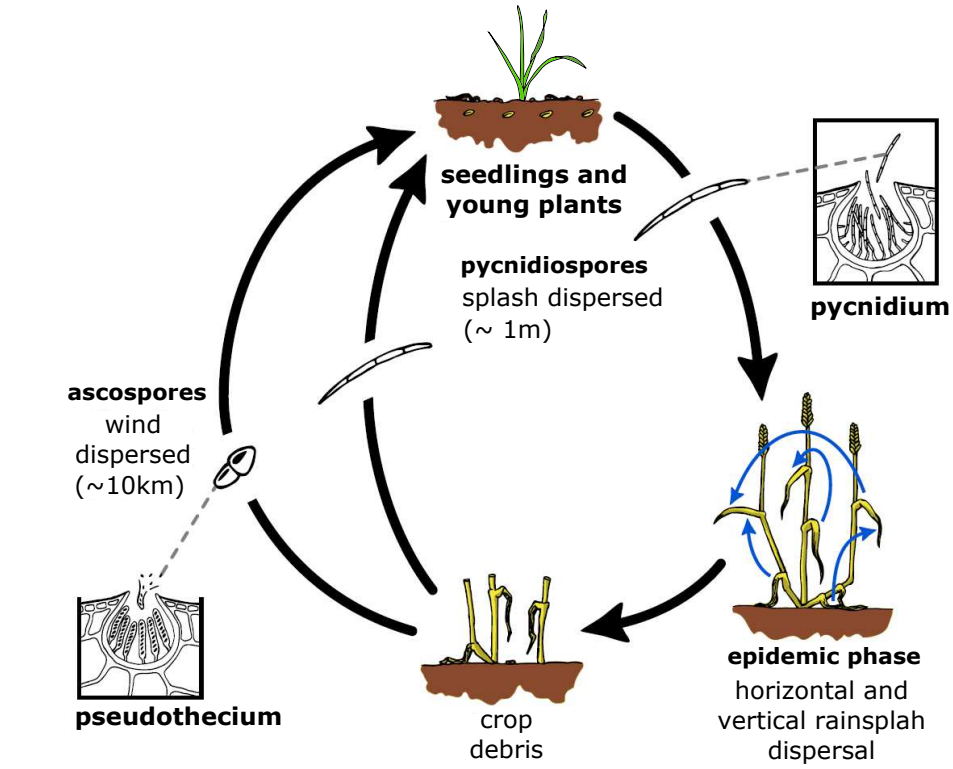


(a)

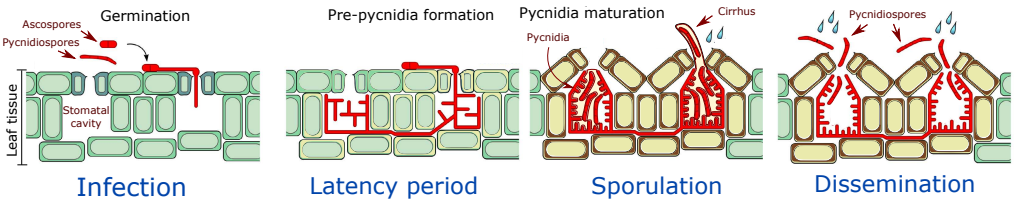


(b)

Figure 1.2: (a) Simplified biological cycle of the septoria leaf blotch fungus (Zymoseptoria graminicola). Ascospores (resp. pycnidiospores), issued from the sexual (resp. asexual) reproduction, are produced in modified sub-stomatal cavities, named pseudothecium (resp. pycnidium). [Adapted from Gigot (2013)] (b) Summary of plant infection stages by septoria leaf blotch. Ascospores or pycnidiospores land on the wheat leaf epidermis, where they germinate and enter the leaf tissue via stomata (Infection). The pathogen colonizes the substomatal cavity and invades the surrounding tissue. Pre-pycnidia are formed in the colonized substomatal cavities (Latency period). When the necrotrophic phase begins, the release of plant nutrient from the dying host tissue allows rapid fungal growth and proliferation. Fungal pre-pycnidia mature into pycnidia, which produce pycnidiospores. In the presence of water, these can be exuded in a mucilagenous substance named cirrhus (Sporulation). The pycnidiospores are removed by water splash and able to spread the infection (Dissemination). [Adapted from Steinberg (2015)]

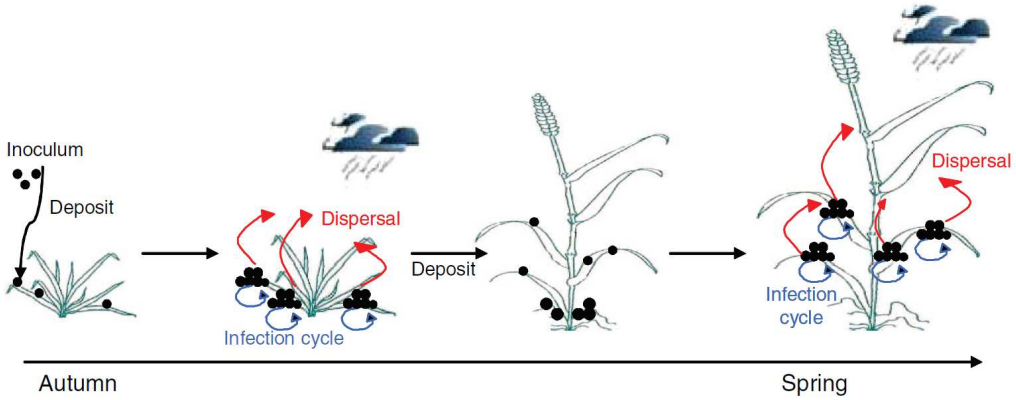


Figure 1.3: Schematic of the development of a polycyclic foliar epidemic resulting from the succession of infection cycles (during which spores are produced) and spores dispersal. During the growing season, as the wheat plants develop, spores reach new green tissues and the epidemic progresses from the lower infected leaves to the upper leaves of the plants at every favourable rain event. [Adapted from Robert *et al.* (2008)].

of time (Castilla *et al.*, 1996). This infection process is estimated to last between 12 and 24 hours (Rapilly & Jolivet, 1976).

- Latency period. Once the pathogen has entered the leaf tissue, it invades intercellular space and develops at first without visible consequences. When the pycnidium, i.e., the reproductive fructification bodies (or pseudothecium in the case of sexual reproduction), is ready to develop, it induces the destruction of cell walls of the leaf and lesions become apparent at the leaf surface. This takes between 11 and 42 days depending on the temperature and environmental conditions (Lovell *et al.*, 2004).

- Sporulation. This phase is characterized by the appearance of black necrotic sporulating symptoms at the lesion sites with the formation of pycnidiospores in the sub-stomatal cavities. Upon wetting, these structures release the spores in a whitish mucilage called cirrhus.

- Dissemination. This final stage consists in the dissolution of the cirrhus in water and the release of contaminated water at the surface of the leaf. Further incoming raindrops will then splash these spores away. The spores contained in the splashed droplets will travel with them until reaching a new leaf and the cycle starts anew.

This cycle lasts 15 to 21 days on average so it takes place during the whole growth season and dispersal can occur at each rain event (Fig. 1.3). Note that ascospores are also produced during the whole season.

Each type of spore has a preferential way of detaching and travelling. Ascospores [10-15 x 2-3$\mu m$ (Eyal, 1987)] are very light and easily detachable. They can be detached from the leaves through wind-induced leaf motion [(Sache, 2000) for rusts], by rain-induced motion or by direct contact with an impacting drop (Alt & Kollar, 2010; Suffert *et al.*, 2011). Once detached from the leaves, they will mainly be advected by wind which allows them to travel considerable distances of the order of kilometers (Shaw & Royle, 1989). Pycnidiospores [35-98 x 1-3$\mu m$ (Eyal, 1987)], are trapped in a mucilage, a mixture of sugar and proteins that dissolves in water (Fitt *et al.*, 1989). The spores thus require the presence of water for release. They will mainly be dispersed by rain splash and travel much shorter distances, typically ranging from a few centimetres to 1 meter (Fitt *et al.*, 1989). Splash dispersal allows an upward propagation towards newly formed healthy leaves (Walklate, 1989). Contamination of new leaves can also occur by direct contact with infected ones

during wind or rain-induced motion, or through insect or human vectors (Castilla *et al.*, 1996).

The asexual reproduction cycle can thus be quite short given the right humidity conditions and allows the septoria to propagates quickly in a field. The sexual reproduction cycle takes longer to create new spores [in the order of several weeks (Ponomarenko *et al.*, 2011)] but the resulting spores participate to the genetic diversity and can travel much longer distances through wind advection. It is the combination of this double modes of reproduction (sexual and asexual) and propagation (wind and rain) that renders the septoria hard to mitigate.

The sexual reproduction mode of the pathogen generates a mix of the genetic pool. The large distances of propagation of its spores allow the transmission of these pools of genes across fields. The asexual reproduction ensures a fast spreading of the selected pathogens. This can cause high damages on the yields of fields with reduced genetic diversity especially on susceptible cultivars (Fones & Gurr, 2015). The septoria is thus particularly efficient to adapt to new chemicals and resistant varieties and to quickly spread the selected pathogens. It explains the current state of the mitigation techniques without fully resistant cultivar or fully working chemicals, products which are both costly and time consuming to develop (Leroux *et al.*, 2008). It it thus important to limit the selection pressure on the pathogens by limiting the amount of chemicals sprayed and by working on combined strategies using mixtures of cultivars for example (Pertot *et al.*, 2017; Jorgensen *et al.*, 2017). The development and increased implementation of more sustainable mitigation techniques is thus a key component for the agriculture of tomorrow.

## 1.3 Mitigation techniques

Beside fungicides and resistant cultivars, more sustainable classical mitigation techniques are already widely used, such as crop rotation or the burning of crop residues on which primary inoculum hivernates. More recently, new biopesticides have been developed and we observed a renewed interest for alternative mitigation techniques (Pertot *et al.*, 2017). Such methods include the use of cultivar mixtures with various resistance. These mixed varieties reduce the incidence of diseases both in general (Calonnec *et al.*, 2013) and on large scales as shown by the experiment conducted in China on rice blast by Wolfe (2000). A reduction by around 40% of the disease impact on susceptible wheat cultivar was evidenced in mixture fields when compared to the pure strand by Gigot *et al.* (2013). The mixing of varieties with various levels of resistance also appears to have additional effects such as the stabilization of yield (Gigot *et al.*, 2013). A non-uniform canopy architecture also displays protective properties as evidenced in the work by Vidal *et al.* (2017, 2018) where susceptible plants displayed significantly lower disease incidence in heterogeneous mixtures than in pure strands. Associating lower yield strands that have a high resistance to diseases with more susceptible strands presenting a higher yield would allow to reduce the amount of pesticide (and save money) and to alleviate the selection pressure on disease strands while maintaining high yield potential (Metcalfe *et al.*, 2000).

Mathematical predictions of risk of outbreaks have been associated with monitoring decision aid programs to better target the use of chemicals (Pertot *et al.*, 2017; Jorgensen *et al.*, 2017). This area of research has a large field of application and not only for the control of septoria. For example, there is an increased demand for more sustainably produced vine and growing concerns about the effects of the chemicals on human health. In vineyards however, many sustainable traditional techniques cannot be applied. Rotation would mean to loose the traditional varieties and mechanical protections like insect nets would induce unacceptable visual pollution. In such cases, the use of decision support systems have proven efficient to identify optimal timings of application and thus reducing

sprayed chemical amounts. In an experiment in France, application of fungicide against downy mildew could be reduced in one case by around 55%, saving between 174 and 224€€ per hectare (Pertot *et al.*, 2017). Such results are stimulating for further research in this domain and notably motivates the improvement of the mathematical models predicting risks of outbreaks.

## 1.4 Disease dispersal models

To better understand disease dynamics and improve our mitigation techniques, models of disease propagation have been developed using two very different approaches. The first relies on empirical data, using disease dispersal gradients measured at the field level and relating rainfall intensity to disease spreading (Gregory, 1968; Fitt *et al.*, 1987; Ojiambo *et al.*, 2017). These models are easy to implement but do not offer any insight on the physics behind the spreading and their results are not easily transposable to other crops or situations. The other approach is based on a physical process modelling. These models also rely on statistical data that are now collected at the rain and plant level and used as inputs to take into account the physical ingredients underlying the transport of diseases. As such, they can offer a better understanding of the influence of various parameters on the spread of the diseases as well as be used as aid-to-decision tools. One of these early model is the one by Rapilly & Jolivet (1976), which is based on a light-scattering approximation to model splash dispersal through canopy. Another approach by Yang *et al.* (1991a) uses a diffusion equation to describe the splash dispersal. These early models are based on simplifying assumptions like a homogeneous medium of dispersal. Piling up on these results, complexities have been added over the years, aided by the increasing computational power available, notably, to take into account the 3D canopy structure using Monte-Carlo integration as illustrated in Fig. 1.4a (Saint-Jean *et al.*, 2004). Robert *et al.* (2008) used Rapilly & Jolivet (1976) results coupled to a 3D virtual wheat model adding a temporal variation of the structure of the plant. They simulated the effect of canopy architecture on the plant-pathogen interactions and identified the plant architectural traits most susceptible to have an effect on disease spreading. Following these results, the effect of sowing density (Baccar *et al.*, 2011) and cultivar mixture (Gigot *et al.*, 2014) have been investigated, all examples illustrating the insights to be gained from physical approaches. Confirming the growing interest for such models, a general modelling framework has been proposed by Garin *et al.* (2014) to help regrouping knowledge around these functional-structural-plant models (FSPM) illustrated in Fig. 1.4b. Fungal epidemics are challenging to model since they include many aspects related to various fields of expertise (e.g., meteorology, biology, physics, computer science). The proposed framework divided the various "knowledge sources" into separate entities so that blocks can be modified and new ones added. This tool should help bring together this multidisciplinary knowledge and facilitate community interactions. One of the major input in the developed models is the link between incoming drops and resulting splash droplets as well as the content of these latter in pathogenic material. For this reason, this link has been widely investigated for the past thirty years as will be shown in the next section. Yet, very little has been done from a physical point of view, an observation that has led to the present work.

## 1.5 Rain splash dispersal

Rain is a key factor for the propagation of diseases. It can indeed intervene in the three steps usually identified (Fitt *et al.*, 1989) to transport a pathogen from one host to the next:

- Removal of the pathogen from the host leaf.
- Transport from the host leaf to a new location.

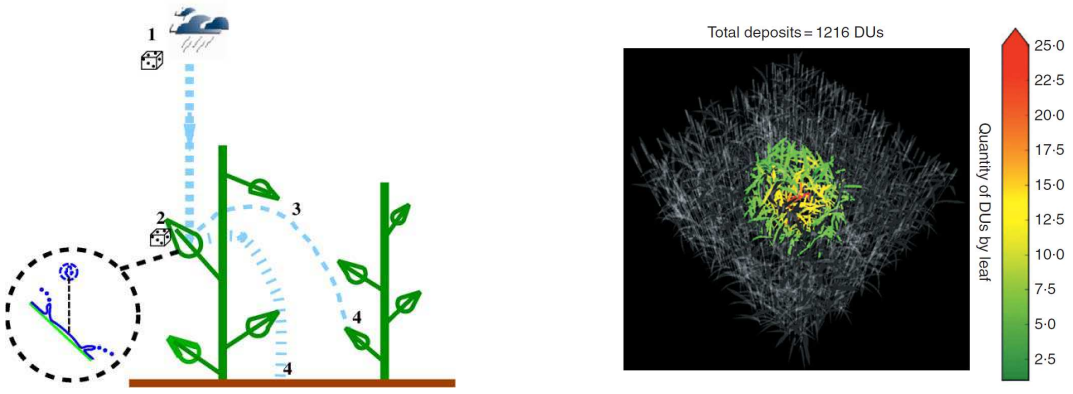


(a) (b)

Figure 1.4: (a) Schematic representation of the interaction between raindrops and canopy elements. One iteration step of a Monte-Carlo integration modelling water transfer by rain-splash is shown: (1) sampling of the raindrops (2) the interception of the raindrop by an element of the canopy structure, followed by the production of the splash droplets and sampling of their characteristics (3) calculation of the curvilinear trajectories of the droplets (4) interception of each droplet by either the elements of the canopy or the ground. The model simulates stages (1), (2), (3) and (4). [Adapted from Saint-Jean *et al.* (2004)]. (b) Simulation of foliar fungal epidemics using functional-structural plant models. Distribution of dispersal units (DU) after one dispersal event due to rain, with source leaf indicated in pink on the figure, on a wheat cultivar. [Adapted from Garin *et al.* (2014)].

- Deposition of the pathogen on the new tissue where the infection cycle can begin (cf., section 1.2).

Removal mechanisms in which rain plays a direct or indirect role have been identified. Some spores are designed to be wind carried (such as the ascospores) and are waiting for a gust of wind to trigger their release. One indirect removal method is through the impact of a drop on a leaf carrying such spores, which can transmit enough kinetic energy to reach the discharge threshold (Alt & Kollar, 2010). Air-borne spores are then advected by wind or they can then be caught by incoming raindrops and contaminate them. The same spores sitting on the leaves can also be carried away by accumulated water on the leaf or by drops directly impacting the contaminated zone (Fitt *et al.*, 1989; Sache, 2000; Huber *et al.*, 2006). Other types of spores, among which the pycnidiospores from the Septoria, are formed in a sticky mucilage (cirrhus, Fig. 1.2b) in the sub-stomatal cavity and are exuded only in the presence of water (Fournet, 1969). This mucilage prevents the dispersal of the spores by wind alone but it can be dissolved if it remains wet for a sufficiently long time, leaving a suspension of spores on top of the leaf (Fitt *et al.*, 1989).

The kinetics of the pycnidiospore liberation from the sub-stomatal cavity has been analysed (Eyal, 1987) as well as the properties of the cirrhus (Fournet, 1969). For prolonged rain events, a mechanism of washing-off of the leaves by rain resulted in a depletion in the number of spores (Ntahimpera *et al.*, 1999). Yet, little is known about the properties of the contaminated liquid itself, resulting from the cirrhus dissolved in water. To our knowledge, no study reports the viscosity or the density of the spores to be expected in this resulting liquid. A high concentration of spores can change the rheological properties of the fluid, making it non-Newtonian as it is the case for red blood cells in full blood. Potential release of tensio-active substances by the cirrhus could also affect the surface tension of the liquid. Such informations are of primary importance when looking at the physics behind the splash mechanism. Viscosity and surface tension are well known to affect drop splashing and breakup (Stone, 1994; Clanet & Villermaux, 2002). Recent experiments involving impact of particle laden drops also highlighted significant effects of such solutions on the fragmentation (Grishaev *et al.*, 2015, 2017; Sauret *et al.*, 2017).

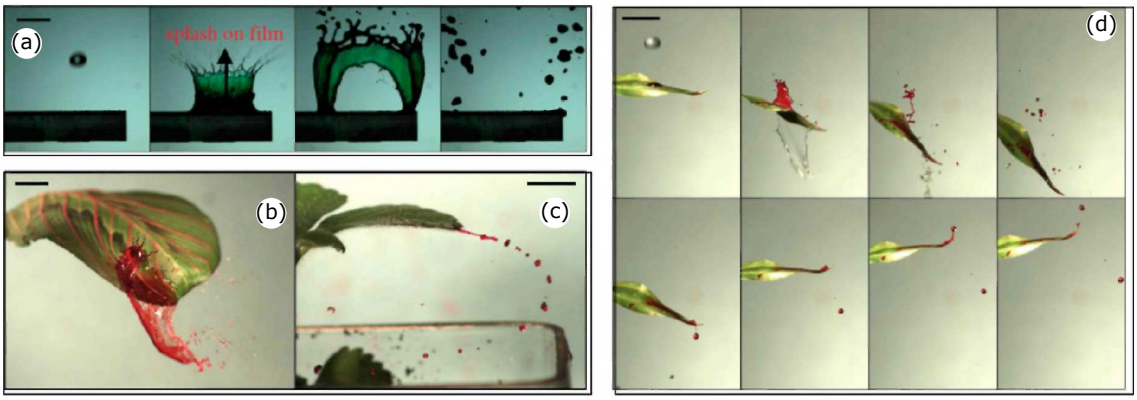


Figure 1.5: Ejection of potentially contaminated droplets (highlighted with dyed water) triggered by the impact of a raindrop (diameter 2.5 mm, velocity 6 m $s^{-1}$) on (a) a green liquid film (here in a 1 mm depth pool at the upper surface of a cantilever beam) at -2.5, 2.5, 17.5 and 62.5 ms after impact;(b) a prayer plant leaf at 6 ms after impact; (c) a strawberry leaf at 55 ms after impact; (d) a lucky bamboo leaf at -2,4, 8, 16, 52, 61, 69 and 74 ms after impact. In (b-d), a sessile drop containing pathogen analogue (red dye) is initially placed close to the impact point. Scale bars are 1 cm. [Adapted from Gilet & Bourouiba (2015)].

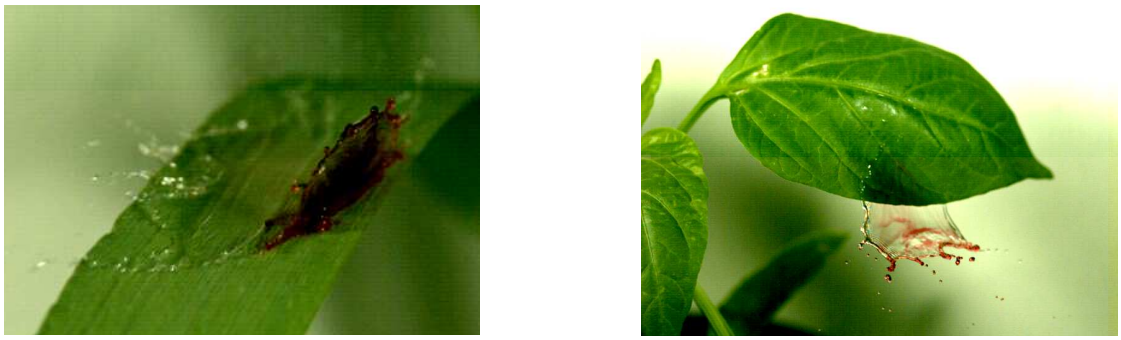

(a) (b)

Figure 1.6: (a) *Crescent-moon* scenario. A clear water drop impacts in the vicinity of a red dyed droplet sitting on a grass leaf. (b) A clear water drop impacts directly on a red dyed water residue sitting on a pepper leaf.

Further study concerning the proprieties of the contaminated liquid is thus required but falls beyond the scope of this work.

Analysis of the removal mechanisms showed that contaminated liquid will be present at the surface of the leaves but can also be found in impacting drops. Transport of spores through raindrops can thus occur through dripping of large contaminated drops which may fragment on a leaf beneath or by the direct impact of a contaminated drop. Yet until recently in the literature, the main rain-induced dispersal mechanism was considered to arise from the droplets emitted from the impact of a drop onto a contaminated water film (Fitt *et al.*, 1989).

Characterization of this method of dispersal has thus received much attention. Indeed, the number and size of the ejected droplets (or the number of spores), in relation to a given rain event or drop impact, is usually a key information in disease spreading models. Experiments to collect droplets and spores after rain events have been performed using traps and microslides in fields (Paul *et al.*, 2004; González-Domínguez *et al.*, 2014). The number of spores that land at a given position for example is then related to the rain intensity, namely the amount of rain received by a given area in a certain time expressed in mm $h^{-1}$. Rain-intensity has however been shown to be a poor indicator of splash dispersal as it neglects raindrop size distribution (Reynolds *et al.*, 1987; Walklate, 1989). A rainsplash index, which is a threshold value based on the kinetic energy of the drops, has been proposed to take the drop size and speed into account (Walklate, 1989). Another encountered way of characterizing splash dispersal distance is through the use of simulated rain [such as proposed by Reynolds *et al.* (1987)] or single (successive) drop impact experiments in laboratory. A correlation between raindrop characteristics such as its kinetic energy and the splashed heights and distances has been observed based on statistical droplet collection (Walklate *et al.*, 1989; Saint-Jean *et al.*, 2004; Perryman *et al.*, 2014). Yang *et al.* (1991b) used photographic measurements to study the size and speed of the ejected droplets resulting from drop impacts on strawberry fruits and Pietravalle *et al.* (2001) proposed a way to model rain splash trajectories. However, these results do not account for the drop-plant interactions nor for the fragmentation physics despite evidence of effects of the substrate such as the ground cover (Ntahimpera *et al.*, 1998) or leaf angle (Fitt *et al.*, 1992). Thus generalisation of these results to various plants and types of rain are challenging (Pietravalle *et al.*, 2001; Garin *et al.*, 2014).

Recent studies have shed new insights on the raindrop-leaf interaction (Gilet & Bourouiba, 2014, 2015). The study first highlighted the rarity of the commonly accepted scenario of impact on a uniform liquid film [Fig. 1.5 - (a)] (Rapilly & Jolivet, 1976; Fitt *et al.*, 1989) and instead, highlighted two other processes both frequent in natural raindrop-leaf interactions and efficient at emitting droplets. These mechanisms rely on the presence of sessile contaminated drops at the surface of the leaves. Drops instead of films are indeed more likely to be present at the surface of leaves due to their wettability that usually goes from slightly hydrophilic to super-hydrophobic for which the most famous example is the lotus (Gilet & Bourouiba, 2014). The first mechanism is called the *crescent-moon* and results from the direct interaction between the impacting raindrop and the contaminated sessile drop [Fig. 1.5 - (b)]. The second was coined inertial detachment as it results from the ejection of droplets through the motion of the leaf. This mechanism does not necessarily involve direct contact between the impacting and the sessile drop [Fig. 1.5 - (c)]. Combinations of both mechanisms have also been observed [Fig. 1.5 - (d)].

## 1.6 Content of the thesis

Crops around the world are still subject to losses due to pests and particularly to plant diseases. Feeding the ever growing population of the world will require to increase our food production in the future while developing sustainable techniques that will allow future

generations to prosper. Improving our mitigation techniques through a better understanding of disease propagation constitutes one step in this direction. One major propagation vector of these diseases is the rain. During rain events, pathogens are suspended in the water present on the leaves. Upon impact of an incoming raindrop, these pathogens are carried away in splashed droplets to the next healthy leaves. The interest for the physics of this phenomenon has been recently renewed by close observations of these individual splashes (Gilet & Bourouiba, 2014, 2015). The aim of this thesis is to investigate in detail one of these mechanisms to give insight into the key physical parameters governing the propagation of these droplets. Such physical building block could then be used to improve disease forecast and risk-assessment models to better target chemical uses. These models are indeed based on empirical statistical laws of droplets ejected upon impact, so taking the physics of liquid fragmentation into account could greatly improve their robustness.

In particular, we will focus on the *crescent-moon* scenario illustrated in Figs. 1.6a and 1.6b. Upon impact of the raindrop, the contaminated sessile drop is pushed aside and stretched into an asymmetric liquid sheet that develops in the air. This sheet then retracts and fragments into a myriad of contaminated droplets that are ejected away from the plant. These droplets are potentially the main carriers of splash-dispersed pathogens responsible for epidemics in field. We will thus look into the mechanism of the liquid sheet creation and destabilization into droplets.

After a review of the literature concerning drop impacts and fragmentation in Chapter 2, we develop a methodology to study a simpler analogue to the fully 3D *crescent-moon* and present the setup, experimental conditions and parameters that will be investigated (Chapter 3). The phenomenology is first introduced in Chapter 4. We then study how the asymmetry of the liquid sheet is influenced by our control parameters in Chapter 5. The ejection pattern is then related in Chapter 6 to the sheet kinematics and to the asymmetry patterns observed in Chapter 5 and we conclude on the influence of considering an asymmetric liquid sheet as primary source of ejected droplets in the context of foliar disease spreading in Chapter 7.

We have partly published these results in Physical Review Fluids (Lejeune *et al.*, 2018).

# Chapter 2

# State of the art

Drop impacts and fragmentation are relevant in a broad range of industry processes such as inkjet printing (Martin *et al.*, 2008), spray coating (Kang & Ng, 2006), cooling (Breitenbach *et al.*, 2018), air-wings de-icing (Antonini *et al.*, 2011) or for fuel engine injection (Moreira *et al.*, 2010). Applications can also be found in soil erosion (Furbish *et al.*, 2007), spraying (Wirth *et al.*, 1991), air-sea transfers (Yarin, 2006) and disease propagation (Gilet & Bourouiba, 2014) which is our main focus here. Drop impacts have received an increased attention from the scientific community for the past decades. From the work of Worthington (1877) and its first visualizations of impacts on liquids, huge progress has been made in the performance and democratization of high-speed imaging and computational power (Thoroddsen *et al.*, 2008). Thus thousands of scientific works on drop impacts only were published in the last 20 years. New technologies also broaden the scope of parameters to be varied, allowing the creation of microtextured substrates, varying wettability and geometry [e.g., Reyssat *et al.* (2006)].

Drop impacts on liquid layers have been the subject of extensive literature for which a good review can be found in the work by Yarin (2006). Yet, plant leaves are more likely to be hydrophobic, rendering the presence of liquid films on leaves less likely as pointed out by Gilet & Bourouiba (2014). The following brief review will thus focus on impacts on dry solid surfaces. For the same reason, literature investigating phase transitions during impacts (Jin *et al.*, 2015; Liang & Mudawar, 2017; Breitenbach *et al.*, 2018) or non-Newtonian fluids (Grishaev *et al.*, 2015; Boyer *et al.*, 2016) will not be discussed here.

## 2.1 Definitions

An extensive literature exists on drop impacts and fragmentation. Notations and terms are sometimes different from one reference to another. In this work we chose to apply the following definitions:

- Drop vs droplet: the term 'drop' will refer to the impacting drop while the term 'droplet' will be used when talking about the product resulting from the fragmentation.
- Sheet vs lamella: in this work, we reserve the term 'sheet' for a thin layer of liquid fully in the air, only possibly connected to the solid by its edge. When discussing spreading of liquid on a solid substrate, the terms 'lamella' or 'spreading liquid' will be used.
- Filament vs ligament: the term 'filament' is sometimes encountered in the literature to refer to the elongated ligaments that precede the destabilisation of liquid 'cylinders' into droplets. In this work, we reserve 'filament' for a phenomenon that will be introduced in Chapter 4, which is related to a mechanism of droplet ejection. 'Ligaments' will be used to refer to the elongated corrugations that destabilize into

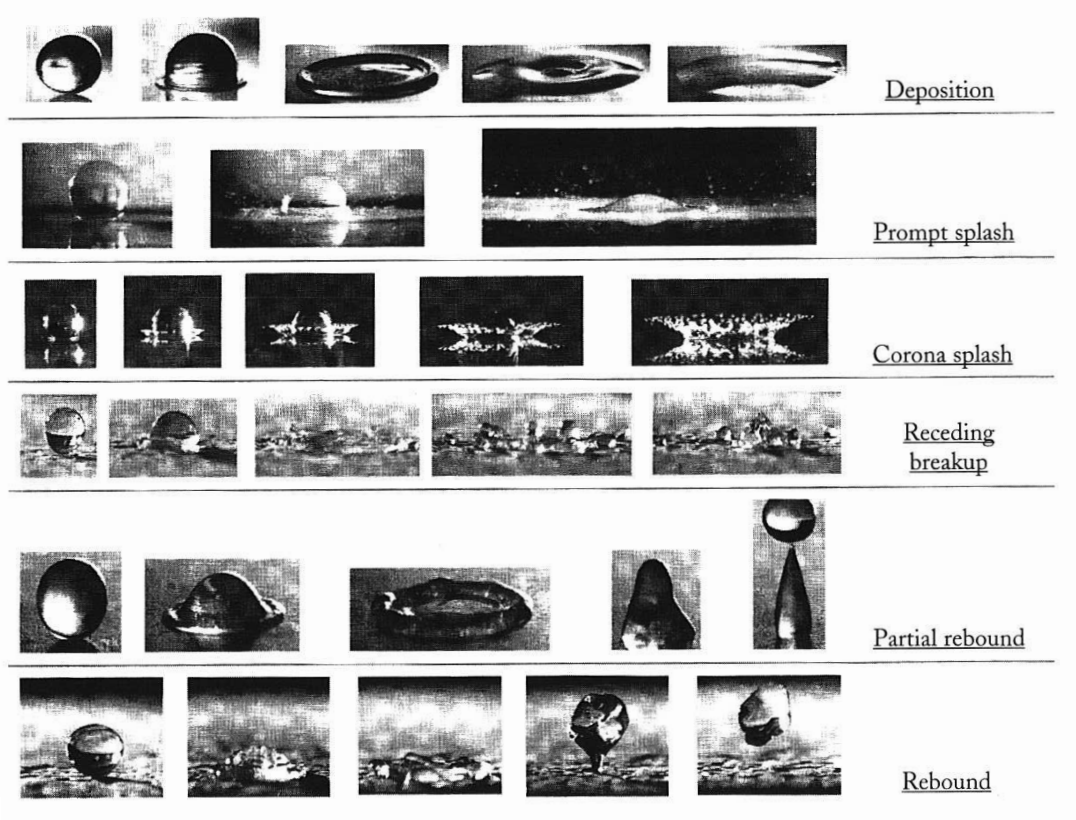


Figure 2.1: Examples from the six kinds of outcomes for a drop impacting a dry solid substrate [image from (Rioboo *et al.*, 2001)].

droplets either originating directly from the rim of the sheet or resulting from the liquid leftover from a collapsed sheet.

## 2.2 Drop impact on a dry solid surface

When a drop impacts on a solid surface, six main behaviours can arise (Rioboo *et al.*, 2001), as illustrated in Fig.2.1.

- The first is the 'deposition', where the drop upon impact deforms but remains in one piece on the surface during the entire process. This is usually observed for low impact speeds and smooth, wettable surfaces.
- The 'prompt splash' is observed for higher impact speed and rougher surfaces. It generates droplet ejections emerging from the contact line, so, at the interface of liquid, solid and gas phases. These droplets are emitted at early times when the spreading liquid has a high velocity.
- The 'corona splash' is observed when the spreading liquid lifts-off from the solid, resulting in a corona that eventually destabilizes into droplets. The difference with the prompt splash is that the corona is detached from the solid surface. Such phenomenon is usually associated with reduced surface tension or viscosity and is also characteristic of impacts on liquid films. The last three categories are classified depending on the retraction phenomenon observed.
- In the 'receding breakup', fragments of water remain on the substrate while the main drop recedes at the end of the impact, due to surface tension forces. This is directly linked to the decrease of the dynamic contact angle during the receding phase. If its value is low enough, droplets will be left behind.

- 'Partial rebounds' are only observed when a receding phase is present, so, for high values of contact angles, but also high impacting kinetic energy from the drop. When the receding liquid accumulates at the impact point, it is squeezed upwards. Depending on both the kinetic energy left to the fluid and on the receding contact angle, part of the liquid remains on the surface and part leaves it and we observe a partial rebound.

- The 'total rebound' is very similar to the partial one with the exception that the totality of the fluids jumps off the substrate.

These six phenomena are known to depend on the competition between inertia, viscous and capillary stresses (Bartolo *et al.*, 2005). The importance of each is usually quantified in terms of dimensionless numbers. For a spherical drop of radius $R_0$, density $\rho$, dynamic viscosity $\mu$, surface tension $\sigma$ and impacting normally a substrate at speed $V_0$, several dimensionless groups can be formed.

- The Weber number
$$We = \frac{2\rho R_0 V_0^2}{\sigma},$$
will be the main dimensionless number in this work. It compares the kinetic energy of the impacting drop $\rho\pi(2R_0)^3V_0^2/6$, to its surface energy $\sigma\pi(2R_0)^2$ which arises from the cohesive forces between the water molecules. The $We$ number can also be seen as the ratio of two timescales. We can define the impact time of the drop, meaning the time that the liquid located on top of the drop of radius $2R_0$ and falling at speed $V_0$ will take to reach the substrate if not slowed down. It is here equal to $t_i = 2R_0/V_0$. The lamella lifetime, meaning the time for the sheet to expand then retract, can be estimated by considering the system as an harmonic oscillator of mass $(4\pi/3)\rho R_0^3$ and stiffness coefficient $\sigma$. The characteristic time of the lamella lifetime, named the capillary time, scales thus as $t_c \sim \sqrt{4\rho R_0^3/(3\sigma)}$ (by definition we omit a $\pi$ factor). The Weber number then scales as $We \sim (t_c/t_i)^2$.

- The Reynolds number
$$Re = \frac{2\rho R_0 V_0}{\mu},$$
assesses the importance of inertial to viscous energy, which scale as $\mu(2R_0)^2V_0$.

- The Ohnesorge
$$Oh = \frac{\mu}{\sqrt{\rho\sigma D_0}} = \frac{\sqrt{We}}{Re}$$

- and the Capillary number,
$$Ca = \frac{\mu V_0}{\sigma} = \frac{We}{Re},$$
both assessing effects of viscous to surface energy, are also often encountered. The dimensionless groups are chosen depending on the characteristics of the system to be investigated.

A great deal of the literature has been devoted to determining transition regions for the different outcomes, investigating in detail effects of impact speed and size, wettability and roughness of the substrate (Mundo *et al.*, 1995; Range & Feuillebois, 1998; Rioboo *et al.*, 2001). Prompt splash for example, occurs when inertia largely overcomes capillary effects and a splashing parameter $K = We\mathrm{Oh}^{-2/5}$ was soon introduced by Stow & Hadfield (1980), yet it was also shown that this parameter does not account for roughness of the substrate (Rioboo *et al.*, 2001). Numerous impact conditions have been added that are not taken into account by the $K$ splashing parameter, such as the air pressure (Xu *et al.*, 2007)

or the motion of the substrate (Bird *et al.*, 2009). Even more recently, more complex substrates have been tested such as compliant ones (Howland *et al.*, 2016), illustrating furthermore the unlikeness of finding a universal criteria for disintegration mechanisms. The problem of splashing is thus not yet resolved as pointed out by Marengo *et al.* (2011) and Palacios *et al.* (2013) which provide good overviews of recent developments on the subject. A comprehensive fuel-spray-oriented review on the topic can also be found in Moreira *et al.* (2010).

Besides qualitative outcomes, each of these phenomena has received its own attention through experimental, theoretical and/or numerical studies. Comprehensive reviews can be found in Rein (1993) and Yarin (2006), dealing with impacts on both liquid and solid surfaces. Complex surfaces, such as substrates with non-uniform wettability, are investigated in Marengo *et al.* (2011). Even more recently, the review from Josserand & Thoroddsen (2016) gives a great overview of impacts on solid surfaces. This latter phenomenon will be our focus.

When a drop approaches and impacts a solid substrate, the fluid motion is brutally converted from normal to tangent to the substrate, leading to complex phenomena observed on various time and length scales. For example, observing the entrapment of an air bubble (Chandra & Avedisian, 1991; Thoroddsen *et al.*, 2005), the presence of an air-layer beneath the spreading liquid (Liu *et al.*, 2013) or ejections at the very early times (Thoroddsen *et al.*, 2012), all illustrated in Fig. 2.2, requires space resolution of a few micrometers and time resolution of nanoseconds (Thoroddsen *et al.*, 2012; Li & Thoroddsen, 2015; Visser *et al.*, 2015). By opposition, drop sizes are usually in the millimetre range and the spreading time of the order of a few milliseconds (Fig. 2.3a). The multiple time and length scales, added to the numerous changes of topology, explain the challenge of visualization and numerical simulation of such events. The time evolution of the liquid spreading factor $R_s/R_0$, defined as the radius of the spreading liquid over the impacting drop radius, is usually divided in four main sequences named by order of appearance (i) kinematic, (ii) spreading, (iii) relaxation and (iv) wetting phases as illustrated in Fig. 2.3b. Most studies that will be discussed in the following focus usually on one of these phases, such as the kinematic or the spreading phase, notably as it has been shown that the spreading behaviours dependencies to the entry parameters change depending on the phase observed (Rioboo *et al.*, 2002).

## 2.3 Drop impact dynamics

### Early dynamics

The impact early dynamics refers to the time period relevant in the kinematic phase, where there is no lamella apparent and the drop resembles a truncated sphere as in Figs. 2.2a and 2.3a [top left column] (Rioboo *et al.*, 2002). This period, which lasts usually less than a millisecond, is relevant for the bubble entrapment mentioned earlier and illustrated in Fig. 2.2a. Its behaviour is known to be self-similar and to depend on the drop size and impact velocity solely. It has been studied both numerically, experimentally and theoretically (Roisman *et al.*, 2009; de Ruiter *et al.*, 2010; Riboux & Gordillo, 2014; Philippi *et al.*, 2016) in order to derive the thickness and velocity profile of the liquid but also its temporal spreading, shown to grow as the square root of time (Rioboo *et al.*, 2002). The emergence of micro-droplets at these very early times has been captured by Thoroddsen *et al.* (2012) using 500 000 frames per second video imaging as illustrated in Fig. 2.2b. Finally, the recent study by Philippi *et al.* (2016) has shed some new insights on the dynamic and geometry of the early times of drop impact. They also highlighted new features through extensive drop simulation such as stagnation point structures, pressure distribution or contact line motion, showing that early time drop impact is not yet fully resolved despite decades of study.

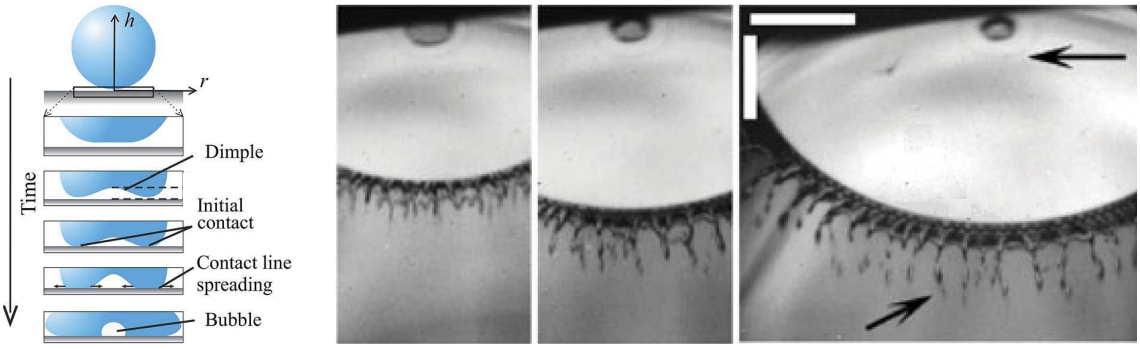


Figure 2.2: (a) Drop–substrate interaction in the initial stage of impact. The rectangle in the top image is enlarged in the subsequent images. Initially the drop flattens and forms a dimple, due to compression of the ambient gas between the drop and the surface. After the initial contact, the air under the dimple is entrained and contracts into a bubble. [Adapted from Visser *et al.* (2015)] (b) Observing the initial contact dynamics and micro-splashing of a water drop for $Re = 20200$ and $We = 1020$. The frames are taken from a 500 000 f.p.s. video sequence and show 24, 34 and 40 $\mu$s after the first contact. The arrows point to the edge of the entrapped air disc (top) and to the fingers shedding droplets (bottom). The scale bars are both 500 $\mu$m long, owing to the slightly oblique view. [Adapted from Thoroddsen *et al.* (2012)].

### Late dynamics

When no splashing is involved other variables are of interest. The maximum spreading radius $R_{sM}$ is relevant in many applications such as forensics (Adam, 2012; Laan *et al.*, 2014) or inkjet printing (Derby, 2010). In the context of this work, both the time evolution of the spreading radius $R_s(t)$ and its maximum value $R_{sM}$ are key informations. The history of the spreading on the solid substrate will condition the behaviour of the liquid sheet in the air observed in the *crescent-moon* scenario (introduced in Chapter 1). The maximum spreading radius will also condition the range of one of our entry parameter. A particular attention will thus be given to this topic.

Many studies have investigated the maximum spreading radius reached by drops after impact and various scaling laws or models have been proposed (Pasandideh-Fard *et al.*, 1996; Rioboo *et al.*, 2002; Roisman *et al.*, 2002; Clanet *et al.*, 2004; Roisman *et al.*, 2009; Eggers *et al.*, 2010), all in good agreement with the experimental data. All reported an increase in maximum radius with the impact speed but with various coefficients or scaling laws (Moreira *et al.*, 2010). The maximum spreading ratio of drop impact $R_{sM}/R_0$, indeed, does not vary as much as the impact speed. Moreover, asymptotic regimes where the viscosity can be neglected can hardly be investigated. To neglect viscosity and boundary layer effects, a very high impact speed is required. Yet, splashing occurs in such cases, and through ejected droplets, mass is removed from the bulk of the liquid. Mass conservation arguments applied to the bulk of the liquid are then no longer valid.

Nevertheless, two regimes are usually identified for maximum spreading of drops, viscous dominated and capillary dominated, both components being opposed to inertia. In the viscous regime (Chandra & Avedisian, 1991), the impacting kinetic energy

$$E_K \sim \rho R_0^3 V_0^2$$

is assumed to be entirely dissipated by viscous shear at the liquid-solid interface. The force per unit area opposing a radial flow, moving at speed $v_r$, until a maximum extension $R_{sM}$ can thus be written $\mu \partial v_r/\partial z$ where $z$ is the distance normal to the substrate. Assuming that the radial flow speed is of the order of magnitude of $V_0$ and $h$ is the thickness of

the liquid at maximum spreading, the viscous force scales as $(\mu V_0/h)(\pi R_{sM}^2)$ and the dissipated energy as

$$E_\mu = \frac{\mu V_0}{h} R_{sM}(\pi R_{sM}^2)$$

where $h$ is estimated by mass conservation as $hR_{sM}^2 = R_0^3$. Equating $E_K$ to $E_\mu$ leads to a scaling of the maximum spreading ratio

$$\frac{R_{sM}}{R_0} \propto Re^{1/5}. \tag{2.1}$$

This assumes that the drop at maximum extension takes a pancake shape of uniform thickness $h \sim R_0 Re^{-2/5}$.

In the second regime, inertia and capillarity are approximately balanced, with various terms introduced to account for viscous dissipation. Until recently, two models were in competition. The first one is based on an energy balance and scales the initial kinetic energy of the impacting drop to its surface energy at maximum spreading

$$\rho R_0^3 V_0^2 \sim \sigma R_{sM}^2.$$

The spreading factor thus scales as

$$\frac{R_{sM}}{R_0} \propto We^{1/2} \tag{2.2}$$

for large $We$ values ($We \gg 1$). This regime is difficult to reach experimentally due to the appearance of the splashing behaviour and corrections have to be introduced to account for viscous dissipation (Roisman, 2009; Eggers *et al.*, 2010; Lastakowski *et al.*, 2014). The second model uses mass and momentum conservation and estimates the thickness of the liquid film at maximum spreading based on the effective acceleration $g_{eff}$ experienced by the drop during impact. At maximum spreading, the drop is flattened and resembles a gravity puddle, a shape only observed if gravity overcomes surface tension. In such case, the thickness of the film would scale as the capillary length $h \sim \sqrt{\sigma/(\rho g_{eff})}$. Since the speed of the drop upon impact goes from $V_0$ to 0 in a time $V_0/R_0$, the effective acceleration is defined as $g_{eff} = V_0^2/R_0$. Mass conservation $R_0^3 \sim R_{sM}^2 h$ then leads to the scaling

$$\frac{R_{sM}}{R_0} \propto We^{1/4} \tag{2.3}$$

which is in good quantitative agreement with experimental data, especially on superhydrophobic substrates. In this scaling, the initial kinetic energy is not entirely transferred into surface energy. Some of the energy remains as kinetic energy in internal flows (Clanet *et al.*, 2004; Gilet & Bush, 2012).

Later dynamics of drop spreading are where the various outcomes can be observed. Dependencies of outcomes such as splashing and rebound dynamics to substrate wettability and geometry have been extensively studied (Rioboo *et al.*, 2001; Xu *et al.*, 2007; Dhiman & Chandra, 2010; Bird *et al.*, 2009). Such behaviours are of interest for anti-icing or self cleaning surface, and notably the reduction or enhancement of the contact time of bouncing drops (Bird *et al.*, 2013; Kwon *et al.*, 2014; Kim *et al.*, 2014).

The resolution between these models came from an improvement in the understanding of the time evolution of the spreading radius and of the investigation of the lamella thickness and flow velocity. Thickness measurement is a challenge as the lamella is bounded by a thicker rim which occults it when imaged from the side (Fig. 2.3a). Top views require to incline the camera and correcting factors must be introduced in light absorption techniques as in (Lastakowski *et al.*, 2014). Nevertheless, numerical simulation have often been used to obtain such information and ingenious experimental techniques have been developed. One example is the use of spherical targets, illustrated in Fig. 2.4a, where the

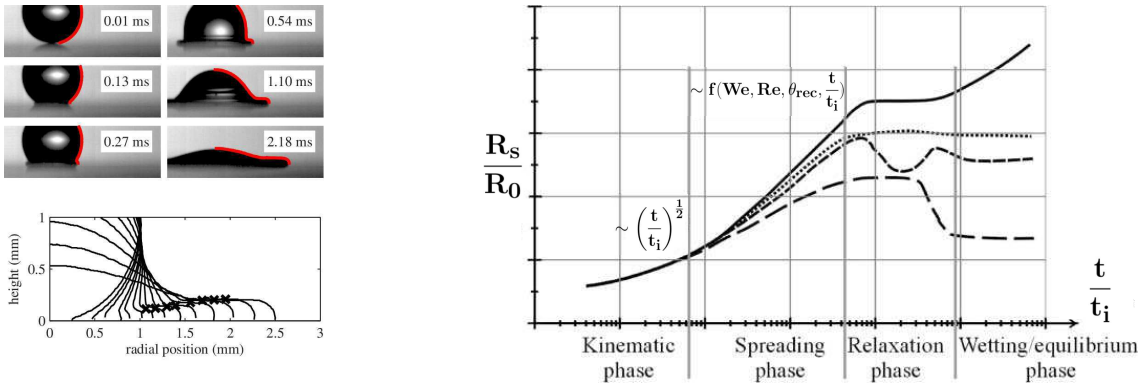


(a) (b)

Figure 2.3: (a) Top: Impact of an ethanol drop ($R_0$ =1.01 mm) onto a mirror taken up to $t_i = 2R_0/U_0$ = 2.18 ms after impact. Thick red lines show height profiles determined by image-analysis software. Bottom: Height profiles of the drop shown in (a) as function of radial position for the right side of the recorded impacting drop. Frames selected for analysis are taken at $t/t_i$ = 0.004, 0.04, 0.06, 0.10, 0.12, 0.16, 0.20, 0.25, 0.32, 0.40, 0.50, 0.63, 0.79, and 1.00 after impact. The lamella expands radially. The crosses mark the location where the rim height of each profile is measured (for profiles that show a plateau-shaped lamella only). [Adapted from de Ruiter *et al.* (2010)]. (b) Schematic representation of the spreading factor $R_s/R_0$ with time $t/t_i$. The different lines correspond to an arbitrary choice of possible spreading histories, depending on the parameters of the impact ($\theta_{rec}$ is the receeding contact angle). The kinematic phase occurs usually for $t/t_i < 0.1$, the spreading from $0.1 < t/t_i < 1 - 10$ depending on the impact parmeters. The relaxation phase is usually in the time interval $1 - 10 < t/t_i$ while the wetting/equilibrium phase comes at very large $t/t_i$ and corresponds to the final stage. [Adapted from Rioboo *et al.* (2002)].

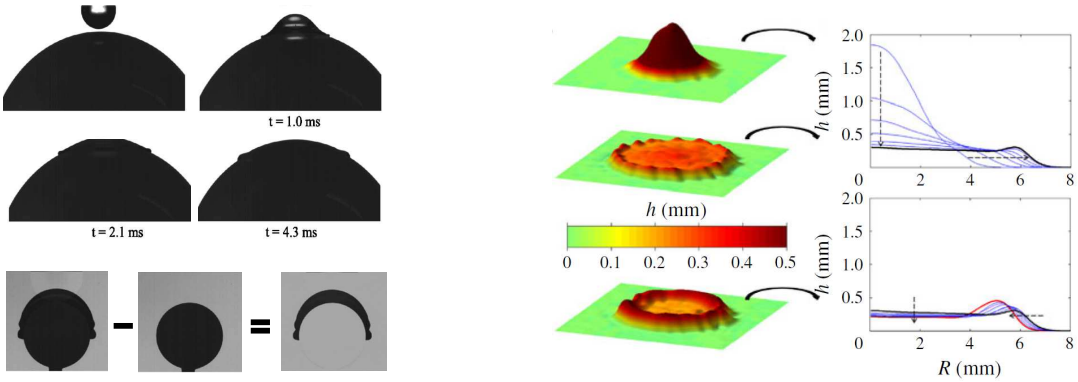


(a) (b)

Figure 2.4: (a) Top: Snapshots of the impact of an isopropanol drop 2.2 mm in diameter onto a stainless steel spherical target 15 mm in diameter (times as indicated). The impact velocity is 1.37 m/s. Bottom: The temporal and spatial variation of the flowing lamella on a spherical target can be tracked by subtracting the post-impingement images from the pre-impingement image. [Adapted from Bakshi *et al.* (2007)]. (b) Evolution of drop shape with time for a 50% water-glycerol drop of radius 1.98 mm, impacting a Parafilm surface at a speed of 1.91 m $s^{-1}$ ($We$ = 235 and $Re$ = 1413). Left: Height mapping of the drop for an early time (t = 3.5 ms, top), the maximal radial expansion (t = 10.3 ms, middle) and the minimal thickness (t = 19.7 ms, bottom). Right: Successive drop profiles of the same experiment. The time step is 0.74 ms. Top: Successive profiles up to the maximal lateral expansion symbolized by the bold black line. Bottom Successive profiles from top to bottom between the maximal lateral expansion and the minimal thickness (bold black line and bold red line, respectively). [Adapted from Lagubeau *et al.* (2012)].

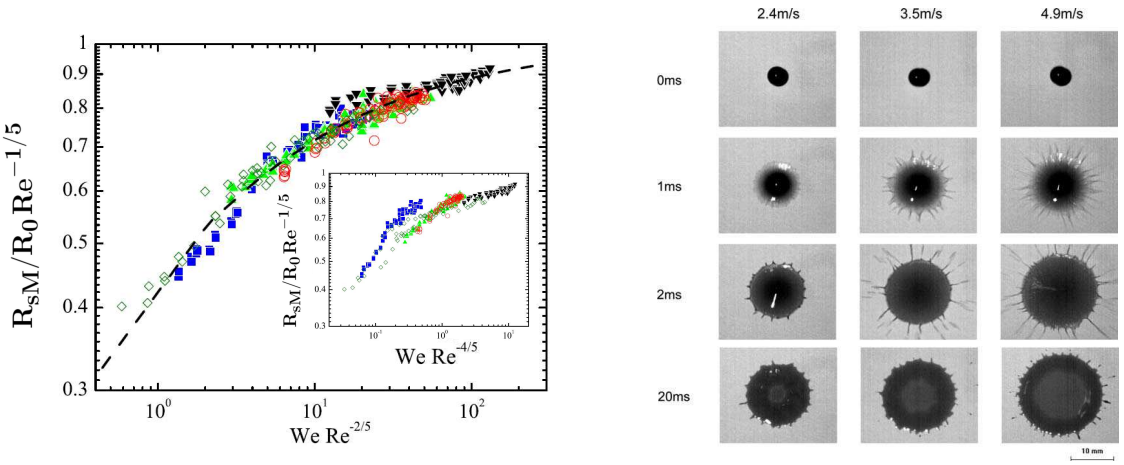


(a) (b)

Figure 2.5: (a) Rescaled maximum spreading ratio as a function of $WeRe^{-2/5}$, with the dashed line showing the Padé-approximation function of Eq. (2.4) fitted to the data points: water (□), water-glycerol 6 mPa s (△), water-glycerol 51 mPa s (▽), and blood (◯). (Inset) Rescaled maximum spreading ratio as a function of $WeRe^{-4/5}$. To emphasize the strength of the approach, earlier data of water-glycerol mixtures from (Bartolo *et al.*, 2005) are also shown (◇). For reasons of clarity, the errors bars are not shown. [Adapted from Laan *et al.* (2014)] (b) Time series of a single blood drop impact onto paper. Drop diameter is 4.3 mm and impact velocity is varied as indicated. [Adapted from Hulse-Smith *et al.* (2005)]

curvature allows, by image subtraction, the direct measurement of the thickness (Bakshi *et al.*, 2007). Illustrated in Fig. 2.4b, Lagubeau *et al.* (2012) used a space-time-resolved Fourier transform profilometry technique.

To rationalize the time evolution of the spreading factor, the thin film approximation proposed by Yarin & Weiss (1995) has usually served as a basis for the subsequent investigations (Rozhkov *et al.*, 2004; Roisman *et al.*, 2009; Villermaux & Bossa, 2011; Antonini *et al.*, 2012; Lagubeau *et al.*, 2012), using a hyperbolic flow pattern

$$v_r = \frac{r}{t}, \quad v_z = -\frac{z}{t},$$

where $v_r$ and $v_z$ are the radial and vertical velocities of the flow in the lamella, $r$, and $z$ are the radial and vertical coordinates and $t$ is the time from impact. This flow pattern suggests a self-similar evolution of the surface of the drop in

$$h(r,t) = \frac{R_0^3}{V_0^2 t^2} F\left(\frac{r}{V_0 t}\right).$$

The model has been refined to include a viscous boundary layer correction that develops with time and classically scales as $\sqrt{\nu t}$ with $\nu$ the kinematic viscosity of the liquid. The time at which the thickness of the inviscid liquid layer reached this boundary layer was first assumed to scale as $R_0/V_0$ which yielded a long time thickness $h/R_0 \sim Re^{-1/2}$ in the form of a Blasius-type sheet. Experiments and numerical simulations however showed that the effects of the initial hyperbolic flow cannot be neglected, and the time at which the drop thickness reached the boundary layer presented a small dependency in $Re^{1/5}$ so the minimal film thickness scales as $Re^{-2/5}$ also in the capillary dominated regime (Schroll *et al.*, 2010; Eggers *et al.*, 2010; Lagubeau *et al.*, 2012).

The transition for the maximum spreading radius from a viscous to capillary regime can be described in terms of a single scaling relation depending on the $We$ and $Re$ numbers, and that varies depending on the model taken into account (Eggers *et al.*, 2010; Laan

*et al.*, 2014). Interpolating between the viscous [Eq. (2.1)] and the energy conservation models [Eq. (2.2)], the maximum spreading would be

$$\frac{R_{sM}}{R_0} \propto Re^{1/5} f_c(\, WeRe^{-2/5})$$

with $f_c(u)$ satisfying $\lim_{u\to\infty}$ = Cst. and $\lim_{u\to 0} = \sqrt{WeRe^{-2/5}}$. Using the effective acceleration model [Eq. (2.3)], we obtain

$$\frac{R_{sM}}{R_0} \propto Re^{1/5} f_c(\, WeRe^{-4/5})$$

with $f_c(u)$ satisfying the same limit for $u \to \infty$ and satisfying $\lim_{u\to 0} = (\, WeRe^{-2/5})^{1/4}$ in the other case. Experiments conducted by Laan *et al.* (2014) on a wide range of liquid viscosities showed a better collapse using the $WeRe^{-2/5}$ scaling (Fig. 2.5a), confirming the numerical computation results obtained by Eggers *et al.* (2010) and settling this long standing discussion. The proposed law for the spreading factor will thus be described in this work with a smooth crossover between the two asymptotic regimes,

$$\frac{R_{sM}}{R_0} Re^{-1/5} = \frac{P^{1/2}}{A + P^{1/2}}, \tag{2.4}$$

where $P \equiv WeRe^{-2/5}$ and A = 1.24±0.01 is a fitting constant.

After the spreading phase, the liquid behaviour will mainly be dictated by the receding contact angle. On a strongly hydrophilic substrate, the very small contact angle is energetically favourable to wetting and the liquid will keep spreading. On a slightly hydrophilic substrate with contact angle smaller than 90°, the liquid reaches an equilibrium in the spreading phase and the contact line stays pinned. Hydrophobic substrates with contact angles greater than 90° will exhibit dewetting behaviours. The roughness of the surface can also play a role in the perturbation of the rim during this phase and fingering may appear as in Fig 2.5b. Such fingering has been the subject of studies especially to determine the origin and number of such patterns (Thoroddsen & Sakakibara, 1998) and has been of particular interest to determine the size and velocity of the impacting drop in forensic science (Hulse-Smith *et al.*, 2005; Adam, 2012; Laan *et al.*, 2014, 2015). It is from the receding stage that the outcome of the overall impact will be qualified (Rioboo *et al.*, 2002). As mentioned, there has been extensive literature devoted to the determination of outcomes of drop impacts and some attempts to model its dynamics (Roisman *et al.*, 2002; Bartolo *et al.*, 2005). This phase as well as the very long time behaviour (named wetting or equilibrium phase) are however of less importance in this work and will not be discussed further.

## 2.4 Impacts on small targets

We chose to separately discuss the topic of impacts on small flat targets. They consist in letting drops fall on targets of size similar to the size of the impacting drops as seen in Fig. 2.6. Such impacts have applications in the context of inkjet printing for example which must generate droplets with $We \in [5, 500]$ comparable to our regimes but $Re \in [0.3, 10]$ (Derby, 2010). Nevertheless, to ensure a high quality impression, printers inject droplets with sizes in the order of a few tens of micrometers. This scale is comparable to the roughness of some papers so the quality of the printing will depend on the interaction between the droplet and the complex target presented by the paper (Rozhkov *et al.*, 2002). Impacts on poles also allow the study of the liquid spreading dynamics in the air which removes effects of viscosity to a great extent. Indeed, since the target has a size comparable to the one of the impacting drop, the time that the liquid spends on it is reduced. The liquid takes off from the solid before entering into the spreading phase and a liquid sheet is

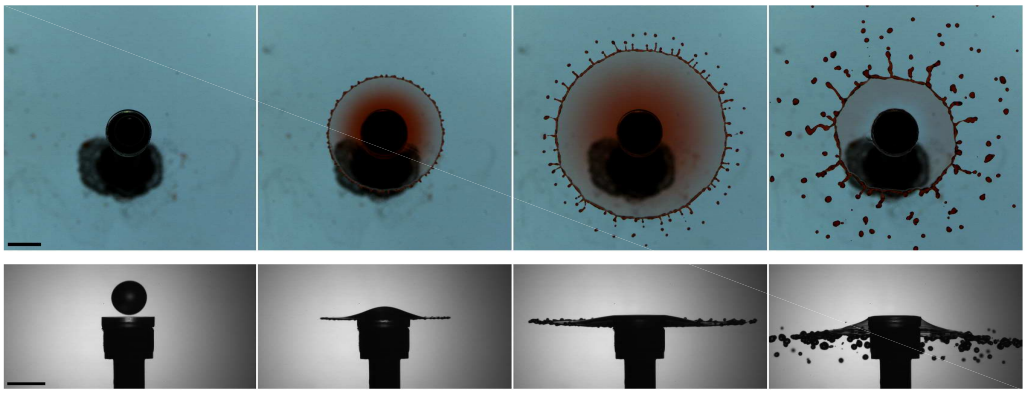

Figure 2.6: Dyed water drop impacting on a small target from top (Top) and side views (Bottom). Images are taken at t = -0.2, 1.2, 3.2 and 11.8 ms from impact, from left to right. Drop radius is 2.4 mm and pole diameter is 7 mm. Scale bars are 5 mm.

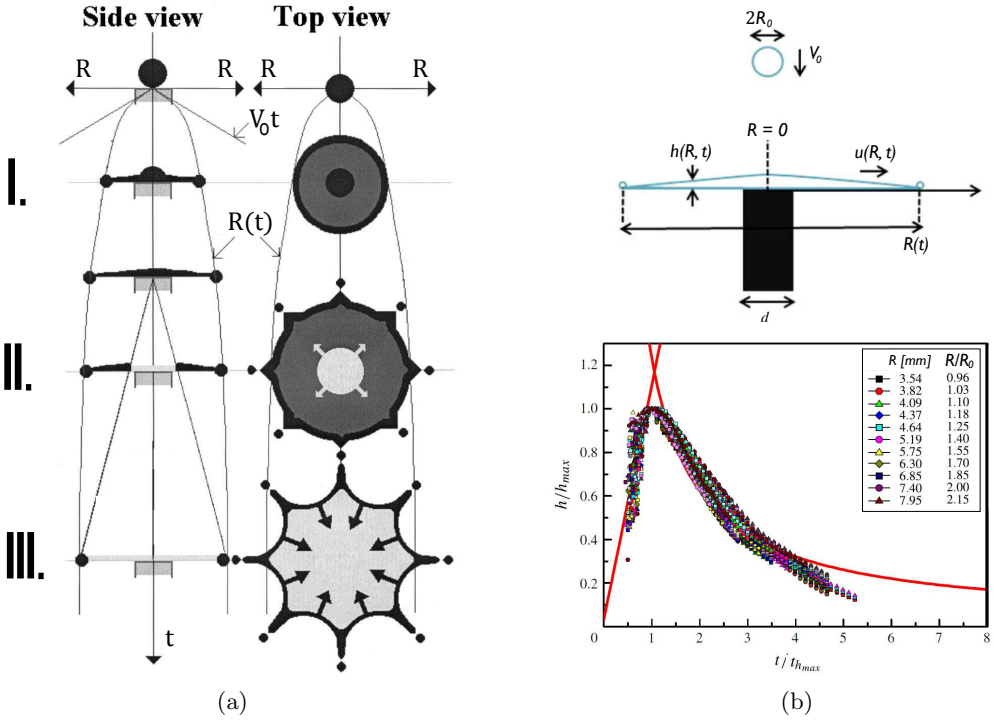


(a) (b)

Figure 2.7: (a) Qualitative model of growth and collapse of the liquid sheet divided in three phases from top and side views. Phase I: Sheet expansion. The drop acts as a point source feeding liquid into the sheet. Phase II: Stable radius $R$. The point source is depleted but the liquid keeps travelling through the sheet. Phase III: Sheet retraction and destabilization. $R(t)$ is the radius of the liquid sheet, $t$ is the time from impact and $V_0$ the speed of the impacting drop. [Adapted from Rozhkov *et al.* (2002)]. (b) Top: Sketch of the drop impact experimental set-up and definition of its experimental parameters with $u$ the radial sheet velocity. Bottom: Time evolution of the thickness of a liquid sheet, for different radial positions $R$, as indicated in the legend, normalized in the x-axis by the time at which the thickness is maximum, $t_{h_{max}}$, and in the y-axis by the maximum thickness, $h_{max}$. The lines correspond to the two asymptotic scaling regimes from Eqs. (2.5) and (2.6). The drop diameter is $2R_0 = 3.7$ mm and the impact velocity is $V_0 = 4.0$ m s$^{-1}$. [Adapted from Vernay *et al.* (2015)]

formed, which is only connected to the solid at one of its edges (Rozhkov *et al.*, 2002, 2004; Villermaux & Bossa, 2011; Vernay *et al.*, 2015; Arora *et al.*, 2016; Wang & Bourouiba, 2017). Unsteady sheet expansion in the air is also one of the major mechanisms of droplet formation (Gilet & Bourouiba, 2014, 2015). Rationalizing the sheet dynamics in this configuration and its subsequent droplet shedding is thus a step in understanding the unsteady sheet fragmentation process leading to raindrop-induced disease propagation.

As the drop impacts the target, an axisymmetric sheet develops in the air bounded by a thicker rim. Then, the sheet retracts, also axisymmetrically, provided that the impact is perfectly centred (Fig. 2.6). Experiments by Rozhkov *et al.* (2002) showed that the velocity of liquid ejection from the target changes with time and that the sheet dynamics could be divided in different phases depending on the injection rate from the drop into the sheet (Fig. 2.7a). In a first phase, the impacting drop acts as a point source and feeds liquid into the sheet. The sheet is expanding (Fig. 2.7a - I). In a second phase, the drop stops acting as a point source but the remaining liquid ejected from the target travels through the sheet. The sheet is metastable and its spreading radius $R/R_0$ remains relatively constant (Fig. 2.7a - II). Finally, in a third phase, no more liquid is supplied from the target, the sheet either retracts under capillary pull and disintegrates as the rim collapses against the target or nucleates from the target and disintegrates as the two antagonist rims meet (Fig. 2.7a - III).

Theoretical rationalizations for the sheet spreading factor have been proposed based on mass and momentum conservation arguments. The evolution of the sheet velocity and thickness profiles were at first not directly accessible and two different sheet thickness profiles were proposed. The first model, introduced by Rozhkov *et al.* (2004), is based on a constant volume flux per unit radian for a given radial position. This led them to a thickness profile of the liquid sheet of

$$h(r,t) \sim t/r^3, \tag{2.5}$$

with $h$ the thickness of the liquid sheet, $r$ its radial position from the impact point and $t$ is the time from impact. The second model proposed by Villermaux & Bossa (2011) is based on a comparison with steady Savart sheets and assumes similar thickness profile, leading to a thickness dependency in

$$h(r,t) \sim 1/rt. \tag{2.6}$$

Both profiles lead to a similar radial velocity field. Interestingly, direct measurement of the sheet thickness by Vernay *et al.* (2015), illustrated in Fig. 2.7b, showed that both proved partially correct. The first profile, described by Eq. (2.5), proved correct for short-time regime ($t \leq 3D_0/V_0 \simeq t_{h_{max}}$) while the other [Eq. (2.6)] described long-time regime. The presence of a local maximum was also highlighted.

In all cases, a dependency of the maximum spreading radius of the sheet in $We$ was found to follow $R_{sM}/R_0 \propto \sqrt{We}$, which is expected from fully inertia-capillary driven systems that turn spheres into pancakes [Eq. (2.2)]. The model developed by Villermaux & Bossa (2011) is indeed from a balance between inertia of the impacting drop and capillary restoring forces at the rim, with a damping term to account for the continuous transfer of momentum from the sheet to the rim. Impacts on small targets have also been performed using viscous and viscoelastic fluids by Arora *et al.* (2016) and the influence of these parameters on the maximum spreading radius was quantified. They proposed a simple semi-empirical model based on an energy conservation argument where part of the impacting kinetic energy is dissipated by a radial flow in the liquid sheet. The model and the experimental data showed good agreement confirming that the dissipation mainly occurs on the target. Finally, Juarez *et al.* (2012) showed that the sheet shape and its subsequent breakup could be influenced by the shape of the target under certain conditions.

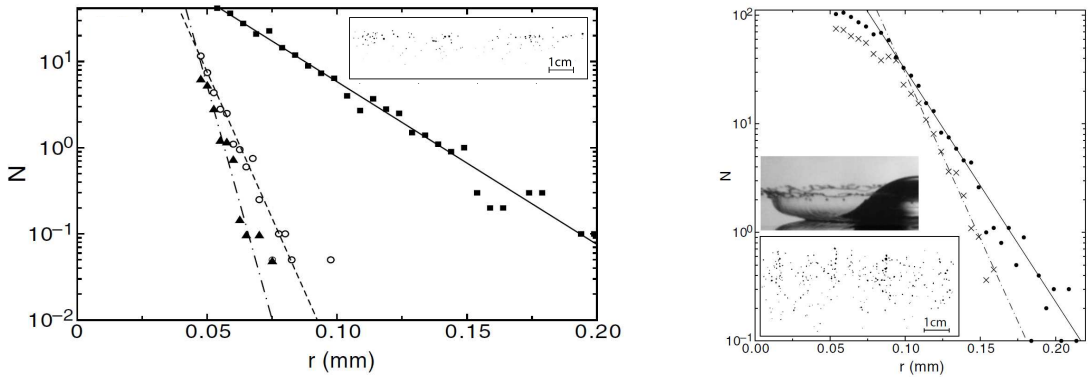


(a) (b)

Figure 2.8: (a) Size distribution $N(r)$ of ejected droplets in a prompt splash on rough substrates with $r$ the radius of the droplets. Three values of substrate roughness are investigated: $R_a$=16 $\mu$m (■), $R_a$=5 $\mu$m (◯), and $R_a$=3 $\mu$m (▲). The exponential fitting functions are Eq. (2.7) with linestyles corresponding to $r_0 = 0.023$ mm (solid), $r_0 = 0.006$ mm (dashed) and $r_0 = 0.004$ mm (dashed-dotted). Inset: one sheet of paper with ink spots produced by $R_a = 25$ $\mu$m. Most spots are randomly distributed within a narrow band. (b) Size distribution of ejected droplets in a corona splash at high pressure. The upper inset shows the corona film before it breaks up. The lower inset is a reproduction of the sheet of paper collecting the ink spots showing that the ejected droplets hit the paper at random locations over a large area. The main panel shows the number of droplets of a given size per impact $N(r)$ versus droplet radius $r$ for a corona splash at two pressures: $P$ = 100 kPa (•) and $P$ = 80 kPa (×). The exponential fitting functions are Eq. (2.7) with linestyles corresponding to, $r_0 = 0.020$ mm (solid) and $r_0 = 0.014$ mm (dashed-dotted), respectively. Droplets with radius below 50$\mu$m were no considered. [Adapted from Xu *et al.* (2007)]

## 2.5 Drop fragmentation

Despite their importance in many industrial applications such as fuel injection, rain-induced disease spreading or forensic sciences (Moreira *et al.*, 2010; Gilet & Bourouiba, 2014; Laan *et al.*, 2015; Gilet & Bourouiba, 2015), the outcomes of sheet fragmentation, namely the properties of the ejected droplets, have received much less attention from the fluid dynamics community than the impacting drop behaviour itself. Splashing is more often than not studied to determine the conditions under which it appears and its products are seldom analysed.

A general review on fragmentation can be found in Villermaux (2007) and some previous work should be highlighted. In 1977, Stow & Stainer (1977) reported number and size distribution of ejected droplets, varying impacting drop size and speed, surface tension, roughness of the substrate as well as curvature of the substrate and the depth of the liquid film on the target. They observed notably a decrease in the size of the droplets with an increase of the impact speed and a log-normal distribution of the size of the droplets. In their conclusion, they urged for further experimental work to correlate the nature of the ejecta to the hydrodynamic events. In 1995, Mundo *et al.* (1995) reported size and velocity distributions of the droplets resulting from the impact of single drops on rough and smooth surfaces. Yarin & Weiss (1995) measured the droplet size distributions for impacts on a thin fluid film. Several other works reported droplet size distributions and velocities after various types of impact on dry solid and some correlation to the type of splashing or impact parameters were proposed (Roisman *et al.*, 2006; Xu *et al.*, 2007; Thoroddsen *et al.*, 2012; Riboux & Gordillo, 2015). Figure 2.8 illustrates the size distribution of the droplets for prompt splashing (Fig. 2.8a) and for corona splashing (Fig. 2.8b), arguing

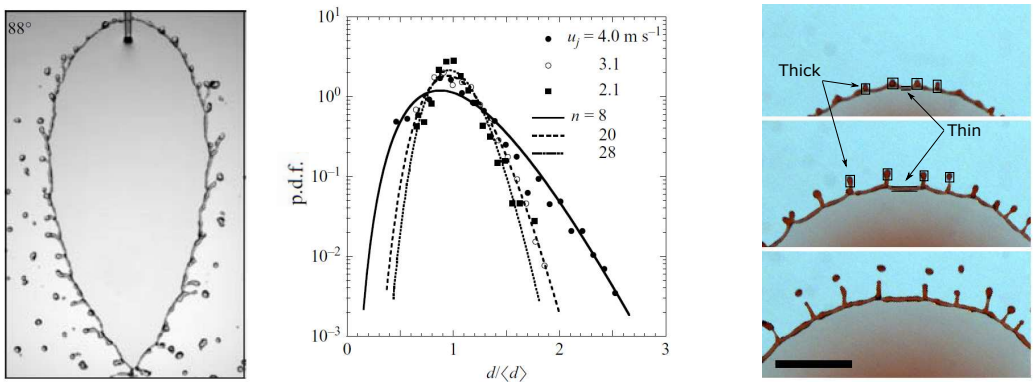


(a) (b) (c)

Figure 2.9: (a) A liquid sheet is formed through the collision of two identical jets impacting at an angle of 88° forming a water sheet that fragments into droplets. The jet velocity is equal to 4 ms$^{-1}$ and the jet diameter is 1.05 mm. [Adapted from Bremond & Villermaux (2006)]. (b) Probability density functions of the droplet sizes normalized by the mean droplet size $d/\langle d \rangle$ for a fixed collision angle $2\alpha = 88°$ and three impacting velocities. The fitted curves are gamma distributions [Eq. (2.8)] with the parameter $n$ as indicated in each case. [Adapted from Bremond & Villermaux (2006)]. (c) Drop impact on a pole. Experimental conditions of Fig. 2.6. Droplets destabilizing from the rim for images taken at 1.8, 2.6 and 3.4 ms after impact, from top to bottom. Scale bar is 5 mm. The uniform rim develops into a series of thick sections (droplets) and thin sections (necks between droplets). Due to higher inertia, the thick sections are less delayed under the action of the surface tension forces than the thin sections. The thicker sections overtake the thinner ones, which generates the fingering pattern. [Adapted from Rozhkov *et al.* (2002)].

that both distributions decay exponentially as

$$N \sim e^{-r/r_0} \tag{2.7}$$

where r is the radius of the ejected droplets and $r_0$ a characteristic decay length. They argued that the length-scale is linked to the droplet creation process: this would provide evidence that sheet history and droplet ejections should be related as the patterns of the insets in Figs. 2.8a and 2.8b suggest.

On Savart's sheet configuration, interesting findings such as a link between local sheet thickness and ejected droplet sizes have been made by Bremond & Villermaux (2006). They created leaf shaped stationary liquid sheets, illustrated in Fig. 2.9a, using two jets colliding at an angle, and showed that the droplet size distribution of the atomization process could be controlled by the experimental parameters. In particular, they observed that the experimental droplet size distribution (Fig. 2.9b) obeyed a gamma distribution

$$p(X) = \frac{n^n}{\Gamma(n)} X^{n-1} e^{-nX} \quad where \quad X = \frac{d}{\langle d \rangle} \tag{2.8}$$

where $\langle d \rangle$ is the average droplet size. Such distribution was already observed in (Villermaux *et al.*, 2004). More recently, a full study of the process to link droplet formation to the history of its liquid sheet has been performed in Villermaux & Bossa (2011) using single drop impact on a small target. In this context of free destabilizing liquid sheet, ligaments, i.e., elongated corrugations along the sheet rim, were shown to originate from a destabilization mechanism localized at the rim and to condition the droplet size distributions. These distributions obey a linear superposition of gamma distributions [Eq. (2.8)] similar to the ones observed on steady sheets.

The ejection of droplets is mostly due to the appearance of corrugations on the liquid rim. There are two main mechanisms of formation of these corrugations that may occur

simultaneously. The first relies on the Rayleigh-Plateau instability that tends to turn a cylindrical rim into a string of droplets. The second, proposed by Yarin & Weiss (1995), relies on the capillary instability of the rim subject to bending disturbances with formation of cusps (Rozhkov *et al.*, 2002). As the rim slightly starts to corrugate owing to the interplay of these two instabilities, thicker and thinner regions appear (Fig. 2.9c). Due to inertia, the thicker regions will be less slowed down than the thinner ones, which increases the destabilization and leads to the formation of ligaments. These ligaments then destabilize into droplets (Rozhkov *et al.*, 2002). A recent study by Gordillo *et al.* (2014) focused on the cusps present in stable sheets, preceding the droplet generation. It showed how these formations accommodate for mass and momentum conservation at the edge. Apart from the few studies mentioned here above, relations between sheet dynamics and droplet ejections are seldom made and few information related to droplet characteristics are reported beside number and size distributions. One of our focus in this thesis has thus been to report size, speed and droplet number distributions as well as angle of ejections and to relate them to the observed sheet cinematic. These quantities are all relevant to determine the distance travelled by the droplets and thus the range of potential contamination.

## 2.6 Asymmetric and oblique impacts

In the *crescent-moon* impact scenario discussed in Chapter 1, an intrinsic horizontal asymmetry leads to a non-axisymmetric liquid sheet (Gilet & Bourouiba, 2015). This latter induces asymmetry in the speed and direction of ejected droplets. Inclination, compliance and finite size of the leaves all amplify this asymmetry (Gilet & Bourouiba, 2015).

Drop impacts associated to asymmetric behaviors are present in the literature. A first category of experiments relies on horizontal gradients of texture and wetting properties to induce non-symmetrical behaviours (Reyssat *et al.*, 2009; Malouin *et al.*, 2010; Vaikuntanathan *et al.*, 2010; Bird *et al.*, 2013; Kwon *et al.*, 2014; Zhang *et al.*, 2017). In Bird *et al.* (2013), adding a macrostructure in the spreading zone splits the drop, which reduces the time during which the drop stays in contact with the substrate. Reducing (or enhancing) this time has applications in self-cleaning materials or cooling processes. Varying the gradient of texture allows a control of the rebound direction of the drop, as shown by Reyssat *et al.* (2009), breaking here the symmetry of the whole rebound dynamic. Such symmetry breaking in rebound can also be achieved by varying inclination of the substrate (Šikalo *et al.*, 2005; Gilet & Bush, 2012; Yeong *et al.*, 2014; Fujimoto *et al.*, 2017). Illustrated in Fig. 2.10a, the effect of inclination on the contact time and drop impact outcome is well documented and has been studied in combination with roughness and wettability of the substrates (Yeong *et al.*, 2014; Antonini *et al.*, 2014). These investigations usually focus on the contact time and rebound dynamics. Literature on the spreading dynamics for oblique impacts is scarce. These impacts are however the norm rather than the exception. Description of oblique impacts can be found in forensic science where, for example, Laan *et al.* (2014) studied the influence of inclination on the spreading factor. They showed that Eq. (2.4), which provides the maximum spreading radius on a horizontal substrate, could be adapted to oblique impacts by taking the component of the $We$ number normal to the substrate. Splat morphology is also a field concerned with oblique sprays and Montavon *et al.* (1997) and Kang & Lee (2000) studied the ellipsoid shape of molten metal drops resulting from impacts on oblique substrates. Such impacts are of particular relevance for this work since leaves are more often inclined than horizontal (Zou *et al.*, 2014) and drop impacts on leaves will thus usually deal with inclination.

An insight into drop spreading on oblique substrates is in the study of impacts on moving substrates, i.e., impacts on substrate experiencing an in-plane horizontal translation motion. Similarities have indeed been observed between these configurations as both oblique impacts and translation motion of the substrate confer a non-zero initial tangential

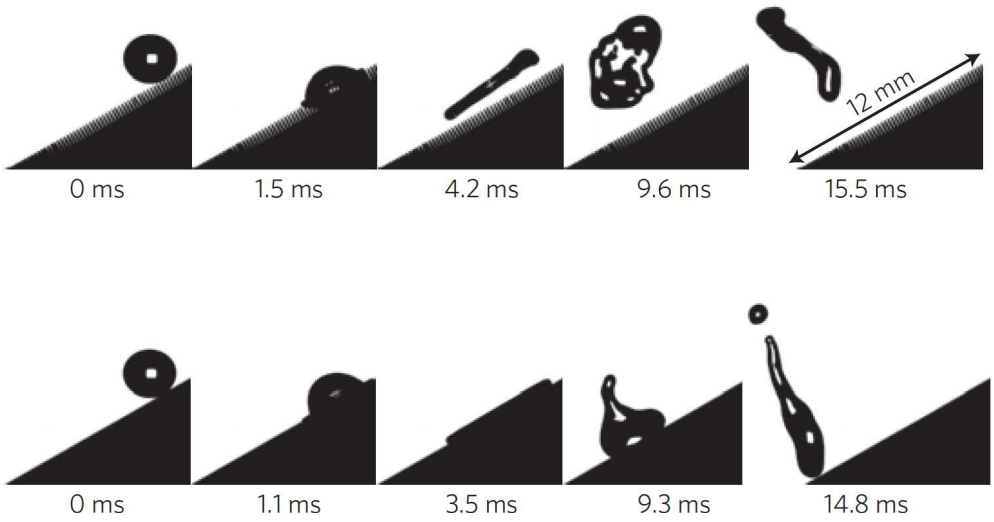


(a)

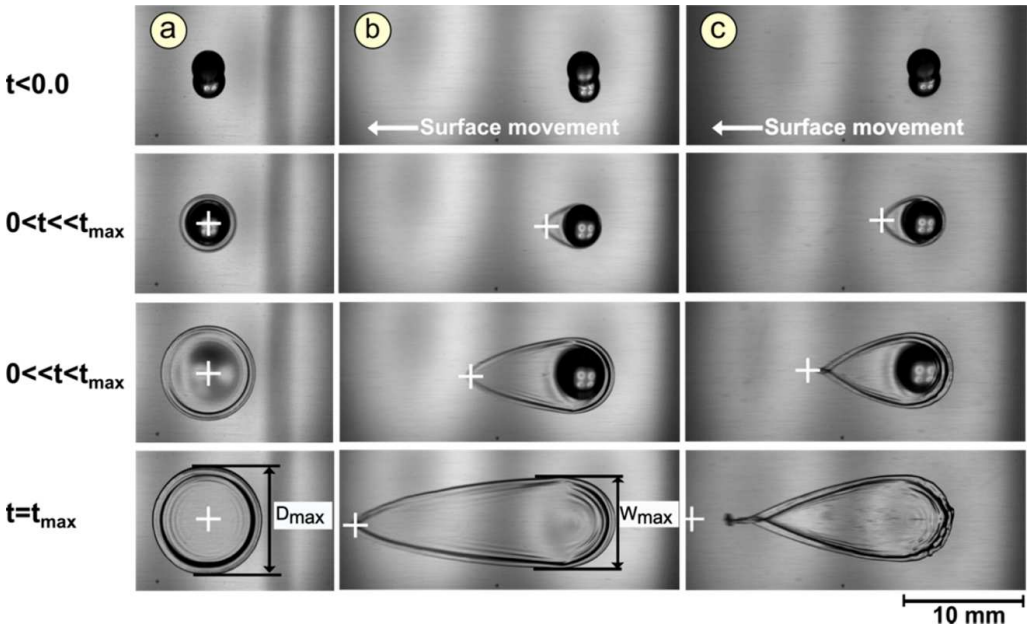


(b)

Figure 2.10: (a) A drop impinging on an engineered superhydrophobic surface (patterned with lattices of submillimetre-scale posts decorated with nanotextures), exhibiting a contact angle of over 165° and contact angle hysteresis less than 2° (top) and on the non engineered superhydrophobic surface (contact angle of 160°) (bottom), under a tilt angle of 30° at $We = 31.2$. The drop impinging on the engineered surface exhibits a pancake bouncing (top), whereas the drop on the non-engineered surface follows a conventional bouncing pathway (bottom). The contact time in the case of pancake bouncing is 3.6 ms, which is fourfold shorter than that on the classical nanostructured superhydrophobic surface. [Adapted from Liu *et al.* (2014)]. (b) Drop impacting a flat dry substrate moving horizontally at constant speed. Overhead views of the water drop spreading over stationary (left), moving hydrophilic (middle) and moving hydrophobic (right) surfaces. Drop velocity is $V_0 = 1.43$ m/s, and surface velocities are $V_s = 0$ m/s (left), $V_s = 8.0$ m/s (middle), and $V_s = 8.0$ m/s (right). White crosses denote the drop impact point on the surface. Surface moves from right to left. [Adapted from Almohammadi & Amirfazli (2017a)].

velocity to the impacting drop (Almohammadi & Amirfazli, 2017a). Impacts on moving surfaces were known to influence the splashing threshold (Bird *et al.*, 2009) but its is only very recently that the spreading dynamics has been the subject of a renewed interest. Almohammadi & Amirfazli (2017b) showed that the envelope resulting from the spreading of a drop impacting on a moving substrate could be described by the superposition of the spreading from a normal drop impact and a horizontal translation motion at constant speed (Fig. 2.10b). In the context of this thesis, we studied impacts on inclined substrates for which the time evolution of the spreading on the solid is a key information.

The relationship between liquid sheet asymmetry and droplet ejections was investigated for a stationary liquid sheet (Bremond & Villermaux, 2006) as discussed in the previous chapter (Chapter 1) but to our knowledge, not in a non-symmetrical unsteady liquid sheet.

Finally, asymmetry can be achieved with non-axisymmetric target shapes (Juarez *et al.*, 2012; Liu *et al.*, 2015), using compliant substrates (Gilet & Bourouiba, 2014), or through multiple drop impacts (Fujimoto *et al.*, 2017). These last two configurations are however quite challenging to study beyond qualitative outcomes due to their inherent 3D nature. An approach to solve this issue is proposed in this thesis and described in the following Chapter.

In summary, if drop impacts on solid substrates begin to be quite well understood, more complex scenarios such as impacts on moving and compliant surfaces are still a very active subject of research. In the context of rain-induced disease propagation we are particularly interested by unsteady sheet fragmentation. Such sheet have been studied in axisymmetric configuration but not in non-symmetrical ones. Moreover, the link between the sheet behaviour and the resulting droplet characteristics such as the mass, velocity and number remains obscure.

# Chapter 3

# Methodology

## 3.1 Raindrop impacts on leaves - From 3D to 2D

Recent studies have shed light on raindrop-leaf interactions (Gilet & Bourouiba, 2014, 2015), identifying the important role of wetting and of sessile drops on leaves. The *crescent-moon* scenario has been identified as one of the main dispersal scenario on semi-rigid leaves, as it is both common and efficient at dispersing pathogens. It consists in the impact of a raindrop in the vicinity of a sessile (contaminated) drop supported by the infected leaf. The system experiences an intrinsic horizontal asymmetry which causes the sessile drop to be stretched into an asymmetric liquid sheet by opposition to an axisymmetric expansion. The sheet then retracts and fragments into a myriad of contaminated droplets ejected away from the plant.

### Parameters identification

As a preliminary step of this work, the observation of a large number of drop impacts on wet leaves, in fields and in the laboratory, confirmed the frequent occurrence of asymmetric liquid sheets in the air and their efficiency in ejecting droplets (Fig. 3.1). Our observations show that these sheets develop either through the *crescent-moon* scenario described in Gilet & Bourouiba (2014) (Figs. 3.1a and 3.1b), by impacts close to edge of leaves (Fig. 3.1c), or by a combination of both (3.1b). In every cases, the development of an asymmetric liquid sheet appears to be the main source of ejected droplets.

A large number of parameters affect the sheet development and corresponding ejection pattern, including the wetting and flexibility of the leaves, their size and roughness, the respective size of the impacting and sessile drops, the distance between those drops (or the distance between the drop and the edge of the leaf) or the speed of the impacting drop. We at first focused on the variation of two parameters, namely the impact speed and a distance, called offset, that measures the initial asymmetry of the impact configuration. This offset is the distance between the impacting and sessile drops (in the case of the *crescent-moon*) or the distance between the impacting drop and the leaf edge (for impacts close to edges). Due to this leaf compliance, both scenarios (*crescent-moon* or impact close to an edge) are inherently three-dimensional (Fig. 3.2a), hence hard to track accurately.

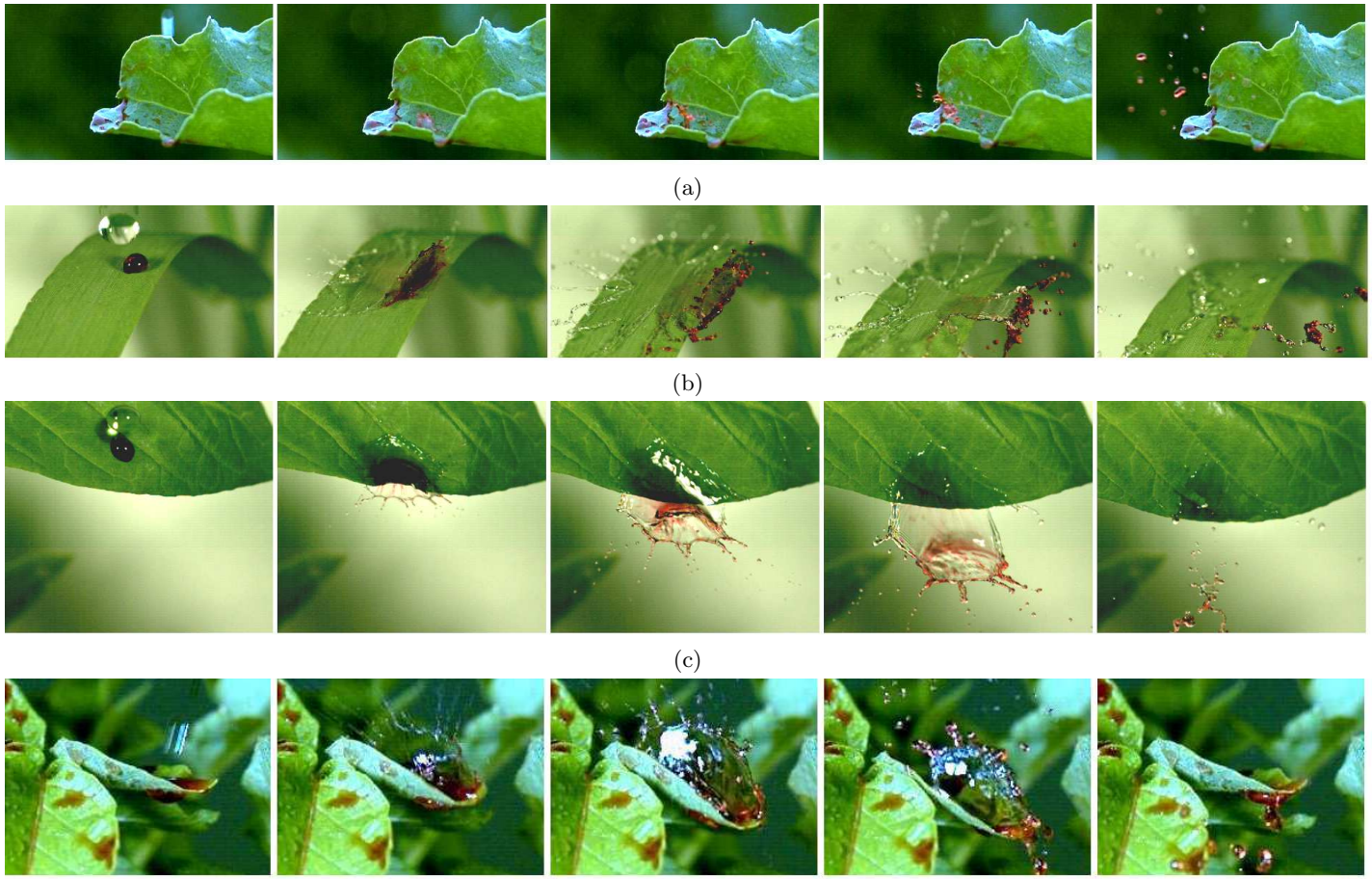

(a)

(b)

(c)

(d)

Figure 3.1: Drop impacts on leaves with liquid sheet formation and fragmentation into droplets. (a) In the field: a raindrop impacts onto a beet leaf on which dyed fluid (red) was deposited. Times are, from left to right, -3, 2, 5, 8 and 24 ms from impact. The sheet is fully three-dimensional and develops into a *crescent-moon*. (b) In lab: A water drop impacts close to a dyed sessile drop on a gramineae leaf. Times are, from left to right, -0.5, 1.5, 4, 7 and 11.5 ms from impact. The sheet first develops in a *crescent-moon*. (c) In lab: A water drop impacts close to a dyed sessile drop on a pepper leaf. Times are, from left to right, -1, 2, 4.5, 7 and 14 ms from impact. The water drop upon impact mixes with the dyed sessile drop and takes off. The sheet is asymmetric but remains largely in the plane of the leaf. (d) In the field: a raindrop impacts onto a potato leaf on which dyed fluid (red) was deposited. Times are, from left to right, -3, 2, 6, 13 and 29 ms from impact. The sheet is fully three-dimensional and develops in a *crescent-moon* before reaching the edge of the leaf.

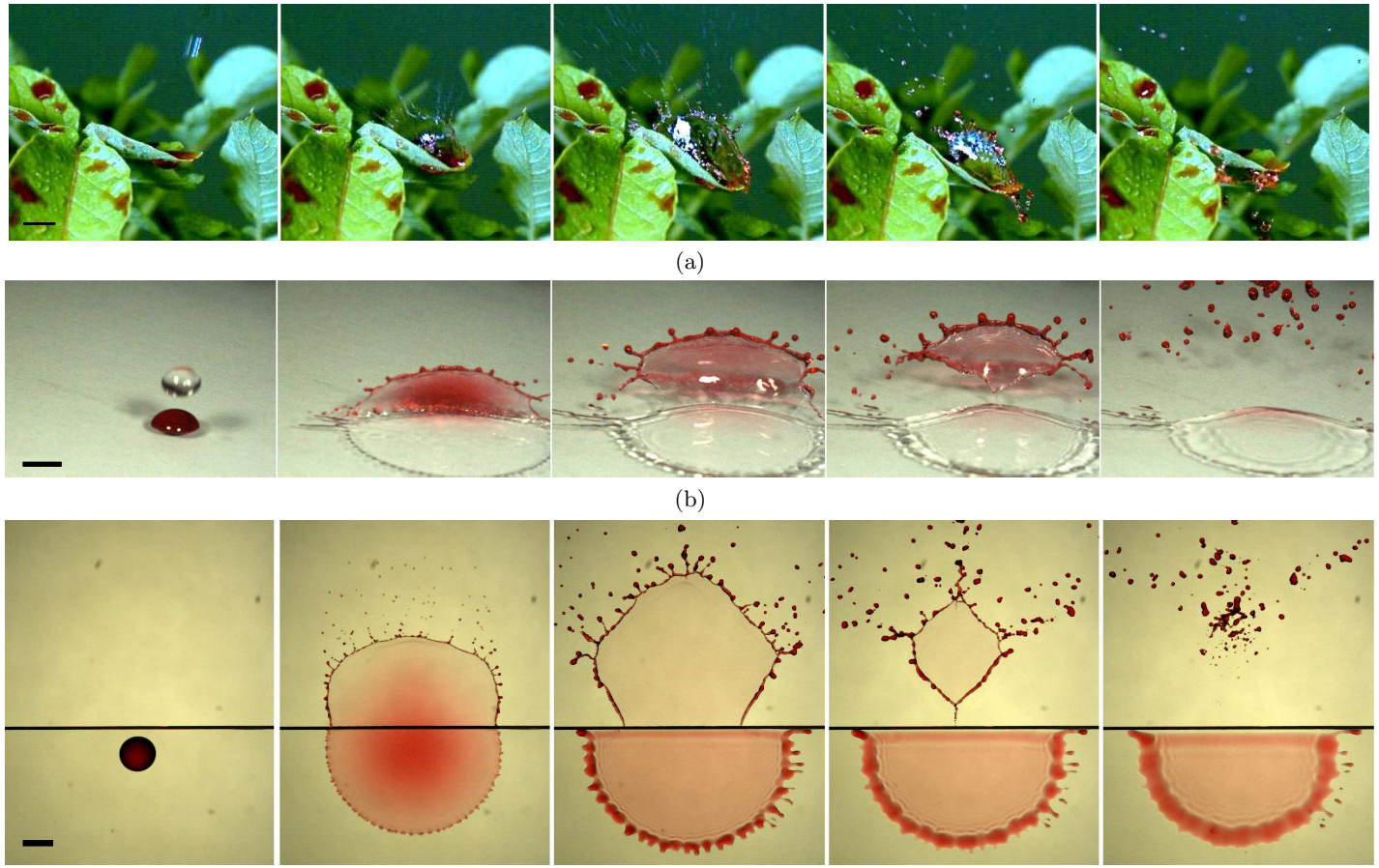

(a)

(b)

(c)

Figure 3.2: Liquid sheet formation and fragmentation into droplets, in three configurations. (a) [Fig. 3.1d] In the field: a raindrop impacts onto a potato leaf on which dyed fluid (red) was deposited. Times are, from left to right, -3, 2, 6, 13 and 29 ms from impact. The sheet is fully three-dimensional and develops in a *crescent-moon* before reaching the edge of the leaf. (b) A water drop impacts close to a dyed sessile drop on a flat horizontal dry plexiglass substrate. Times are, from left to right, -1, 3, 8, 11 and 23 ms from impact. The sheet is still fully three-dimensional. (c) Impact of a dyed drop close to the edge of a flat dry plexiglass substrate. Times are, from left to right, 0, 2.5, 8, 10.5 and 14 ms from impact. The sheet remains approximately in the plane of the substrate. Scale bars are 5 mm.

### From 3D to 2D

The *crescent-moon* mechanism was reproduced in laboratory conditions with a drop impacting close to a sessile drop on a flat, dry and rigid substrate. This corresponds to removing the compliance of the leaf (Fig. 3.2b). The scenario remains fully 3D but we observe key emerging features: (i) the asymmetric shape of the sheet in the air, (ii) the fluid of this sheet originating mainly from the sessile drop, (iii) a destabilizing free rim at the outer-edge of the sheet, and (iv) the presence of a triple solid-liquid-air contact line. These features are also observed when a single drop impacts close to the edge of a straight-cut substrate (Fig. 3.2c).

This latter configuration hence reproduces the key features of the two scenarios that we want to study while keeping the liquid sheet in the plane of the substrate. It will be used in this work to study the influence of asymmetry and impact speed on the liquid sheet evolution and droplet ejection pattern.

### Inclination of the substrate

We slightly modify the configuration to gain insight of the leaf compliance effect on the phenomenon. During a *crescent-moon* on a compliant leaf, one observes a downward movement of the leaf when the liquid sheet develops in the air, having the effect of 'pulling' on the liquid sheet (Fig. 3.3a). This pulling can be seen as an additional tangential speed conferred to the liquid sheet, as represented in the schematic of Fig. 3.3b. One way to reproduce such behaviour while keeping the liquid sheet in the plane of the substrate is by tilting the latter. As the drop hits the inclined substrate, its impacting speed will be decomposed into normal and tangential components (Fig. 3.3c). The amount of tangential speed can then be adjusted through the inclination angle. At the same time, this configuration allows the more direct study of a drop hitting close to the edge of an inclined leaf which is also a frequent scenario (Fig. 3.1c).

This proposed drop impact configuration allows not only to rationalise the consequences of the asymmetry of impacts on leaves close to their edges but it can also be used as a first step to investigate the *crescent-moon* scenario. By tilting the substrate, we can extend our study to drop impact on inclined leaves as well as gain insight on the effect of the compliance of the leaves on the *crescent-moon* scenario.

## 3.2 Experimental setup

### Setup description

The setup is illustrated in Fig. 3.4. A syringe pump (AL-1000 from WPI, Inc.) is filled with dyed (Red Vahine from McCormick, Inc.) water, of surface tension $\sigma \simeq 70$ mN/m, density $\rho \simeq 1000$ kg/m$^3$ and kinematic viscosity $\nu \simeq 10^{-6}$ m$^2$/s at room temperature ($20 \pm 2$°C). The syringe is linked by a tube to a vertical connector (plastic, inner and outer diameters of 3 mm and 3.95 mm, respectively) that releases drops of radius $R_0 = 2.4 \pm 0.03$ mm. These drops fall and impact near the straight edge of a flat substrate. The substrate is dried after each impact using a moist cloth to reduce the deposition of static charges. The substrate can be inclined with an angle $\alpha$ from horizontal, the edge being the axis of rotation. The angle $\alpha = 0°$ corresponds to a horizontal substrate and it is counted positively from the horizontal when the liquid sheet develops downwards as in Fig. 3.4a ($\alpha = 40°$). The substrate is made of dry plexiglass, XT from Superplastic, Inc., 2 mm thick, with advancing and receding contact angles for water of 85° and 55° ($70° \pm 15°$), respectively, cut straight with average roughness of 4 $\mu$m. The offset $d$ is defined as the distance between the impact point and the edge, counted positively when at least half the

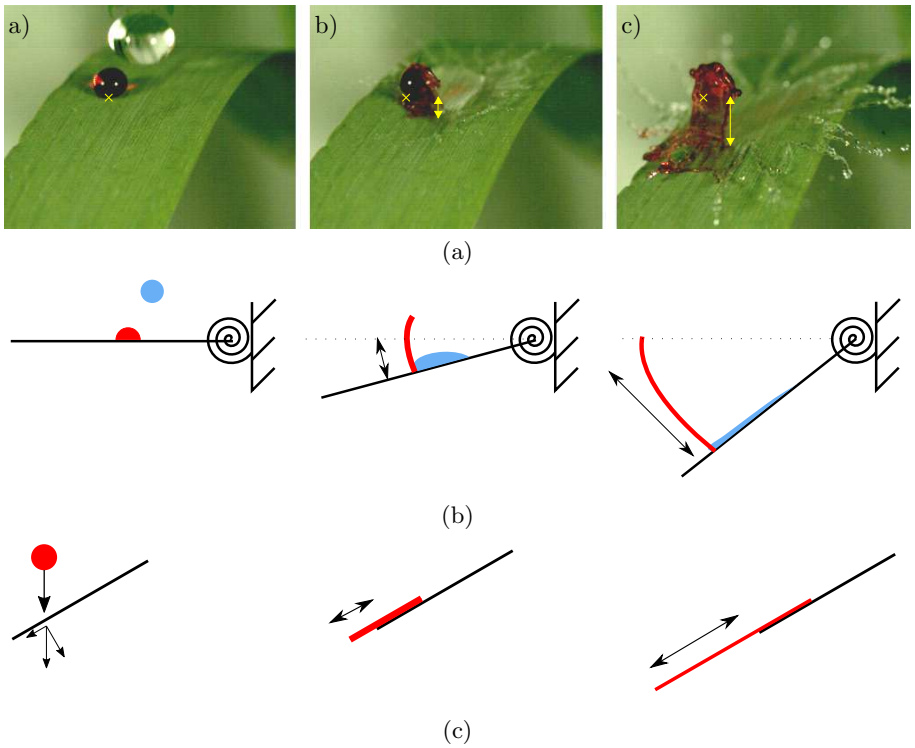


Figure 3.3: (a) A clear water drop impacts on a graminea leaf on which a dyed drop has been deposited. Upon impact, the leaf deflects downwards and stretches the liquid sheet. Times are, from left to right, -0.5, 0.5, 2.5 ms from impact. The yellow crosses and the double arrow indicate the original position of the leaf and the deflection from impact, respectively. (b) Schematic of the stretching of the liquid sheet due to the deflection of a leaf, during a *crescent-moon*. (c) Schematic of the stretching of the liquid sheet following the impact of a single drop on an inclined substrate.

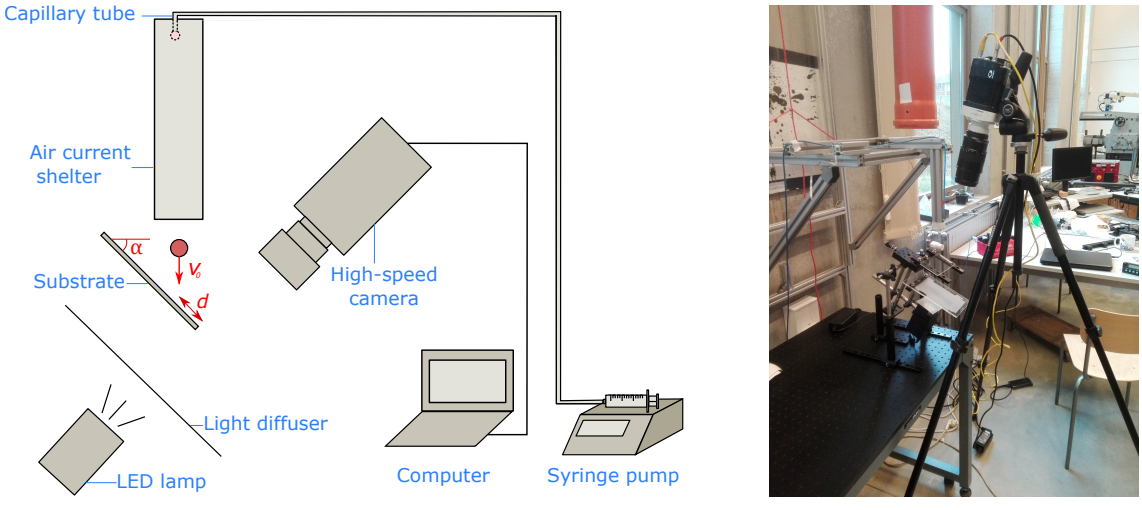


Figure 3.4: Experimental setup

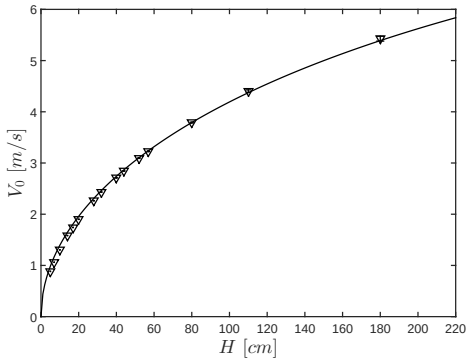


(a)

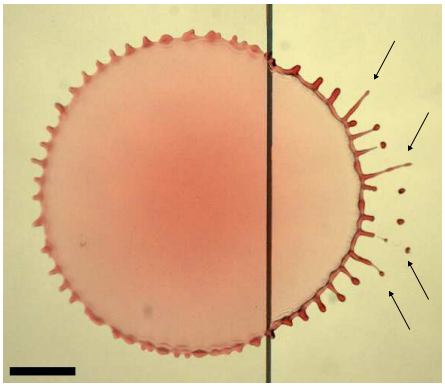

(b)

Figure 3.5: (a) Speed $V_0$ of the impacting drop as a function of its height of release $H$. The solid line corresponds to equation (3.2). (b) Electrostatic effects (arrows) due to local charges deposited on the plexiglass. Scale bar is 5 mm.

drop hits the substrate. It is varied in the range $d/R_0 \in [-1, 16]$ with a millimetre stage (LT1 from Thorlabs, Inc.). Parameters are summarized in table 1. An air shelter was used when the release height was higher than 50 cm to prevent major air currents to influence the trajectory of the falling drop.

### Imaging

The phenomenon is recorded from the top with a high speed camera (MIRO 110 from Phantom, Inc.) at 2000 frames per second and backlighting. The camera is placed perpendicularly to the substrate for all $\alpha \neq 0°$. For $\alpha = 0°$, the inclination of the camera is less than 20° from the vertical, and it is accounted for in the image processing. Depending on the impact speed and substrate inclination, the field of view required to capture the phenomenon varies so the pixel size varies accordingly from 0.056 to 0.1 ±0.002 mm. The position and shape of the spreading liquid on solid, of the liquid sheet in the air and of the droplets are measured by image processing. Interpolations of the motion allows for an accurate detection (less than 0.5 ms) of the time of major events such as the impact of the drop and the entry of the liquid in the air. For each part, i.e., liquid spreading on solid, liquid sheet in the air and droplets, custom routines were designed on which more details will be given in the corresponding sections.

### Measurement of impact parameters

Owing to the controlled injection rate of the syringe pump, the radius of the incoming drop $R_0$ is observed to be fairly constant. A value $R_0 = 2.4 \pm 0.03$ mm is obtained by measuring the drop mass with a precision balance (SE-VWRI611 from VWR, Inc.). Five different impact speeds $V_0$ in the range $1.6 - 6$ m/s were used for the first set of experiment with no substrate inclination (table 1). The variation of $V_0$ was achieved by changing the height of release $H$ of the drop (i.e. the height of the needle), but it could not be accurately measured from top-view. Therefore, a complementary set of visualisations was performed from side-view in order to determine $V_0(H)$. Fifteen different heights were considered, ranging from 5 to 180 cm. The release conditions were exactly the same as in the main experiments. Each measurement was repeated seven times. The average speed of the drop before impact $V_0$ is reported as a function of $H$ in Fig. 3.5a. The error on $V_0$ then mostly results from an error on $H$, which is at most 5 cm at $H = 220$ cm and less than 0.5 cm at $H = 14$ cm. The relative error is then of 3% at most on $H$.

A theoretical model was then fitted on the experimental data from the equation of

motion of the drop during its free fall:

$$F = M_0 \frac{dV}{dt} = M_0 g - \frac{1}{2}\rho_{air} C_d \pi R_0^2 V^2 \tag{3.1}$$

where $M_0$ is the mass of the impacting drop, $V$ the speed of the falling drop, $g$ is the acceleration of gravity, $\rho_{air}$ is the air density and $C_d$ the friction coefficient. This equation can be solved analytically for $C_d$ = Cst. to provide the speed $V_0$ attained by a drop falling from rest over a distance $H$:

$$V_0 = \sqrt{\frac{g}{B}(1 - e^{-2Bh})} \tag{3.2}$$

with $B = 3\rho_{air} C_d/(8\rho_{drop} R_0)$, $\rho_{air} \simeq 1.177 \text{kg/m}^3$ and $\rho_{drop} \simeq 1000$ kg/m$^3$ (Range & Feuillebois, 1998). The friction coefficient $C_d = 0.61$ is the fitting parameter. The Reynolds number associated to the free fall (based on impact speed) $Re = 2\rho V_0 R_0/\nu$ is comprised between 7000 and 30000. For a rigid sphere, $C_d = 0.45$ for $Re > 1000$. The higher value obtained here is expected as the drop will deform during its fall and flattens and its aerodynamic drag increases. Another additional reason may be that the drop starts its fall from rest, where the Reynolds number is 0. In the Stokes regime, the drag coefficient goes as $C_d = 24/Re \gg 1$. The drop however, quickly accelerates, and probably spends most of its fall in the regime $Re \gg 1$. In this model, the equation of motion of the drop was integrated for a fixed $C_d$ and adjusted to the experimental curve. For other heights, $V_0$ is then directly calculated from Eq. (3.2).

In the case of the inclined setup, side-view videos were taken by synchronizing another high-speed camera (Fastcam Mini UX from Photron, Inc) to the first. Images were recorded at 4000 frames per seconds and the falling speed of the drops was directly measured.

Slight oscillations and flattening of the incoming drop were observed during the free fall right before impact. However, since the volume of the drop remains unaffected, the effect of this non-sphericity on the spreading of the liquid was neglected in first approximation. Drops released from the same height are also subjected to sensibly the same deformations at impact.

Plexiglass is a good electrical insulator, so it can accumulate local charges when wiped with a dry cloth. Techniques involving the post-drying removal of charges by rubbing conductive material on the substrate tend to damage the plexiglass. To prevent depositing such charges, the plexiglass was dried using a slightly wet tissue and some time was left for the remaining moisture to evaporate. Nevertheless some electrostatic effects were still visible on rare occasions (Fig 3.5b). These effects are clearly identifiable as they induce the creation of long and fast corrugations that do not destabilize at first. These effects were unmistakably identifiable and a screening of the dataset was performed prior to analysis to remove any impact movie that showed such behaviour.

### Dimensional analysis

Our system has seven dimensional input variables and parameters, which are $d$ [mm], $V_0$ [mm/s], $R_0$ [mm], $\rho$ [kg/mm$^3$], $\nu$ [mm$^2$/s], $g$ [mm/s$^2$] and $\sigma$ [kg/s$^2$] (cf. table 1). Together these variables and parameters are expressed using three fundamentals units: length, time and mass. From the theorem of Vaschy-Buckingham, there exists 7-3 = 4 independent non-dimensional numbers that can be constructed. It means that our whole system can be described not by seven but four variables, which reduces the number of experiments to be done. Angles such as $\alpha$ (the inclination of the substrate) and the advancing and receding contact angles will be considered separately as they are already non-dimensional. We start with dimensionless groups that include one varied input parameter each, then we introduce the dimensionless groups that we will keep constant. In this process, we first

define a non dimensional length $d/R_0$ that should encompass the asymmetry variation in our system.

We then look to compare, on one side, the kinetic energy of the impacting drop, varied through the impact speed $V_0$, which will increase fragmentation, to the surface energy which arises from the cohesive forces between the water molecules. This ratio was introduced in chapter 2 as the Weber number

$$We = \frac{\text{Kinetic Energy}}{\text{Surface Energy}} = 2\frac{\rho R_0 V_0^2}{\sigma}.$$

It was also mentioned that $We$ could be seen as the ratio $We \sim (t_c/t_i)^2$ of the impact time $t_i = 2R_0/V_0 \sim 1$ ms (table 1) and of the capillary time $t_c = \sqrt{4\rho R_0^3/(3\sigma)} = 16.2$ ms (table 1). In our experiments, $We$ varies between 180 and 2400, so it is always much larger than unity, which actually permits the fragmentation of the incoming drop (table 1). Thus, inertia will be dominant is this phenomenon. As a side effect the wetting properties of the substrate will be of minor importance for the initial spreading of the drop. The inclination of the substrate, $\alpha$ is the last of our dimensionless parameters to be varied, here between -40° and 60° from horizontal. Among our initial dimensional variables, only $\nu$ and $g$, expressing the effects of viscosity and gravity, have not been considered yet. Viscosity is traditionally expressed through the common Reynolds number which compares inertia and viscosity (chapter 2). It however involves the impact speed which is varied in our experiments. We prefer to design our dimensionless numbers with a single varying dimensional parameter in each. The Ohnesorge number is the ratio between the viscous time $t_\nu = R_0^2/\nu$, which is the time for the viscosity to take effect (diffusion of momentum and subsequent dissipation of energy), to the capillary time $t_c$, the timescale of our phenomenon. In this case, we observe that viscous effects can be neglected during impact given that the Ohnesorge number $Oh = \sqrt{\nu^2\rho/(2R_0\sigma)}$ is 0.0017 for the considered size of the impacting drop. In our harmonic oscillator analogy (chapter 2), viscosity is also the damping source, which influence is measured through the quality factor Q. It compares the damping time to the natural period of the oscillator. In our case is it thus inversely proportional to $Oh$. We thus have a high-quality factor Q $\simeq$ 588 and viscosity has negligible effects on the system. Viscosity might still affect the break-up and ejection of very small droplets, for which the corresponding $Oh$ would be significantly larger. The resolution of the camera allows the detection of ejected droplets of minimum 0.05 mm diameter, for which $Oh \simeq 0.02$. In the context of partial coalescence, it was observed that viscous forces inhibit inertia-dominated liquid break-up when $Oh \gtrsim 0.025$ (Blanchette & Bigioni, 2006; Gilet *et al.*, 2007). Consequently, we might expect that in our experiment, the radius of the smallest droplets produced by the inertial fragmentation of the liquid sheet is also of the order of 0.02 mm. Our setup should therefore allow to capture most of the spectrum of ejected droplet sizes.

The influence of gravity can be assessed through the Froude number squared $Fr^2 = V_0^2/(2gR_0)$ which compares, for the impact duration, the inertial pressure $\rho V_0^2$ to the hydrostatic pressure over the drop size, $2\rho g R_0$. It ranges between 50 and 800, allowing to neglect hydrostatic pressure effects during the initial crushing. The influence of gravity is also negligible during the sheet expansion and fragmentation in the air. Indeed, a comparison of the hydrodynamic pressure and the Laplace pressure in the rim of thickness $h$ yields the Bond number $\rho g h^2/\sigma$. The thickness $h$ has been estimated to 0.5 mm on a movie at $We = 160$, which gives $Bo = 0.035 \ll 1$ so hydrostatic pressure can be neglected. For inclined substrates, we can also compare the spreading speed of the liquid which should be of the order of $V_0$, to the increase in speed that gravity can confer to the liquid sheet over its characteristic lifetime $t_c = 16$ ms. In our configuration, the impact speed is varied between 3 m/s and 5.6 m/s. The speed increase due to gravity scales as $g \sin\alpha t_c \sim 0.14$ m/s for $\alpha = 60°$, which is much lower than $V_0$. Gravity should thus be negligible at first order with respect to inertia. Overall, our main varied dimensionless numbers will be the dimensionless offset $d/R_0$, the Weber number $We$ and the substrate inclination $\alpha$.

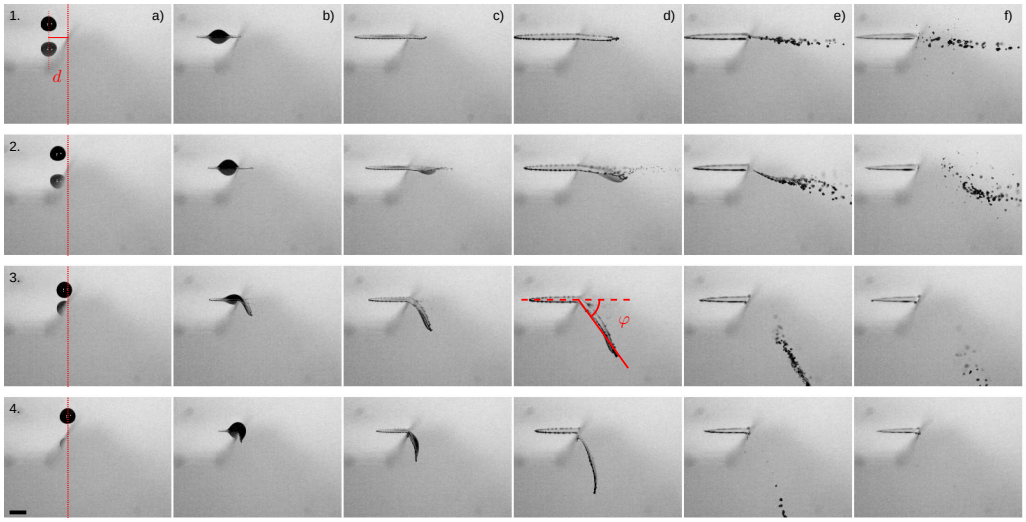


Figure 3.6: Side views of drops impacting close to an edge on a horizontal, flat and dry substrate. The deflection of the sheet at maximum expansion with respect to the substrate is noted $\varphi$. Images are taken at a single impact speed of 4.4 m/s with a decreasing offset $d$. From top to bottom, $d/R_0$ = 2.3, 1, 0.4 -0.1. Images are taken at -0.5, 0.5, 1.5, 3.5, 10.5 and 17 ms from impact, respectively, from left to right. Scale bar is 5 mm.

### Comparison to rainfall parameters

In rainfalls, the diameter and terminal speed of raindrops range from 0.5 mm at 2 m/s to 5 mm at 9 m/s, respectively (Reyssat *et al.*, 2007; Villermaux & Bossa, 2009). These parameters yield $We \in [28, 5800]$, $Fr \in [800, 1700]$ and $Oh \in [0.0017, 0.0053]$. The Weber number will be the main parameter governing fragmentation and it was thus crucial to ensure similarity between the range covered in our experiments and the one encountered in rainfalls. The Froude number being greater than 1 in our experiments as well as in rainfall events is sufficient information to neglect gravity in both cases. The Ohnesorge must be smaller than 1 to neglect viscosity, which is the case. Its exact value however matters as, during the fragmentation process, it probably sets a lower bound to the size of ejected droplets. We can thus assume that both in our experiments as for rainfalls, the dominant effects will be inertia and surface tension while gravity will be negligible and the effects of viscosity may have to be considered for the fragmentation process but can be neglected during impact.

## 3.3 Setup validation - Sheet inclination with respect to the substrate

Analysing drop impacts on leaves is challenging due to the inherently three-dimensional nature of the phenomenon. In the previous chapter, we proposed a way to reproduce the liquid sheet behaviour observed in drop impact on leaves by letting a single drop impact close to the edge of a dry, straight cut substrate. Our hypothesis is that the outcome is an asymmetric liquid sheet that remains in the plane of the substrate. The planar movement of the sheet is crucial for the accuracy of geometric and kinematic measurements from the normal view alone. Our first step consists in verifying this assumption and the range of its validity.

A first set of data was collected on a horizontal substrate to measure the deflection $\varphi$ of the sheet with respect to the substrate when the sheet reaches its maximal expansion. Impacts were recorded from the side at 2000 fps and both offset $d$ and Weber number $We$ were varied. Figure 3.6 shows the time evolution of four impacts for decreasing $d$ at

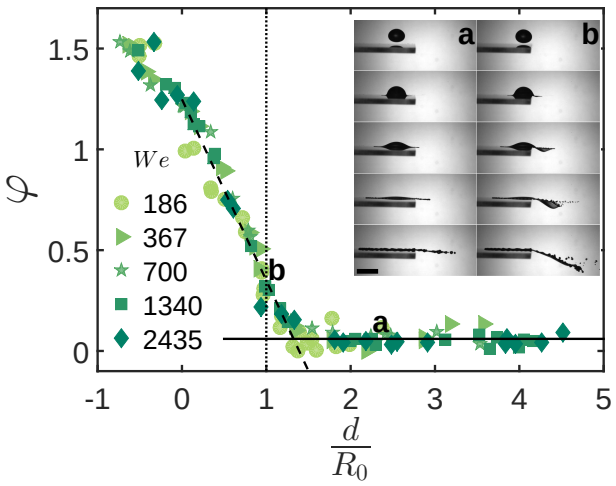


Figure 3.7: Deflection $\varphi$ of the sheet with respect to the substrate as a function of the offset $d/R_0$ for different $We$. The solid line is $\varphi$ = 0.06 rad and the long dotted line represents Eq. (3.3). Inset: Side-view time sequence of a drop impacting near an edge at $We = 680$, for $d/R_0$ = 2.2 (a) and $d/R_0$ = 1 (b). Images are taken at -0.2, 0.4, 1, 2.2 and 6.4 ms from impact, respectively from top to bottom. Scale bar is 4 mm.

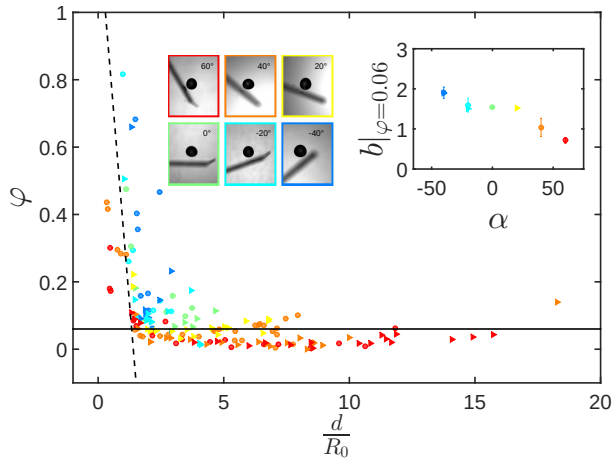


Figure 3.8: Deflection $\varphi$ of the sheet with respect to the substrate as a function of the offset $d/R_0$ for different $We$ (500 ◯, 2000 ▷) and inclination of substrate $\alpha$ with respect to the horizontal (cf. Inset right). The solid line is $\varphi$ = 0.06 rad and the long dotted line represents Eq. (3.3). Inset right: Intersection value between the plateau at 0.06 rad and the best fit of Eq. (3.4) per $We$ and $\alpha$. Inset left: Illustration of the inclination of the substrate.

constant $We$ .

At large offset, such as in the first row of Fig. 3.6, the sheet stays approximately in the plane of the substrate throughout the whole process. The droplets are also ejected in this plane, except during the final collapse of the sheet where antagonistic movements of the rim along the edge give rise to out-of-plane ejections (Fig. 3.6- 1. f). The deflection increases as the drop hits closer to the edge.

Results for five $We \in$ [180 2400] and offsets from $d/R_0 \in$ [-1 5] show that the deflection first decreases linearly with an increased $d/R_0$, then reaches a plateau of mean value 0.06 rad, independent of $We$ (Fig. 3.7). This non-zero value could be explained by the slight hydrophilicity of the substrate (Roisman *et al.*, 2010; Duez *et al.*, 2010) or by an imperfect transfer of momentum from vertical to horizontal during initial crushing and it was also noted for symmetric impacts on poles (Wang & Bourouiba, 2017). A linear fit of the range $d/R_0 \in [0, 1]$ gives

$$\varphi \simeq 0.9(1.4 - \frac{d}{R_0}). \tag{3.3}$$

The intersection of this fit with the plateau occurs at $d/R_0 \simeq 1.3$. For larger offsets, the sheet can be assumed to remain in the plane of the substrate (Fig. 3.7 - inset a). When $d/R_0 < 1.3$ (Fig. 3.7 - inset b), the deformation of the drop at initial crush brings part of the liquid beyond the edge. This creates a bulge and jeopardizes a planar sheet expansion. The bulge however resorbs during the retraction and the sheet becomes planar again but inclined. In the remainder of this work, we exclude experiments with $d/R_0 < 1$, for which drops are split by the edge.

A similar check was performed on the impacts with inclined substrates, based on the synchronized side-view imaging. Two Weber numbers (520 and 2000) and six inclinations ranging from -40° to 60° are tested. Similarly to the horizontal case, a decrease in $\varphi$ is observed as the offset increases without any noticeable variation with $We$ (Fig. 3.8). The black lines indicate Eq. (3.3) (dashed) and $\varphi = 0.06$ rad (solid). The inclination of the substrate shifts the threshold value at which a bulge appears. To quantify this shift, datapoints with values of $\varphi >$0.17 rad were fitted using

$$\varphi = 0.9(b - \frac{d}{R_0}), \tag{3.4}$$

with one different fitting parameter $b$ for each pair of $\alpha$ and $We$ (Fig. 3.8- inset right). The parameter $b$ decreases with increasing $\alpha$. The inclination of the substrate has thus an effect on the deflection of the liquid sheet. No datapoints at smaller offset were taken so we cannot confirm if a constant slope is the correct approximation. Datapoints for which the sheet deflection was higher than 20° (0.34 rad) were removed to limit error during image processing.

# Chapter 4

# Phenomenology

Impacts of single drops near the edge of dry straight cut substrates create asymmetric liquid sheets that destabilize into droplets. These sheets are very similar to those created during raindrop impacts on leaves, which play a major role in the dispersal of foliar diseases. The time evolution of impacts near edges is first discussed on a typical example. The effects of the distance of impact to the edge and of the impact speed on the phenomenology of the liquid sheet and droplet ejection are then discussed. Influence of the inclination of the substrate comes next. Terminology used in this work is recalled in Fig. 4.1.

In Fig. 4.2, the impact near the edge of a horizontal substrate is presented from synchronized top and side views. Along the edge, the extension of the liquid sheet follows the spread on the solid (Fig. 4.2 - panels b-d). By contrast, the strong retraction of the sheet along the edge is desynchronized from the slight dewetting on top of the substrate (Fig. 4.2 - panels e-g). In the direction normal to the edge, the sheet extends further in the air than it spreads on the solid (Fig. 4.2 - panels b-d). The maximum extension of the sheet is reached first along the edge then normal to the edge (Fig. 4.2 - panel e). The differences in these extension and retraction kinematics normal and tangent to the edge are key in shaping the asymmetric liquid sheet. Droplets are emitted from the corrugated rim at the front of the sheet, as well as from the break-up of the ligaments after the collapse of the sheet.

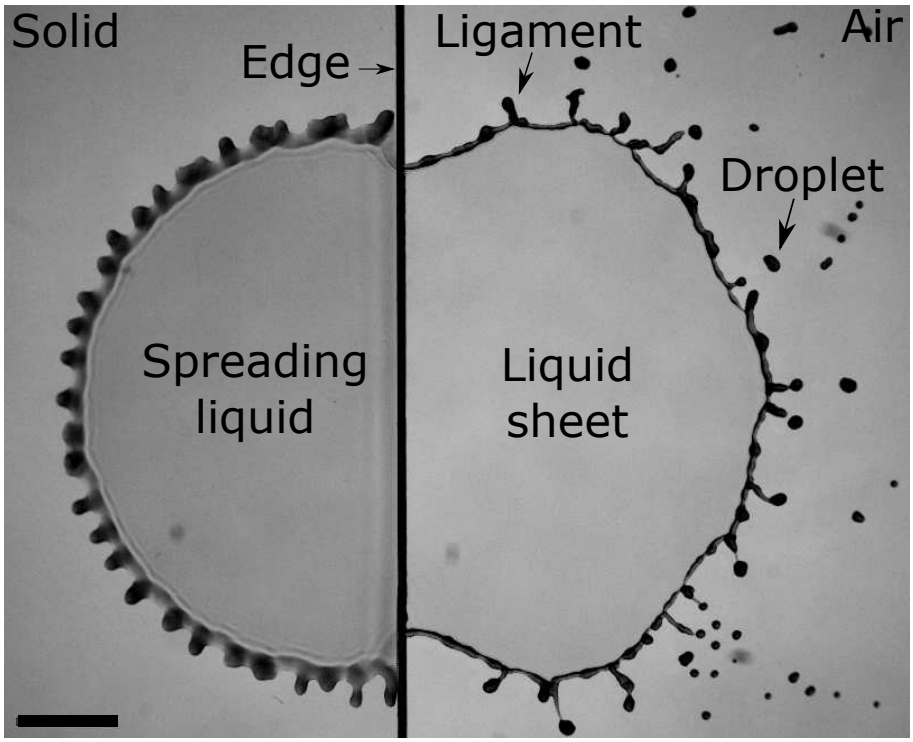


Figure 4.1: Terminology

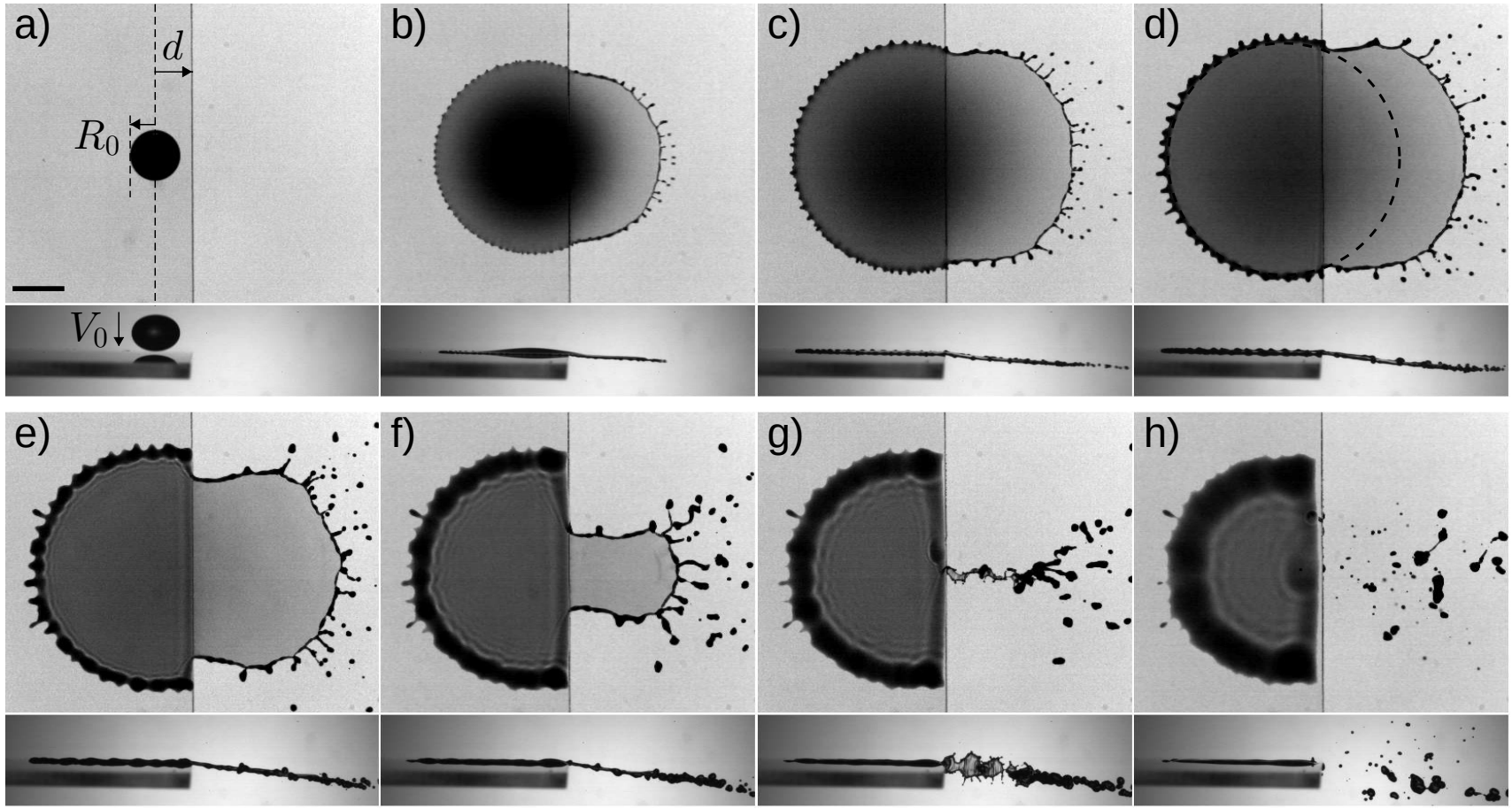


Figure 4.2: Drop impact on a flat surface close to its edge, from top and side views. The radius of the impacting drop is $R_0 \simeq 2.4$ mm and the Weber number $We = 1300$. The offset $d$ is defined as the distance between the impact point and the edge. The scale bar is 5 mm and the times are $t = 0$ ms, 1.6 ms, 3 ms, 4.4 ms, 7 ms, 10.6 ms, 12.4 ms and 19 ms from impact. The dashed circle in (d) shows the alignment between the spreading on solid and the sheet extension along the edge.

Both the shape and the amount of liquid in the sheet vary with the offset. Figure 4.3 shows four impacts with the same $We$ but different $d/R_0$. The initial spreading on solid is obviously identical for all, and almost axisymmetric. With a smaller offset, the liquid reaches the edge and enters the air sooner and consequently at higher speed. The extension of the sheet in the air is faster than the spreading on solid in the direction normal to the edge while it follows the extension speed of the spreading tangentially to the edge. This anisotropy in extension causes a distortion of the sheet that is more pronounced as the offset decreases. The maximal extensions of the sheet in directions normal and tangential to the edge are reached at different times, which strongly conditions the subsequent retraction. The rim away from the edge becomes more corrugated and emits droplets sooner than the rim close to the edge (Fig. 4.3 - column b).

As offset is varied, three main scenarios with increasing asymmetry emerge:

(I) When $d$ is sufficiently large (Fig. 4.3 - row 1), the maximum extension of the sheet is reached simultaneously along and normal to the edge. The shape of the sheet is approximately axisymmetric, analogue to spreading on solid. The sheet retraction is also axisymmetric. Droplets are only emitted during this retraction phase.

(II) As $d$ decreases (Fig. 4.3 - rows 2 and 3), the maximum extension is both larger and reached later in the direction normal to the edge than in the direction tangent to the edge. The retraction of the sheet is mostly dominated by the early motion tangent to the edge. The final shape prior to collapse varies from a small triangle attached to the edge to a rectangle with a width along the edge smaller than its length normal to it. The sheet collapses all at once into a filament (Fig. 4.3 - column 2 e and 3 f-g). The breakup of this filament generates droplets that are significantly smaller than those ejected from the sheet. The term 'filament' will be reserved throughout this work to designate this phenomenon.

(III) Finally at $d/R_0 \sim 1.3$ (Fig. 4.3 - row 4), the sheet anisotropy is so pronounced that it takes a polygonal shape that is conserved during retraction. The retraction along the edge is completed while it has only started in the perpendicular direction. The sheet then pinches and separates from the edge before collapse. This pinching also generates a filament that breaks up into tiny droplets.

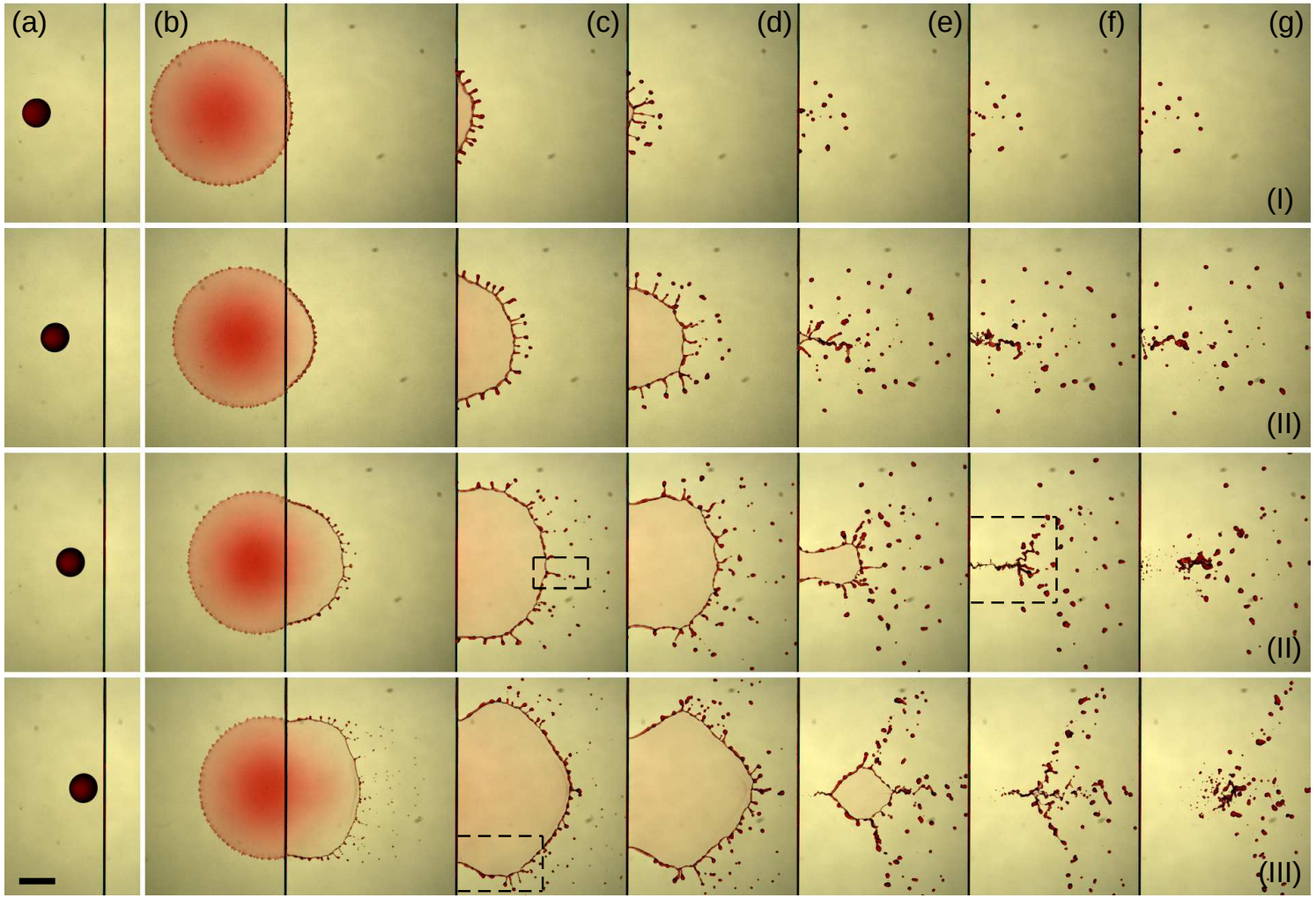


Figure 4.3: Time evolution of the sheet for $d/R_0$ = 4.4, 3.2, 2 and 1.3 (top to bottom) and $We$ = 1340. Rows 1, 2, 3 and 4 correspond to the retraction scenarios I, II, II and III respectively. Snapshots in a same column are taken at the same time $t$ from impact, with $t$ = 0 ms, 3 ms, 6 ms, 8 ms, 11 ms, 12 ms, and 14 ms from left to right. Column (a) illustrates the position of the drops right before impact, with respect to the edge. Scale bar is 5 mm. The dotted frames highlight three different droplet ejection mechanisms illustrated in Fig. 6.3.

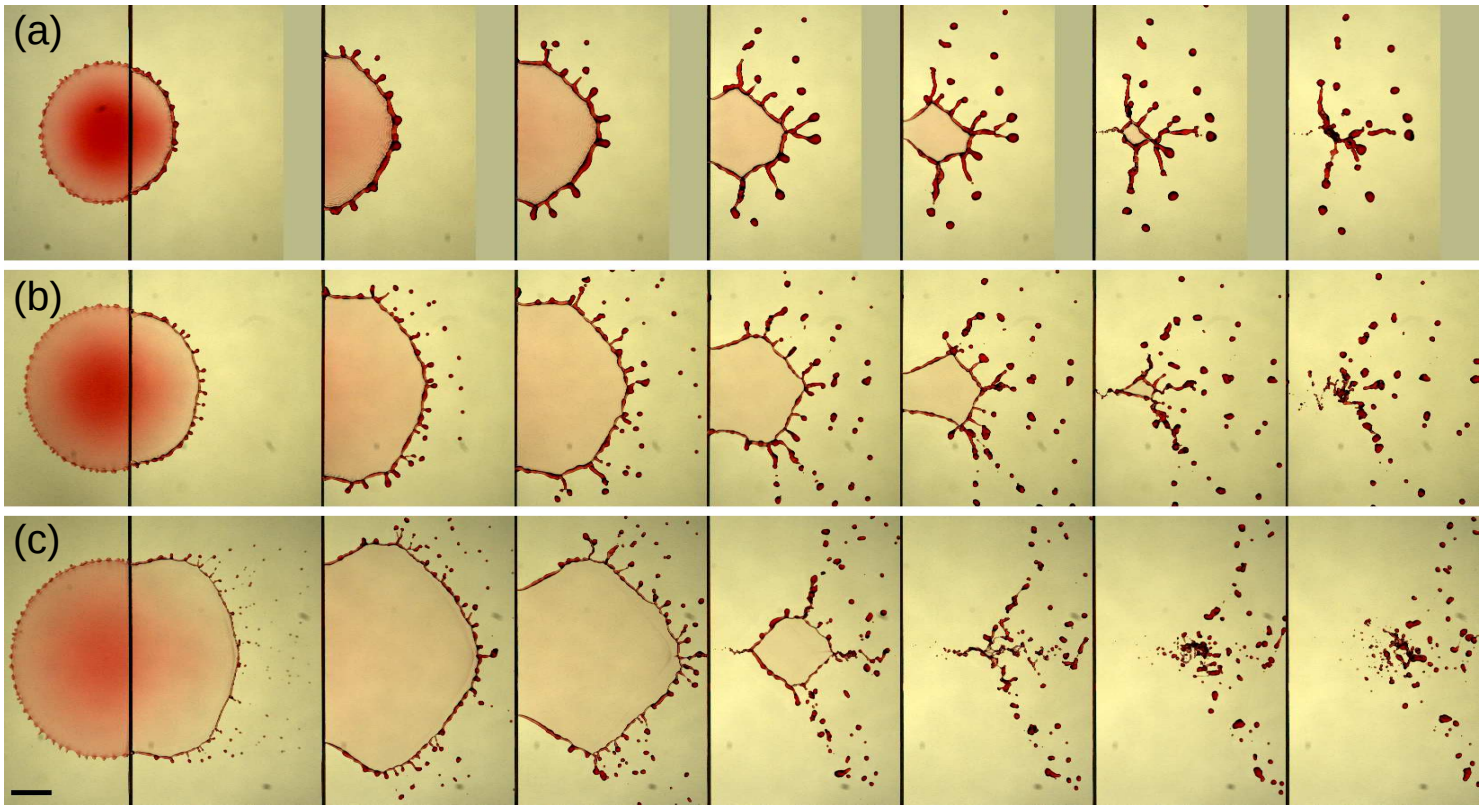


Figure 4.4: Time evolution of the sheet for $We = 367$, 700 and 1340, from top to bottom, for $d/R_0 = 1.3$, all leading to scenario III. Snapshots in a same column are taken at the same time $t = 3$ ms, 6 ms, 8 ms, 11 ms, 12 ms, 13 ms and 14 ms from impact, from left to right. Scale bar is 5 mm.

For a given offset, a variation of the impact speed (and corresponding Weber number) does not strongly modify the shape of the liquid sheet. Three examples of impacts taken at identical $d/R_0 \simeq 1.3$ and different speeds are illustrated in Fig. 4.4, all leading to scenario III. Differences are nevertheless observed, both in terms of temporal evolution and size of the sheet. At higher impact speed, the maximal sheet expansion is larger, but collapses sooner. The ejected droplets are also smaller and are ejected sooner.

When inclining the substrate, the synchronized side and normal views of an impact at 60° in Fig. 4.5 show that the major outline of the phenomenology remains unchanged. The drop hits the substrate and spreads on the solid before entering the air. There, the liquid sheet remains in the plane of the substrate and expands freely normal to the edge while the expansion along the edge follows again the spreading on the substrate. The violent collapse of the retracting sheet in a filament is visible and gives rise to out-of-plane ejections (Fig. 4.5 - top c-e).

The inclination induces changes in the phenomenology such as in the sheet extension normal to the edge which is more stretched for a given offset in the inclined case than on its horizontal counterpart. Figure 4.6 shows three examples of impact on a substrate inclined at 60° for a single impact speed and three decreasing offsets. The type of outcomes remains confined to the three scenarios observed in the horizontal case, namely:

- an isotropic retraction of the sheet towards the edge (Scenario I - Fig. 4.6 - column I),
- a marked tangential retraction speed along the edge with the collapse in a single point along the edge (Scenario II - Fig. 4.6 - column II) and
- a marked retraction speed along the edge with collapse of the sheet in a point close to the edge while part of the sheet still exists beyond this point (Scenario III - Fig. 4.6 - column III).

The spreading liquid on the solid is stretched in the direction normal to the edge in the form of an ellipse (Fig. 4.6 - column I b-g) so a larger interval of offset is available for positive $\alpha$. The value of offset at which the scenario changes is larger than for the horizontal case and thus depends on the inclination. In column (I) and (II) of Fig. 4.6, the liquid sheet expands then retracts towards the edge which is the behaviour that was also observed in the horizontal case. Column (III) of Fig. 4.6 however, shows no such general retraction of the liquid sheet towards the edge. Instead, the body of the sheet keeps moving away from the edge while fragmenting. This behaviour was observed on horizontal substrates but only for $d/R_0 \leq 1$ which were discarded. The droplets ejected from this liquid sheet will inherit a greater initial speed. The formation of corrugations and the ejection of droplets are also delayed and more scarce in this case of positive, downward inclination.

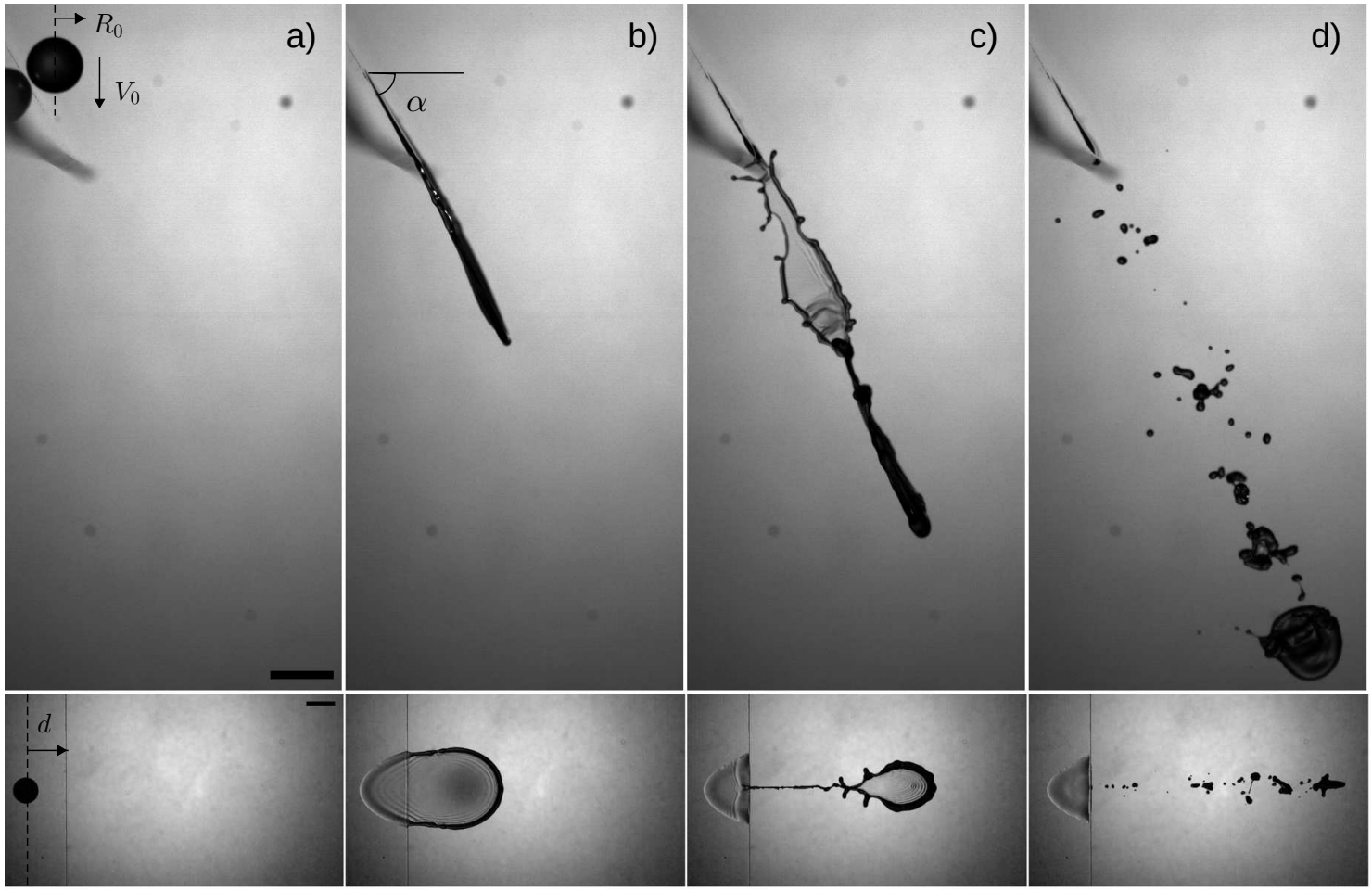


Figure 4.5: Drop impact on an inclined surface (60° from horizontal) close to its edge, from side and top views. The radius of the impacting drop is $R_0 \simeq 2.4$ mm and the impact speed $V_0 = 2.8$ m/s. The offset $d = 5.9$ mm is defined as the distance between the impact point and the edge in the plane of the substrate. The scale bars are 5 mm and the times are $t = 0$ ms, 13 ms, 27 ms, and 38 ms from impact.

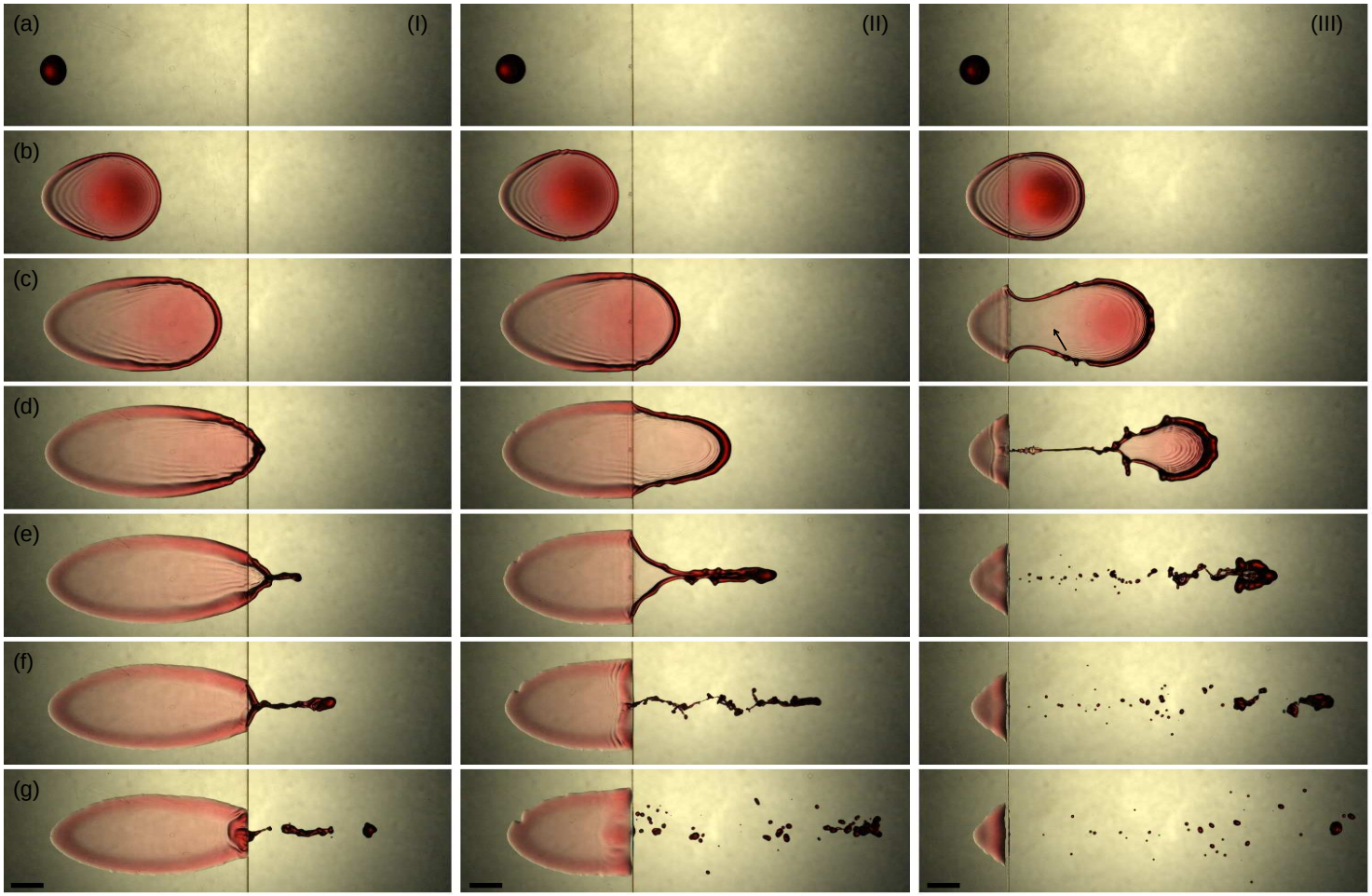


Figure 4.6: Time evolution of the liquid sheet for $d/R_0 = 12$, 7.3 and 1.6 (left to right), inclination $\alpha = 60°$ and $We = 520$. Retraction scenarios are, from left to right, I, II and III respectively. Snapshots in a same rows are taken at the same time $t$ from impact, with $t = 0$ ms, 4 ms, 8 ms, 12 ms, 16 ms, 20 ms and 26 ms, from top to bottom. Row (a) illustrates the position of the drops right before impact, with respect to the edge. The scale bar is 5 mm.

Impacts for five inclinations of the substrate at similar offset and impact speed, in Fig. 4.7, confirms that a change in inclination modifies the offset at which the transition between successive scenarios occurs. In Fig. 4.7, for similar offsets, we observed scenario III in rows a), b) and c) which are inclined by 60°, 40° and 20° respectively (although row c is at the very frontier of scenarios II and III). We observed scenario II in row d), inclined by 0° and scenario I for row e), inclined by -20°. Differences already noticed in Fig. 4.6 are more visible here. We note the ellipsoidal spreading on solid and the increased extension of the sheet normal to the edge as the inclination increases, which results in greater length of the filament upon collapse, when it occurs. Greater angles of inclination also delay the formation of corrugations and droplet ejections while smaller ones promote them. Finally, in the case of scenario III, the sheet, when fully detached from the substrate, inherits some speed and keeps moving instead of remaining stationary. This will result in an increased speed conferred to the droplets ejected from this part of the liquid sheet for strongly positively inclined substrates.

Two additional phenomena were observed in the inclined configuration and will be discussed in a qualitative way in this section but they will not be the object of further quantitative investigation in the rest of the manuscript.

For the horizontal and negative inclined substrates, when the offset corresponded to the maximum expansion of the spreading on the solid, no sheet in the air was formed and thus no droplet ejection was visible. However, for similar values of offset, when the substrate has a strong positive inclination, the liquid on the solid naturally accumulates towards the edge as visible in Fig. 4.8a. This accumulated fluid keeps moving, most likely under the effect of gravity, and flows down further than the maximal spreading distance of the liquid sheet. Such phenomenon has been previously observed in oblique impacts on dry substrate and notably in the case of blood droplet projections such as in Fig. 4.8b from (Adam, 2012). In the presence of an edge, this fluid enters the air to form a ligament that destabilizes into droplets. These droplets are ejected with a non zero initial speed linked to the motion of the ligament. This is a phenomenon that might take part in the dispersal of foliar diseases through raindrop impacts. Yet, since our focus was on the droplet generation through asymmetric liquid sheet, the investigation of this phenomenon will be left for future work.

The second mechanism is related to the entrapment of an air bubble under a drop impacting on a solid surface reported by Chandra & Avedisian (1991) and Thoroddsen *et al.* (2005). We observed the formation of this bubble beneath the impact point while performing our experiments. On our most positively inclined surfaces ($\alpha = 60°$), this bubble was slightly moving at early times and in the case of very small offsets, the bubble entered the liquid sheet in the air, as seen in Fig. 4.9a. Once in the sheet, it kept moving with the surrounding liquid instead of stopping as was observed at larger offsets. We tracked its position with time while the dynamics of the sheet allowed it. The results in Fig. 4.9b show that the speed of the bubble, contrary to intuition, is closer to the normal component of the impact speed, rather than to its tangential one. Although this particular phenomenon was not investigated further, this information helped us in our rationalization of the dynamics of the sheet which will be discussed in the next chapter.

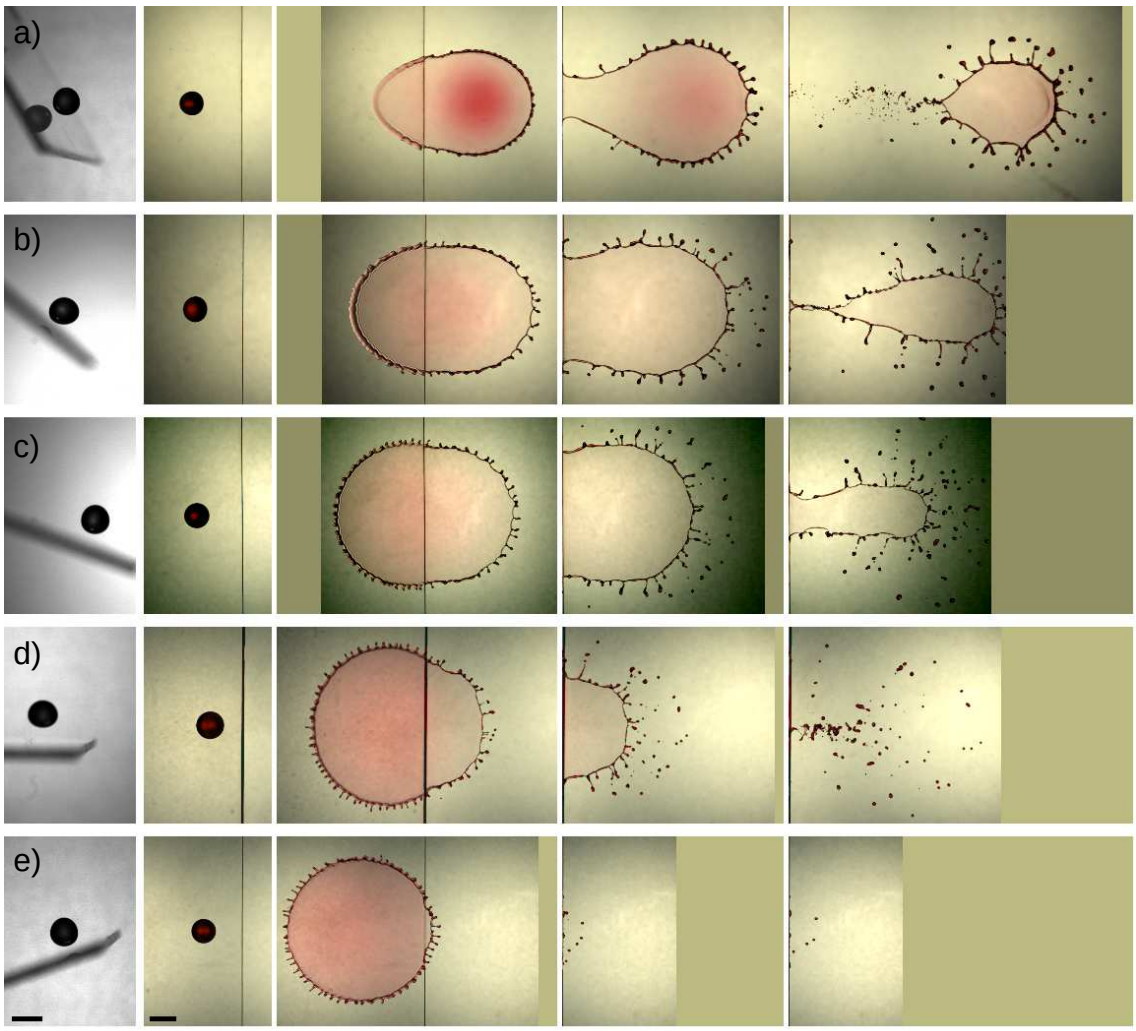


Figure 4.7: Time evolution of the sheet for inclinations from horizontal of 60° (a), 40° (b), 20° (c), 0° (d) and -20° (e) with similar $d/R_0$ (respectively of 2, 3, 3.6, 3.6 and 3.4) and $We = 2100$. The rows display retraction scenarios III for rows a), b) and c), II for row d) and scenario I for row e). The first and second left columns show the moment before impact from side view and top view respectively. Snapshots in a same columns are taken at the same time $t$ from impact, with $t$ = -0.5 ms (side view), -0.5 ms (top view), 4 ms, 7 ms and 11 ms, from left to right. The scale bars are 5 mm.

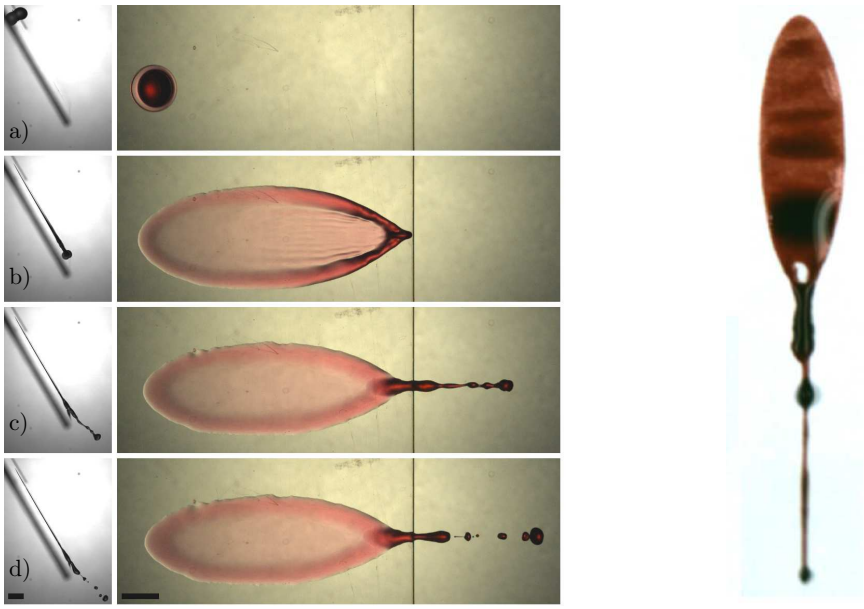


(a) (b)

Figure 4.8: (a) Synchronized side and top views of a dyed water drop impacting a dry substrate, inclined at 60° from horizontal. The drop impacts at a distance from the edge greater than the maximum spreading radius. Times are, from top to bottom, 0.5, 14.5, 24.5 and 28 ms after impact. Scale bars are 5 mm. (b) Stain following non-perpendicular impact of a blood drop falling from 0.8 m on a substrate inclined at 80° from the horizontal [Adapted from Adam (2012)].

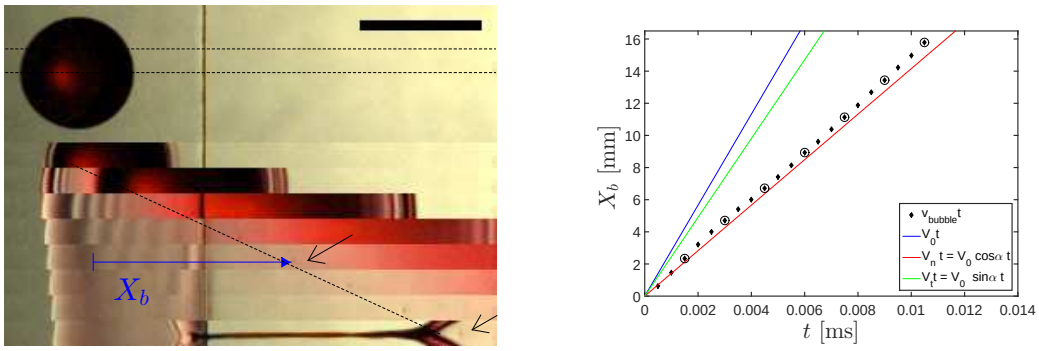


(a) (b)

Figure 4.9: (a) Formation and motion of an air bubble following the impact of a water drop close to the edge of a dry substrate inclined at 60° from horizontal. The moment of impact is shown at the top, with horizontal dashed lines indicating the highlighted portion in the subsequent images. Times are, from top to bottom, 0, 0.5, 1.5, 3, 4.5, 6, 7.5, 9 and 10.5 ms from impact. The inclined dashed line shows the position of the bubble, with arrows pointing it in 6 and 10.5 ms from impact. Scale bar is 5 mm. $X_b$ is the distance travelled by the bubble in the direction normal to the edge measured from the impact point. (b) Distance $X_b$ from the experiment illustrated in (a), as a function of time, from impact until the bubble disappears in the sheet rim (black diamonds). The instants illustrated in (a) are circled. Blue, green and red lines represent motions at constant speed $V_0$, $V_n = V_0 \cos\alpha$ and $V_t = V_0 \sin\alpha$, respectively.

# Chapter 5

# Sheet dynamics

Single drops impacting close to the edge of a substrate form non-axisymmetric liquid sheets, which present characteristics similar to the ones observed during impacts of raindrops on leaves. These impacts generate splashed droplets that participate to the propagation of foliar diseases in fields. Three characteristic scenarios based on the retraction behaviour of the liquid sheet were identified (chapter 4). Our hypothesis is that the droplet ejection pattern is directly linked to these sheet behaviours.

In this chapter, we focus on the sheet dynamics to rationalize the occurrence of these scenarios. Phase diagrams are first analysed to quantify the effect of the offset $d$, namely the distance between the impact point and the substrate edge, of the Weber number $We$ and of the substrate inclination $\alpha$, which are our three control parameters. We then study the liquid expansion on the solid. It is followed by a rationalization of the expansion of this liquid sheet in the direction normal to the edge, and by a comparison of its behaviour to the existing literature on axisymmetric liquid sheets. The extension of the sheet in the direction tangential to the edge is then studied. Finally, these rationalizations give insight on the scenarios and sheet asymmetry occurrence which will be discussed last.

## 5.1 Phase diagrams and variable definitions

The scenarios discussed in chapter 4 are first summarized in an offset vs. Weber diagram (Fig. 5.1a), where the different scenarios are highlighted by colour. For each Weber, the scenarios appear in order as the offset is decreased. For $We \lesssim 186$, only the axisymmetric scenario (I) subsists for $d/R_0 \geq 1.3$. Diagrams of inclination of the substrate $\alpha$ vs offset (Fig. 5.1b) for two Weber numbers show that inclination affects the offset boundaries of each scenario. Positive inclination of the substrate promotes the occurrence of more asymmetric configurations, scenarios II and III, while negative $\alpha$ values can prevent their occurrence, beginning at $\alpha$ = -20° for $We$ = 2000 and $\alpha$ = 0° for $We$ = 520 for scenario III. Data with sheet deflection from the plane of the substrate greater than 20°, i.e., error greater than five percent, have been removed from the dataset (cf. section 3.3). In these phase diagrams, the transitions from one scenario to the next are not straightforward. We thus look at the sheet kinematics to rationalize them.

The sheet kinematics is quantified through the evolution of its extension $l_n(t)$ (resp. $l_t(t)$) in the direction normal to the edge (resp. tangential to the edge), as illustrated in Fig. 5.2. Both $l_n(t)$ and $l_t(t)$ are measured from the edge so the time $t_d$ at which the spreading liquid on the solid reaches the edge will be of importance. We measured the spreading $R_s(t)$ of the liquid on the solid, since this motion is a prerequisite to the expansion of the sheet in the air and notably in the determination of $t_d$. The spreading on solid is axisymmetric in the case $\alpha = 0°$ and measured by fitting a circle on the region covered by the fluid on the solid (Fig. 5.2a). For non-zero $\alpha$, the spreading takes an ellipsoid shape as observed in chapter 4 - (Figs. 4.6 and 4.8 notably). The spreading on solid $R_s(t)$ is defined as the distance covered by the fluid in a given direction from the

impact point. We define $R_{sn}(t)$ as the spreading in the direction normal to the edge, for the contact line moving towards the edge. Moreover, we define $R_{st}(t)$ as the spreading in the direction parallel to the edge (Figs. 5.2b and 5.2c). These definitions imply that $R_{sn}(t)$ and $R_{st}(t)$ might not be available for all values of $d$ and $\alpha$ as the liquid can reach the edge very quickly with respect to our acquisition frame rate. An ellipse can however be fitted on the image resulting from the superposition of snapshots at different times for a given experiment. This allows the definition of maximum spreading distances on solid $R_{snM}$ and $R_{stM}$ as in Figs. 5.2b and 5.2c. This latter corresponds to the half width of the ellipse. These measurements are performed automatically with custom image processing in ImageJ and Matlab. By convention, times are measured from time of impact.

## 5.2 Spreading on solid

### Horizontal substrate

Upon impact, the spreading radius $R_s(t)$ quickly increases and reaches a maximum $R_{sM}$ in a finite time $t_{sM}$ (Fig. 5.3a). Slight dewetting is then observed, due to the weak hydrophilicity of the substrate (Rioboo *et al.*, 2002). At first order, the expansion dynamics on the solid is not affected by the fact that part of the liquid is then expanding in the air. Indeed, the shape of the liquid rim on solid remains circular and centered on the impact point, during the whole expansion and independently of the offset $d$ (Figs. 5.3a and 5.3b). During the retraction, we observe capillary waves parallel to the edge emitted by the dewetting dynamics. They are similar to the ones observed along the rim, on the solid, away from the edge (Fig. 4.2 e-f). They seem to indicate a separation between on-solid and in-the-air dynamics. A travelling wave is also visible along the edge, following the retraction of the sheet in the air, but its effects appear to be localized close to the edge. Previous analysis of the early time of spreading suggests that the spreading radius $R_s(t)$ increases proportionally to $\sqrt{t}$ (Rioboo *et al.*, 2002). This scaling law can be understood by considering a circle that moves at constant speed towards a straight line. From a purely kinematic point of view, as soon as the circle intercepts the line, the corresponding chord length grows as the square root of the time from interception. However, at later time the spreading dynamics involves several dissipation mechanisms and there is no simple model that fully describes its kinematics (Yarin & Weiss, 1995; Roisman *et al.*, 2002; Rioboo *et al.*, 2002; Eggers *et al.*, 2010; Lastakowski *et al.*, 2014). Consequently, we chose to fit an empirical function $R_s(t)$ that grows as $\sqrt{t}$ in the early times and saturates in a finite time:

$$\frac{R_s(t)}{R_{sM}} \simeq \sqrt{\frac{t}{t_{sM}}\left(2 - \frac{t}{t_{sM}}\right)}. \tag{5.1}$$

Both $R_{sM}$ and $t_{sM}$ are obtained by least square fitting for each individual impact.

The observed maximum spreading $R_{sM}$ increases with $We$ (Fig. 5.3a - left inset). This variation is well captured by the empirical law of Laan *et al.* (2014):

$$\frac{R_{sM}}{R_0} = \frac{We^{1/2}}{(1.14 + We^{2/5}Oh^{1/5})} \tag{5.2}$$

where the constant 1.14 is fitted on our data. The approximation proposed by Clanet *et al.* (2004),

$$\frac{R_{sM}}{R_0} = We^{1/4} \tag{5.3}$$

describes also well the data.

The time at which the spreading radius reaches its maximum also increases with $We$ (Fig. 5.3a - right inset). It can be adjusted with the power-law

$$t_{sM} \sim We^{1/4} t_i, \tag{5.4}$$

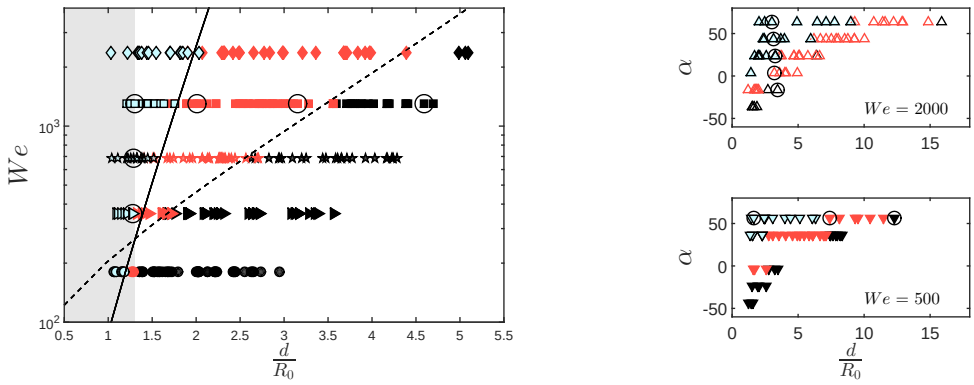


Figure 5.1: Phase diagrams in which different sheet asymmetry scenarios are coloured differently: I (black- Isotropic retraction towards the edge), II (reddish/grey- Pronounced tangential retraction with collapse in a filament) and III (blue/clear- Detachment of the sheet from the edge, before its total collapse) (see chapter 4). (a) Phase diagrams $We$ vs. $d/R_0$, $\alpha = 0°$. Symbols correspond to different $We$ (186 (◯), 367 (▷), 700 (☆), 1340 (□), 2435 (◇)). The data corresponding to the examples of Figs. 4.3 and 4.4 are circled. The shaded region $d/R_0 < 1.3$ corresponds to experiments for which the sheet is not in the plane of the substrate. The solid and dashed lines correspond to Eqs. (5.39) and (5.40), respectively. (b) Phase diagram of inclination of substrate $\alpha$ vs. $d/R_0$ for $We = 2000$ (top) and 520 (bottom). The data corresponding to the examples of Figs. 4.6 and 4.7 are circled.

with $t_{sM} = 0.8\,We^{1/4}t_i$ where the factor 0.8 is fitted and $t_i = 2R_0/V_0$ is the impact time (table 1). The exponent 1/4 suggests that the time of maximum spreading is almost inversely proportional to $\sqrt{V_0}$, as observed by Antonini *et al.* (2012). The alternative scaling

$$t_{sM}/t_i \simeq 0.3\,We^{3/10}\,Oh^{-1/10} \tag{5.5}$$

proposed by Lagubeau *et al.* (2012) is also in good agreement with our data.

The normalized spreading radius $R_s/R_{sM}$ as a function of the normalized time $t/t_{sM}$ is shown in Fig. 5.3b. Data from different $We$ collapse onto a single curve, which is very well approximated by Eq. (5.1) for $t < t_{sM}$. Eq. (5.1) is not valid beyond $t > t_{sM}$ as dewetting obeys a different dynamics that is sensitive to the surface properties of the substrate. From Eq. (5.1), we can predict the time $t_d$ at which the liquid arrives at the edge of the substrate ($R_s(t_d) = d$):

$$\frac{t_d}{t_{sM}} = (1 - \sqrt{1-\delta^2}), \tag{5.6}$$

where

$$\delta = \frac{d}{R_{snM}} < 1$$

is defined as the dimensionless offset for the general case. Figures 5.2a, 5.2b and 5.2c indeed show that $R_{sM} = R_{snM} = R_{stM}$ for $\alpha = 0°$. It is here important to highlight that we define $\delta$ as the offset normalized by the maximum spreading on the solid measured in the direction normal to the edge for consistency with the remaining of this work. When inclining the substrate, $R_{snM}$ differs from $R_{stM}$ so a choice had to be made and will be discussed when appropriate. Equation (5.6) is also in good agreement with the experimental values (Fig. 5.3b - inset).

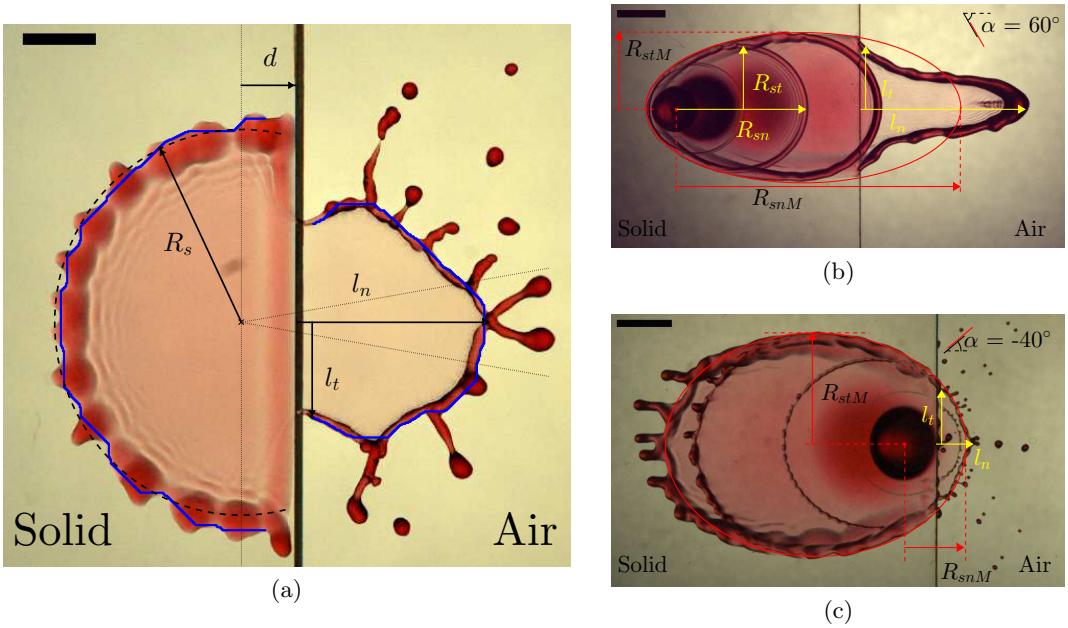


(a) (b) (c)

Figure 5.2: Main variables that characterize the kinematics of the spreading on solid and liquid sheet in the air. (a) Horizontal substrate. The contours (blue lines) are detected by image processing, after thresholding and morphological removal of the corrugations. Scale bar is 4 mm. The radius $R_s$ of the spreading liquid on solid, the extension of the liquid sheet tangent to the edge $l_t$ and the normal extension of the sheet $l_n$ are represented. This latter is taken to be the quantile 85% in distance to the edge of the contour of the sheet located in a sector of $\pm 10^o$ (fine dotted lines). (b) Positively inclined substrate $\alpha = 60°$. Time superposition of images taken at 0, 1, 3, 6 and 14 ms from impact. The red solid line is a fit of the spreading envelope by an ellipse. The maximum extension of spreading on solid is denoted $R_{snM}$ (resp. $R_{stM}$) in the direction normal (resp. tangential) to the edge. The temporal evolution on solid normal $R_{sn}(t)$ and tangential $R_{st}(t)$ to the edge are shown in yellow as well as $l_n(t)$ and $l_t(t)$. Scale bar is 5 mm. (c) Negatively inclined substrate $\alpha$ = -40°. Time superposition of images taken at $t$ = 0, 1.5, 5.5 and 10.5 ms from impact. Scale bar is 5 mm.

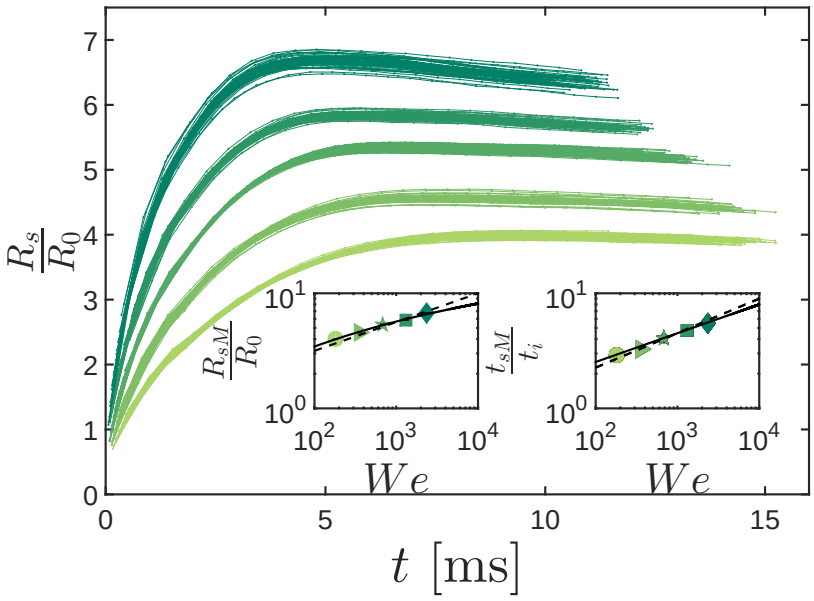


(a)

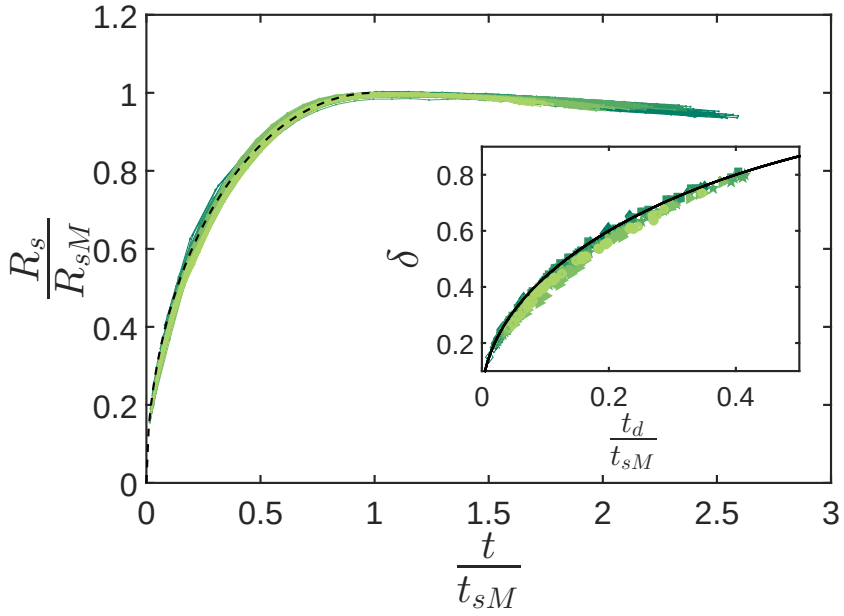


(b)

Figure 5.3: (a) Time evolution of the spreading radius $R_s/R_0$ for increasing $We$ (from bottom to top, $We$ = 180, 350, 680, 1300, 2600) and $\alpha = 0°$. Insets: (Left) Maximum spreading $R_{sM}/R_0$ as a function of $We$. The solid line corresponds to Eq. (5.2) and the dashed line to Eq. (5.3). (Right) Time $t_{sM}/t_i$ of the maximum spreading as a function of $We$. The solid line corresponds to Eq. (5.4). The dotted line is Eq. (5.5) from Lagubeau *et al.* (2012). (b) Rescaled time evolution of the spreading radius $R_s/R_{sM}$ vs. $t/t_{sM}$, for the five $We$ values in table 1. The dotted line shows Eq. (5.1). Inset shows dimensionless offset $\delta = d/R_{sM} = d/R_{snM}$ as a function of $t_d/t_{sM}$. The solid line corresponds to Eq. (5.6). Symbols correspond to different $We$, from 186 to 2435 (table 1).

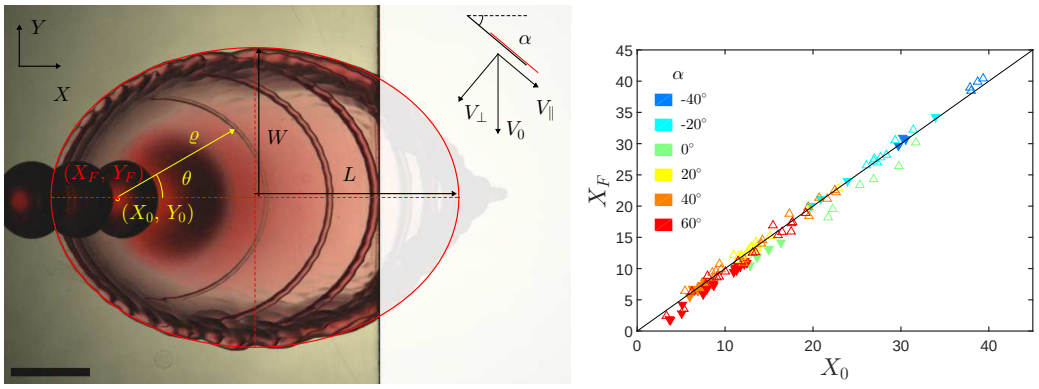


(a) (b)

Figure 5.4: (a) Time superposition of an impact on inclined substrate ($\alpha = 40°$) at $We = 520$. The envelope is approximated by an ellipse of minor and major axes $W$ and $L$ respectively and focus coordinates $(X_F, Y_F)$. The impact point coordinates $(X_0, Y_0)$ are computed based on the trajectory of the falling drop. $\varrho$ and $\theta$ define the polar coordinates centred on the impact point. Inset: The impact speed $V_0$ on a inclined substrate is divided into two components, a speed perpendicular to the substrate $V_\perp = V_0 \cos\alpha$ and a speed parallel to the substrate $V_\parallel = V_0 \sin\alpha$. (b) Parity plot of the focus position $X_F$ vs. $X_0$, the impact point position, both along the X symmetry axis. $We = 520$ ($\triangledown$ - full) and $We = 2000$ ($\triangle$- empty) for $\alpha \in$ [-40° to 60°].

### Inclining the substrate

On an inclined substrate, the envelope of the spreading on solid can be fitted by an ellipse of minor and major axes $W$ and $L$ respectively and focus $(X_F, Y_F)$ as defined in Fig. 5.4a. This focus coincides with the impact point $(X_0, Y_0)$ calculated by extrapolation of the impacting drop trajectory, as confirmed by the parity plot of Fig. 5.4b. This was already noticed by Kang & Ng (2006) in the case of splat morphology.

Almohammadi & Amirfazli (2017b), in the similar experiment of impacting drops on horizontal translating substrates, showed that the ellipsoidal shape could be reconstructed numerically by considering the spreading liquid motion as a combination of an axisymmetric spreading and a translation motion at the speed of the substrate. In our configuration, we consider the spreading on horizontal solid from Eq. (5.1) and add a velocity $V_c$ translating the expanding circles in the direction normal to the edge.

The circles of radius $R_s(t)$ are then centred in $(X, Y) = (V_c t, 0)$, where X and Y are measured from the impact point:

$$(X - V_c t)^2 + Y^2 = R_s(t)^2 \tag{5.7}$$

We define a dimensionless time $t/t_{sM}$ and a dimensionless translation speed $v_s = V_c t_{sM}/R_{sM}$ so that Eq. (5.7) becomes

$$\left(\frac{X}{R_{sM}} - v_s \frac{t}{t_{sM}}\right)^2 + \left(\frac{Y}{R_{sM}}\right)^2 = \left(\frac{R_s(t)}{R_{sM}}\right)^2 = \frac{t}{t_{sM}}\left(2 - \frac{t}{t_{sM}}\right). \tag{5.8}$$

In polar coordinates $(\varrho, \theta)$ centred at the impact point (Fig. 5.4), $X/R_{sM} = \varrho\cos\theta$ and $Y/R_{sM} = \varrho\sin\theta$, so Eq. (5.7) becomes

$$\varrho^2 - 2\varrho v_s \frac{t}{t_{sM}}\cos\theta + (1 + v_s^2)\frac{t}{t_{sM}}^2 - 2\frac{t}{t_{sM}} = 0. \tag{5.9}$$

In each direction $\theta$, the maximum spreading is achieved at time $\frac{t}{t_{sM}} = \frac{t_{\theta M}}{t_{sM}}$ for which

$$\left.\frac{\partial \varrho}{\partial(t/t_{sM})}\right]_\theta \equiv \dot{\varrho} = 0. \tag{5.10}$$

Differentiating Eq. (5.9) according to time yields $(t_{\theta M}/t_{sM}) = (1+\varrho v_s\cos\theta)/(1+v_s^2)$. Substitution of $t/t_{sM} = t_{\theta M}/t_{sM}$ in Eq. (5.9) yields the quadratic equation $\left(1+v_s^2\sin^2\theta\right)\varrho^2 - 2\varrho v_s\cos\theta - 1 = 0$ which is solved for $\varrho(\theta)$. Only the solution $\varrho > 0$ is kept:

$$\varrho = \frac{v_s\cos\theta + \sqrt{1+v_s^2}}{1+v_s^2\sin^2\theta} = \frac{1}{\sqrt{1+v_s^2} - v_s\cos\theta}. \tag{5.11}$$

This is the polar equation of an ellipse, which focus is at the impact point (i.e., in $\varrho = 0$) and axis ratio $W/L$ (Fig. 5.4a) equals to $1/\sqrt{1+v_s^2}$.

We compare this theoretical result with the vertical impact of a drop of radius $R_0$ at speed $V_0$ on a surface of inclination $\alpha$. The impact speed is divided into its components perpendicular and parallel to the substrate, $V_\perp = V_0\cos\alpha$ and $V_\parallel = V_0\sin\alpha$, respectively, as in Fig. 5.4a. On such inclined substrates, two values exists for the maximum spreading radius, the one reached in the direction normal to the edge $R_{snM}$ and the one in the direction tangential to it $R_{stM}$ (Figs. 5.2b and 5.2c). In our theoretical development, the maximum spreading radius $R_{sM}$ to consider is the one reached in the direction tangential to the edge which corresponds to the minor axis $W$ of the ellipse. It is indeed the direction that will not be affected by $V_\parallel$ and thus corresponds to the spreading in a horizontal direction. The law proposed by Laan *et al.* (2014),

$$R_{stM} = W = R_0\frac{We_\perp^{1/2}}{1.14 + We_\perp^{2/5}Oh^{1/5}} \tag{5.12}$$

shows good agreement with the experimental data in Fig. 5.5 in the range of $We$ of interest, provided we used $V_\perp$ in our definition of the Weber number $We_\perp = 2\rho R_0 V_\perp^2/\sigma = We\cos^2\alpha$. A simplified expression

$$R_{stM} = W \simeq R_0\, We_\perp^{1/4} = R_0\, We^{1/4}\sqrt{\cos\alpha} \tag{5.13}$$

based on the scaling of Eq. (5.3) proposed by Clanet *et al.* (2004), presents similarly good agreement (Fig. 5.5) and its simplified form will be the one used in the remaining of this work.

Considering the analogy with the horizontal case, adaptation of Eq. (5.4) to the inclined case

$$t_{stM} = t_W \simeq \frac{1.48R_0}{V_\perp}\, We_\perp^{1/4} \tag{5.14}$$

also shows good agreement with the experimental data (Fig. 5.5 - Inset). The fit in $We_\perp^{1/4}$ gives a coefficient of 1.48, which is close to 1.6 obtained in Eq. (5.4).

We make the hypothesis that the translation speed of the circles $V_c$ should be of the order of $V_\parallel$. We verified this assumption by fitting circles on the first half of the advancing liquid on the solid as illustrated in Fig. 5.6a. The motion along the symmetry axis of the center $X_c$ of these circles has been plotted as a function of time and illustrated for two examples in Fig. 5.6b. These examples show that if the translation motion of these circles begins with a speed close to $V_\parallel$, it decreases to end up with an average value of $V_\parallel/1.38$ between t = 0 and t < $2t_{stM}$ (Fig. 5.6b - Inset). We thus obtain at first order $V_c \simeq V_\parallel/1.38$.

From there, we calculate the dimensionless translation speed $v_s$, :

$$v_s = \frac{V_\parallel}{1.38}\frac{t_W}{W} \simeq 1.07\tan\alpha \tag{5.15}$$

More generally, we can assume that $v_s \simeq \beta\tan\alpha$, from which we obtain:

$$\frac{W}{L} = \frac{1}{\sqrt{1+v_s^2}} \simeq \frac{\cos\alpha}{\sqrt{\beta^2 - (\beta^2-1)\cos^2\alpha}}. \tag{5.16}$$

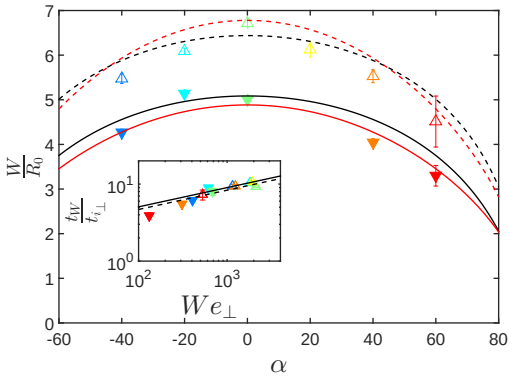


Figure 5.5: Normalized minor axis $W$ of the ellipse obtained by fitting the envelope of the spreading liquid on the substrate as a function of $\alpha$. Solid and dashed lines are Eq. (5.12) (black) and Eq. (5.13) (red). Inset: Time $t_{stM}$ at which $R_{st} = W$, normalized by $t_{i\perp} = 2R_0/V_\perp$ as a function of $We_\perp$. Dashed line is Eq. (5.14) and solid line is Eq. (5.14) with a coefficient 1.6 obtained from Eq. (5.4). Weber numbers are $We = 520$ ($\triangledown$ - full) and $We = 2000$ ($\triangle$ - empty).

In the limit $\beta \to 1$, it becomes

$$\frac{W}{L} \simeq \cos\alpha. \tag{5.17}$$

Using $V_c \simeq V_\parallel/1.38$ indeed yields $\beta = 1.07$ close to one which was reported in (Laan *et al.*, 2014) and corresponds well to the experimental data in Fig. 5.7. The simpler hypothesis that the translation speed of the circles $V_c$ is identical to $V_\parallel$ yields $\beta = 1.48$ for which the experimental agreement is worse. Here, $V_c \simeq V_\parallel/1.38$ is a first order model and further analysis that goes beyond the scope of this thesis are required to better explain this behaviour. Nevertheless, we can now use this model to approximate the circles motion and observe that Eq. (5.9) predicts well the spreading envelope (Fig. 5.6a).

In the same manner as for the horizontal substrate, the maximum spreading radius normal to the edge on an inclined substrate $R_{snM}$ can be computed based on the impact speed $V_0$ and the inclination of the substrate $\alpha$. Indeed, considering that the impact point is the focus of the ellipse,

$$R_{snM} = L + \mathrm{sign}(\alpha)\sqrt{L^2 - W^2} = L(1 + \sin\alpha) = \frac{W}{\cos\alpha}(1 + \sin\alpha), \tag{5.18}$$

taking $\beta = 1$ and using relations 5.13 and 5.17, we obtain

$$R_{snM} = R_0\, We^{1/4}\left(\frac{1 + \sin\alpha}{\sqrt{\cos\alpha}}\right) \tag{5.19}$$

which aligns well on the experimental data (Fig. 5.8a). This definition of the maximum extension normal to the edge is the one that will be used for the non-dimensional offset

$$\delta = \frac{d}{R_{snM}}.$$

To normalize $d$, $R_{snM}$ is preferable to $R_{stM}$. If both $R_{snM}$ and $R_{stM}$ correspond to $R_{sM}$ for $\alpha = 0°$, the normal value takes the angle sign into account.

The time at which the liquid reaches the edge can also be computed based on Eq. (5.9) in $\varrho|_d = d/R_{stM}$ which yields a second order equation

$$\left(\frac{1 + v_s}{t_{stM}}\right)^2 t_d^2 - 2\left(\frac{\varrho|_d v_s + 1}{t_{stM}}\right) t_d + \varrho|_d{}^2 = 0. \tag{5.20}$$

The solution of Eq. (5.20) aligns well on the experimental data computed using $dR_{sn}(t)/dt$ in Fig. 5.8b. Surprisingly, this time does not vary much with the inclination but is inversely proportional to the impact speed $V_0$.

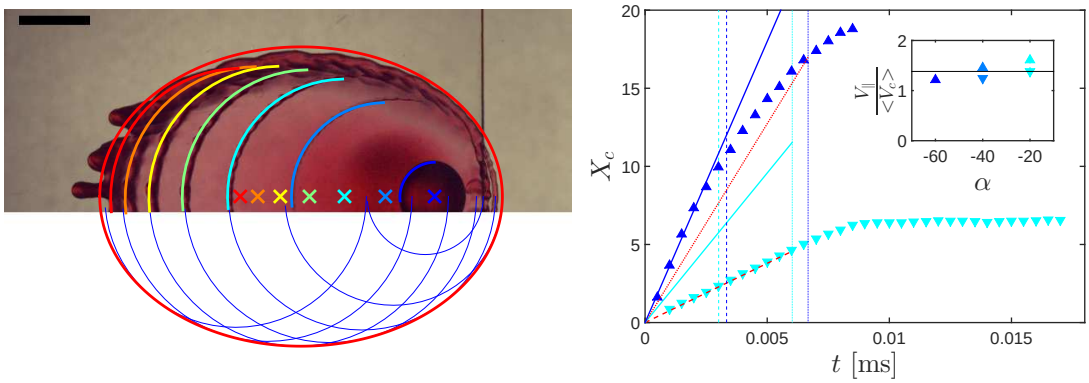


(a) (b)

Figure 5.6: (a) Top half: Time superposition of a drop impacting at $We = 520$ on a substrate inclined at $\alpha = $ -40°. The colored arc circles are fitted on the advancing fluid from its most left point to the maximum value parallel to the edge. The color-corresponding crosses are their center position. The scale bar is 5 mm and the times are t = 0 ms, 1.5 ms, 3 ms, 4.5 ms, 6 ms, 7.5 ms and 9 ms from impact. Bottom half: Equation (5.9) for t = 0 ms to t = 15 ms and a time interval of 0.8 ms. The red contour is Eq. (5.11). (b) Distance from the impact point of the circle centers $X_c$ fitted on the first half of the advancing liquid on the solid as illustrated in (a) (colored arc circles). (Cyan) $We = 520$ and $\alpha =$ -20° and (blue) $We = 2000$ and $\alpha =$ -40°. The solid lines represent $V_\parallel$, the vertical dashed lines correspond to $t_{stM}$ and the vertical solid ones to $2t_{stM}$ ($We = 520$ - cyan, $We =$ 2000 blue). The red lines show the speed average value between t = 0 ms and t = $2t_{stM}$ from $We = 520$ (dashed) and $We = 2000$ - (dotted). Inset: Ratio of $V_\parallel$ and the average speed of $X_c$ between t = 0 and t = $2t_{stM}$ as a function of $\alpha$ for $We = 520$ ($\nabla$ - full) and $We = 2000$ ($\triangle$ - empty). The solid line is the average value of the ratio across $\alpha$ and is equal to 1.38.

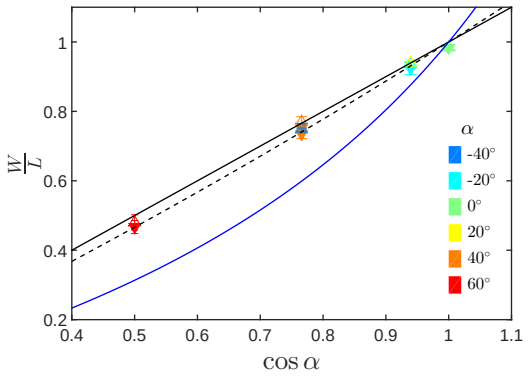


Figure 5.7: Aspect ratio $W/L$ of the envelope ellipse as a function of $\alpha$. Lines are Eqs. (5.17) for $\beta = 1.07$ (dashed), $\beta = 1.48$ (blue) and $\beta = 1$ [Eq. (5.17)] (solid). Weber numbers are $We = 520$ ($\nabla$ - full) and $We = 2000$ ($\triangle$ - empty).

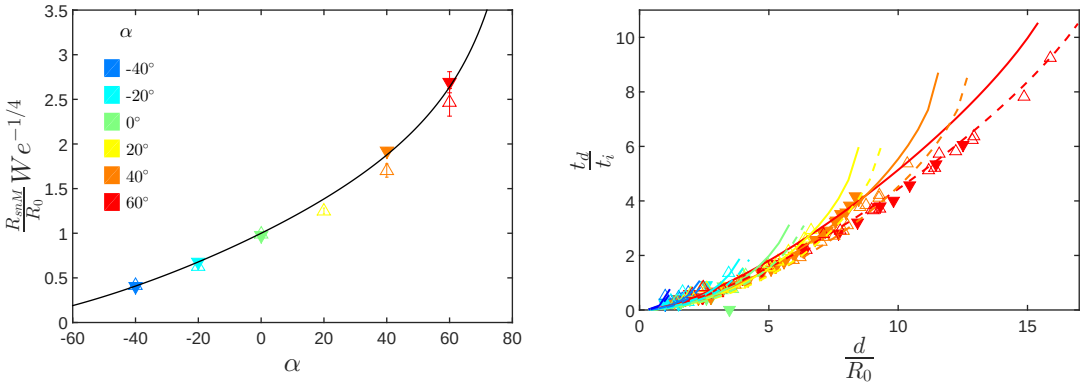


(a) (b)

Figure 5.8: (a) Maximum spreading distance of the liquid in the direction normal to the edge $R_{snM}$ as a function of the substrate inclination angle $\alpha$ (cf. color code in legend). Symbols correspond to $We = 520$ ($\triangledown$ - full) and $We = 2000$ ($\triangle$ - empty). Solid line is Eq. (5.19). (b) Time at which the spreading liquid reaches the edge $t_d$, normalized by the impact time $t_i$ as a function of $d/R_0$ for $We = 520$ ($\triangledown$ - full) and $We = 2000$ ($\triangle$ - empty) and $\alpha$ in color. Lines are solutions to Eq. (5.20) for $We = 520$ (dashed) and $We = 2000$ (solid) with $\alpha$ in color [cf. legend in (a)].

## 5.3 Expansion and retraction of the liquid sheet normal to the edge

### Horizontal substrate

As soon as it takes off from the edge, the liquid is not subjected anymore to the shear induced by the no-slip on solid. We describe the extension of the sheet normal to the edge $l_n(t)$ by defining a dimensionless time

$$\tau_n = \frac{t - t_d}{t_{nM} - t_d} \tag{5.21}$$

from fluid entry in the air $t - t_d$, divided by the time $t_{nM} - t_d$ of maximum extension in the air, normal to the edge. Similarly, the normal extension of the sheet is normalized by its maximal extension $l_{nM}$. With this normalization, all experimental data collapse onto a single curve

$$\frac{l_n}{l_{nM}} = \tau_n(2 - \tau_n), \tag{5.22}$$

as shown in Fig. 5.9a. The theoretical relations of these results were compared to previous theoretical work on centrosymmetric free sheet. Both the theoretical relations in Rozhkov *et al.* (2002) and Villermaux & Bossa (2011) for the expansion of axisymmetric liquid sheets, once rescaled, show relative good agreement with our experimental data during the expansion of the sheet, but not during its retraction. The experimental data are better captured by a simple harmonic oscillator in the form $l_n/l_{nM} = \sin(\pi\tau_n/2)$ as suggested by Biance *et al.* (2006) and Andrew *et al.* (2017) for bouncing droplets at lower Weber number. This solution to the harmonic oscillator is not very different from Eq. (5.22).

Interestingly, Eq. (5.22) suggests that the acceleration of the sheet normal to the edge is approximately constant during extension and retraction. The acceleration of the sheet in the air normal to the edge is obtained theoretically by differentiating Eq. (5.22) twice:

$$a_n = \frac{-2l_{nM}}{(t_{nM} - t_d)^2}. \tag{5.23}$$

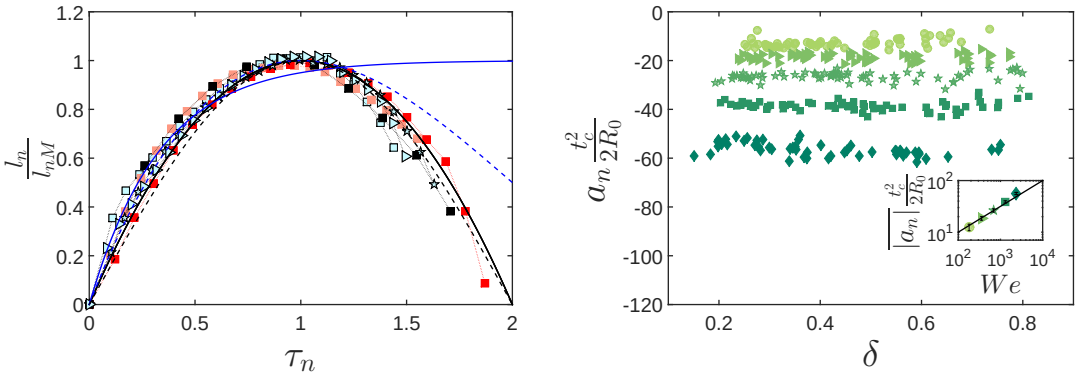


(a) (b)

Figure 5.9: (a) Normalized time evolution of the sheet extension normal to the edge $l_n(t)$ for the six examples of Figs. 4.3 and 4.4. The colours represent the different scenarios corresponding to these examples: I (black), II (reddish/grey) and III (blue/clear). The solid black line is Eq. (5.22). The blue lines correspond respectively to the theoretical results from Rozhkov *et al.* (2002) (solid), from Villermaux & Bossa (2011) (dashed) and the black dashed line to an harmonic oscillator suggested in Biance *et al.* (2006) and in Andrew *et al.* (2017). (b) Non-dimensional acceleration $a_n$ of the sheet normal to the edge as a function of offset $\delta$. Inset shows the absolute value of $a_n$, averaged over $\delta$, as a function of $We$ for $\alpha = 0°$. The solid line is Eq. (5.24).

Figure 5.9b shows that the experimental acceleration $a_n$, obtained by least-square fitting Eq. (5.22) for each impact, and scaled by $(2R_0)/t_c^2$, is independent of the offset $\delta$. Its average $\overline{a_n}$ over the full range of $\delta$ follows a fitted power law in $We^{0.6}$ very close to $\sqrt{We}$:

$$\overline{a_n}\frac{t_c^2}{2R_0} \simeq -\sqrt{We}, \tag{5.24}$$

in which case the best fitted coefficient is 1. This dependency suggests that $\overline{a_n}$ is close to $V_0/t_c$. Similarly, we can show that the speed at which the liquid takes off from the edge is

$$V_d = \frac{2l_{nM}}{t_{nM} - t_d}. \tag{5.25}$$

Experimental values are shown in Fig. 5.10 normalized by the impact speed $V_0$, which captures well the dependency in Weber number. We observe a sublinear increase in $V_d$ as $\delta$ decreases which appears to be well fitted by

$$\frac{V_d}{V_0} = 1.34\sqrt{1-\delta}. \tag{5.26}$$

Eqs. (5.23) and (5.25) then lead us to expressions for $l_{nM}$ and $t_{nM}$. The normal extension is expected to depend both on $We$ and on the history of the liquid on the surface prior to reaching the edge. To investigate this latter dependency, the maximum normal extension $l_{nM}$ is shown as a function of the dimensionless offset $\delta$ in Fig. 5.11a. A linear decrease of $l_{nM}$ with $\delta$ is observed, which is consistent with the expressions derived from $a_n$ and $V_d$ such that

$$\frac{l_{nM}}{R_0} = -\frac{1}{2R_0}\frac{V_d^2}{a_n} = 0.3(1-\delta)\sqrt{We} \tag{5.27}$$

$$\simeq 0.37\frac{V_0 t_c}{R_0}(1-\delta). \tag{5.28}$$

It appears from the experimental data in Fig. 5.11a that a dependence $(0.9 - \delta)$ in Eq. (5.27) might fit the data better. This would indicates that $l_{nM} = 0$ for $\delta = 0.9 < 1$.

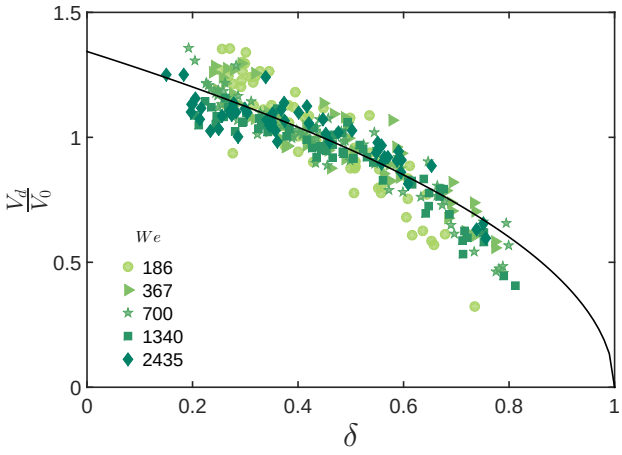


Figure 5.10: Normalized speed $V_d$ of the liquid when it takes-off from the edge, as a function of $\delta$ for $\alpha = 0°$, symbols correspond to different $We$ (cf. legend in inset). Solid line is Eq. (5.26).

This is counter-intuitive as it suggests that on the solid, away from the edge, the spreading is slightly larger (by 10%) despite surface shear. However, corrugations around the sheet form earlier when it is in the air than when the liquid is spreading on the solid. This could be due to a larger deceleration experienced by the sheet in the air than on the solid. Since our measurement of the sheet extension does not include such corrugations: $l_{nM} = 0$ for $\delta = 0.9$. Since these corrugations are here cropped by image processing, the corresponding $l_{nM} + d$ may be smaller than $R_{sM}$. We nonetheless chose to approximate the $l_{nM}$ dependency with the simplest expression so in $(1 - \delta)$.

The time $t_{nM} - t_d$ needed to reach maximum sheet extension is also deduced from Eqs. (5.23) and (5.25) and their expression from Eqs. (5.26) and (5.24). In dimensionless form:

$$\frac{t_{nM} - t_d}{t_c} = -\frac{V_d}{a_n t_c} = 0.55\sqrt{1-\delta}. \tag{5.29}$$

This result matches the experimental data well (Fig. 5.11b). In summary, the kinematics of the sheet extension normal to the edge as a function of $We$ and $\delta$ is well captured by the combination of Eqs. (5.22), (5.28) and (5.29).

### Inclining the substrate

We apply the same strategy of analysis for the sheet expansion on an inclined substrate. The first challenge in this endeavour is the detection of the sheet maximum extension $l_{nM}$ and of its time of occurrence $t_{nM}$. For positively inclined substrate (particularly 40° and 60°), an artificial jump in the automated measurement of $l_n(t)$ can occur as in Fig.5.12a. Such behaviour is caused by the stretched liquid sheet that experiences a strong tangential retraction and pinches all at once beyond a certain point, creating the jump in value (Fig. 5.12b). In some occurrences of scenario III, the part of the sheet that remains beyond the pinching point keeps advancing until it is fully destabilized. Our definition of the maximum expansion is therefore jeopardized. By analogy with the horizontal substrate, we make the hypothesis that the extension of the sheet still follows a parabolic motion in the inclined case, which we fitted to data for times before the tangential collapse. From these fits, values for $l_{nM}$ and $t_{nM}$ are derived, but they might correspond to virtual positions and times that are never really achieved by the sheet. For this reason, we focus instead on the acceleration of the liquid sheet in the direction normal to the edge $a_n$ which exists for all experiments. The acceleration appears independent on the offset $d$ at first order as shown in Fig. 5.13a, which is consistent with the results from

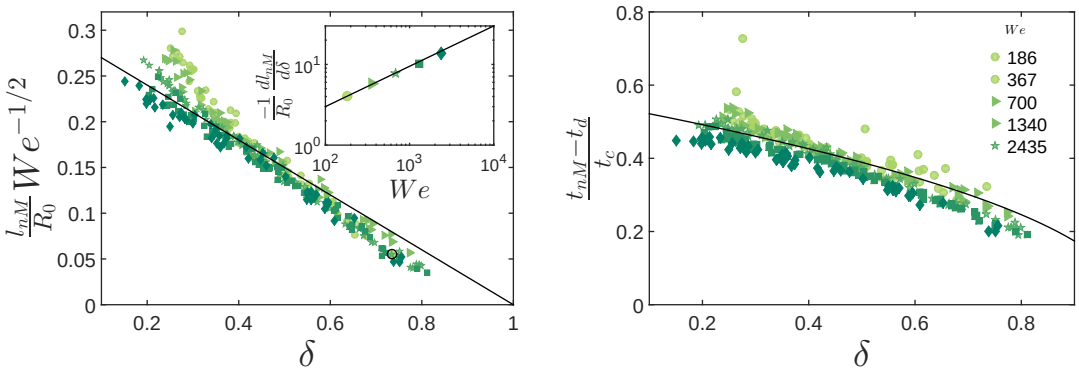


(a) (b)

Figure 5.11: (a) Maximum normal extension of the liquid sheet $l_{nM}$ normalized by $R_0 We^{1/2}$ as a function of $\delta$. The solid line shows Eq. (5.27), which is fitted on all the data points (with $d/R_0 > 1.3$). Symbols for different $We$ are 186 (◯), 367 (▷), 700 (☆), 1340 (□), 2435 (◇). $\alpha = 0°$. Inset: Slope of $l_{nM}/R_0$ vs. $\delta$, as a function of $We$. (b) Normalized time of maximum normal extension $(t_{nM} - t_d)/t_c$ as a function of the offset $\delta$. The solid line corresponds to Eq. (5.29). Symbols in $We$ (cf. legend in inset). $\alpha = 0°$.

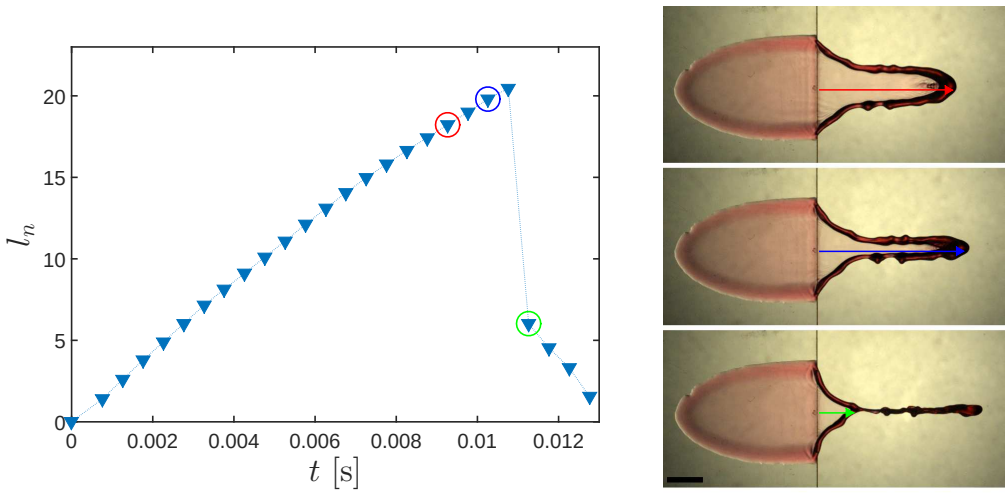


(a) (b)

Figure 5.12: (a) Time evolution of the maximum extension of the liquid sheet normal to the edge, $l_n(t)$ for $\alpha = 60°$ and $We = 520$ from t = $t_d$ to sheet collapse. (b) Snapshots of the example in (a) with $l_n(t)$ highlighted and taken, from top to bottom, at times t = 9 ms (red), 10 ms (blue) and 11 ms (green). Scale bar is 5 mm.

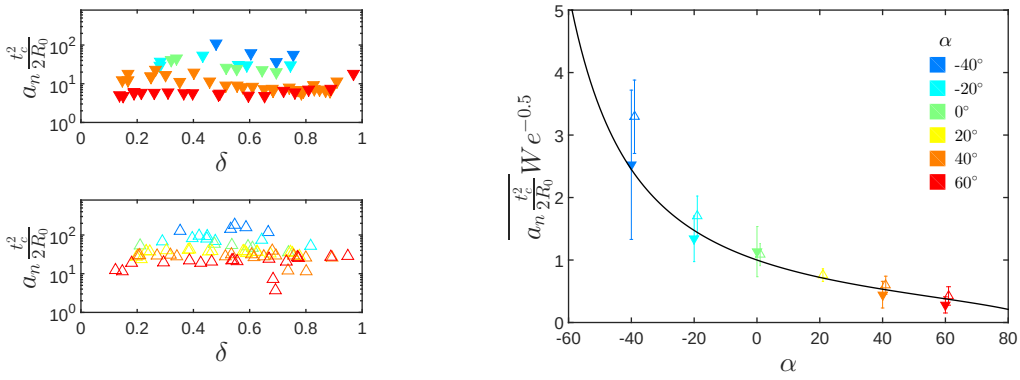


(a) (b)

Figure 5.13: (a) Normalized $a_n$ as a function of $\delta$ for $We = 520$ (top - $\triangledown$ - full) and $We = 2000$ (bottom - $\triangle$ - empty) for $\alpha \in$ [-40° 60°] (color cf. (b)). (b) Averaged $a_n t_c^2/(2R_0)$ over $\delta$ as a function of $\alpha$, normalized by $We^{0.5}$ for $We = 520$ ($\triangledown$ - full) and $We = 2000$ ($\triangle$ - empty). The solid line is Eq. (5.30). The error bar is the standard deviation.

the horizontal case.

The average over all offsets $\overline{a_n}$ shows a decrease in $We$ similar the one for the horizontal substrate (Fig. 5.13b) but also a decrease as $\alpha$ increased. This latter appears to be at first order well captured by the dependency in $(1+\sin\alpha)/\sqrt{\cos\alpha}$ given by $R_{snM}$ [Eq. (5.19)].

In first approximation, we have

$$\frac{\overline{a_n}}{2R_0}\frac{t_c^2}{2R_0} = -\sqrt{We}\frac{\sqrt{\cos\alpha}}{(1+\sin\alpha)}. \tag{5.30}$$

An additional dependency due to the contribution of $V_\parallel$ is not to be excluded but considering the limited number of datapoints in -20° and -40°, we left this to future work.

Since $a_n$ is a constant across offset at first order, the parabolic fit of $l_n(t)$ is recomputed with an imposed acceleration $\overline{a_n}$ per $We$ and $\alpha$ obtained from the experimental data. The speed $V_d$ of the liquid when it takes-off from the edge can also be deduced from the parabolic fit of $l_n(t)$. Considering how the independence of $a_n$ in $d$ is conserved from the horizontal substrate to the inclined one, we may assume from Eq. (5.26) that the dependency of $V_d$ will take the shape in square root of 1-$\delta$. Equation

$$\frac{V_d}{V_0} \simeq 1.28\sqrt{1-\delta} \tag{5.31}$$

describes well the experimental data (Fig. 5.14) with 1.28 being the best fitting coefficient. We notice however that $V_d$ slightly increases with $\alpha$. The value of the best fitting coefficient of Eq. (5.31) is shown per $\alpha$ in inset of Fig. 5.14. This dependency may arise from the first order approximation of the acceleration which does not entirely capture the variations in $\alpha$. Another explanation for this dependency may come form noting that, in the horizontal case, the time of maximum extension $t_{nM} - t_d$ also displayed a weak dependency in $We$ which could in this case be a dependency in $We_\perp$ or $We_\parallel$, explaining the ordering in $\alpha$. No straightforward dependency was however found and we left this to future work.

Finally, as a final verification of the previous assumptions, we plotted the time evolution of $l_n$ normalized by its maximum value as a function of its normalized time for five $\alpha$ in Fig. 5.15a. The normal sheet expansion follows well a parabolic motion and it is the retraction behaviour that is affected by the inclination of the substrate. The virtual maximum extension $l_{nM}$ follows well linear law in $\delta$ deduced from Eqs. (5.30) and (5.31),

$$\frac{l_{nM}}{R_0} = 0.3(1-\delta)\sqrt{We}\left(\frac{1+\sin\alpha}{\sqrt{\cos\alpha}}\right) \tag{5.32}$$

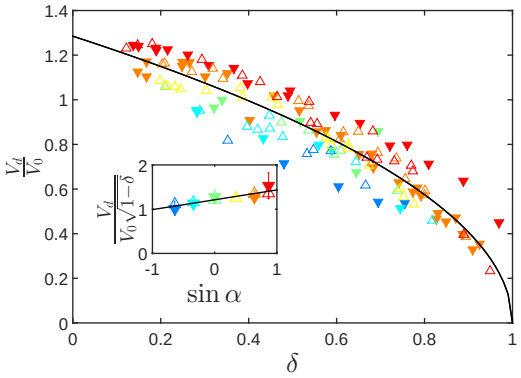


Figure 5.14: Normalized speed $V_d$ of the liquid when it takes-off from the edge as a function of $\delta$ for $We = 520$ ($\triangledown$ - full) and $We = 2000$ ($\triangle$ - empty) and $\alpha \in$ [-40° (dark blue) 60° (red)]. Solid line is Eq. (5.31). Inset: Best fit coefficient per $\alpha$ and $We$ of Eq. (5.31). Solid line is $0.22 \sin\alpha + 1.2$.

where the dependency in $\alpha$ is captured by the dependency of $R_{snM}$ in $\alpha$ (Inset of Fig. 5.15b). Datapoints for the highest $\alpha$ and lowest $We$ present a deviation from Eq. (5.32) which could be due to an increased stretch due to gravity or to the speed along the substrate plane $V_\parallel$, either resulting in an accumulation of the fluid in the tip, shifting the results even more. Experimental values of the rim thickness $\overline{b}$, averaged over $\delta$, indeed show an increase of the thickness with the inclination of the substrate $\alpha$ but also, and more pronounced, with a decrease in $We$ (Fig. 5.16).

Similarly, the dependency of the time of maximum extension, $t_{nM} - t_d$ is

$$\frac{t_{nM} - t_d}{t_c} = \frac{3}{2\sqrt{6}}\sqrt{1-\delta}\left(\frac{1+\sin\alpha}{\sqrt{\cos\alpha}}\right), \tag{5.33}$$

which fits well the experimental data of Fig. 5.17 again with the exception of the high $\alpha$ for the lowest Weber.

### Comparison to the radial extension in axisymmetric impact configurations

The impact near a horizontal edge involves spreading on solid followed by expansion of the liquid sheet in the air. This configuration is an intermediate between two axisymmetric configurations already investigated: an impact on infinite solid (Laan *et al.*, 2014) and a centred impact on a circular target of comparable size to the drop (Rozhkov *et al.*, 2002) (Fig. 5.18a - top). In order to compare the maximum distance reached by the liquid in these three configurations, we performed additional experiments of impacts on a pole. The pole radius $d$ corresponds to the distance the liquid travels on solid before taking off, so it is equivalent to the offset $d$ defined for the impact near an edge. We considered two ratios of pole to drop size, $d/R_0 \in \{1.5, 2.4\}$ and three Weber numbers $We \in \{370, 700, 1340\}$. The substrate material and the impacting drop (size, composition) are the same as for the edge configuration. Fig. 5.18b compares prior models of sheet extension: (i) the maximum spreading radius on a horizontal substrate $R_{sM}$ from Laan *et al.* (2014) [Eq. (5.2)], (ii) the maximum radial extension of the liquid sheet (from impact point) from Rozhkov *et al.* (2002), and Vernay *et al.* (2015):

$$\frac{l_{nM} + d}{R_0} \simeq 0.227\sqrt{We}, \tag{5.34}$$

with a prefactor corresponding to the rounded average between the prefactor 0.224 for $d/R_0 \in \{1, 1.4\}$ by Rozhkov *et al.* (2002) and the prefactor 0.229 for $d/R_0 = 1.67$ in Vernay

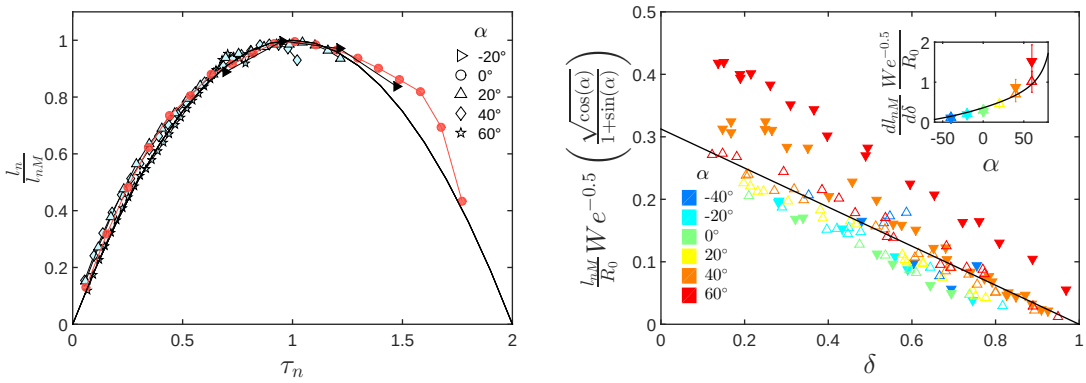


Figure 5.15: (a) $l_n(t)$ normalized by its maximum extension obtained from the fit of a parabola with constrained acceleration $a_n$ for the five examples illustrated in Fig. 4.7. The time is normalized by its maximum value obtained in the same way as the maximum extension. Solid line is Eq. (5.22). (b) Normalized maximum sheet extension $l_{nM}$ as a function of $\delta$ for $We = 520$ ($\triangledown$ - full) and $We = 2000$ ($\triangle$ - empty) and angles from -40° (dark blue) to 60° (red). Solid line is Eq. (5.32). Inset: Normalized slope of $l_{nM}$ vs $\delta$ as a function of $\alpha$. Solid line is Eq. (5.32).

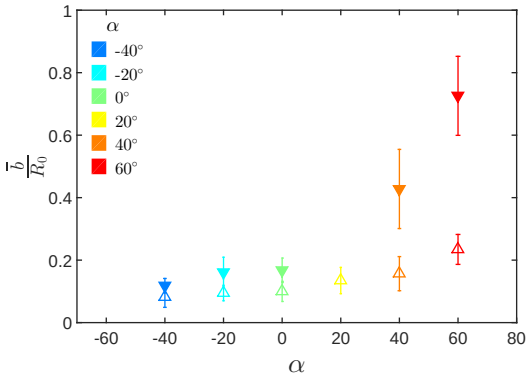


Figure 5.16: Estimation of the rim thickness $b$ of the sheet average over $\delta$ and normalized by $R_0$. The thickness is measured by image processing at 1 ms before the sheet maximum extension on the symmetry axis normal to the edge. Symbols correspond to $We$ (520 $\triangledown$, 2000 $\triangle$). All offsets are pooled together.

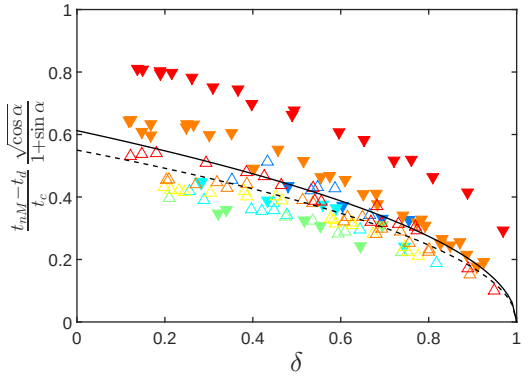


Figure 5.17: Normalized time of the maximum normal extension $(t_{nM}-t_d)/t_c$ as a function of the offset $\delta$. The solid line corresponds to Eq. (5.33) and the dasehd line to Eq. (5.29). Symbols in $We$: 520 ($\triangledown$) and 2000 ($\triangle$). Colour in $\alpha$ from -40° (dark blue) to 60° (red).

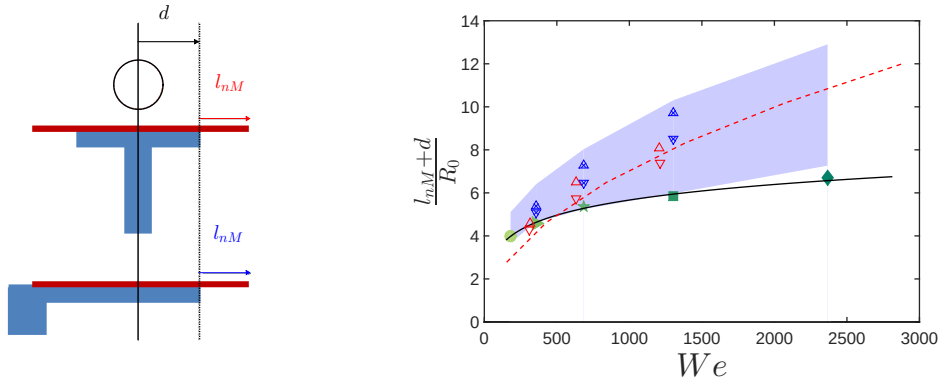


(a) (b)

Figure 5.18: (a) Schematics of the geometrical similarity between the sheet extension for the edge and pole configurations. (b) Comparison of the maximum radial distance from the impact point reached by the liquid for three configurations: full spreading on a solid (filled green symbols, $R_{sM}/R_0$), liquid sheet from a horizontal flat edge [shaded area, $(l_{nM}+d)/R_0$], and liquid sheet from a pole [empty triangles, $(l_{nM}+d)/R_0$]. Two ratios of pole to drop radius were considered: $d/R_0 = 1.5$ ($\triangle$) and $d/R_0 = 2.4$ ($\triangledown$). The crossed $\triangledown$ and $\triangle$ represent the maximal distance reached in edge experiments with the same offsets $d/R_0$. The solid and dashed lines correspond to Eqs. (5.2) and (5.34), respectively.

*et al.* (2015). Equation (5.34) is in good agreement with our experimental data on pole. The power-law $l_{nM} \sim \sqrt{We}$ [Eq. (5.27)] for the edge is similar to the dependence in $\sqrt{We}$ of Eq. (5.34) obtained for the pole (Rozhkov *et al.*, 2002; Villermaux & Bossa, 2011; Vernay *et al.*, 2015; Wang & Bourouiba, 2017).

Fig. 5.18b shows that for large $We$ and small offsets, the liquid sheet goes further than the liquid only spreading on the solid. Indeed, spreading on solid dissipates energy through viscous friction well captured by a Blasius-type boundary layer (Rozhkov *et al.*, 2002; Eggers *et al.*, 2010; Wang & Bourouiba, 2017), that reduces liquid spreading. The experimental values of $R_{sM}$ are in good agreement with Eq. (5.2). More surprisingly, the maximal distance reached by the liquid sheet is always higher with a straight edge than with a circular edge at the same distance $d/R_0$ from impact point. This is counter-intuitive since in all directions not normal to the straight edge, the liquid spreads more than $d$ on the solid prior to taking-off from the edge. By contrast, in the pole configuration, the liquid sheet forms at the same time after the same spreading distance $d$ in every direction. A possible explanation for this larger distance reached by the sheet from a straight edge is that the rupture of symmetry enables retraction from the back of the sheet leading to further extension normal to the edge.

## 5.4 Expansion and retraction of the liquid sheet along the edge

We proceed by rationalizing the time evolution of the liquid sheet in the vicinity of the edge. As seen in Figs. 4.2 and 4.6, the extension of the sheet along the edge initially closely follows the spreading on solid during the expansion phase. By contrast, dewetting on solid is much slower than the retraction of the sheet along the edge. The tangential extension should therefore be geometrically related to the spreading law $R_s(t)$ through $l_t(t) = \sqrt{R_s(t)^2 - d^2}$ in the direction tangential to the edge.

For the horizontal case, combining this equation with Eqs. (5.1) and (5.6) yields

$$l_t(t) = R_{sM}\sqrt{1-\delta^2}\sqrt{\tau_s(2-\tau_s)}, \text{ with } \tau_s = \frac{t-t_d}{t_{sM}-t_d}. \tag{5.35}$$

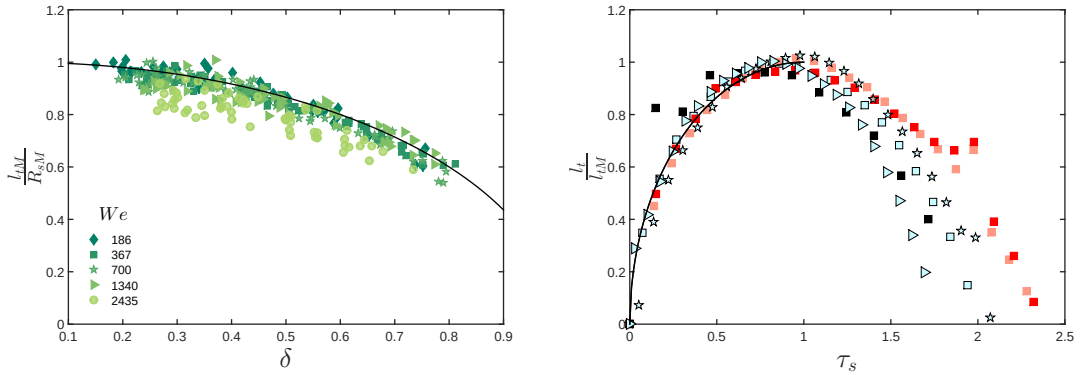


(a) (b)

Figure 5.19: (a) Maximum tangential extension $l_{tM}$ of the liquid sheet along the edge normalized by the maximum spreading on solid $R_{sM}$, as a function of offset $\delta$ for $\alpha = 0°$. The solid line is $\sqrt{1-\delta^2}$, in agreement with Eq. (5.36). (b) Time evolution of the sheet extension along the edge $l_t(t)$, normalized by its maximum value $l_{tM}$ for the six examples of Figs. 4.3 and 4.4. Colours correspond to scenarios: I (black), II (reddish/grey) and III (blue/clear). The solid line for $\tau_s < 1$ represents Eq. (5.35). Symbols are *We*: 186 (◯), 367 (▷), 700 (☆), 1340 (□), 2435 (◇) and $\alpha = 0°$.

This square root of time can be interpreted as a kinematic signature of an expanding circle (the sheet) intercepting a straight line (the edge). By identification of Eqs. (5.1) and (5.35), we would infer that

$$l_{tM} = R_{sM}\sqrt{1-\delta^2}. \tag{5.36}$$

This prediction is fairly well verified by the experimental measurements of the maximum tangential extension in Fig. 5.19a.

In Fig. 5.19b, the extension $l_t(t)$ tangent to the edge is represented for the 6 examples of Figs. 4.3 and 4.4, normalized by its maximum value $l_{tM}$ and plotted as a function of $\tau_s$. Thanks to this normalization, data from these different experiments collapse well onto the curve of Eq. (5.35) during the expansion phase ($\tau_s < 1$). However, data from different offsets $\delta$ diverge from each other during the retraction phase ($\tau_s > 1$). This scattering of the retraction kinematics along the edge may be linked to the uncontrolled dewetting on this flat vertical edge.

A similar process is applied to the expansion along the edge on an inclined substrate. The dependency in $\alpha$ of the maximum extension tangential to the edge is deduced from the one on the solid [Eq. (5.12)], using geometrical relations solely, and takes the form

$$l_{tM} = R_{stM}\sqrt{1-[\sin\alpha-(1+\sin\alpha)\frac{d}{R_{stM}}]^2}. \tag{5.37}$$

This equation describes well the experimental data (Fig.5.20a). The temporal evolution takes the shape

$$\frac{l_t}{l_{tM}} = \sqrt{\frac{t-t_d}{t_{tM}-t_d}\left(2-\frac{t-t_d}{t_{tM}-t_d}\right)} \tag{5.38}$$

where $t_{tM}$ is the time at which the sheet reaches its maximum extension along the edge, which differs from $t_{sM}$ on inclined substrates. Equation 5.38 is still directly deduced from the shape for the horizontal case (5.35) and it similarly, follows well the extension represented in Fig. 5.20b for the five examples of Fig. 4.7. The retraction phase, however presents again an important scatter.

From our data, no clear ordering in offset appears (Fig 5.21a) although a tendency to have a later collapse time for larger $\alpha$ (Fig. 5.21b) seems to arise.

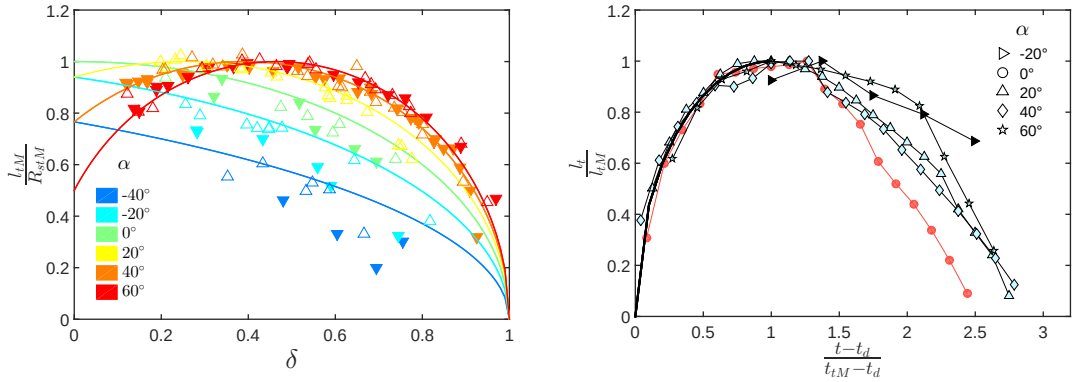


(a) (b)

Figure 5.20: (a) Maximum tangential extension $l_{tM}$ of the liquid sheet along the edge normalized by the maximum spreading on solid $R_{stM}$, as a function of offset $\delta$, for $\alpha \in$ [-40° - 60°] (cf. legend in inset). The solid line is Eq. (5.37). (b) Time evolution of the sheet extension along the edge $l_t(t)$, normalized by its maximum value $l_{tnM}$ for the five examples of Fig. 4.7. Colours correspond to scenarios: I (black), II (reddish/grey) and III (blue/clear). The solid line for $\tau_s < 1$ represents Eq. (5.38). Symbols are $\alpha$ (cf. legend in inset) and $We = 2000$.

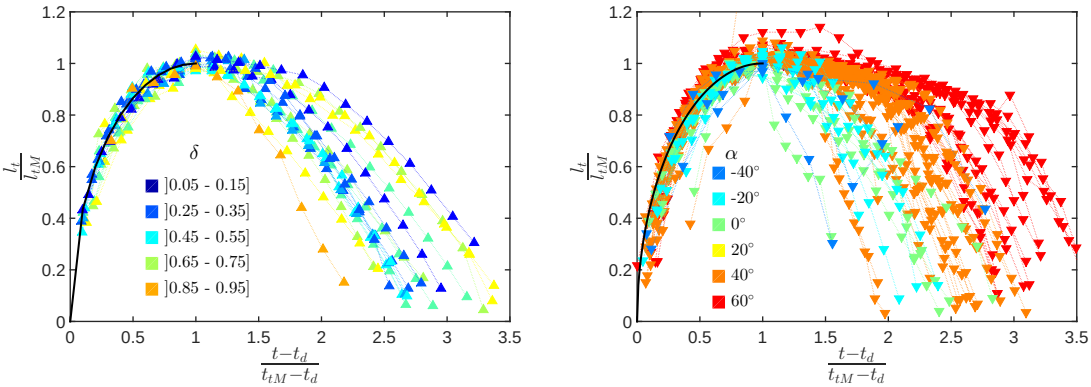


(a) (b)

Figure 5.21: Time evolution of the sheet extension $l_t(t)$, along the edge, normalized by its maximum value $l_{tM}$ (a) for $We = 520$ ($\triangledown$), $\alpha = 40°$ and offset $\delta$ in color. (b) for all offsets $\delta$, $We = 520$ ($\triangledown$) and $\alpha$ in color. The solid line for $\tau_s < 1$ represents Eq. (5.38)

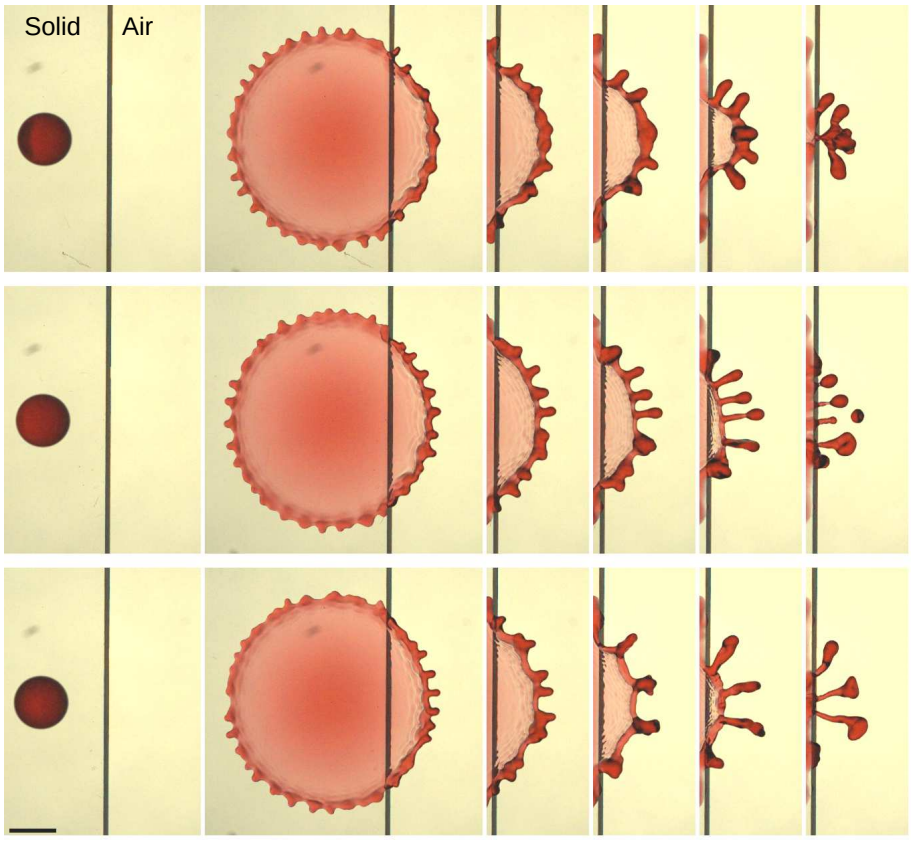


Figure 5.22: Stochastic variations of the retraction behaviour for three impacts at $\alpha = 0°$, $We = 184$ and $\delta = 0.5$. Times are, from left to right: 0, 6, 8.5, 10.5, 12.5 and 15.4 ms after impact. Scale bar is 4 mm.

For both horizontal and inclined substrates, the retraction behaviour along the edge indeed proved strongly affected by the local state of the edge, which could induce momentary pinning of the liquid sheet. The horizontal dispersion of the impact point around the vertical axis of the release position increases with the release height of the drop. In our data collection process, this natural variation of the impact point was used to randomly vary the offset for high release height. This however also meant that the drop did not always impact at the exact same location along the edge. In consequence, the portion of the edge covered by the liquid varied. This can influence the motion of the contact line along the edge and cause some local pinning on the unavoidable edge roughness. This is a possible origin for the observed scatter in the retraction dynamics of the liquid sheet along the edge. Another source of scatter is the presence of local ligaments or corrugations close to the edge. By adding localized mass as well as through their motion, these appeared to also affect the retraction behaviour. Such a stochastic difference for three impacts with identical impact parameters is visible in Fig. 5.22.

From Figs. 5.21 and 5.22, we observe the important noise in these data which rendered the rationalization of the retraction behaviour challenging and requires more accurate and specific measurements. We left it to future work.

Finally, the time at which the sheet collapses along the edge is defined as $t_r - t_d$. This time is different from the full collapse of the liquid sheet only for the experiments of scenario III. This collapse time normalized by the time of maximum normal extension is defined as

$$\tau_r = \frac{t_r - t_d}{t_{nM} - t_d}$$

and is illustrated in Fig. 5.23a for the horizontal substrates and in Fig. 5.23b for the inclined ones. These data present an important noise coming from the sensitivity of $l_t(t)$

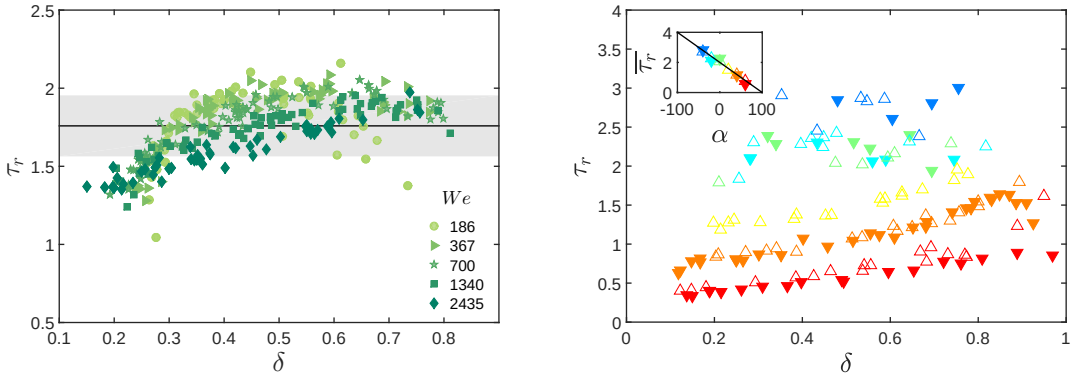


(a) (b)

Figure 5.23: Normalized time of collapse $\tau_r = (t_r - t_d)/(t_{nM} - t_d)$ of the liquid sheet along the edge as a function of the offset $\delta$ (a) for $\alpha = 0°$ with symbols corresponding to $We$ (cf. legend in inset). The solid line is the average across $We$ and $\delta$ and the grey area corresponds to one standard deviation. (b) for $\alpha$ from -40° (dark blue) to 60° (red) and symbols corresponding to $We$ (520 - $\triangledown$ -full, 2000 - $\triangle$ - empty). Inset: Average value of $\tau_r$ over $\delta$ as a function of $\alpha$ for $We$ 520 ($\triangledown$ - full) and $We = 2000$ ($\triangle$ - empty).

to local disturbances mentioned above. This retraction time however plays an important role in the process of droplet creation as it marks the moment of the filament breakup in scenarios II and III, hence a brief description of its behaviour here. For the horizontal substrate, it increases from $\tau_r \simeq 1.3$ at low $\delta$, then saturates at $\tau_r \simeq 2$ at large $\delta$. It is only slightly dependent to $We$ for intermediate $\delta$. Its average value is $\tau_r = 1.76$, with a standard deviation of 0.2 (Fig. 5.23a).

On the inclined case, we see an important effect of the inclination $\alpha$ where large values of inclination reduce the time of collapse (Fig. 5.23b). This tendency is confirmed by taking the average value of $\tau_r$ over all $\delta$ plotted as a function of $\alpha$. A clear decrease of $\overline{\tau_r}$ with $\alpha$ is visible in inset of Fig. 5.23b. A small effect of the offset appears for large values of $\alpha$ where the time appears reduced for small $\delta$. A possible explanation can be that the retraction speed along the edge depends on the local thickness of the sheet which would be more stretched for small $\delta$, reducing the time $\tau_r$. As we could not measure the film thickness here, this rationalization is left to future work. Finally, we observe that some of these ratio values are below 1 when normalized by $t_{nM} - t_d$, meaning that the time of collapse along the edge occurs before the time of maximum extension. This fits with our observations on the normal extension of the liquid sheet for large $\alpha$ where occurrences of the maximum spreading could not be directly seen and measured due to the tangential collapse occurring before reaching a maximum value, notably in scenario III.

## 5.5 Asymmetry and sheet envelope

### Asymmetry

In chapter 4, we have observed three qualitatively different scenarios of sheet expansion and retraction. For the horizontal substrate, each scenario is observed in a given region of the diagram ($We$, $d/R_0$) in Fig. 5.1a. Boundaries between these regions are non-trivial in this diagram. The preceding investigation of the sheet kinematics highlighted the importance of the dimensionless offset $\delta = d/R_{snM}$ which is equal to $d/R_{sM}$ for $\alpha = 0°$. Moreover, a key difference between the scenarios is the relative asymmetry of the sheet, which could be represented by the ratio $l_{nM}/l_{tM}$. The separation of scenarios appears more clearly in the diagram ($\delta$, $l_{nM}/l_{tM}$) of Fig. 5.24a. With this representation, the transition from

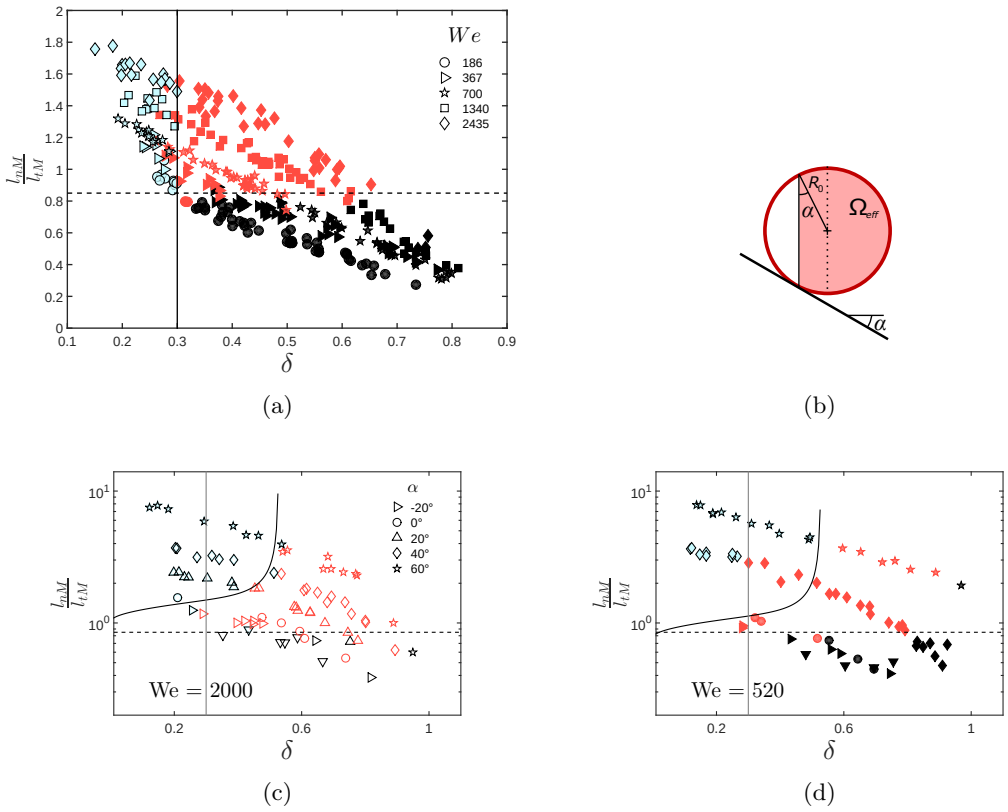


Figure 5.24: Scenarios of liquid sheet expansion/retraction with the colours showing different scenarios: I (black), II (reddish/grey) and III (blue/clear) (a) in a $(l_{nM}/l_{tM}, \delta)$ diagram. The symbols correspond to different $We$ (cf. legend in inset). The solid and dashed lines correspond to Eqs. (5.39) and (5.40) respectively. (b) Schematic defining the variables for the calculation of the effective volume $\Omega_{eff}$ using $\alpha$ and $R_0$ in Eq. (5.42). (c - d) Scenarios in a $(l_{nM}/l_{tM}, \delta)$ diagram for $We = 2000$ (c) and $We = 520$ (d). The symbols correspond to different $\alpha$ [cf. legend in (c)]. The solid and dashed straight lines correspond to Eqs. (5.39) and (5.40) respectively. The curved solid lines to Eq.(5.42).

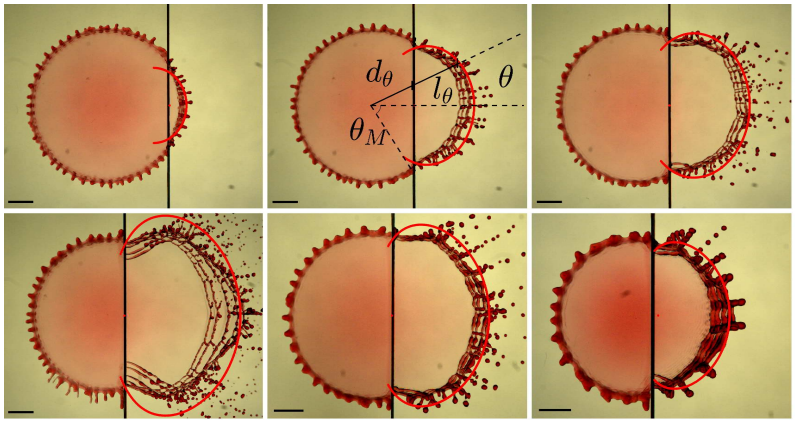


Figure 5.25: Time superposition of snapshots from a given experiment, with $t \in [t_{sM}, t_{nM}]$. The red curved solid lines represent the reconstructed envelope region accessible to the sheet, predicted by Eq. (5.43). (Top line) From left to right, $We$ = 1300 and $\delta$ = 0.79, 0.54, 0.34. (Bottom line) From left to right, $We$ = 1340, 700, 367 and $d/R_0$ = 1.3, with $\delta$ = 0.22, 0.24, 0.28. Scale bars are 4 mm.

scenario II to III occurs approximately at

$$\delta = 0.3, \tag{5.39}$$

and the transition from scenario I to II at

$$\frac{l_{nM}}{l_{tM}} = 0.85. \tag{5.40}$$

Inclining the substrate shifts the transition regions of the scenarios. Diagrams in Figs. 5.24c and 5.24d show that the asymmetry ratio of $l_{nM}/l_{tM} = 0.85$ remains valid to differentiate scenario I from the others. The transition from scenario II to III however was not captured by the ratio $\delta = 0.3$. An increased inclination indeed shifts the transition region towards larger values of $\delta$. One possible explanation to this phenomenon could be that in tilting the substrate, the fluid repartition is not uniform anymore on the substrate as more will tend to accumulate in the downwards direction as illustrated in Fig. 5.24b. A first model approximation of this effect can be deduced from assuming that a greater fraction than half the liquid from the impacting drop will move downwards for positively inclined substrates. The volume of effective liquid moving downwards $\Omega_{eff}$ (Fig. 5.24b) being approximated by taking the spherical cap delimited by the impact point and situated towards the edge of the substrate. Such approximation yields

$$\Omega_{eff} = \frac{\pi R_0^3}{3}(2 + 3\sin\alpha - \sin\alpha^3) \tag{5.41}$$

and the transition from scenario II to III can thus be approximated by

$$\delta = 0.3\frac{\Omega_{eff}}{4/3\pi R_0^3}, \tag{5.42}$$

as illustrated in Figs. 5.24c and 5.24d.

### Sheet envelope

The distance travelled by the liquid spreading on the solid strongly influences the subsequent shape of the liquid sheet in the air. Based on this observation, we propose a first-order model to reconstruct the maximal region accessible to the expanding sheet for the horizontal case. On the solid, the liquid spreads radially from the impact point and reaches the edge after a distance $d_\theta = d/\cos\theta$, where $\theta$ is the angular position from the impact point, measured from the symmetry axis (Fig. 5.25). Since $d_\theta$ is bounded by $R_{sM}$, $\theta$ must be smaller than $\theta_M = \cos^{-1}\delta$. By replacing $d$ by $d_\theta$ (or equivalently $\delta$ by $\delta/\cos\theta$) in Eq. (5.27), we obtain a prediction of the maximum extension $l_\theta$ reached by the sheet in direction $\theta$ from the normal to the edge:

$$\frac{l_\theta}{R_0} = 0.3\sqrt{We}\left(1 - \frac{\delta}{\cos\theta}\right). \tag{5.43}$$

Since the time of maximum extension varies with the direction considered (i.e., $t_{nM} \neq t_{sM}$), Eq. (5.43) does not predict the shape of the sheet at a given instant. It rather gives the envelope accessible to the sheet during its expansion, as shown in Fig. 5.25, for various $We$ and $\delta$. Eq. (5.43) captures well the sheet outer envelope and only overestimates that envelope for the largest $We$ and smallest $d$ (bottom left picture in Fig. 5.25) that corresponds to scenario III. In that particular case, the time of the maximum normal distance to the edge occurs much later than the tangential one which depends on the details of pinning and contact line not captured by Eq. (5.43).

The sheet reconstruction is not possible for the inclined substrate following this method. For the above developed equations for $l_{nM}$ on inclined substrate [Eq. (5.32)], the maximum extension $l_\theta$ reached by the sheet in direction $\theta$ from the normal to the edge is

$$\frac{l_\theta}{R_0} = 0.3\sqrt{We}\left(1 - \frac{d_\theta}{\cos\theta R_{snM}}\right)\left(\frac{1+\sin\alpha}{\sqrt{\cos\alpha}}\right). \tag{5.44}$$

The liquid on the solid does not spread radially anymore and it reaches the edge after a distance $d_\theta = d/\cos\theta$ where $d_\theta$ is bounded by $R_{stM} = R_{sM}|_{\alpha=0°}$. It is however normalized by $R_{snM}$ so in this situation, $\delta$ does not tend towards 1 when $\theta$ reaches $\theta_M$ for $\alpha \neq 0°$ and the envelope is not closed along the edge.

In this chapter, we have rationalized the sheet asymmetry behaviours by proposing three categories of scenario based on the retraction kinematics of the liquid sheet. By analysing first the evolution of the liquid on the solid, we were able to derive key components such as the time at which the liquid reached the edge of the substrate as well the maximum distance the liquid can spread on the solid as a function of the impact speed and the inclination of the substrate. This last parameter is a key information for the rationalization of the liquid sheet asymmetry whose maximum extension values in the direction normal and tangential to the edge govern the transitions from one scenario to the next. An increase in impact speed and in inclination increases the asymmetry of the liquid sheet as well as a decrease of the offset, $d$. These findings will now be used to rationalize the droplet shedding behaviours and relate them to the impact parameters.

# Chapter 6

# Droplet ejection

In this section, we characterize the ejected droplets from a statistical point of view, and we relate their properties to the asymmetric kinematics of the sheet. We first present the detection methods. We then discuss the mechanisms and direction of ejection and the initial speed and mass to rationalize the travelled distance of ejected droplets. Finally, we take a look at the number of ejected droplets and we summarize the effect of sheet asymmetry on droplet distributions.

## 6.1 Droplet detection

On each frame, all the objects detached from the main body of the sheet were considered as ejected droplets (Fig. 6.1a). Their area, perimeter and position with respect to the impact point was recorded. Their trajectory was then reconstructed starting from the last frame and going backward. During this process, only objects that could be consistently tracked over at least five frames were considered. This condition removed fluid particles that either quickly merged with others, or that quickly fragmented (Fig. 6.1b - green and yellow crossed detections). The ejection time of the droplets is defined as the time at which they were first detected. The ejection velocity $\mathbf{v}$ (norm $v$) is calculated from the first frames after ejection. In both cases, these values are computed based on the trajectory (circles in Fig. 6.1b). Merging and break-up of droplets are common, especially during sheet retraction in the most asymmetrical scenarios (II - III). We chose to only consider as droplets the objects that either left the field of view before the end of the recording (green and blue detections of Fig. 6.1b), or that were still present in its last frame (yellow detections in Fig. 6.1b). By doing so, we reduced the likelihood of counting multiple times the same fluid particle since the tracking is performed backward. As illustrated in Fig. 6.1b, detected droplets marked with a cross have not been considered and, as an example, the green trajectory is detected as a single droplet instead of four different objects. Another option considered was to keep solely droplets that we could trace back to the liquid sheet. However choosing to keep droplets leaving the field of view before the end of the recording or the ones still present in its last frame has the advantage to also remove highly deformed droplets that are usually short lived and to exclude huge ligaments left by the destabilizing sheet. However, we also arbitrarily selected large merged droplets instead of keeping the smaller droplets that were initially ejected. Furthermore, sometimes the residues of the collapsed sheet did not fully fragment by the time they left the field of view and many of them are tracked before they can fully relax to a spherical shape. Some keep oscillating such as the blue marked droplet in Fig. 6.1b or are still quite deformed.

Estimating the mass $m$ of a droplet is challenging. We estimated the droplet volume $\Omega = m/\rho$ based on a combination of the perimeter $P$ and the area $A$ measured on each image. A droplet pinching off from a fluid ligament is initially elongated, so at first order, it can be approximated by a pill shape, i.e., a cylinder of length $L$ and radius $R$ surrounded by two spherical caps of radius $R$ as in Fig. 6.2. Note that this approximation

only works when the droplet is a pill or a sphere but it does not work when the droplet is a pancake. Every droplet oscillates between prolate (pill) and oblate (pancake) shapes as far as only the first mode of oscillation is considered. So both the pill and the pancake should occur equally often. What is seen then depends on the alignment of the observation axis and the oscillation axis (i.e., the axis of rotational symmetry of both shapes). If both axes are aligned, both the pill and the pancake appear as disks. If they are misaligned, both the pill and the pancake appear as elongated disks (i.e., a rectangle with two half disks, see Fig. 6.2). However, since the pancake extends in 2D while the pill extends in 1D, a given droplet will show a small value of L at maximum extension in the pancake state, and a larger value of L at maximum extension in the pill state so the pill shape should dominate over the pancake one. Moreover, the volume is computed with a time average over the trajectory which should reduce errors arising from these shape oscillations. Nevertheless, it is still worth taking the observed droplet elongation in consideration. For large deformations, $L \gg R$, variables $\Omega$, $A$ and $P$ are proportional to $R^2L$, $RL$ and $L$, respectively, so the ratio $\Omega P/A^2$ should be constant. In general (for any $L$ and $R$),

$$\frac{\Omega P}{A^2} = \frac{2\pi x^2 + \left(2\pi^2 + \frac{8\pi}{3}\right)x + \frac{8\pi^2}{3}}{4x^2 + 4\pi x + \pi^2} \tag{6.1}$$

where $x = L/R$. The ratio $\Omega P/A^2$ indeed tends to a constant value of $\pi/2$ for an elongated pill ($x \gg 1$). In the other limit of a quasi-spherical pill ($x \ll 1$), $\Omega P/A^2 \simeq 8/3$, which is slightly larger. More complicated elongated shapes, such as when the sheet collapses after separation from the edge (scenario III), could be seen as a sum of elongated droplets, and it is likely that their ratio $\Omega P/A^2$ remains in the range $[\pi/2, 8/3]$.

In order to estimate the droplet volume, we first calculate an approximation of $x$. Since $P = 2R(\pi + x)$ and $A = R^2(\pi + 2x)$, $x$ satisfies the second order equation:

$$x^2 + 2\left(\pi - \frac{P^2}{4A}\right)x + \pi\left(\pi - \frac{P^2}{4A}\right) = 0 \tag{6.2}$$

This equation admits a single positive solution $x$ when $P^2 \geq 4\pi A$ (the equality yields a spherical droplet). The volume is then calculated from Eq. (6.1).

In conventional image processing functions (e.g., in Matlab), $A$ is calculated as the sum of the selected pixels, while $P$ is calculated by joining the centres of the edge pixels. Consequently, $A$ is overestimated compared to $P$, which may erroneously result in $P^2 < 4\pi A$. This artefact may be corrected by removing the excess of area, i.e., by replacing $A$ by $A - \epsilon P/2$, where $\epsilon$ is the pixel size. This correction is sufficient to ensure $P^2 \geq 4\pi A$ for all droplets. We estimated that the resulting error on droplet mass is limited to 30%.

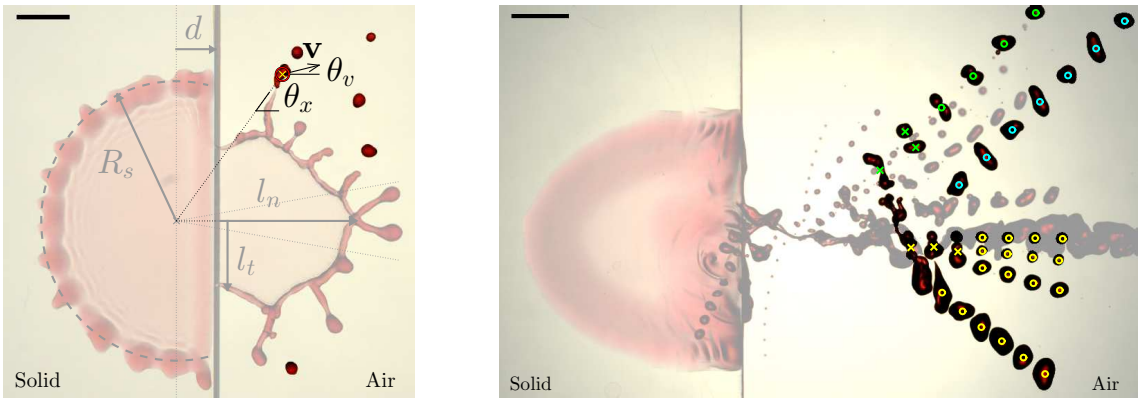


(a) (b)

Figure 6.1: (a) Detected droplets in the snapshot. The velocity vector **v**, position angle $\theta_x$ and ejection angle $\theta_v$ characterizing the ejection velocity of the droplet marked by a yellow cross are defined. The red circle is the equivalent radius corresponding to the measured size of the droplet. Scale bar is 5 mm. (b) Time superposition of an impact illustrating the droplet tracking challenges in three cases, from t = 16 ms to 36 ms with a time interval of 2.5 ms. (Green) Splitting then re-merging of a droplet. (Blue) Oscillation during ejection. (Yellow) Multiple sequential splitting. Scale bar is 5 mm. Crosses represent centres of mass of the droplets that were rejected. Circles indicate valid droplets taken into account in droplet trajectories computation. See text for criteria.

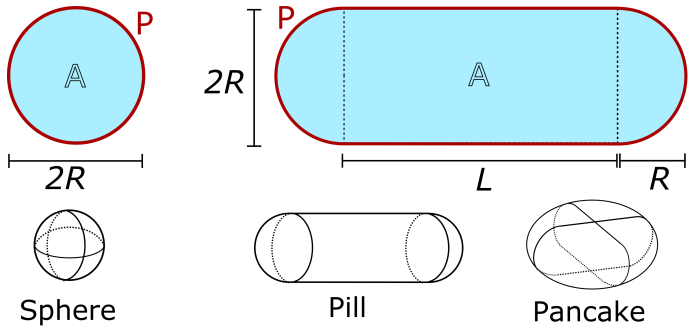


Figure 6.2: Schematic of the reference shapes, a disk and an elongated disk (i.e., a rectangle with two half disk at its extremities) used to compute the droplet volumes. The disk approximates a sphere while the elongated disk can approximate either a pill shape or a pankake shape. The labels are respectively A (area), P (perimeter), R (radius), L (length).

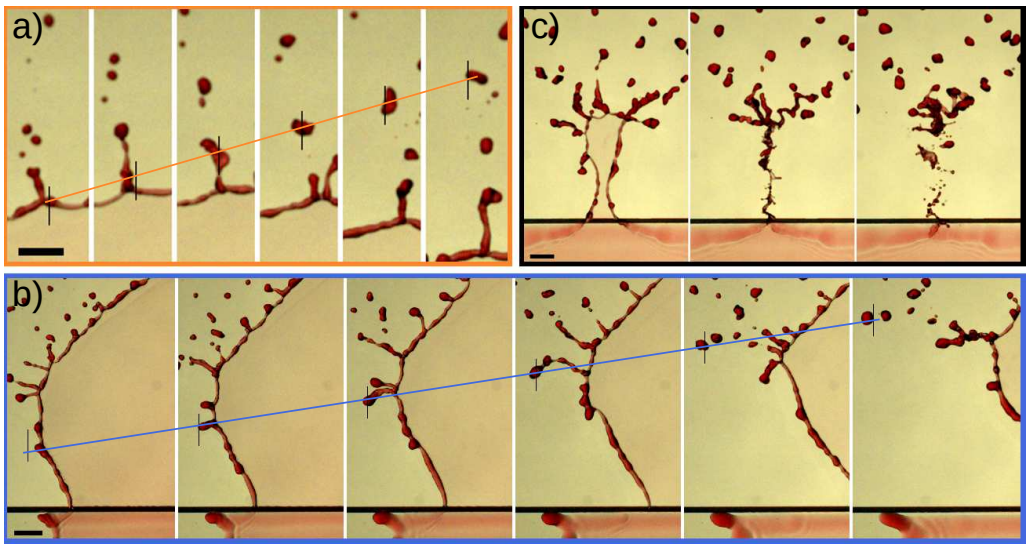


Figure 6.3: Mechanisms of droplet ejection: (a) Radial ejection from the rim. Successive snapshots are separated by 0.5 ms, from 6.2 ms after impact. The highlighted droplet is ejected at $\tau_n = 1.02$, with a mass $m = 0.23$ mg and a speed $v = 0.28\ V_0$. Its ejection angles are $\theta_x = 4°$ and $\theta_v = -9°$. (b) Tangential ejection from the rim. Successive snapshots are separated by 0.6 ms, from 4 ms after impact. The highlighted droplet is ejected at $\tau_n = 1.17$, with a mass $m = 0.29$ mg and a speed $v = 0.46\ V_0$. Its ejection angles are $\theta_x = 48°$ and $\theta_v = 7°$. (c) Collapse of the sheet. Snapshots are taken at 11.8 ms, 12.2 ms and 13 ms after impact. Scale bars are 2 mm. The orange and blue solid lines join the centre of mass of the ejected droplets across frames. The vertical black lines are at fixed position, so they highlight the left-to-right motion of the droplets. These three snapshots correspond to zooms on the droplet ejections framed in Fig. 4.3. Panels b) and c) display also a small part of the solid substrate. The edge is then the horizontal black line.

## 6.2 Ejection mechanisms and direction of ejection

Three ejection mechanisms are identified for the horizontal substrate and illustrated in Fig. 6.3. They are differentiated according to the time, position, and directionality of the ejections (Fig. 6.4). The selected snapshots correspond to parts of the movies illustrated in Fig. 4.3.

- The first mechanism is called radial ejection (Fig. 6.3 - a). It concerns droplets from the rim of the sheet (i.e., before sheet collapse), for which the ejection direction $\theta_v$ is closely aligned on the radial position from the impact point $\theta_x$ (definition in Fig. 6.1a). Each droplet originates from a corrugation along the rim. This corrugation grows in a radial ligament (almost normal to the sheet) by inertia, owing to the constant deceleration of the sheet. The ligament then destabilizes into one or several droplets that are ejected perpendicularly to the rim. The droplets mostly inherit the normal velocity that the sheet had during the early growth of the corrugations. They also inherit a small velocity tangent to the rim, that corresponds to a slight lateral displacement of the corrugation.

- The second mechanism is called tangential ejection (Fig. 6.3 - b) and it again concerns droplets ejected from the rim of the sheet. In this case, the ejection direction $\theta_v$ is not aligned anymore on the radial position $\theta_x$. This mechanism mostly appears on the sides of the sheet in the most asymmetric scenarios, i.e., II and III. Owing to inertia, the corrugations in which liquid accumulates travel along the rim, away from the edge. When the rim retracts tangentially to the edge, these corrugations destabilize into droplets. However, the velocity inherited by the droplets now mostly comes from the motion of the corrugations along the rim, and not anymore from the

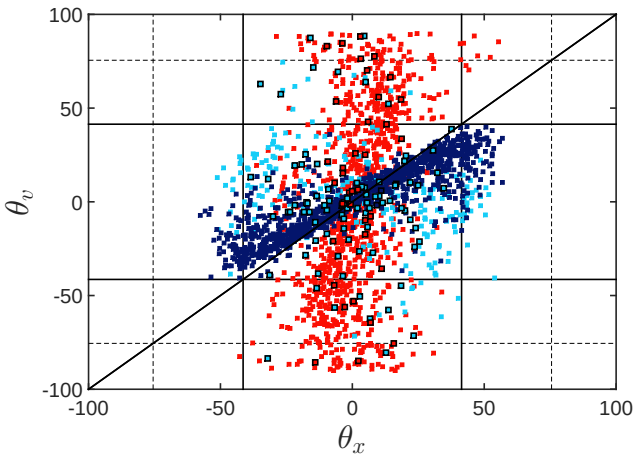


Figure 6.4: Angle $\theta_v$ of the ejection velocity as a function of the angular position of ejection $\theta_x$ (defined in Fig. 6.1a) measured from the impact point, for $We = 1300$ and $\alpha = 0°$. Symbols without black contour (resp. with black contour) correspond to $\delta \in [0.2, 0.3]$ (resp. $\delta \in [0.7, 0.8]$). The colour refers to the ejection time: (dark blue) during sheet expansion, i.e., $\tau_n < 1$, (light blue) during sheet retraction, i.e., $1 < \tau_n < \tau_r$, and (red) after sheet collapse, i.e., $\tau_n > \tau_r$. The inclined solid line is the bisector $\theta_v = \theta_x$. The vertical lines correspond to the maximum sheet angle $\theta_M$ (defined in Fig. 5.25), for $\delta = 0.25$ (dotted) and $\delta = 0.75$ (solid).

velocity of the sheet. Consequently, these droplets are ejected in a direction almost parallel to the rim, and perpendicular to its retraction velocity. As the capillary force from the sheet does not directly oppose the motion of these corrugations, the resulting droplets tend to go faster than the radially ejected droplets.

- The last mechanism occurs when the sheet collapses (Fig. 6.3 - c). The resulting liquid ligament has a very complex shape and it breaks up in a wide variety of droplets. These droplets may inherit from the late retraction speed of the sheet. A particular collapse event is present when the sheet retracts in scenarios II and III. The two rims of the sheet near the edge converge quickly towards each other. Their violent collision generates a filament that breaks up into many droplets. These latter are much smaller than those emitted from the first two mechanisms. The direction of ejection can also be out of the plane of the sheet (Fig. 4.2 g-h).

The prevalence of each ejection mechanism is observed in Fig. 6.4, where the direction $\theta_v$ of droplet ejections is plotted against their angular position $\theta_x$. Droplets are distinguished according to the sheet kinematics (expansion, retraction, collapse) at the moment of their ejection. During sheet expansion ($\tau_n < 1$), most droplets are ejected radially, i.e., with $\theta_v \simeq \theta_x$. Tangential ejections only appear during sheet retraction ($1 < \tau_n < \tau_r$), when the sheet asymmetry is sufficiently developed. At small offset $\delta$, most of them satisfy $|\theta_v| < |\theta_x|$, so their ejection direction is more normal to the edge than a droplet ejected radially from the same position. Droplets ejected from the collapse of the sheet ($\tau_n > \tau_r$) remain localized close to the symmetry axis, in $|\theta_x| \lesssim 20°$. However, their ejection direction $\theta_v$ is much more scattered than for other mechanisms.

The radial ejection mechanism was already observed in the axisymmetric configuration of impact on a pole (Rozhkov *et al.*, 2002; Villermaux & Bossa, 2011), and the mass distribution was characterized. The collapse mechanism is also observed in such impacts when the sheet experiences local piercing (Rozhkov *et al.*, 2002; Villermaux & Bossa, 2011) - this typically occurs when the impact is not perfectly centred on the pole. The tangential ejection mechanism and the filament breakup are not present in axisymmetric impacts such as impact on pole.

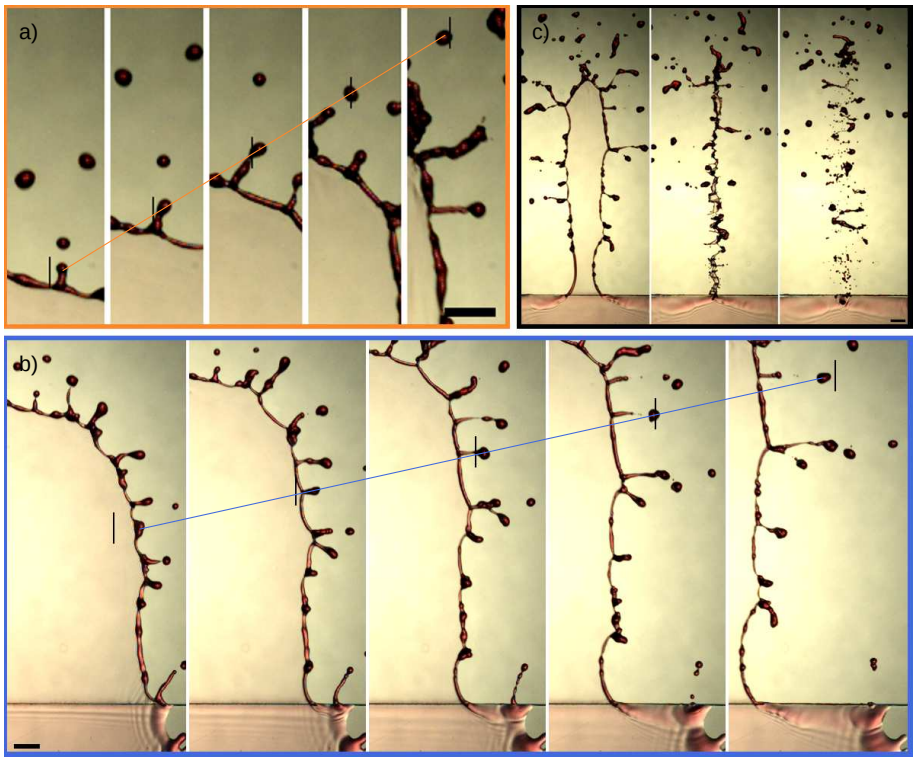


Figure 6.5: Mechanisms of droplet ejection observed for $\alpha = 40°$ and $\delta = 0.5$. (a) Radial ejection from the rim. Successive snapshots are separated by 1 ms, from 7.5 ms after impact. The highlighted droplet is ejected at $\tau_n = 0.84$, with a mass $m = 0.1$ mg and a speed $v = 0.4V_0$. Its ejection angles are $\theta_x = -2°$ and $\theta_v = 6°$. (b) Tangential ejection from the rim. Successive snapshots are separated by 1 ms, from 8 ms after impact. The highlighted droplet is ejected at $\tau_n = 0.83$, with a mass $m = 0.4$ mg and a speed $v = 0.54$ $V_0$. Its ejection angles are $\theta_x = -12°$ and $\theta_v = 15°$. (c) Collapse of the sheet. Snapshots are taken at 11.5 ms, 12.5 ms and 13.5 ms after impact. Scale bars are 2 mm. The orange and blue solid lines join the centre of mass of the ejected droplets across frames. The vertical black lines are at fixed position, so they help visualize the left-to-right motion of the droplets.

These three ejection mechanisms are also identified in the inclined substrate experiments as seen in Fig. 6.5. The link between inclination and the occurrence of tangential and filament breakup droplets becomes even more evident in these cases. The decrease in $\alpha$ leads to more symmetrical sheet behaviours which are linked to radially ejected droplets. More positive $\alpha$ promotes its asymmetry, increasing the extension normal to the edge. This promotes the occurrence of tangential droplets. This effect may result from the tangential velocity of the initial drop, that is somehow transferred to the sheet and to the droplets. In Fig. 6.5 (b), the sheet has not reached its maximum extension, yet the formation of the tangential droplets can already be seen, indicating that the formation of these droplets also occurs sooner with respect to the behaviour on the horizontal substrate. Increased $l_{nM}$ with $\delta$ and $\alpha$ means that the filament breakup mechanism will occur on a longer distance (longer length along which the sheet collapses in a filament) increasing the number of droplets ejected through this mechanism.

The tendencies suggested by the link between sheet asymmetry and droplet ejection mechanisms can be observed in the $\theta_v$ vs. $\theta_x$ diagrams of Fig. 6.6 for the inclined substrates. For the same $\delta$ intervals than in Fig. 6.4, namely [0.2 - 0.3] and [0.7 - 0.8], more radial droplets are ejected for $\alpha =$ -20° (Fig. 6.6a). These datapoints here represent the droplets ejected for a single experiment (one datapoint per droplet) which illustrates also

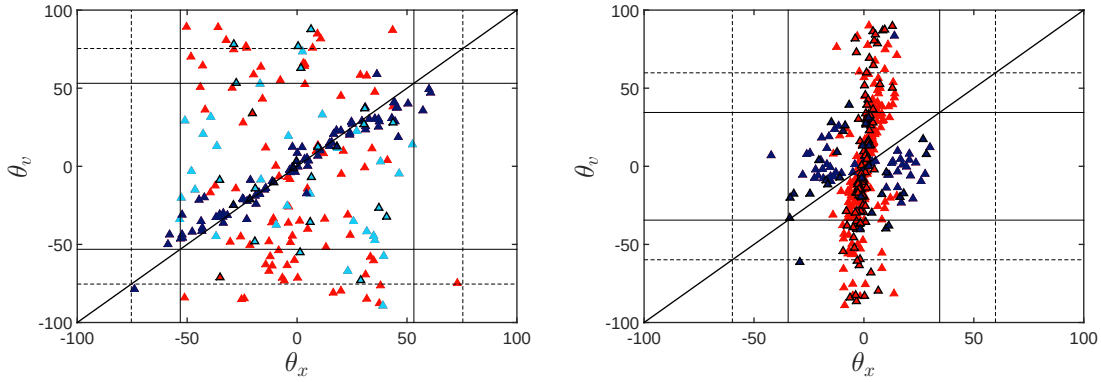


Figure 6.6: $\theta_v$ vs. $\theta_x$ (cf. Fig. 6.4), for $We$ = 2000 and substrate inclination of (a) -20° and (b) 40°. Symbols without black contour (resp. with black contour) correspond to $\delta \in [0.2, 0.3]$ (resp. $\delta \in [0.7, 0.8]$). The colour refers to the ejection time: (dark blue) during sheet expansion, i.e., $\tau_n < 1$, (light blue) during sheet retraction, i.e., $1 < \tau_n < \tau_r$, and (red) after sheet collapse, i.e., $\tau_n > \tau_r$. The inclined solid line is the bisector $\theta_v = \theta_x$. The vertical lines correspond to the maximum sheet angle $\theta_M = \tan^{-1}(l_{tM}/d)$ for $\delta = 0.25$ (dotted) and $\delta = 0.75$ (solid).

the reduction in number of ejected droplets $N$ for negative $\alpha$, e.g., from $N$ = 226 at $\alpha$ = 40° and $\delta \in$ [0.2 0.3] to $N$ = 160 at $\alpha = -20°$ for the same $\delta$ interval. For $\alpha = 40°$, the number of tangential droplet increases during the expansion phase as the dark blue points are further away from the bisector in Fig. 6.6b, e.g., from $N$ = 52 at $\alpha = -20°$ to $N$ = 132 at $\alpha$ = 40°, both for a $\delta \in$ [0.2 - 0.3].

The time of first ejection can be calculated as the quantile 1% ($Q_{0.01}$) of the distribution of ejection times $\tau_n$. For the horizontal substrate, it is represented in Fig. 6.7a, where data from all experiments have been pooled by $We$ and $\delta$. The time of first ejection increases with $\delta$ and decreases with $We$. For scenarios II and III, the first ejections occur during the expansion of the sheet ($\tau_n < 1$). Conversely, in the isotropic scenario (I), ejections only start during the retraction of the sheet ($\tau_n > 1$). For inclined substrates, Figs. 6.7b and 6.7c do not seem to indicate any statistical dependence to $\alpha$. Note however the sudden drop at $\delta \sim 0.6$ for $\alpha = 40°$ and 60°. This is the signature of a fourth mechanism illustrated in Fig 6.8 which was attributed to the tangential momentum conferred to the liquid. In Fig. 6.8a, the substrate is inclined at -40° and no such ejection is visible. However, we notice an important fingering of the liquid spread on the solid in the downward direction. For the 40° inclination in Fig. 6.8b, the liquid within the fingers moves downwards and beyond the edge. We will refer to this mechanism as the fingering ejection mechanism. The destabilization of the ligaments thus created occurs faster which explains the earlier time at which the first droplets are ejected. Such fingering was also present for the smaller $We$ number investigated but the thickness of the rim was much larger which may explain why this phenomenon is not noticed at lower $We$.

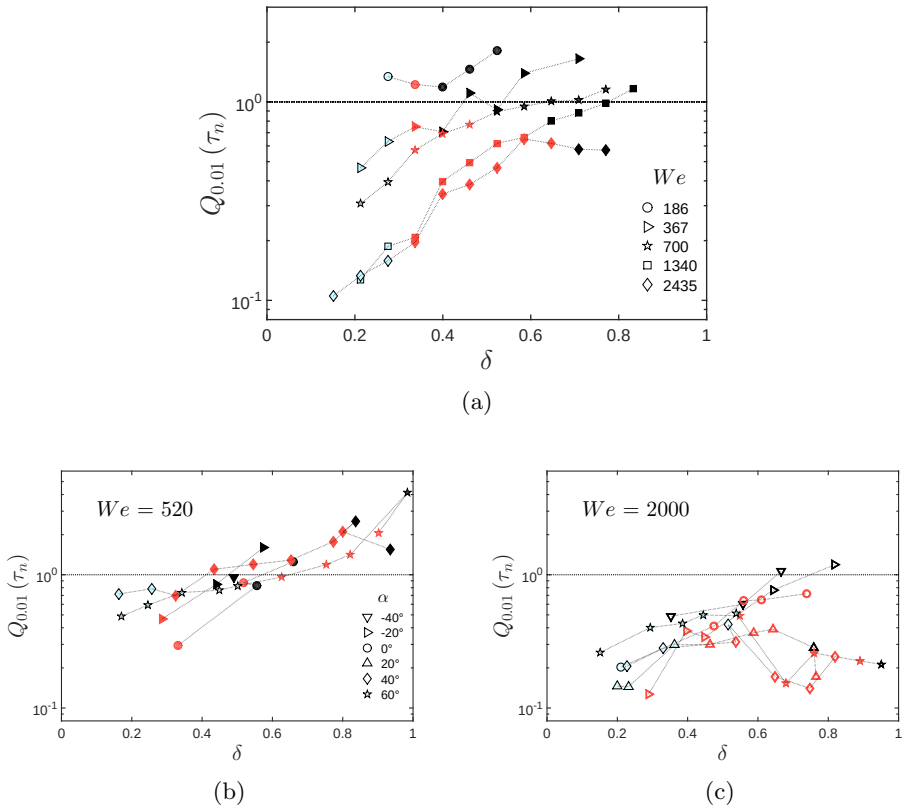


Figure 6.7: Quantile 1% of the ejection time $\tau_n$, as a function of the offset $\delta$ (a) on horizontal substrate with symbols in $We$, (b) for $We$ = 500 and symbols in $\alpha$ and (c) for $We$ = 2000 and symbols in $\alpha$. Legends in insets. Colours indicate degree of asymmetry (scenario) from lowest (I) to highest (III) with I (black), II (reddish/grey) and III (blue/clear). The solid line corresponds to the time $\tau_n$ = 1 of maximum extension of the sheet normal to the edge.

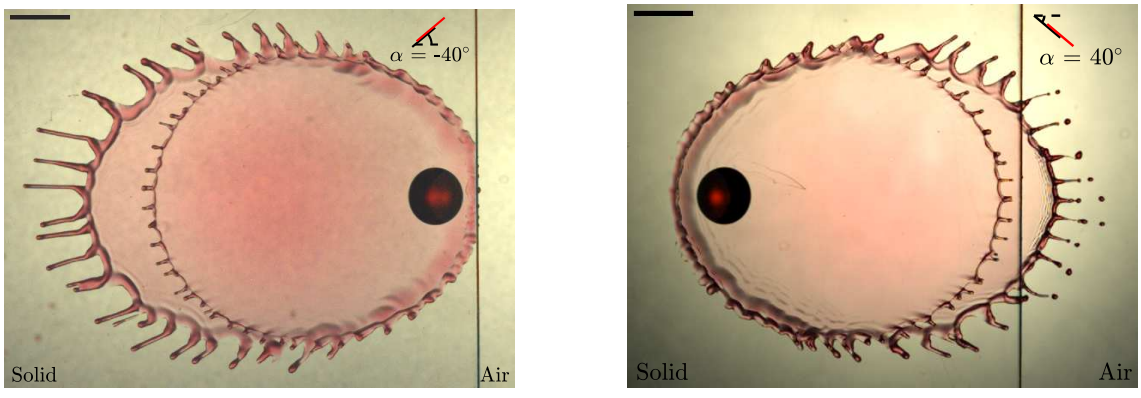


Figure 6.8: Fingering on inclined surfaces leading to droplet ejection in positively inclined surfaces. Time superposition of a drop impacting at $We$ = 2000, taken at 0 ms, 4ms , 7ms and 9ms from impact for (a) $\alpha$ = -40° and (b) $\alpha$ = 40°.

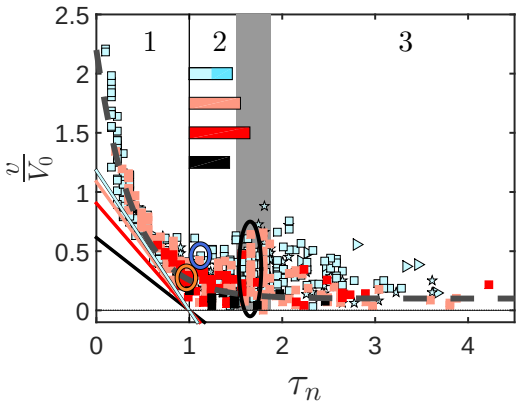


Figure 6.9: Normalized time evolution of the droplet ejection speed $v$ for the six examples of Figs. 4.3 and 4.4. The time $\tau_n$ is normalized according to the normal extension of the sheet. Each data point corresponds to a single droplet. Symbols correspond to Weber number, $We$ = 367 (▷), 700 (☆), 1340 (□), while colours indicate scenario: I (black), II (reddish/grey) and III (blue/clear). The grey area indicates the time $\tau_r$ at which the sheet has fully retracted from the edge (average across $We$ and $\delta$, ± one standard deviation). The numbers 1, 2 and 3 indicate periods of time of the sheet (1 - expansion, 2 - retraction and 3 - after full sheet retraction along the edge). Horizontal rectangles represent the duration of the sheet retraction. The darker blue rectangle in scenario III corresponds to the retraction of the sheet after it has pinched from the edge. The inclined solid lines correspond to Eq. (6.3) for the six examples (one line per scenario). The dotted line is Eq. (6.4). Circled data points correspond to the snapshots of Fig. 6.3.

## 6.3 Droplet ejection speed

We now examine how the mechanisms of ejection can affect the speed of the droplets through the asymmetry of the sheet.

### Temporal evolution

The speed $v$ at which each droplet is ejected is represented as a function of its ejection time in Fig. 6.9, for the six examples of Figs. 4.3 and 4.4. The speed $v$ is naturally normalized by the impact speed $V_0$, while the time $\tau_n$ is $t - t_d$ normalized by the time of maximum extension of the sheet normal to the edge. All the data corresponding to normal extension ($\tau_n < 1$) from a horizontal substrate collapse onto a single curve, so $v/V_0$ is a decreasing function of $\tau_n$ only, for all $We$ and $\delta$. The ejection speed becomes more scattered as soon as $\tau_n > 1$, i.e., during the retraction and collapse of the sheet. The time $\tau_r$ at which the sheet collapses along the edge also corresponds to a maximum scatter of the ejection speed.

The influence of the sheet kinematics on droplet ejection can be better assessed by looking at the speed of the sheet in the direction normal to the edge [derived from Eq. (5.22)]:

$$\frac{1}{V_0}\frac{dl_n}{dt} = \frac{2l_{nM}}{V_0(t_{nM} - t_d)}(1 - \tau_n) \simeq 1.34\sqrt{1-\delta}(1 - \tau_n). \tag{6.3}$$

The normal extension speed of the sheet is again proportional to the impact speed $V_0$ at first order. It is reported in Fig. 6.9, where it sets a lower limit to the droplet ejection speed. Indeed, ejected droplets during the sheet expansion must go faster than the sheet from which they detach.

A careful examination of Fig. 6.9 indicates that, for $\tau_n > 1$, the scattering of ejection speed at a given time depends on the considered scenario. In order to better quantify this scattering, we define the average speed $v_T(\tau_n)$ of all the radially ejected droplets at a given $\tau_n$. These considered droplets are from all scenarios together when $\tau_n < 1$, and only

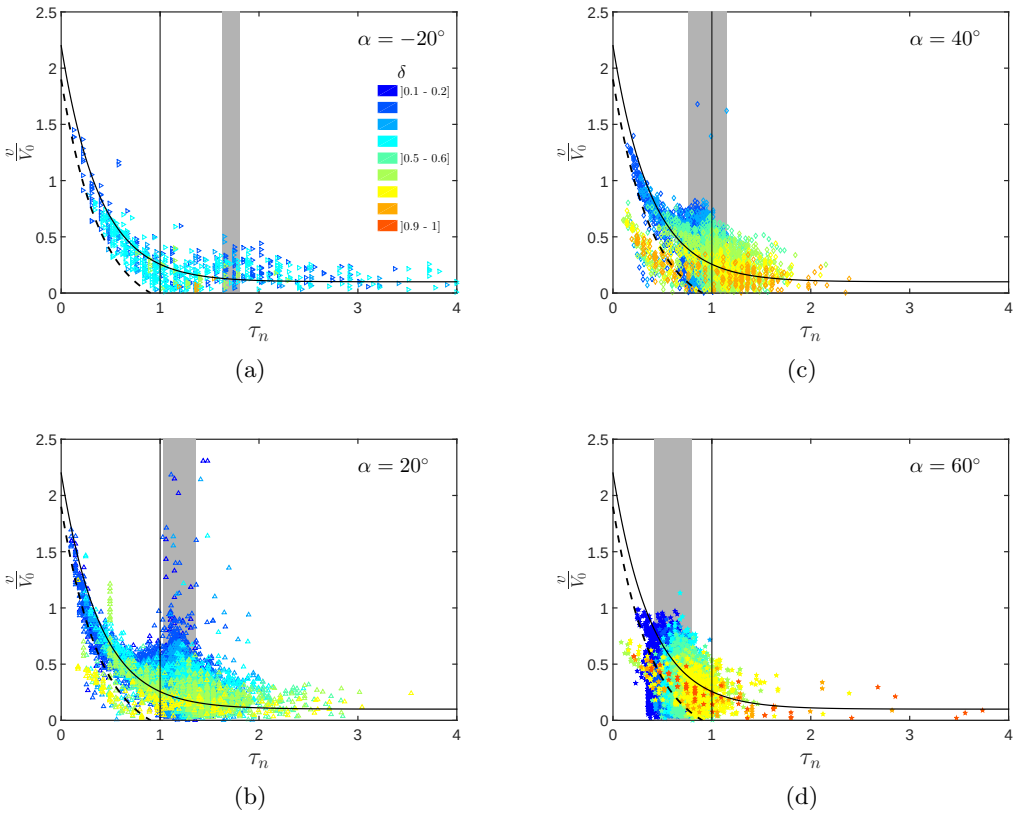


Figure 6.10: Time evolution of the droplet ejection speed $v$ as a function of the normalized time $\tau_n$ for $We = 2000$ and $\alpha$ = -20° (a), 20° (b), 40° (c) and 60° (d). Each data point corresponds to a single droplet. Colours correspond to $\delta$ [cf. legend in (a)]. The vertical black line indicates the time of maximum sheet extension. The grey area indicates the time $\tau_r$ at which the sheet has fully retracted from the edge (average across $\delta$, plus/minus standard deviation). The solid lines represent Eq. (6.4) and the dashed ones, Eq. (6.5).

from scenario I when $\tau_n > 1$. This average velocity is well approximated by:

$$\frac{v_T}{V_0} = 2.1e^{-2.6\tau_n} + 0.1, \tag{6.4}$$

as illustrated in Fig. 6.9.

Data from scenario I align in the continuity of the curve observed for $\tau_n < 1$, without much scattering. The corresponding droplets are radially ejected, through the same mechanism as the droplets ejected in $\tau_n < 1$. By contrast, the ejection speed at $\tau_n > 1$ is much more scattered for scenarios II and III, which suggests the emergence of tangential ejections. The filament breakup occurs in $\tau_r$ and it coincides with the maximum of scattering for these scenarios.

The decrease of ejection speed with time is also recovered for the inclined substrates and across all $\alpha$ and $\delta$ as seen in Fig. 6.10. We can however notice several effects of the inclination. Negative inclinations such as in Fig. 6.10a promote the more axisymmetric scenario which in turn reduces the amount of tangential and filament breakup droplets. The scatter of the droplets around $v_T$ is thus reduced. The opposite effect is observed for positively inclined substrates. The presence of a peak in the scatter at the moment of filament breakup is more pronounced in Figs. 6.10b, 6.10c and 6.10d. We also noticed that this peak occurs earlier as $\delta$ decreases as noticed in Fig. 5.23b but also in Fig. 5.23a for the horizontal case. The filament breakup occurs earlier for large $\alpha$, for which the asymmetry is more pronounced. For $\alpha = 60°$, shown in Fig. 6.10d, this even occurs before

the sheet reaches its maximum extension. This leads to modify the definition of the sheet expansion as being the time interval for which $\tau_n < \min(1, \tau_r)$. As $\alpha$ increases, the time of maximum extension can occur after the collapse and the tangentially ejected droplets are not distinguished from the filament breakup ones anymore.

Experimentally, datapoints for high $\alpha$ values (40° and 60°) were challenging to image as the sheet extension was not only stretched but kept a forward motion without ever retracting towards the edge. This behaviour has already been discussed when trying to determine the sheet maximum extension and was dealt with by measuring the acceleration and initial speed of the sheet instead. For some experiments, the final destabilization of the liquid sheet occurred outside the field of view of the camera. In Figs. 6.10c and 6.10d, the consequence might be that some dark blue droplets might be missing for large $\tau_n$. Their potential absence will thus be discussed when appropriate.

The time at which the first droplets appear presents a discontinuity for positively inclined $\alpha$ due to the occurrence of an additional mechanism (section 6.2). Another population of droplets is indeed visible in the temporal evolution of the droplet speed for large $\alpha$, especially in Figs. 6.10c and 6.10d. Below the dashed line, which corresponds to

$$\frac{v_T}{V_0} - 1.5STD\left(\frac{v}{v_T}\right)_{\tau_n<1} \tag{6.5}$$

and where $STD$ stands for 'standard deviation', another cluster of droplets appears across all values of $\delta$ including the large ones. On the horizontal or negatively inclined substrates, large offsets do not present any ejection at early times and we can assume that these clusters are the fingering droplets. A major effect of the inclination is thus to trigger the occurrence of these early droplets. For the large offsets, where no ejections would occur on the horizontal substrate, the speed of these droplets is greater than the speed of the droplets ejected later on [and following Eq. (6.4)].

### Single boundary until maximum spreading

The scattering of ejection speeds can be investigated more systematically through the definition of averages over specific time intervals for all experiments at given ($We$, $\delta$). These averages are defined for any variable $X$ as follows:

$$\begin{aligned}
\langle X\rangle^1 &: \quad \text{average over sheet expansion,} && \tau_n < 1 \\
\langle X\rangle^2 &: \quad \text{average over sheet retraction,} && 1 < \tau_n < \tau_r \\
\langle X\rangle^3 &: \quad \text{average after full sheet retraction from the edge,} && \tau_n > \tau_r \\
\langle X\rangle &: \quad \text{average over all time} && \tau_n > 0.
\end{aligned} \tag{6.6}$$

As seen in Fig. 6.11a for the horizontal substrate, the average speed during sheet expansion is very close to the theoretical speed of radially-ejected droplets, i.e., $\langle v/v_T\rangle^1 \sim 1$, for all $We$ and $\delta$, which is expected from the definition of $v_T$. The corresponding standard deviation is about seven times smaller than the average value, which confirms the good collapse of the data already seen for $\tau_n < 1$ in Fig. 6.9. Furthermore, the Probability Distribution Function $PDF\left(\langle v/v_T\rangle^1\right)$, that includes all droplets ejected for $\tau_n < 1$, follows a Gaussian model of mean 1.01 and standard deviation 0.2 (Fig. 6.11a - inset).

For the inclined substrates, the scattering of the ejection speed $\langle v/v_T\rangle$ over the sheet expansion has been calculated for all droplets ejected before the sheet reaches its maximum extension $t_{nM}$ but also in omitting all droplets ejected after the sheet collapse along the edge. This average speed shows the same behaviour as for the horizontal case with a collapse not only in $We$ but also in $\alpha$, and falling close to 1, as shown in Fig. 6.11b. The only deviations from the average are observed for large values of $\alpha$ where the droplets

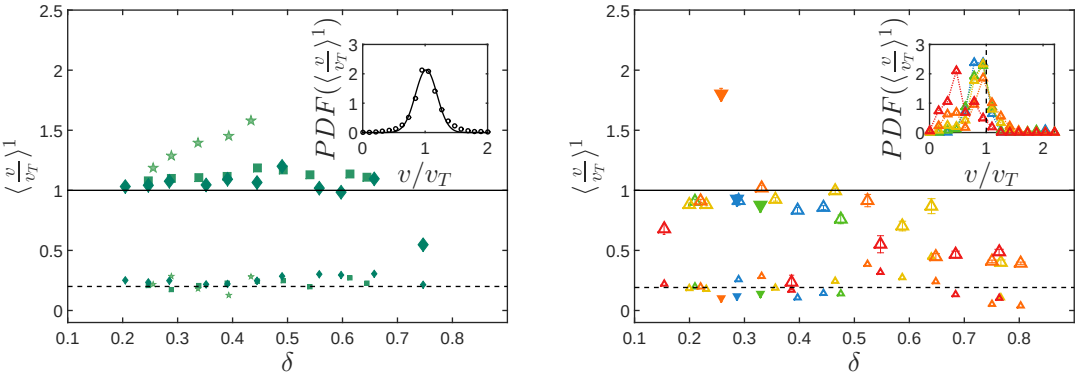


(a) (b)

Figure 6.11: Average (large symbols) and standard deviation (small symbols) of $v/v_T$ over the sheet expansion [$\tau_n < min(1, \tau_r)$]. **(a)** for $\alpha = 0°$, for each ($We$, $\delta$). $We \in$ [186 2435] (cf. table 1). The solid line is $v = v_T$ and the dashed line is the average of the standard deviations (small symbols) over all ($We$, $\delta$) Inset: PDF of $v/v_T$ during the sheet expansion. The solid line is a fit with a Gaussian model of mean 1.01 and standard deviation 0.2. **(b)** for each $\alpha$ value -20° (blue), 0° (green), 20° (yellow), 40° (orange) and 60° (red), $\delta$ and $We = 500$ ($\triangledown$) and $We = 2000$ ($\triangle$). The solid line is $v = v_T$ and the dashed line is the average of the standard deviations (small symbols) over all ($We$, $\alpha$, $\delta$). Inset: PDF of $v/v_T$ during the sheet expansion per $\alpha$ in colour for $We = 2000$ ($\triangle$). The dashed line corresponds to $v = v_T$.

ejected by the fingering mechanism shift the average to lower values. Its effect is also visible in the PDF($\langle v/v_T \rangle^1$) where the Gaussian distribution for small $\alpha$ becomes bimodal as $\alpha$ reaches 40° and 60° in inset of Fig. 6.11b. Since these droplet ejections begin during the expansion of the sheet, a temporal criteria is not useful to distinguish them from the radially ejected one. In inset of Figs. 6.10c and 6.10d, the Eq. (6.4) is plotted (solid line) as well as Eq. (6.5)[dashed line], which is Eq. (6.4) minus one standard deviation of $v/v_T$ taken for $\tau_n < 1$ on all $\delta$ for all $We$ and $\alpha$. All droplets that fall below the curve of Eq. (6.5) during the expansion of the sheet are considered to be fingering ejected droplets. We will not consider these droplets beyond the time of maximum extension of the sheet as we can observe from Fig. 6.10 that their speed is not distinguishable anymore from the one from the other mechanisms beyond this time.

### Asymmetry signature during sheet retraction and collapse

During the retraction and collapse of the sheet (so as soon as $\tau_n \gtrsim 1$), both the average $\langle v/v_T \rangle$ and corresponding standard deviation decrease linearly with increasing $\delta$ for horizontal substrates (Fig. 6.12a and inset of Fig. 6.12b). The larger scatter at small $\delta$ can be attributed to the presence of additional ejection mechanisms (namely the tangential ejection mechanism and the filament breakup). There is almost no dependence to $We$, which indicates that the sheet asymmetry (measured by $\delta$) drives the droplet ejection pattern both during the sheet retraction and during the collapse. Fig. 6.12b shows the average of the speed of the droplets after collapse normalized by $v_T$ taken at the averaged moment of collapse $\overline{\tau_r}$ over all $We$ and $\delta$. We observe the same tendency as when the speed was normalized by the temporal evolution. This normalization was chosen to take the slight increase of $\tau_r$ with increasing $\delta$ into account but also for comparison sake with the inclined configuration which is discussed hereafter.

When inclining the substrate, the average behaviour during retraction is quite similar to the horizontal case with respect to the offset variation (Fig. 6.12c). During the retraction but before the collapse along the edge, an increase in the tangential mechanism increases

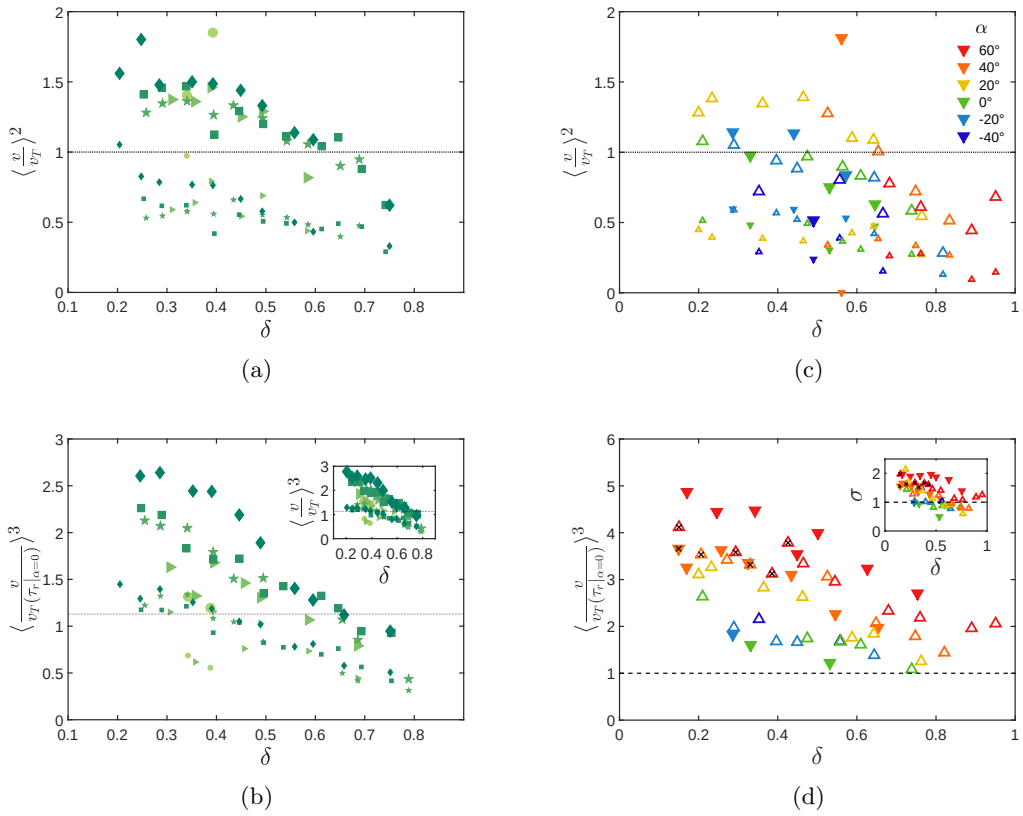


Figure 6.12: **(a and c)** Average (large symbols) and standard deviation (small symbols) of $v/v_T$ over the sheet retraction ($\tau_n > 1$) for **(a)** $\alpha = 0°$ over all ($We$, $\delta$) and **(c)** $\alpha \in$ [-40° 60°] in colour (cf. legend in inset) over all ($We$, $\delta$, $\alpha$) for $We = 500$ ($\triangledown$) and 2000 ($\triangle$). **(b and d)** Average (large symbols) and standard deviation (small symbols) of $v$ after the sheet collapse ($\tau_n > \tau_r$) normalized by $v_T(\tau_r|_{\alpha=0°})$, the average value of $v_T$ at the collapse along the edge for the horizontal substrate over all $We$. **(b)** $\alpha = 0°$. The datapoints are computed for each ($We$, $\delta$). The inset shows the same data but normalized by $v_T(\tau_n)$. **(d)** $\alpha \in$ [-40° 60°] in colour [see legend in inset of (c)]. The datapoints show the average value (standard deviation in inset) for each ($We$, $\delta$, $\alpha$). $We = 500$ (filled $\triangledown$) and 2000 (empty $\triangle$).

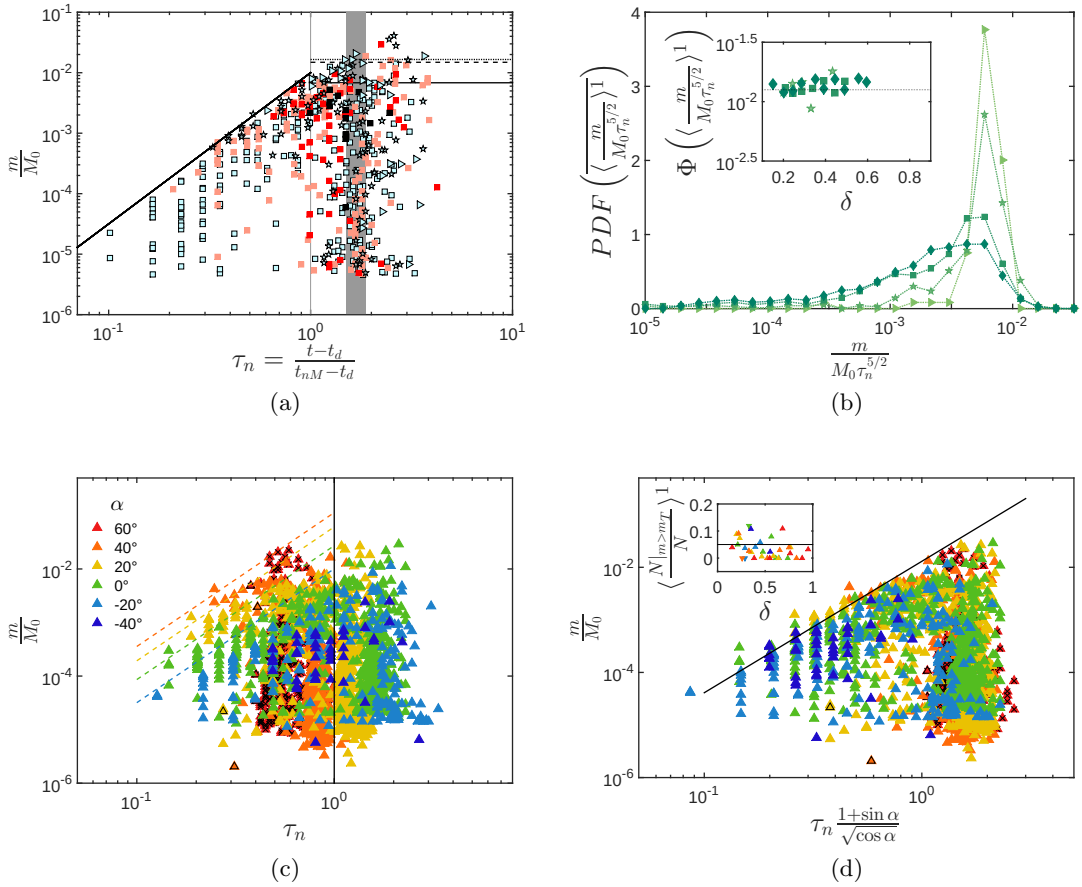


Figure 6.13: **(a)** Time evolution of the mass $m$ of the ejected droplets (normalized by the mass $M_0$ of the impacting drop) as a function of their normalized time of ejection $\tau_n$ for the six examples of Figs. 4.3 and 4.4. $\alpha = 0°$ and colours indicate scenario, I (black), II (reddish/grey) and III (blue/clear). The grey area indicates the time $\tau_r$ at which the sheet has fully retracted from the edge (average across $We$ and $\delta$, plus/minus standard deviation). The inclined solid line represents Eq. (6.7). The horizontal lines correspond to Eq. (6.9) with $We = 367$ (dotted - ▷), $We = 700$ (dashed - ☆) and $We = 1340$ (solid - □). Each data point corresponds to a single droplet. **(b)** Probability Distribution Function (PDF) of the normalized mass $m/(M_0{\tau_n}^{5/2})$ of droplets ejected during sheet expansion ($\tau_n < 1$), pooled per $We$ (all $\delta$ together). The values of $We$ are 186 (◯), 367 (▷), 700 (☆), 1340 (□) and 2435 (◇). Inset: Saturation value $\Phi$ of the PDF, for each $We$ and $\delta$. The dotted line is Eq. (6.7). **(c)** Time evolution of $m/M_0$ as a function of $\tau_n$ for six experiments with varying $\alpha$ (in colour, cf. legend), with $\delta \in [0.2 - 0.4]$ and $We = 2000$. The vertical solid line is the time of the sheet maximum extension, $\tau_n = 1$. The inclined dashed lines represents Eq. (6.7) with a fitted coefficient per $\alpha$. Data with a black cross correspond to experiments where some droplets ejected after collapse may be missing. Each data point corresponds to a single droplet. **(d)** Same data as in (c) but plotted as a function of the time $\tau_n(1 + \sin\alpha)/\sqrt{\cos\alpha}$. The solid line is Eq. (6.7). The inset shows the number $N$ of droplets whose mass is greater than the boundary mass $m_T$ given by Eq. (6.7) as a function of $\delta$ per $\alpha$ in colour and $We = 520$ (▽) and 2000 (△). The solid line corresponds to a 5% threshold.

the scatter almost linearly with $\delta$. The average value is generally lower for the inclined substrates dataset (including the control one with $\alpha = 0°$) which may be due to a reduced number of droplets or small differences in the experimental conditions. We observe a collapse of the datapoints in $\alpha$ for large $\delta$. A tendency for small $\delta$ is more difficult to assess. The positive angles $\alpha = 20°$ and $40°$ are indeed a bit higher but not significantly so and there are no datapoint for the highest $\alpha$ if $\delta > 0.6$. In these configurations, $t_{nM} < t_r$, and the sheet collapses before reaching its maximum value. The tangentially ejected droplets have thus either no time to develop or are mixed with the filament breakup ones. We would expect the increased asymmetry linked to the increased inclination of the substrate to promote the tangentially ejected droplets to some extend but additional experiments will be required to confirm this hypothesis.

The scattering of the droplet speed after collapse is computed as $\langle v/v_T(\tau_r|_{\alpha=0°})\rangle$ so we observed the change in scatter compared to the value of $v_T$ at the moment of collapse on the horizontal substrate ($\tau_r|_{\alpha=0°} = 1.75$). Indeed, since the increase in $\alpha$ shifts the collapse time to lower values and $v_T$ is a decreasing function of $\tau_n$, an average computed as $v(\tau_n)/v_T(\tau_n)$ would artificially lower the scattering values for greater $\alpha$. In Fig. 6.12d, the scatter increases with decreasing $\delta$ and increasing $\alpha$, while remaining independent on the $We$. This is similar to what was observed in Fig. 6.12b for the horizontal case but it also confirms the tendency of the inclination to increase asymmetry and thus the scatter of the filament breakup droplets. The standard deviation increases following the same trend as the average and even becomes comparable to it. For this reason and to improve readability, it was put in inset of Fig. 6.12d. Datapoints marked with a black cross represent the events where the sheet final-collapse took place partly outside the field of view although most of the destabilization and the filament breakup had already occurred in it. The general trend of these datapoints align on the correctly detected ones. The reduced value of the average for $\alpha = 60°$ and the highest $We$ number might be attributed to this detection problem but additional experiments would be needed to confirm this, and they are left to future work.

## 6.4 Droplet mass

We now focus on the mass of the ejected droplets which is a key property for foliar disease propagation. Indeed, not only does it condition the amount of pathogens a leaf may receive (Fitt *et al.*, 1989) but it also determines the distance travelled when combined with the ejection speed of the droplets.

### Temporal evolution and upper bound before $\tau_n = 1$

The mass $m$ of the ejected droplets is reported as a function of their normalized ejection time $\tau_n$ in Fig. 6.13a, for the six examples of Figs. 4.3 and 4.4 (horizontal substrate). Contrary to the ejection speed $v$, the mass $m$ varies over more than three orders of magnitude and it is scattered at all time. Nevertheless, $m$ is clearly bounded by a maximal mass that increases with time for $\tau_n < 1$ and saturates to a constant value for $\tau_n > 1$. This maximal droplet mass is still 50 times smaller than the mass $M_0 = 4\pi\rho R_0^3/3$ of the impacting drop. Viscosity sets a lower bound to the size of ejected droplets. In the context of partial coalescence, the inhibition of inertial liquid break-up by viscosity was observed for Ohnesorge numbers $Oh \gtrsim 0.025$ (Blanchette & Bigioni, 2006; Gilet *et al.*, 2007). It here corresponds to a minimum radius of 0.02 mm, and a mass $m/M_0 \simeq 5 \times 10^{-7}$. This size is slightly below the resolution of our camera.

On a horizontal substrate, the increase of the upper bound on mass during sheet expansion ($\tau_n < 1$) satisfies a power law

$$\frac{m}{M_0} \leq 0.013\tau_n^{5/2}, \tag{6.7}$$

that is valid for each scenario so it is presumably independent of the offset $\delta$.

Equation (6.7) suggests to analyse the statistical distribution of droplet mass, normalized by $\tau_n^{5/2}$. This distribution is now calculated on all our data. Data are pooled per $We$ (all $\delta$ together), which is denoted with a simple overline. The Probability Distribution Function

$$PDF\left(\overline{\langle\frac{m}{M_0\tau_n^{5/2}}\rangle^1}\right)$$

presents a mode that approximately varies as $We^{-0.2}$, so faster incoming drops generate smaller ejected droplets. There is indeed a cut-off on the right end of this PDF, which corresponds to the maximal mass (Fig. 6.13b). We define the maximal value of any variable $X$ as the cut-off $\Phi(X)$ of its statistical distribution. This cut-off is here obtained by approximating the tail of the corresponding Cumulative Distribution Function (CDF) of $X$ with a quadratic function that reaches a maximum of 1 in $\Phi$. The least-square fit is performed with data from quantiles 0.85 to 0.995.

The cut-off mass at $\tau_n < 1$ is determined for each $\delta$ and $We$ independently (Fig. 6.13b - inset). It is remarkably independent of $\delta$ and $We$, and its average value is given by $\Phi\left(m/M_0\right) \simeq 0.013\tau_n^{5/2}$. Again, once this cut-off mass is expressed as a function of the sheet time $\tau_n$, the explicit dependence to $We$ and $\delta$ disappears, which is characteristic of the droplets radially ejected during sheet expansion.

Varying the inclination does not modify the temporal increase of the mass of the droplets as seen in Fig. 6.13c which represents six experiments of varying $\alpha$ with $\delta \in [0.2 - 0.4]$. Yet, the prefactor of Eq. (6.7) increases strongly with $\alpha$. From our previous understanding of the sheet and droplet behaviour, the offset conditions the asymmetry of the liquid sheet but is taken into account through the sheet behaviour by normalizing the time using $t_{nM} - t_d$. From the success of normalizing the temporal evolution of the speed of the droplets by $t_{nM} - t_d$, we were expecting a collapse in $\alpha$ for the masses on the inclined substrates as well, instead of an increase of the cut-off value. We assumed however that the temporal evolution of Eq. (6.7) could be recovered through an $\alpha$ dependent factor. For inclined substrates, the expression $(t_{nM} - t_d)/t_c$ [Eq. (5.33)] displays such an explicit dependency in $\alpha$ as $(1+\sin\alpha)/\sqrt{\cos\alpha}$. Expressing the temporal evolution of the masses as a function of $\tau_n(1+\sin\alpha)/\sqrt{\cos\alpha}$ brings the largest droplets along the boundary described by Eq. (6.7) as seen in Fig. 6.13d. Finally, the average percentage of droplets above the prediction of Eq. (6.7) is below five percent across all $\delta$, $\alpha$ and $We$ (inset of Fig. 6.13d). We thus conclude that a general upper bound for the temporal increase of the mass of ejected droplets can be expressed as

$$\frac{m}{M_0} \simeq 0.013(\tau_n\frac{1+\sin\alpha}{\sqrt{\cos\alpha}})^{5/2}. \tag{6.8}$$

The analysis is performed based on the droplet ejection time with respect to the sheet behaviours as it allows a first order separation of the droplets by their mechanisms of ejection. These are determined based on the droplet time of ejection so that we have a majority of radially ejected droplets during the expansion, a mix of radially and tangentially ejected during the retraction and both of them plus the filament breakup ones after collapse. The proportion of each population after the collapse depends on the asymmetry of the liquid sheet. Other methods to identify and separate the droplets by their ejections mechanisms were tried, but they proved less robust.

There is however one mechanism which partly takes place during the expansion of the sheet, namely the fingering. It was first revealed by the presence of ejected droplets earlier than expected at large offsets, and by a secondary cluster of droplets in the speed vs time diagrams (Fig 6.10). In the previous section (section 6.3), droplets ejected for $\tau_n < min(1, \tau_r)$ with a speed below Eq. (6.5) were identified as fingering ejected droplets. This first order selection was used to highlight the droplets in black in Fig. 6.14, showing that these droplets actively participate to the boundary predicted by Eq. (6.8) for large

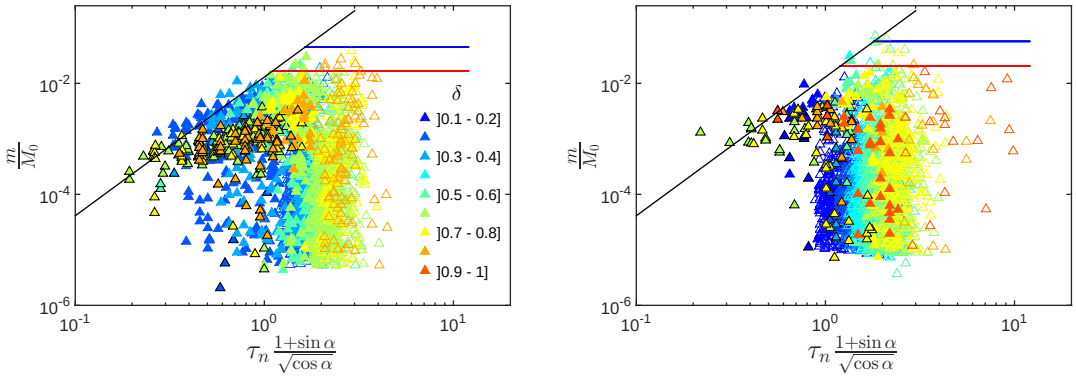


(a) (b)

Figure 6.14: Time evolution of the mass $m$ of the ejected droplets (normalized by the mass $M_0$ of the impacting drop) as a function of the normalized time of ejection $\tau_n(1+\sin\alpha)/\sqrt{\cos\alpha}$ **(a)** for $\alpha = 40°$ and **(b)** for $\alpha = 60°$, $We = 2000$ and colours in $\delta$ (cf. legend). Each data point corresponds to a single droplet. The inclined solid line is Eq. (6.8). The black contoured symbols are droplets identified as resulting from the fingering ejection mechanism [cf. Eq. (6.5)]. The red lines are Eq. (6.11) and the blue lines are Eq. (6.12). Full symbols: droplets ejected during the extension of the sheet [$\tau_n < min(1, \tau_r)$], empty symbols: droplets ejected during the retraction or after the collapse.

value of $\delta$. Note however that other normalizations for the mass and time of the droplets were available which all induced non trivial dependencies in $\delta$ and $\alpha$. We observe in Fig. 6.14 that some droplets are above the boundary set by Eq. (6.8), particularly for small $\delta$ (Fig. 6.14a) which may indicate a second order effect of the inclination such as an accumulation of fluid under the effect of the tangential speed or gravity. Eq. (6.8) however still accounts well at first order for all $\delta$ and $\alpha$.

### Retraction and after collapse ejection

In this work, we are mainly interested in the maximum size and distance travelled by the droplets. We thus chose to focus on the cut-off values of their mass. An analysis of their probability distribution function during retraction and after collapse for both horizontal and inclined substrates can however be found in appendix A.

For horizontal substrate first, during retraction, the variation of $\Phi\left(\langle m/M_0\rangle^2\right)$ with $\delta$ is very small (Fig. 6.15a). Consequently, data from different $\delta$ can be pooled, which reveals a power-law dependence in $We$ (Fig. 6.15a - inset):

$$\Phi\left(\overline{\langle\frac{m}{M_0}\rangle^2}\right) = 2.9\,We^{-3/4} \tag{6.9}$$

After the collapse of the sheet, $\Phi\left(\langle m/M_0\rangle^3\right)$ is almost independent of $\delta$ at high $We$, but it sharply decreases with increasing $\delta$ at lower $We$. The pooling of scenarios II and III reveals a decrease of the average cut-off with increasing $We$:

$$\Phi\left(\overline{\langle\frac{m}{M_0}\rangle^{2\text{-}3}}^{II\text{-}III}\right) = 10^4\,We^{-1.7} \tag{6.10}$$

The comparison of Eqs. (6.9) and (6.10) reveals that, for $We \lesssim 4000$, the maximal droplet mass is larger after collapse than during retraction of the sheet. This fact could be the consequence of (i) the likely merging of ejected droplets after collapse, and (ii) the presence of a very large liquid ligament detached from the edge (e.g. in scenario III) that does not instantly destabilise into smaller droplets.

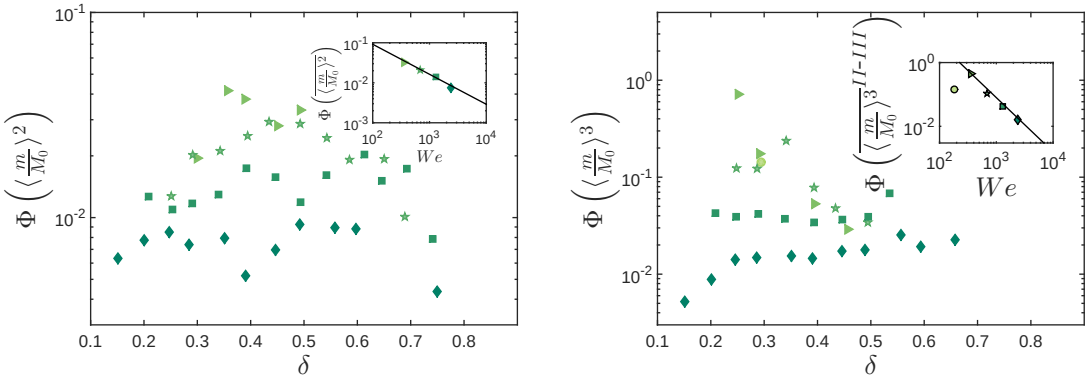


(a) (b)

Figure 6.15: Cut-off $\Phi$ of the mass distribution of ejected droplets, pooled per $We$ and $\delta$ for $\alpha = 0°$: (a) during the retraction of the sheet, and (b) after collapse of the sheet. Symbols correspond to different $We$ = 186 (◯), 367 (▷), 700 (☆), 1340 (□), 2435 (◇). Insets: Dependence to $We$ of the cut-off $\Phi$: (a) after pooling all $\delta$. The solid line is Eq. (6.9). (b) After pooling scenarios II and III. The solid line is Eq. (6.10).

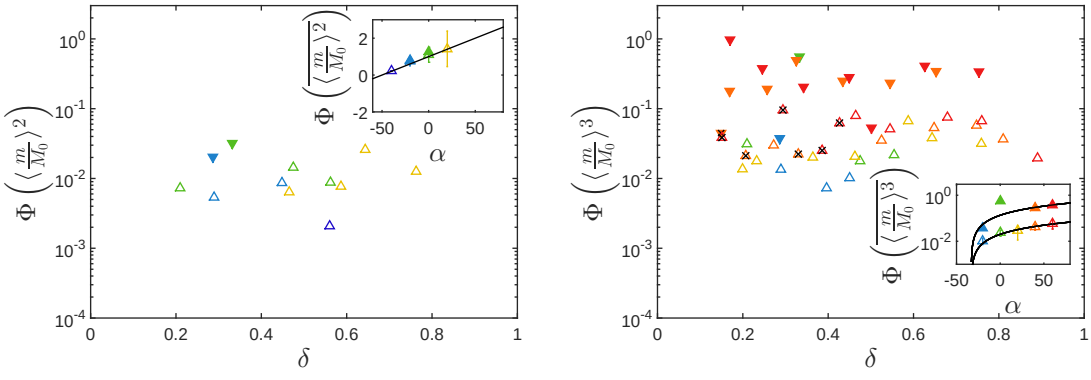


(a) (b)

Figure 6.16: Cut-off $\Phi$ of the mass distribution of ejected droplets, pooled per $We$ and $\delta$ for $\alpha$ values in colour: -20° (blue), 0° (green), 20° (yellow), 40° (orange) and 60° (red). **(a)** During the retraction of the sheet, and **(b)** after collapse of the sheet. Symbols correspond to different $We$ = 500 (▽ - filled), 2600 (△ - empty). Insets: Dependence to $We$ of the cut-off $\Phi$: (a) after pooling all $\delta$. The solid line is Eq. (6.11). (b) After pooling scenarios II and III. The solid line is Eq. (6.12). Symbols with a black cross correspond to a pooling with experiments where some final collapse droplets are missing.

The influence of the inclination on the maximum droplet size shows similar trends as the one found for the horizontal substrate. Indeed, the cut-off values of their PDFs pooled per $We$, $\alpha$ and $\delta$ in Figs. 6.16a and 6.16b confirm the independence of the maximum droplet size with $\delta$ both during retraction and after collapse. Their average value per $\delta$, identified by an overline, indicates a slight increase of the maximum size of the droplets with an increase in $\alpha$ as shown in inset of Figs. 6.16a and 6.16b. This increase is however more pronounced during the retraction than after the collapse and it interestingly follows Eq. (6.9) with a linear dependency in $\alpha$ which yields

$$\Phi\left(\overline{\langle\frac{m}{M_0}\rangle^2}\right) = 2.9\,We^{-3/4}(0.02\alpha + 1). \tag{6.11}$$

After the collapse, the same dependency as for the horizontal case is not recovered. A best fit gave

$$\Phi\left(\overline{\langle\frac{m}{M_0}\rangle^3}\right) = 920\,We^{-7/5}(0.03\alpha + 1). \tag{6.12}$$

This fit in $We$ was however performed on two values only so its validity may have to be confirmed in subsequent experiments. The decrease of the droplet size with increasing $We$ is here less marked than for the horizontal substrate and we chose to pool all droplets per $\delta$ regardless of the scenario.

Datapoints with a black cross highlight cases where some late destabilization droplets are missing. This was assumed not to affect too much the results as these droplets are supposed to be among the largest ejected but also less numerous. A counterbalance of this defect is that all ejected droplets leaving the images are considered as valid droplets. In the present case, this choice results in the detection of bigger droplets since they are not fully fragmented before leaving the field of view. Finally, the method of calculation of $\Phi$ should smooth the presence of outliers. For these reasons, we expect the results to remain valid. A definite conclusion as to the role of the inclination on the final size of the droplet remains however delicate and will require further investigation. The small increase of the droplet size with an increasing $\alpha$ can however find an explanation. For greater inclination, fluid tends to accumulate downwards most likely due to tangential momentum conferred to it upon impact. As a result the thickness of the rim increases (Fig. 5.16) which may result in an increased size of the droplets, the two quantities being related (Bremond & Villermaux, 2006; Villermaux & Bossa, 2011).

The inclination of the substrate thus seems to slightly increase the mass of the droplets while an increase in the $We$ number decreases it. Inclination also increases the asymmetry thus promoting tangential and filament breakup ejections. Positive inclinations generate an additional population of droplets. These droplets are created at an earlier time, for large $\delta$, than what was observed for a horizontal substrate. They are however close to the upper bound of droplet mass [Eq. (6.8)]. We also showed that the speed and mass of the droplets became at first order independent on the offset if the sheet dynamics is accounted for through the time normalization in $\tau_n$. The speed of the droplets also showed an independence in $\alpha$ while the maximum mass during sheet expansion increased with increasing inclination of the substrate (more positive $\alpha$). We will now combine these results of mass and speed to gain insight on the distance travelled by the droplets.

## 6.5 Distance travelled by the droplets

The distance travelled by the droplets is a ballistic computation of the trajectory where we neglect wind effects. The ballistic trajectory $\mathbf{x}(t) = x(t)\mathbf{e}_x + z(t)\mathbf{e}_z$ of each ejected droplet in a vertical plane $(\mathbf{e}_x, \mathbf{e}_z)$ can be computed from Newton's law, as a function of

its mass $m$ and ejection speed $v$:

$$\begin{aligned} m\frac{d^2\mathbf{x}}{dt^2} &= -mg\mathbf{e}_z - 6\pi\mu_a r\frac{d\mathbf{x}}{dt}\left[1+\frac{c}{100}Re^{2/3}\right] \quad \text{for} \quad Re = \frac{2r\rho_a}{\mu_a}\left|\frac{d\mathbf{x}}{dt}\right| < 1000 \\ m\frac{d^2\mathbf{x}}{dt^2} &= -mg\mathbf{e}_z - \frac{3(1+c)}{125}\frac{\pi}{2}\rho_a r^2\frac{d\mathbf{x}}{dt}\left|\frac{d\mathbf{x}}{dt}\right| \quad \text{for} \quad Re > 1000 \end{aligned} \tag{6.13}$$

where $Re$ is the Reynolds number, $r = (3m/4\pi\rho)^{1/3}$ is the droplet radius, g is the acceleration of gravity, $c$ is a fitting parameter, and $\rho_a$ and $\mu_a$ are the density and dynamic viscosity of the air, respectively. In Eq. (6.13), the air drag is calculated with an approximation valid for spherical objects in a large range of Reynolds number [cf. similar models in Clift *et al.* (1978)]. A fit on experimental data from Duan *et al.* (2015) yields $c \simeq 16$. We here consider $\mathbf{e}_x$ as the horizontal direction of ejection, and $x(t)$ is the distance travelled horizontally since ejection, no matter in which direction $\theta_v$ or inclination of the substrate $\alpha$. At the moment of ejection, each droplet departs from $(x_0, z_0) = (0,\ 0)$ with initial velocity

$$(v_x, \quad v_z) = \left(\sqrt{(v_n\cos\alpha)^2 + v_t^2}, \quad -v_n\sin\alpha\right), \tag{6.14}$$

where $v_n$ and $v_t$ are the speed of the ejected droplets in the direction normal and tangential to the edge respectively, in the plane of the substrate (Fig. 6.17). The cosine of $v_n$ is combined to $v_t$ to yield the horizontal component of the initial velocity $v_x = \sqrt{(v_n\cos\alpha)^2 + v_t^2}$. Only the component normal to the edge is projected according to the inclination. The sine of $v_n$ indeed gives the initial vertical speed $v_z = -v_n\sin\alpha$.

Owing to air drag, the horizontal speed decreases with time and $x(t)$ reaches an asymptotic value $\Psi = \lim_{t\to\infty} x$ called the aerodynamic wall (Cohen *et al.*, 2013). As shown in appendix B,

$$\Psi \simeq \frac{2\rho_a r^2 v_x}{9\mu_a}F(\beta), \qquad \beta = \frac{4\rho_a\rho g r^3}{9\mu_a^2} \tag{6.15}$$

The function $F(\beta)$ satisfies $F(0) = 1$ (low Reynolds limit), and it scales as $F \sim \beta^{-1/2}$ for $\beta \gg 1$ (high Reynolds limit). Since $\beta$ is only dependent on droplet size $r$ and not on horizontal speed $v_x$ or inclination of the substrate $\alpha$ (see Fig. B.2 in appendix B), the aerodynamic wall at a distance $\Psi$ is always approximately proportional to $v_x$.

The ratio $v_n/v_t$ is linked to the angle $\theta_v$ that measures the direction of ejection from the impact point. The maximum distance travelled is thus proportional to

$$\Psi \propto v\sqrt{\cos^2\theta_v\sin^2\alpha + \sin^2\theta_v}, \tag{6.16}$$

where $v$ is the ejection speed. On an inclined substrate, the effect of the inclination $\alpha$ and of the ejection angle $\theta_v$ were investigated. The inclination reduces the distance travelled for given mass and initial speed, and it is the horizontal substrate that yields the maximum distance for a given $\theta_v$ (Fig. B.1a in appendix B). This can be deduced from Eq. (6.16) since the square root is here an even function of $\alpha$. However at a given $\alpha$ (significantly different from 0°), the ratio $v_n/v_t$ can affect the distance travelled, especially for large $\theta_v$. Indeed, in the extreme configuration, if $\theta_v$ is 90°, the droplet is ejected tangentially to the edge and as a result, its distance travelled is not affected by the inclination of the substrate. Effects of inclination are thus complex to assess because they also depend on direction of ejection.

For the horizontal substrate, the cut-off $\Phi(\Psi)$ of the statistical distribution of $\Psi$ is calculated by pooling all ejected droplets from different experiments at given $We$ and $\delta$ (Fig. 6.18a). When the offset $\delta$ is in the range of scenarios II and III, $\Phi(\Psi)$ is fairly independent of $\delta$. By contrast, when $\delta$ is in the range of scenario I, $\Phi(\Psi)$ decreases with increasing $\delta$. The similarity of $\Phi(\langle\Psi\rangle)$ [maximum on all droplets] and $\Phi(\langle\Psi\rangle^1)$ [maximum

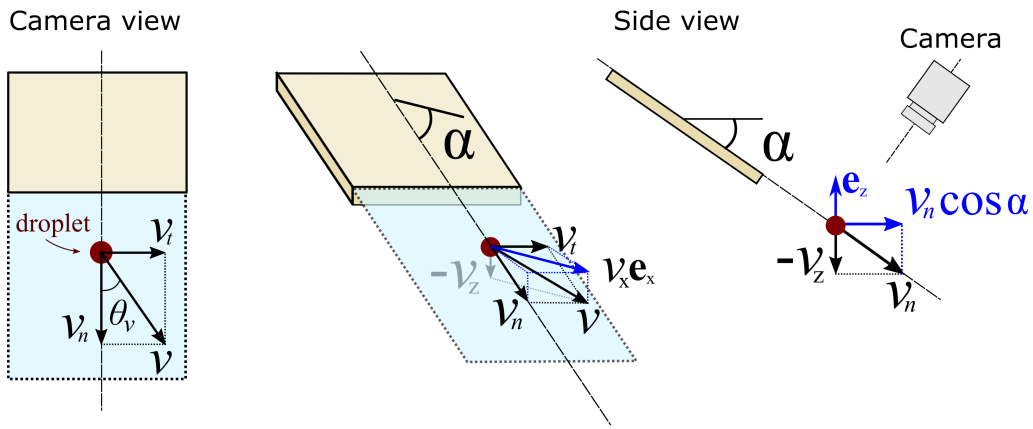


Figure 6.17: Schematic defining projections of the initial droplet velocity.

on droplets ejected during sheet expansion only], illustrated in inset of Fig. 6.18a, suggests that the cut-off distance $\Phi(\Psi)$ is already reached by the droplets ejected during the sheet expansion ($\tau_n < 1$). That is, if any droplets are ejected during this time interval (i.e., for scenarios II and III). Droplets ejected afterwards ($\tau_n > 1$) can travel as far, but not significantly farther. This independence of $\Psi$ to $\delta$ in scenarios II and III can be understood by observing the time evolution of the distance travelled $\Psi(\tau_n)$ (Fig. 6.18b). At $We = 1340$ and small offset $\delta \in [0.2 - 0.3]$, this maximal travelled horizontal distance first increases with time, until a maximum value is reached at $\tau_n \lesssim 1$. Since both the maximal mass and the speed distribution of the ejected droplets are independent of $\delta$ during sheet expansion (Figs. 6.11 - left and 6.13b - inset), the maximum travelled distance $\Psi$ is also independent of $\delta$. With the same $We$ but a larger offset $\delta \in [0.7 - 0.8]$ (which falls in scenario I), droplets are only ejected in $\tau_n > 1$, as already seen in Fig. 6.7. In that time range, the average speed decreases for scenario I (Fig. 6.11 - middle) while the mass is not necessarily larger (Fig 6.15a). As a result, the droplets from scenario I travel much less far.

The upper bound of $\Psi$ illustrated in Fig. 6.18b for $We = 1340$, first increases with time, until a maximum value $\Psi_M$ is reached slightly before $\tau_n = 1$. This maximum $\Psi_M$ during expansion can be fairly predicted from the maximal mass $\Phi(m/M_0)$ given by Eq. (6.7), and the quantile 90% of the ejection speed. During sheet expansion, the speed distribution is approximately Gaussian with mean $v_T$ and standard deviation $0.2\ v_T$ (Fig. 6.11), so this quantile is estimated as

$$Q_{90}\left(\frac{v}{V_0}\right) = \left(1 + 0.2\sqrt{2}\mathrm{erf}^{-1}(0.8)\right)\frac{v_T}{V_0} = 1.26\frac{v_T}{V_0}. \tag{6.17}$$

This temporal upper bound remarkably captures variations of $\Psi(\tau_n)$, including the presence of a maximum $\Psi_M$ for some $\tau_n < 1$. Since both mass and speed bounds are independent of $\delta$ during sheet expansion (Figs. 6.11a - and 6.13b - inset), $\Psi_M$ is also independent of $\delta$. For the range of $We$ considered in this study, $\Psi_M$ is approximately given by

$$\frac{\Psi_M}{R_0} \simeq 23\, We^{2/5}, \tag{6.18}$$

which provides a practical first-order approximation of the distance that ejected droplets can possibly reach from the edge of a horizontal substrate at a given $We$ in the worst case scenario (scenarios II and III).

This upper bound on travelled distance, originally derived from droplets ejected during sheet expansion, seems to hold for droplets ejected when the sheet retracts and collapses. This implies that the sheet early dynamics conditions the maximum distance travelled by the droplets for scenarios II and III independently of the offset.

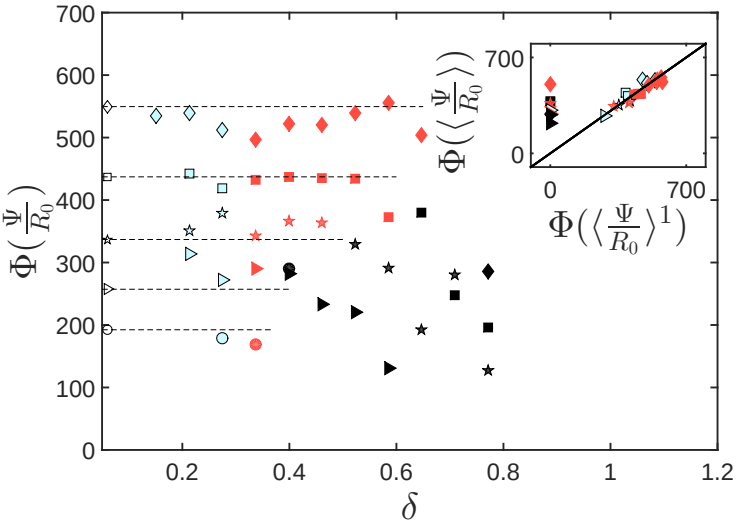


(a)

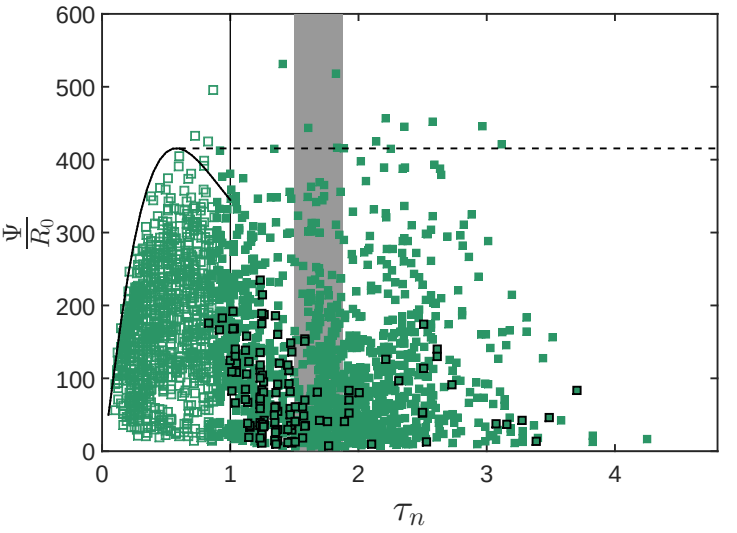


(b)

Figure 6.18: **(a)** Maximum horizontal distance $\Phi(\Psi/R_0)$ travelled by the ejected droplets, pooled together per $We$ and $\delta$ for $\alpha$ = 0°. The dashed lines correspond to Eq. (6.18). Inset: Upper bound $\Phi(\Psi/R_0)$ of the distance $\Psi$ travelled by all the droplets, compared to the same upper bound for droplets ejected during the sheet expansion only. The solid line is the bisector. Symbols are values of $We$ 186 (◯), 367 (▷), 700 (☆), 1340 (□), 2435 (◇) and colours indicate scenario, I (black), II (reddish/grey) and III (blue/clear). **(b)** Horizontal distance $\Psi$ travelled by the ejected droplets as a function of their ejection time $\tau_n$. The Weber number is $We$ = 1340, and the offset is $\delta \in$ [0.2- 0.3] (green symbols) and $\delta \in$ [0.7- 0.8] (black contoured symbols) for $\alpha = 0°$. The solid curve corresponds to the prediction obtained numerically from Eqs. (6.13), (6.7) and (6.17). The vertical solid line indicates the time of maximum of the sheet expansion ($\tau_n$ = 1) and the gray area shows the average collapse time of the sheet ($\tau_n = \tau_r$) plus or minus one standard deviation. The horizontal dashed line indicates the maximum $\Psi_M$.

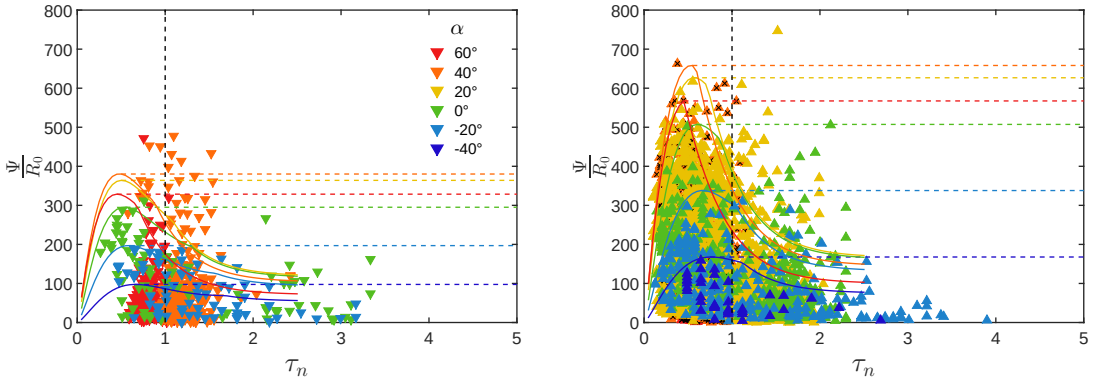


Figure 6.19: Horizontal distance travelled by the droplets as a function of their normalized time of ejection $\tau_n$, for various values of $\alpha$ (in colour, cf. legend in inset) with $\delta \in [0.2 - 0.4]$ with and **(a)** $We = 520$ **(b)** $We = 2000$. Each data point corresponds to a single droplet. The vertical dashed lined is the time of the sheet maximum extension, $\tau_n = 1$. Data with a black cross correspond to experiments where some after-collapse droplets may be missing. The solid curve corresponds to the prediction obtained numerically from Eqs. (6.13), (6.8) and (6.17). The vertical dashed lines indicate the time of maximum of the sheet expansion ($\tau_n = 1$) and the horizontal dashed lines indicates the maximum $\Psi_M$ per $\alpha$ with the corresponding colours.

The time evolution of the travelled distance for various $\alpha$ shows similar behaviours than the ones observed on the horizontal substrate (Fig. 6.19). The distance increases with time until it reaches a peak at around the time of the maximum sheet expansion. The temporal theoretical prediction of the envelope gives a quite accurate estimation of the maximum distance travelled.

The computation was performed using Eq. 6.8 for the mass and Eq. (6.4) for the speed. When computing the distance travelled by the droplets using Eq. (6.13), the measured components of $v_n$ and $v_t$ are used. However, when computing a theoretical distance for $\alpha \neq 0°$ based on theoretical predictions for the bounds of $v$ and $m$, we chose to set the angle $\theta_v$ to 0° (so $v_n = v$ and $v_t = 0$). This ratio yields the maximum distance for $\alpha$ values relatively close to zero. For $\alpha = 60°$, changing $\theta_v$ to 20°, 40° and 60° increases the distance travelled by 8, 25 and 40 percent respectively. The choice to set $\theta_v = 0°$ arise from several considerations. Firstly, we checked that the probability distribution of the ejection direction $\theta_v$ was centered around 0°, and highly peaked (see Fig. B.1b in Appendix B). The average is indeed close to zero with a standard deviation around 20°. Moreover we assumed that the droplets ejected with the highest speed where the one following the natural slope of the substrate (for positively inclined $\alpha$) and inheriting some parallel speed of the initial drop [$V_\parallel = V_0 \sin\alpha$, cf. Fig. 5.4a]. These droplets should therefore have a small $\theta_v$. Finally, it was shown for the horizontal substrate that the peak in distance was reached around the time of maximum extension which corresponds to radially ejected droplets or tangentially ejected ones. Yet as $\alpha$ increases, the sheet is more stretched which reduces the range of $\theta_v$ available for radially ejected droplets. Finally, the main characteristics of tangentially ejected droplets is their tendency to be ejected in the main direction of the stretching liquid sheet. For all these reasons, we chose to set $\theta_v$ to 0°. Equation (6.8) was used for the mass as it explicitly shows the dependency in $\alpha$ that will influence the distance travelled. The overall consequence of the inclination is to increase in a certain range the maximum distance travelled by the droplets as shown in Fig. 6.20. The relative independence in $\delta$ (except for large $\delta$) is also recovered while the dependency $We$ appears similar to the one observed for the horizontal substrate. The dependency in $\alpha$ given by the theory predicts relatively well the experimental values as seen in both Figs. 6.20 and in Fig. 6.21 which

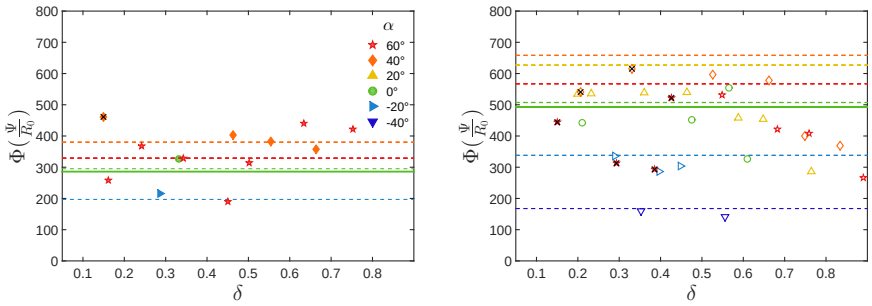


(a) (b)

Figure 6.20: Maximum horizontal distance $\Phi\,(\Psi/R_0)$é reached by the droplets as a function of $\delta$ pooled per $\alpha$ in colour (cf. legend in inset) for (a) $We = 500$ and (b) $We = 2000$. The dashed lines correspond to the maximum theoretical distance computed using Eqs. (6.13), (6.17) and (6.8). The solid lines are Eq. (6.18)

shows the average value of $\Psi(\Phi)$ per $\alpha$ for scenarios II and III. Figure 6.21 particularly shows that the increase of the maximum distance presents an optimum visible at $\alpha = 40°$ as seen in Fig. 6.21. Moreover, this optimum is also predicted by our computation.

This increase in the maximum distance observed with small positive inclinations of the substrate ($\alpha$ more positive) is at first counter intuitive as the optimum angle at given mass and speed was shown to be $\alpha = 0°$. However we showed that an increase in $\alpha$ increases droplet mass while its speed approximately remains the same. By enhancing the asymmetry, the inclination also enhances the number of tangential droplets which are shown to be the furthest travelling ones. This increase in asymmetry however, through the increase of the mass can thus at first counterbalance the decrease in distance due to the inclination and may explain the presence of an optimum in $\alpha = 40°$ (Fig. 6.21). Several other effects can also intervene in this distance optimisation and notably a variation of the $\theta_v$ ratio. However, our prediction slightly overpredicts the maximum distance for the largest $We$ number while the general influence of $\alpha$ is well captured although we neglected variations of $\theta_v$ by setting it to 0°. The presence of the optimum is thus more likely to be related to other factors. Another possibility for the presence of this optimum is that a larger inclination of the substrate induces an earlier filament breakup. This reduces the time available for tangential droplets to be ejected and so their number. The filament breakup droplets, although very numerous are indeed quite small and thus do not participate in the maximum distance travelled as far as there is not any additional wind. This competition between the occurrence of the tangential mechanism versus filament breakup thus may create optimal situations where the asymmetry is sufficient enough to promote tangentially ejected droplets without the filament breakup inhibiting their formation. This needs however to be considered carefully as the experiments in the concerned range and notably for $\alpha = 60°$ and $We = 2000$ were also the ones where part of the late sheet destabilization occurred out of the field of view as already mentioned. The optimum is however observed for both $We$ which indicates a certain level of robustness.

## 6.6 Global effects of the sheet asymmetry

The previous section showed that there is an optimum inclination angle around $\alpha = 40°$ for which the distance travelled by the ejected droplets is maximal. This optimum results from a complex interplay between ballistics (that would predict an optimum in $\alpha = 0°$) and distributions of droplet speed and mass. It also showed that the maximum distance travelled by the ejected droplets is fairly insensitive to the sheet asymmetry originating from the offset $\delta$ (Figs. 6.18a and 6.20). However, this asymmetry still greatly influences

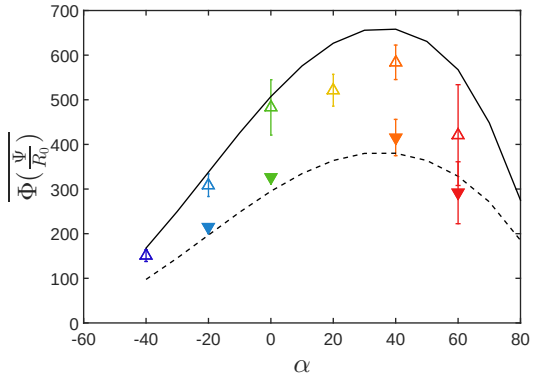


Figure 6.21: Maximum horizontal distance $\Phi(\Psi/R_0)$ averaged over $\delta$ reached by the droplets as a function of $\alpha$ for $We = 500$ ($\triangledown$) and $We = 2000$ ($\triangle$). Solid and dashed lines are the theoretical values computed based on Eqs. (6.13), (6.17) and (6.8).

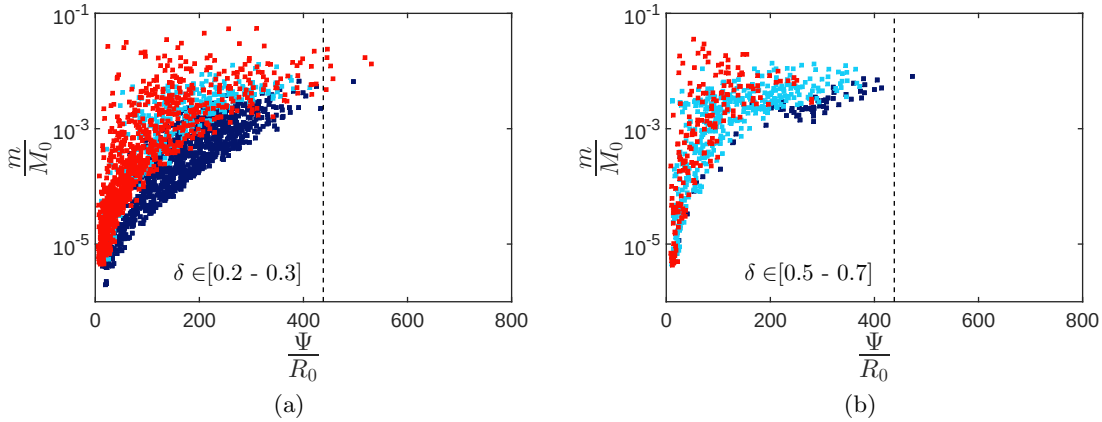


Figure 6.22: Mass $m$ of the ejected droplets, normalized by the mass of the impacting drop, as a function of their travelled distance $\Psi$ for $We = 1340$ ($\square$) and $\alpha = 0°$. (a) $\delta \in [0.2 - 0.3]$. (b) $\delta \in [0.5 - 0.7]$. The colour indicates the ejection time: during sheet expansion ($\tau_n < 1$, dark blue), during sheet retraction ($1 < \tau_n < \tau_r$, light blue) and after sheet collapse ($\tau_n > \tau_r$, red). The vertical dotted lines represent Eq. (6.18).

the dispersal ability. For example, the mass of droplets ejected at a given distance $\Psi$ (usually during sheet retraction and collapse) can be 10 times larger than the mass of droplets ejected during the sheet expansion, provided that the offset is sufficiently small. This is illustrated for the horizontal substrate in the $(m/M_0, \Psi)$ diagrams of Figs. 6.22a and 6.22b for two different ranges of $\delta$. Tangentially-ejected droplets are often among these outperforming droplets, since they inherit from a mass similar to the radially-ejected droplets, with a possibly larger speed. Figure 6.22a also displays a large number of small droplets ejected during the collapse phase which correspond to the droplets ejected by the filament breakup mechanism.

The diagrams for various inclinations also show that larger droplets are ejected during the retraction for small $\delta$ (Figs.6.23 a-d). This effect is however counterbalanced in part by the earlier occurrence of the filament breakup, which generates many smaller droplets and reduces the number of tangentially ejected droplets. Indeed in Figs. 6.23b and 6.23d the collapse occurs before the sheet maximum extension which explains the absence of retraction droplets.

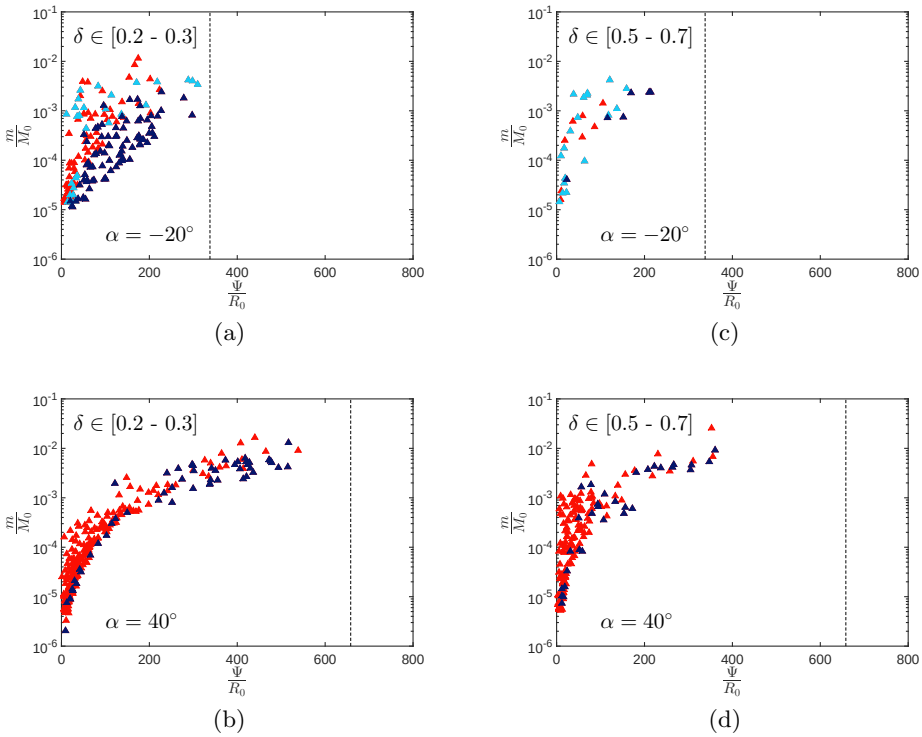


Figure 6.23: Mass $m$ of the ejected droplets, normalized by the mass of the impacting drop, as a function of their travelled distance $\Psi$ for $We$ = 2000. Two offset intervals $\delta$ are considered, $\delta \in [0.2 - 0.3]$ in (a - b) and $\delta \in [0.5 - 0.7]$ in (c - d). (a and b) $\alpha$ = -20°, (c and d) $\alpha = 40°$. The colour indicates the ejection time: during sheet expansion ($\tau_n < 1$, dark blue), during sheet retraction ($1 < \tau_n < \tau_r$, light blue) and after sheet collapse ($\tau_n > \tau_r$, red). The vertical dotted lines represent the maximum distance travelled computed using Eqs. (6.13), (6.17) and (6.8).

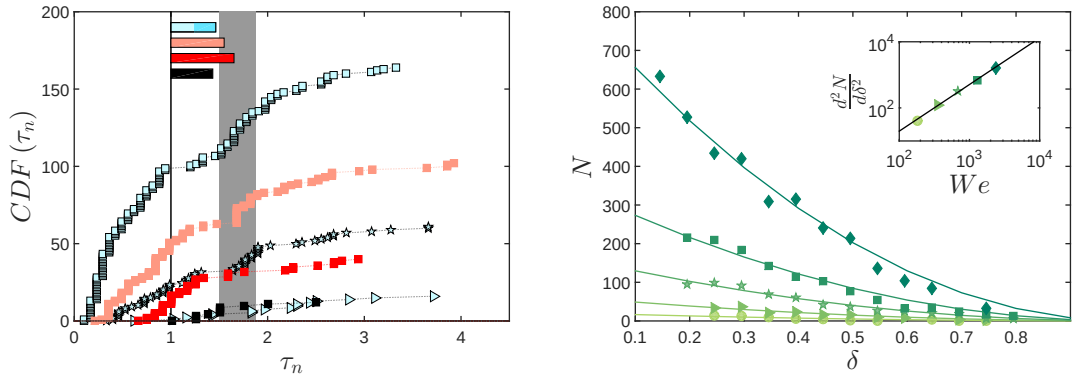


(a) (b)

Figure 6.24: (a) Non-normalized Cumulative Distribution Function (CDF, expressed in number of ejected droplets) of the normalized time $\tau_n$ for the six examples of Figs. 4.3 and 4.4. Symbols correspond to Weber number, $We = 367$ (▷), 700 (☆), 1340 (□), while colours indicate scenario, I (black), II (reddish/grey) and III (blue/clear). The substrate is horizontal ($\alpha = 0°$). The grey area indicates the time $\tau_r$ at which the sheet has fully retracted from the edge (average across $We$ and $\delta$, plus/minus standard deviation). (b) Average number $N$ of droplets ejected per impact, as a function of $\delta$, $\alpha = 0°$. Symbols correspond to $We = 186$ (◯), 367 (▷), 700 (☆), 1340 (□), 2435 (◇). Solid lines are Eq. (6.19). (Inset) Second derivative of $N$ with respect to $\delta$, as a function of $We$. The solid line corresponds to $d^2N/d\delta^2 = 0.03\,We^{1.4}$ in Eq. (6.19).

### Number of droplets

In terms of number of droplets, the Cumulative Distribution Function (CDF) of the normalized time $\tau_n$ at which droplets are ejected, i.e., the number of droplets ejected before a given $\tau_n$, is represented in Fig. 6.24a for the 6 examples of Figs. 4.3 and 4.4 ($\alpha = 0°$). The number of droplets increases with $We$ and decreases with increasing $\delta$. For all scenarios, the ejection rate (slope of the CDF) remains steady during sheet extension, then it strongly decreases during retraction. In scenarios II and III, there is an additional outburst of droplets at the moment of collapse $\tau_r$, which corresponds to the filament breakup mechanism. The ejection rate decreases again for larger $\tau_n$. For scenarios II and III, the first ejections occur during the expansion of the sheet. Conversely, in the isotropic scenario (I), ejections only start during the retraction of the sheet.

For the horizontal substrate, the average number $N$ of ejected droplets per impact is represented in Fig. 6.24b, where data from all experiments have been pooled by $We$ and $\delta$. This number of droplets increases with $We$, and it decreases almost quadratically with increasing offset $\delta$. This number also vanishes in $\delta = 1$, which corresponds to a vanishing liquid sheet [Eq. (5.27)]. As confirmed in Fig. 6.24b, it can be approximated by

$$N = 0.03\,We^{1.4}(1-\delta)^2. \tag{6.19}$$

The increase of number of droplets with the decrease of $\delta$ could originate from three main causes: as $\delta$ decrease, (i) more fluid crosses the edge, (ii) the filament breakup mechanism occurs which is responsible for a high number of small droplets and, (iii) the shedding of droplets begins earlier.

Similar trends in the number of droplets are observed when the inclination of the substrate is varied. Equation (6.19) falls relatively well on the experimental data for $\alpha = 0°$ in Figs. 6.25a and 6.25b where droplets are pooled per $\delta$, $\alpha$ and $We$. We observe an ordering of the data in $\alpha$ where negatively inclined substrates generate a reduced number of droplets. Positively inclined substrates, however, show first an increased number with

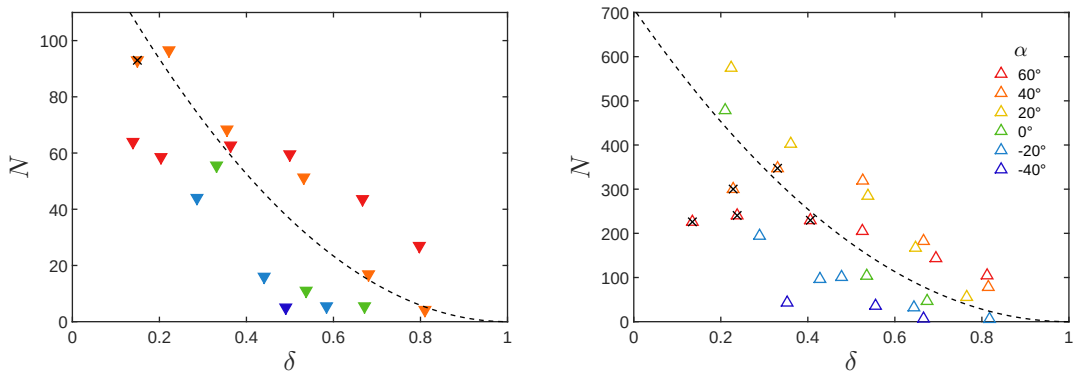


(a) (b)

Figure 6.25: Average number $N$ of droplets ejected per impact, as a function of $\delta$ for various inclination ($\alpha$ in colour, cf. legend in inset) with (a) $We = 520$ and (b) $We = 2000$. Dashed lines are Eq. (6.19). Crossed datapoints indicate pooling in which, experiments where the final destabilization occurred outside the field of view, may be present.

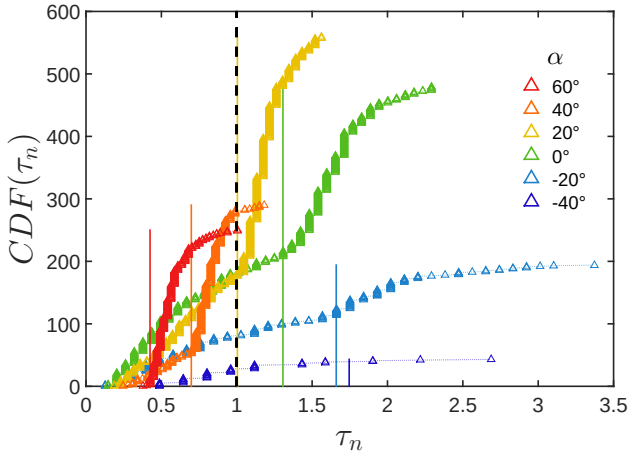


Figure 6.26: Non-normalized Cumulative Distribution Function (CDF, expressed in number of ejected droplets) of the normalized time $\tau_n$ for six experiments with $\alpha$ in colour (cf. legend in inset) and $\delta \in [0.2 - 0.4]$, $We = 2000$. The dashed black line corresponds to $\tau_n = 1$ and the coloured lines to $\tau_n = \tau_r$.

decreasing $\delta$ but a saturation is observed for small values of $\delta$, particularly for the largest values of $\alpha$. This saturation seems counter-intuitive with the general principle of increased asymmetry leading to more numerous droplets. This can result from several factors. The first is that there may be some droplets missing for the black crossed datapoints since the final destabilization may have occurred outside the field of view of the camera. The filament breakup was however visible in these experiments which is the primary source of droplets in the small offset regimes. Moreover the decrease is visible for the highest $\alpha$ in the lower $We$ value (Fig. 6.25a) where no droplet is missing. Another possible explanation could be linked to the increased thickness of the rim with $\alpha$, observed experimentally in Fig. 5.16 (chapter 5). If the rim is thicker, the sheet corrugations and ligaments will also tend to be bigger and so will the droplets. Finally, in the case of scenario II, the whole sheet breaks up all at once in a filament, which generates most of the droplets. In this case, for large $\alpha$, the sheet is quite stretched and the length of the filament is consequent which may explain the increase in the number of droplets with increasing $\alpha$ and decreasing $\delta$. For scenario III and large $\alpha$ however, when the filament breakup occurs, part of the sheet is still advancing. The length of the filament is thus reduced. In addition to that, the remains of the sheet keeps moving away from the edge. This generates a less violent final collapse which may explain a reduced number of droplets. The CDF of the normalized time for different $\alpha$ in Fig. 6.26 confirms the maximum number of droplets for $\alpha = 20°$. The ejections before $\tau_n = 1$ are visible for the various inclinations as a relatively constant slope with a sudden increase in the slope when $\tau_n = \tau_r$. The constant slope however is visible neither for the highest inclination which seems to consist solely of a filament breakup mechanism nor for the lowest $\alpha$ which corresponds to a scenario I experiment. These observations confirm the tendency of the inclination to increase the asymmetry of the sheet but they also show how the various mechanisms of ejections thus subsequently enter in competition. This leads to interesting trade-offs that influence both the mass, speed, distance travelled as well as number of ejected droplets.

# Chapter 7

# Conclusions

Raindrops can impact on plant leaves in many different configurations and subsequently fragment into droplets. Some of these configurations are particularly efficient at ejecting droplets far away. They are consequently of primary relevance for the dispersal of pathogens initially present on infected leaves. A common feature observed in most impact configurations is the formation and break-up of an asymmetric liquid sheet, connected to the substrate on one side, and delimited by a rim entirely in the air on the other side. In this work, we investigated the impact of a drop at speed $V_0$ next to the straight edge of a flat substrate. A similar sheet is formed and fragmented, but the kinematics is much easier to visualise and quantify since both the sheet and the ejected droplets move approximately in the plane of the substrate. We have varied three main parameters: the Weber number $We$, the distance from the impact point to the substrate edge (offset $d$) and the inclination of the substrate $\alpha$.

The Weber number has been varied in a range similar to that of raindrops. Changing the offset allowed to investigate the various levels of asymmetry of the liquid sheet. It was varied over the range in which the subsequent liquid sheet approximately remained in the plane of the substrate. We also varied the inclination of the substrate to get insights into impacts not only on inclined rigid leaves but also on compliant substrates. Leaves will often deform and move under the impact of a drop. When a leaf moves in reaction to the impact of a drop, the resulting liquid sheet is stretched more because the edge from which it originates moves downwards in the vicinity of the impact point. When a drop impacts on an inclined substrate, an additional tangential speed is conferred to the liquid upon impact, which can be considered as the analogue of a downward motion of the sheet edge when the leaf is deflected. Leaves are moreover seldom horizontally oriented, which fully justifies our choice of investigating the influence of substrate inclination. Both positively and negatively inclined substrates have been investigated. From video recordings, we have systematically tracked and quantified the motion of both the sheet and the ejected droplets.

The temporal evolution of the spreading on the substrate is axisymmetric on horizontal substrate and solely depends on the impact speed. We investigated the spreading phase to derive both maximum spreading radius $R_{sM}$ as well as the time $t_d$ spent by the liquid on the solid before reaching the edge. These two quantities are sufficient to characterize the history of the liquid on the solid, relevant for the study of the subsequent liquid sheet in the air. Doing so, we relied on existing literature and used simplified scaling laws (Eggers *et al.*, 2010; Laan *et al.*, 2014). Inclining the substrate deforms the spreading into an ellipsoidal shape which focus corresponds to the impact point. This observation had been experimentally evidenced in the context of splat formation (Kang & Ng, 2006) but not in this context of drop impacts. The temporal evolution of this ellipse was shown to be described by a superposition of translated circles similarly to what was shown by Almohammadi & Amirfazli (2017b) for impacts on horizontally translated substrates. We however connected the translation motion to the inclination of the substrate, derived ex-

pressions related to the maximum extension for hydrophilic substrates and explained the origin of the ellipse focus at the impact point. These steps were essential for the subsequent understanding of the liquid sheet kinematics in the air which derives from its history on the solid substrate.

The sheet kinematics in the air was decoupled between its components normal and tangential to the edge. The evolution of the sheet in the direction normal to the edge is approximately symmetric in time for the horizontal substrate while it becomes asymmetric when the substrate is inclined. In both cases, it is advantageously described by measuring the time from its birth, at the instant $t_d$ at which the liquid takes-off from the substrate. The duration of the sheet extension $t_{nM} - t_d$ is then approximately proportional to the capillary time $t_c$ [Eq. (5.29)], with a first corrective factor that mostly depends on the ratio $\delta$ between the offset $d$ and the maximum spreading distance on the solid, measured normal to the edge $R_{snM}$. The sheet kinematics is first analysed on horizontal substrate then it is generalized to inclined substrates. The generalization usually only involves a corrective factor of the form $(1 + \sin\alpha)/\sqrt{\cos\alpha}$ and $\delta$, which explicitly depends on $\alpha$ through its normalization by $R_{snM}$. This dependency vanishes on horizontal substrate where $R_{snM} = R_{sM}$.

This generalization is valid for the time $t_{nM}-t_d$ of the sheet maximum extension despite the fact that the temporal evolution cannot be considered symmetric in time anymore for $\alpha \neq 0°$. This time $t_{nM} - t_d$ also occurs later for smaller offsets, an effect which we believe is linked to the amount of liquid in the air. The increase of the inclination also increased the amount of fluid in the air and so increases $t_{nM} - t_d$ even further.

The maximum extension $l_{nM}$ of the sheet normal to the edge is approximately proportional to $R_0We^{1/2}$, so to $V_0t_c$ [Eq. (5.28)], with again a corrective factor to take the initial spreading on solid into account. This latter is linearly decreasing with $\delta$. For the inclined substrate, the correction factor $(1+\sin\alpha)/\sqrt{\cos\alpha}$ multiplies this dependency, showing that an increased inclination leads to an even greater extension of the liquid sheet normal to the edge. Remarkably, the corresponding acceleration, which then scales as $V_0/t_c$, is constant in time and does not depend on $\delta$ anymore. It still however increases with the inclination of the substrate. We have also shown that, against intuition, the sheet can extend farther from the substrate when a drop impacts at a distance $d$ from a flat edge than when it impacts at the centre of a pole of radius $d$, in the horizontal configuration.

The evolution of the sheet along the edge is not symmetric in time in any configuration. Its extension follows the adjacent spreading on the substrate, while its retraction involves some dewetting of the edge. The important scatter of the corresponding data suggests the presence of uncontrolled contact line pinning during this retraction phase.

We identified four scenarios, that correspond to characteristic shapes of the sheet. The boundaries between these scenarios can be rationalised by considering the competition of sheet kinematics in directions normal and tangent to the edge. The asymmetry of the sheet shape strongly depends on $\delta$, with an additional dependency on the inclination angle $\alpha$ for the inclined case.

Ejected droplets were characterised statistically in terms of number, mass, speed, direction and time of ejection. The ejection statistics is strongly time-dependent, and it also varies with $d$, $\alpha$ and $We$. Nevertheless, most of the dependence to both $d$ and $\alpha$ is removed when the rescaled ejection time $\tau_n$ (ejection time normalised by the time of maximal extension of the sheet) is considered. This is especially true during the sheet expansion, where droplets are mostly ejected radially starting from a time that increases with $d$ and $\alpha$. Droplets ejected at the same $\tau_n$ have approximately the same speed, which decreases as $\tau_n$ increases. Their mass distribution is more scattered, but it is bounded by a maximal ejectable mass that is an increasing function of $\tau_n$ and $(1 + \sin\alpha)/\sqrt{\cos\alpha}$ only.

When the sheet retracts and collapses, both speed and mass distributions spread con-

siderably for the two most asymmetrical sheet scenarios. This is partly due to the additional ejection of droplets in a direction parallel to the sheet and normal to its retraction. This mechanism generates droplets of mass similar to that of radially ejected ones but with a greater speed. In the most asymmetrical cases (small $d$), the final collapse of the sheet near to the edge triggers the out-of-plane ejection of a large number of tiny droplets. In the configuration of positively inclined substrates, an additional ejection mechanism is observed which we believe linked to the fingering observed on the substrate. This mechanism generates early ejected droplets even for large $\delta$ values.

We could then estimate the maximum horizontal distance that each ejected droplet would travel ballistically, as a function of its mass and ejection speed. The upper bound of this distance is independent of $\delta$ for the two most asymmetric scenarios. It can be predicted by considering the speed and maximum mass of droplets ejected during the sheet expansion. Droplets ejected during the retraction and collapse of the sheet can go as far but not significantly farther. However, for the same travelled distance, their mass can be larger. Inclining the substrate should theoretically reduce the distance travelled by the droplet. However, inclining the substrate increases the mass of the droplets and promotes the occurrence (up to a certain point) of the tangentially ejected droplets. These droplets are usually faster. In consequence, the maximum distance travelled by the droplets present an optimum in inclination angle which results from a competition between a reduced distance travelled but an increase of mass and speed linked to the enhanced asymmetry of the sheet, both due to the inclination of the substrate.

These results can be discussed in the context of the rain-induced dispersal of foliar pathogens. From an epidemiology point of view, each droplet ejected from an infected leaf is susceptible to carry some pathogenic content. The number, mass and ejection speed of these droplets are key inputs for the epidemiological models based on droplet ballistics (Saint-Jean *et al.*, 2004; Robert *et al.*, 2008; Gigot *et al.*, 2014; Vidal *et al.*, 2017). The likelihood of infection certainly grows with each of these factors. Our experiments at $We \in [180, 2400]$ covered most of the range of Weber number experienced by raindrops ($We \in [28, 5800]$). We also covered a range of inclination of the substrate from -40° to 60° which should help quantify the effect of leaf inclination and compliance. We may therefore expect that our conclusions on the impact near a flat edge are still valid, at least qualitatively, for more complex impact scenarios encountered by raindrops on leaves. In particular, the number, the speed of the ejected droplets and their maximal travelled distance all increase with increasing $We$ but at the same time, the maximal droplet mass decreases. The asymmetry of the sheet, here measured with $\delta$ and omnipresent in complex natural impacts, does not seem to increase the maximum distance travelled by the droplets but it does increase their number and maximal mass at a given distance. It should consequently increase the likelihood that a droplet containing a critical amount of pathogens lands on a distant leaf, and so increases the overall dispersal speed of the disease. The inclination has various effects on the mass, speed and distance travelled which resulted in an optimum for a downward inclination $\alpha = 40°$. Such information confirms once more the importance to take into account the plant architecture, leaf inclination and the physics of the fragmentation process.

Current mitigation techniques of foliar diseases, such as the intensive use of chemicals or genetically modified organisms cannot be solely relied upon on the long term (Strange & Scott, 2005; Newton *et al.*, 2010; Chakraborty & Newton, 2011; Pangga *et al.*, 2011; Derksen *et al.*, 2012; Enserink *et al.*, 2013; Sherman & Gent, 2014; Jorgensen *et al.*, 2017). Some complementary approaches include polyculture (Wolfe, 2000; Gigot *et al.*, 2013; Vidal *et al.*, 2017) or integrated culture (Newton *et al.*, 2010). The risk of epidemics is a major factor to take into account in the optimisation of such crops (Vidal *et al.*, 2017). Our work has showed how $We$, $\delta$ and $\alpha$ shape the statistics of ejected droplets upon raindrop impacts, and the subsequent risk of epidemics. Our results will hopefully be implemented

in future ballistic-based epidemiological models and help improve their robustness and predictive power.

# Chapter 8

# Future work

This work is, to our knowledge, a first investigation of the impact of a drop in the vicinity of a straight edge. We investigated both sheet kinematics and droplet shedding. We derived scaling laws based on the entry parameters that capture the main features observed. If the general qualitative and part of the quantitative behaviour of these asymmetric liquid sheets have been investigated, a lot remains to be done to fully comprehend them. As the analysis of the dataset progressed, new elements revealed their importance. In the following, possible improvements, suggestions concerning next steps and discussion concerning the possibilities opened by this work are discussed.

## 8.1 Going further with this experimental configuration

### Robustness

The number of experiments per $We$ and offset was significantly higher for the horizontal substrate dataset than for the inclined one. Robustness of the results may be improved for the inclined case by collecting additional experiments in order to compute the statistical result on greater sample sizes. The range of inclination could also be extended, particularly on the negatively inclined angles ($\alpha < 0°$) as well as the number of values for the $We$ number.
As mentioned in section 6.3, for high $We$ and $\alpha$ values, the final motion and fragmentation of the sheet occurred outside the field of view due to experimental limitations. We discussed the possible effects of such issue and concluded that its effects should be, at first order negligible, but a validation through experimental measurements would still be welcome.
The number of ejected droplets varies greatly with both $We$ and offset (cf. section 6.6). The robustness of the statistical results of some datapoints on droplets might benefit from taking additional data, especially for low $We$ and large offsets. In our datasets, we indeed aimed to uniformly distribute the number of datapoints taken on the Weber-offset diagram. Post-analysis consideration shows that a greater number of datapoints should be taken in the range that are less efficient at emitting droplets.

### Additional result analysis

In complex configurations such as the impact of a drop near the edge of a substrate, choices are made concerning the analysis performed. We here focused on kinematics parameters such as maximum extension normal and tangential to the edge. The most straightforward analysis to be continued may be the retraction behaviour along the edge and the comparison with the retraction normal to the edge. In this work, we did not pursue this line of research as the results showed strong scatter of the data, which even appeared stochastic depending on the edge local state and positions of the corrugations

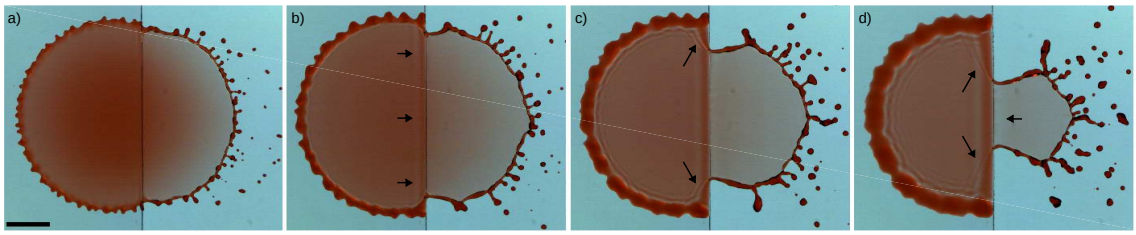


Figure 8.1: Impact of a drop on a flat horizontal plexiglass substrate with $d/R_0 = 1.21$ and $We \sim 700$. Times are, from left to right, 4.2, 6.4, 8.6 and 10.8 ms from impact. Scale bar is 5 mm. Arrows in panel b) point out the uniform rim on solid along the edge that forms after the liquid has reached its maximum expansion. Oblique arrows in panels c) and d) indicate a travelling wave on solid that moves along the edge and follows the retraction of the liquid sheet in the air. The horizontal arrow in panel d) points out the depigmentation of the liquid sheet along the edge, indicating its thinning at this location.

and ligaments (see section 5.4). Knowing this issue, it may be possible to derive scaling laws using large sample sizes and by paying a particular attention to the edge roughness.

We did measure the temporal evolution of the retraction along the edge as well as its mean value in an attempt to investigate the thickness profile of the liquid sheet along the edge. The results were too scattered to obtain robust results so they were not included in this manuscript. The behaviour of the liquid in the vicinity of the edge remains nevertheless intriguing. In particular, the question of the transfer of liquid from solid to the air, after the maximum expansion on the solid is reached, remains open. Indeed, once the liquid on the solid reaches its maximum expansion, a rim grows on the solid away from the edge. A smaller but uniform rim also grows along the edge [Fig. 8.1 - b]. This may suggest that liquid transfer from solid to the air stops at this moment but we do not possess quantitative evidence of such behaviour. A travelling wave along the edge, on the solid, highlighted in panels c) and d) of Fig. 8.1, also follows the retraction of the liquid sheet in the air along the edge. This may on the contrary indicate communication between solid and air. Finally, on some experiments such as illustrated in Fig. 8.1 - d), a clear depigmentation of the liquid sheet along the edge with time is visible, suggesting thinning of the sheet thickness.

From the droplets point of view, we chose to report the norm of the ejection speed (section 6.3) but the decomposition of this value in normal and tangential components is available and may also be relevant for a better characterization of spatial distributions. We also noticed that some spatial areas did not receive any droplet in some $We$, offset and inclination configurations. The characterization of such depleted zones from both a qualitative and quantitative point of view may be of interest for disease spreading modelling. Another aspect that was not discussed in this work is the out of plane ejection of droplets observed upon filament breakup (Fig. 4.2 - h side view) as well as the vertical motion of the droplets in general. Relating droplet motion in our configuration to vertical motion in field is of importance for the upward propagation of diseases and is an aspect that should be investigated in priority. Finally, deriving general distribution laws describing the probability distribution function of the overall droplet mass, speed and direction of ejection would be relevant for further use in the ballistic-based disease propagation models.

### Theoretical considerations

Most results are here described by empirical relations. It would be interesting to investigate more the theoretical point of view and justify the observed scaling laws from first-principle arguments. Spring mass systems to describe the expansion and retraction of the liquid sheet normal to the edge gave some preliminary good results for the hori-

zontal substrate (section 5.3). As mentioned in the section above, there might also be a relation to be found between the retraction behaviour along the edge and the thickness of the liquid sheet, although the latter will first have to be measured. Techniques relying on light absorption for example may be used in that endeavour. We also derived first order scaling laws to describe the kinematics of the sheet and droplets on inclined substrates and used a single parameter depending on $\alpha$ to account for the inclination. It is however likely that the various relationships of the kinematics of the liquid sheet actually involve a combination of the perpendicular and parallel impact speed ($V_\perp$ and $V_\parallel$, defined in Fig. 5.4a). Explicit dependencies and contributions of each components might be derived.

Several ejection mechanisms with characteristic mass, speed and number of ejected droplets were identified, that varied with both offset, $We$ and $\alpha$. The physical mechanisms behind these properties are in our opinion a key element to be investigated further. In particular, the physics explaining the increased delay before the apparition of the first droplets as offset increased (section 6.2) was a problem which we turned around without solving. It should however be possible to relate it to some characteristic length scale of the liquid sheet, such as the thickness, and characteristic local deceleration. The temporal dependency on the upper bound of the droplet mass may also be a clue towards a better understanding of the droplet size and time of ejection (section 6.4).

### Additional phenomena

Through the investigation of the impact of a drop near an edge, we observed a few additional phenomenona such as the deflection of the liquid sheet from the substrate plane, for impacts at a very short distance from the substrate edge (see section 3.3). We have shown that there was a threshold in offset beyond which the sheet deflection from the substrate plane increases linearly in the horizontal case. We did not have time to develop a theoretical model regarding this phenomenon but we believe the endeavour however feasible. A similar behaviour was suggested by our data for the inclined substrate. Taking a full dataset to investigate the effect of the inclination would allow to confirm if the linear decrease observed on the horizontal substrate is recovered. It would also indicate if the inclination $\alpha$ of the substrate modifies the slope of the decrease, the threshold of the plateau or even both. Such information may offer insights for a comprehensive theoretical model.

Specific effects linked to the inclination of the substrate were also noticed. When a drop impacts on an infinite substrate that is positively inclined, liquid accumulates in the downward direction forming streaks as reported by Adam (2012) and illustrated in Fig. 4.8b. This phenomenon leads to ejection of large droplets when the accumulated fluid goes beyond the edge, as reported in chapter 4 (Fig. 4.8a). Analysis of offset, drop size, impact speed and inclination limits that lead to such ejections as well as the characteristics of the latter could be of interest for more than pathogen spreading applications.

Another observation reported in the same chapter is linked to the entrapped bubble that appears when drops impact on solid substrates. For sufficiently large inclination and small offsets, this bubble was entrained with the fluid and moved with it, an observation which we have not yet seen reported in the literature.

Finally, an additional ejection mechanism observed solely for positively inclined substrate was also identified (chapter 6). We attributed it to the increased fingering of the spreading liquid.

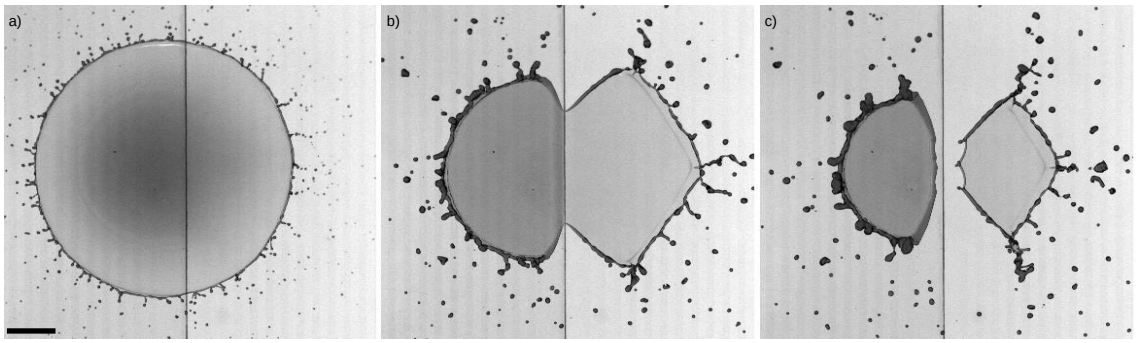


Figure 8.2: Impact of a drop on a flat horizontal substrate with $d/R_0 = 1.3$ and a substrate with superhydrophobic coating (wheel protectant from ArmorAll Inc., contact angle ~ 165±2°). Times are, from left to right, 2.6, 7.4 and 8.7 ms from impact. Scale bar is 5 mm. $We$ ~ 1300.

## 8.2 Variations around the edge configuration

### Additional parameters

From a more general perspective, wettability and roughness of the substrate are in our sense two of the major parameters to be investigated next in this problem. Plants indeed present a large spectrum of wetting properties although these go usually from slightly hydrophilic to superhydrophobic (Gilet & Bourouiba, 2014) and display many textures, from smooth and waxy to rough and furry. Such characteristics may also be affected by leaf age and health state. Understanding the effects of wettability is primordial. For example, drop impacts on superhydrophobic surfaces are known to exhibit in some cases partial or total rebounds (cf. chapter 2). We can indeed expect to see changes in the retraction dynamics of the liquid sheet if the rebound time of the drop (the time the drop spends in contact with the surface) is comparable to the time $t_{nM}$ of the sheet maximum extension, for example. I performed a few experiments on superhydrophobic substrates, using superhydrophobic coated surfaces (Fig. 8.2). The splashing threshold on superhydrophobic substrates is reached for lower impact speed and ejection on the solid side are visible in Fig. 8.2, which might make more complex the analysis of the phenomenon. The coating was also quickly damaged by the impacts, which is an experimental issue that may be dealt with using front lighting and pure Teflon substrates, for example, or by silanization of the substrate.

A change in the wettability of the substrate is also very likely to affect the retraction dynamics on inclined substrates. In our configuration, the substrate was slightly hydrophilic and dewetting occurred on a much longer timescale than the spreading. The time superposition of the maximum intensity of the images during expansion and retraction thus lead to an elliptical shape (Fig. 4.6). If the substrate is hydrophobic, we can expect the dewetting to occur on a shorter timescale than the spreading and the time superposition would likely lead to a half-ellipse shape. Such behaviour would however require quantification through additional experiments and it might modify significantly the expansion behaviour of the liquid sheet in the air.

Similarly, the roughness and patterning of the substrate may play a role in the spreading and breakup mechanisms. In their work on rice leaves, Kwon *et al.* (2014) showed that the contact angle in the longitudinal and transversal directions changed due to the patterning of the leaf. Also, when the three-dimensional liquid sheet is created upon impact on leaves, its solid-liquid-air contact line moves across the surface of the leave and a ligneous pattern such as seen in Fig.3.1b on a gramineae, may also affect in various ways the sheet adhesion and motion. In Fig.3.1b (fourth panel), we also observe that the impacting drop presents a star shaped fragmentation pattern which does not appear to modify the crescent-moon scenario that takes place in this case. The independence between the late

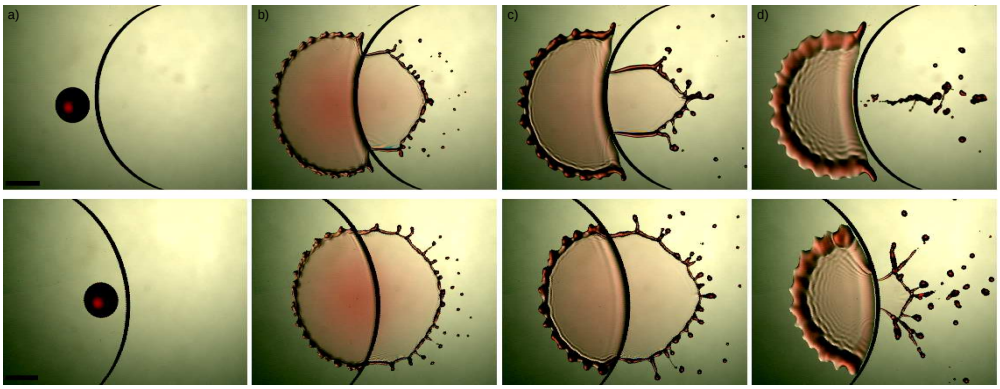


(a)

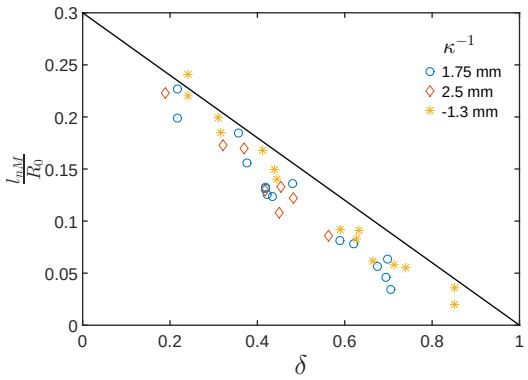


(b)

Figure 8.3: (a) Dyed water drop impacting close to an edge with curvature radius $\kappa^{-1}$ = 1.3 mm (top) and -1.75 mm (bottom). $We = 565$. Scale bars are 5 mm. Times are, from left to right, 4.5, 7.5, 10.5 and 12.5 ms after impact. (b) Maximum extension $l_{nM}$ reached by the liquid sheet normal to the edge normalized by the drop radius ($R_0 = 2.3$ mm) for three curvature radii $\kappa^{-1}$ (cf. legend in inset). $We = 2000$. The solid line is Eq. (5.27)

behaviour of the impacting drop and the sheet expansion of the crescent moon should nonetheless be verified.

Additional variations such as non-flat (e.g., curved), or soft substrates may also present an interest although the range of variation of the parameters may be limited by the depth of the field of view of the camera. These parameters will indeed return the liquid sheet to a three dimensional expansion, which is challenging to image.

Effect of a change in the edge shape, using concave and convex edges instead of straight ones as seen in Fig. 8.3a were also investigated in preliminary tests. The first results indicate an indifference at least in the maximum distance reached normally to the edge with respect to the edge curvature (Fig. 8.3b). Such configurations are relevant in the context of impacts on leaves due to the broad variety of leaf edge shapes encountered but also to their relative size to the liquid sheet expansion.

In a similar domain, the edge own roughness and the shape of the cuts were not investigated beyond preliminary tests (Fig. 8.4) and by noticing that a rough edge created early nucleation of the liquid sheet (section 5.4). We can however observe, in Fig. 8.4, a selection of preferential directions of sheet expansion and droplet ejection. The corresponding droplets may be going much faster than expected since there might be a convergence of energy that would propel them farther. Such configurations are intriguing and are probably worth being investigated further.

Change in the rheological properties of the fluid (e.g., viscosity, surface tension) can also be investigated. These properties could indeed be affected by pathogens present

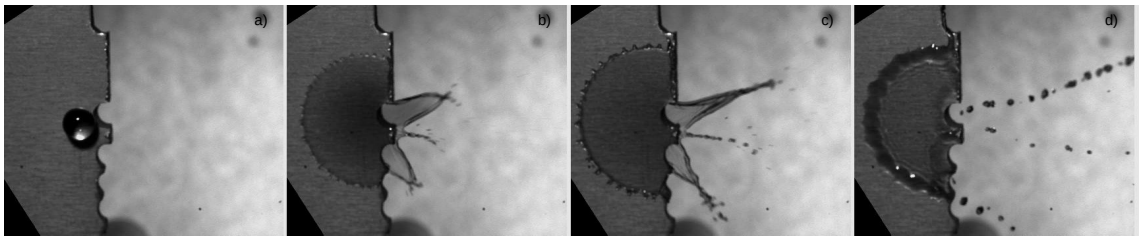


Figure 8.4: Impact of a water drop ($R_0$ = 2.4 mm) on a flat horizontal substrate with variation of the edge shape. Times are, from left to right, 0, 2.6, 4.4 and 11.6 ms from impact.

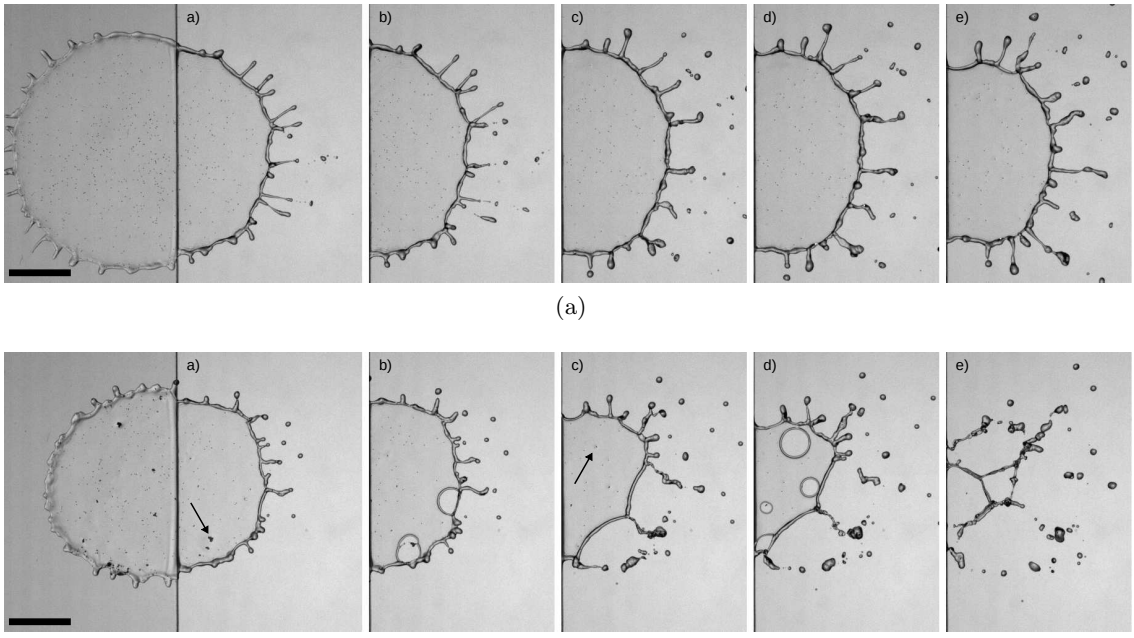


Figure 8.5: (a) Particle-loaded drop impacting at $We \sim 620$ on a flat horizontal plexiglass substrate. Particles are 100$\mu$m in diameter. Scale bar is 5 mm. (b) Particle-loaded drop impacting at $We \sim 520$ on a flat horizontal plexiglass substrate. The particles have in part aggregated. Arrows indicate two particles from which nucleation originate. Scale bar is 5 mm. Times are, for both (a) and (b), from left to right, 3.3, 3.7, 5, 5.4 and 6.4 ms after impact.

in the fluid, especially at sufficiently high concentration. Variations are countless and asymmetric drop impacts are nonetheless encountered in many other contexts than leaf-drop interactions, in which these properties may vary significantly (e.g., paint spraying or agricultural sprays).

Impacts of particle-laden drops are experiments that are of interest for many industrial process and have been studied on axisymmetric drop impacts (Grishaev *et al.*, 2017; Sauret *et al.*, 2017). If the particles are sufficiently small as in Fig. 8.5a, they allow the measurement of the local velocity field in the liquid. We also observed that when these particles aggregate as in Fig. 8.5b, they lead to local nucleation of the liquid sheet and a change of the fragmentation scenario. The size of the particles that lead to nucleation would be interesting to identify and compare to the size of the various rain-spread pathogens. Quantitative assessment of nucleation effects on the droplet shedding is also relevant in this context.

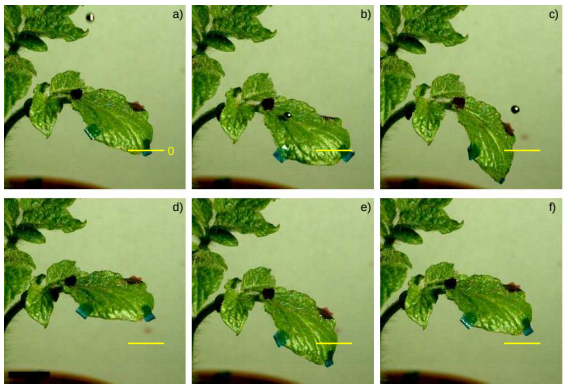


(a)

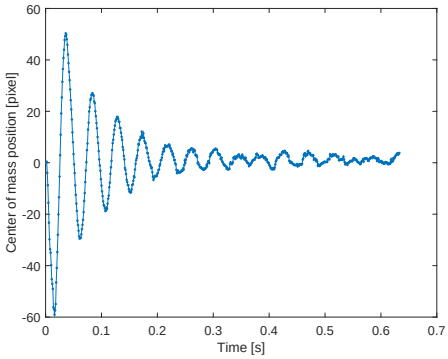


(b)

Figure 8.6: (a) A steel bead of 2 mm in diameter is released and impacts a young potato leaf on which coloured markers have been put. Times are, from left to right and top to bottom, -4, 3, 15, 35, 60, 82 ms from impact. The yellow lines are the vertical original position of the tip marker. (b) Temporal evolution of the vertical motion of the tip marker of the leaf illustrated in (a). The position is measured in pixels and is counted positively upwards with respect to its original position.

### Generalization of the phenomenon

The edge configuration studied here can be seen as a two dimensional idealization of more complicated, three dimensional, impact-induced fragmentation scenarios such as the *crescent-moon*. The transposition of this 2D single-drop configuration to the 3D phenomenon, resulting from the interaction between two drops, is likely to involve some correction factors to relate, notably, the offset $d$ to the actual distance between the drops. The transfer of energy, from the impacting drop to the sessile one, is likely to induce losses of energy so that the $We$ number will also likely have to be adapted. Investigations relating the respective size of the impacting and sessile drops to the scenario and edge-configuration entry parameters will also have to be carried out in this context. Experiments investigating the maximum size of drops that may be found as residue on leaves would also be of the utmost interest as part of this work.

Finally the effect of leaf compliance was here examined, at first order, using inclined substrates but much remains to be done in this endeavour. The link between the inclination angle of the substrate and the corresponding downward motion of the leaf (or substrate) is not yet established. Experiments using hinged rigid substrates, on which a *crescent-moon* experiment is performed, could be at first order used to investigate this issue. Such experiments however, once again, involve three dimensional liquid sheet motion and will most likely have to be image mainly from the side to maintain the focus on the motion of the liquid sheet.

Following this, it will also be necessary to characterize the mechanical response of the leaves to drop impacts, and its influence on sheet development. The link between substrate motion and inclination must be refined further. Various plant species will exhibit various compliance levels. The position of the impact point on the leaf and the growth stage of the leaf may also affect its mechanical response. Simple ways to test leaves response and relate them to various inclination angles and drop impact characteristics will thus need to be designed. Some preliminary experiments were performed to study the response of single impacts on plant leaves. We used beads as illustrated in Fig. 8.6a to simplify the impact response by removing deformation and mass loss that a drop would otherwise experience. By applying coloured markers on specific sites of the leaf, we could measure amplitude and frequency response (Fig. 8.6b). This experiment was however not pursued further but is an interesting starting point and it gives rise to a plethora of possible new experiments.

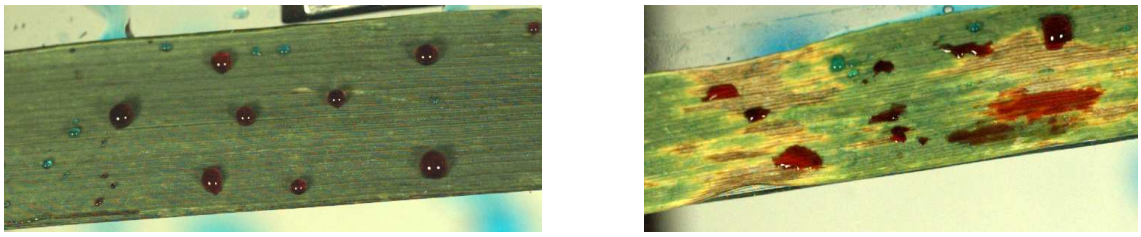

(a) (b)

Figure 8.7: (a) Dyed water droplets deposited on a healthy wheat leaf, glued on a glass lamella, display a high contact angle. (b) Dyed water droplets deposited on Septoria Blotch lesions on a wheat leaf present a reduced contact angle. (pictures taken at INRA with the help of S. Saint-Jean)

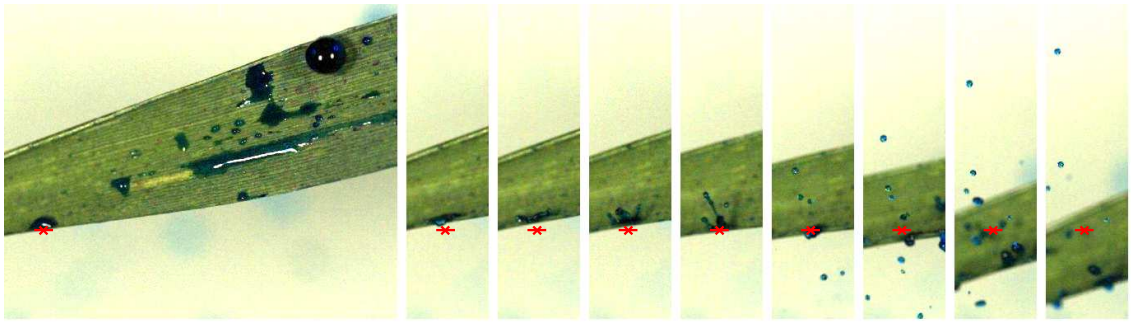

Figure 8.8: Droplets originating from a sessile drop on a wheat leaf are ejected by the upward motion created upon impact of a drop far away. The red stared bars indicate the position of the sessile drop prior to impact. (pictures taken at INRA with the help of S. Saint-Jean)

## 8.3 Investigations relevant for foliar disease spreading

From a more pathogen-spreading point-of-view, the exact distribution of the mass and speed of the droplets as well as other quantities such as number of droplets, for example, could have been wrapped in a format that would be directly implementable in the risk-prediction models. An increased communication with on-field specialists would be interesting at this stage. In-lab and in-field validations of the results would also be interesting at a broader scale than the leaf.

Key informations to this project reside in the properties of the fluid used. Very little remains known on the integration mechanisms of the pathogens in the water and on the properties of the resulting contaminated water. Experiments investigating the timing of contamination of the water on leaves, the concentration of pathogens reached, but also the effects of the presence of various particles or substances on the water properties would be key elements to gain insight into the physics of raindrop-induced pathogen dispersal.

Systematic characterization of leaf wettability, roughness and mechanical properties relevant to this problem should also be carried out. Investigation of changes in the wettability of the leaves depending on their health state and, maybe, mechanical response, are also questions that would need answers. Healthy and sick leaves indeed appear to display quite different contact angle as can be seen in Fig. 8.7.

As Gilet & Bourouiba (2014) reported, there are other ejection mechanisms that intervene in the disease propagation process. Mention was made in introduction (chapter 1) of the inertial detachment where the ejection is performed in a catapult like movement through the leaf motion. Additional imaging of drop impacts on leaves revealed that this inertial detachment can also take place in an upward phase of the leaf motion as seen in

Fig. 8.8. These mechanisms as well as the dripping process should also be studied as part of the rain-induced disease propagation process. Dripping can indeed be a key mechanism as the dripped droplets may be both contaminated and reach a consequent size, conferring them a high Weber number. They may then impact other leaves beneath and create additional splashed droplets. High $We$ will then have to be taken into account even for low Weber rain events.

Finally, the number of pathogens present in the initial fluid is important to characterize to relate it to their distribution in the ejected droplets. Studies have shown that greater droplet sizes statistically carried away more pathogens (Perryman *et al.*, 2014) but much remains to be done concerning this topic. Spores can display various levels of hydrophilicity, so some will be carried at the surface of the droplets if they are superhydrophobic, while others, hydrophilic, may be present in the bulk of the fluid. There is also to our knowledge no studies relating the number of spores landing on a healthy tissue and risk of infection or severity of the lesions.

All these elements show that there is still much to do in very diverse fields, which may open the road to various collaborations. We hope that it will inspire future contributions to this field.

# Appendices

# Appendix A

# Probability distribution functions of the droplet masses ejected for $\tau_n > 1$

The PDF of the mass of the droplets ejected after the sheet expansion ($\tau_n > 1$) is represented in Fig. A.1 per *We* and pooled by scenario, on a horizontal substrate. Ejections during the sheet retraction ($1 < \tau_n < \tau_r$) are separated from ejections after the sheet collapse ($\tau_n > \tau_r$). During retraction, the mass distribution is fairly peaked, almost independent of scenario, and it is slightly shifted to lower mass with increasing *We* (Fig. A.1 left). By contrast, the distribution after collapse does depend on both scenario and *We* (Fig. A.1 right). The isotropic scenario (I) (black symbols) presents a peaked distribution similar to those of the retraction, especially at low *We*. The distribution evolves similarly with both an increase in *We* and a decrease in scenario number towards a much less peaked, more uniform distribution. In scenarios II and III, the proportion of very small droplets is significantly higher, especially at high *We*. This is a signature of the tiny droplets ejected close to the edge after the collapse of the sheet, which speed increases with the impact speed. It generates a much wider distribution, shifted towards smaller droplet size, as the asymmetry increases. The absence of a clear double peak however illustrates the complexity and variety of droplet sizes that are obtained through the combination of the different ejection mechanisms.

Influence of the inclination on the tangential and filament breakup droplet populations can be assessed through the description of their PDFs in Fig. A.1. The PDFs of the droplet masses ejected during the retraction are highly similar to the ones observed for the horizontal substrate (Figs. A.2a and A.2b). Namely, they present a major peak with a centred value that does not vary with the asymmetry of the sheet (so with the scenario) but presents a greater standard deviation than the one observed during the extension. These peaks are fairly similar across $\alpha$ too, suggesting that the radial and tangential mechanisms are independent on the inclination of the substrate. A secondary peak is also visible for all $\alpha$ and scenarios II and III but its position vary. These droplets could be satellite droplets, i.e., secondary droplets formed during ligament break-up.

The PDFs after collapse also show similar trends as the one found for the horizontal substrate, namely a more peaked distribution for scenario I and a much less peaked one for higher asymmetry levels (scenarios II and III) where the proportion of very small droplets ejected from the filament breakup increases (Figs. A.2c and A.2d). This further confirms that an increased asymmetry leads to a greater number of smaller droplets ejected through the filament breakup mechanism.

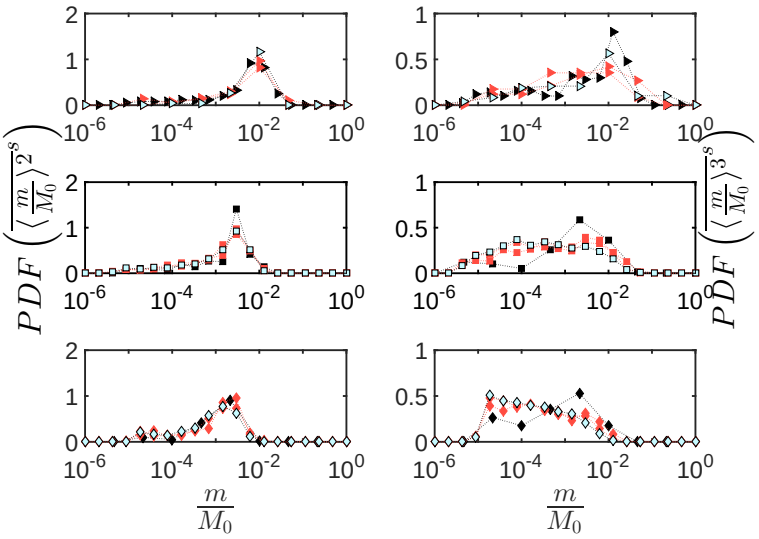


Figure A.1: Probability Distribution Function (PDF) of the droplet mass pooled by scenario (I- black, II - red, III blue) for a horizontal substrate. The left column corresponds to droplets ejected from the sheet maximum extension until its collapse along the edge. The right column corresponds to droplets ejected after the collapse along the edge. The rows correspond to $We = 350$ ($\triangleright$), 1300 ($\square$) and 2600 ($\diamond$), from top to bottom. The 's' index of the y coordinate indicates pooling by scenario.

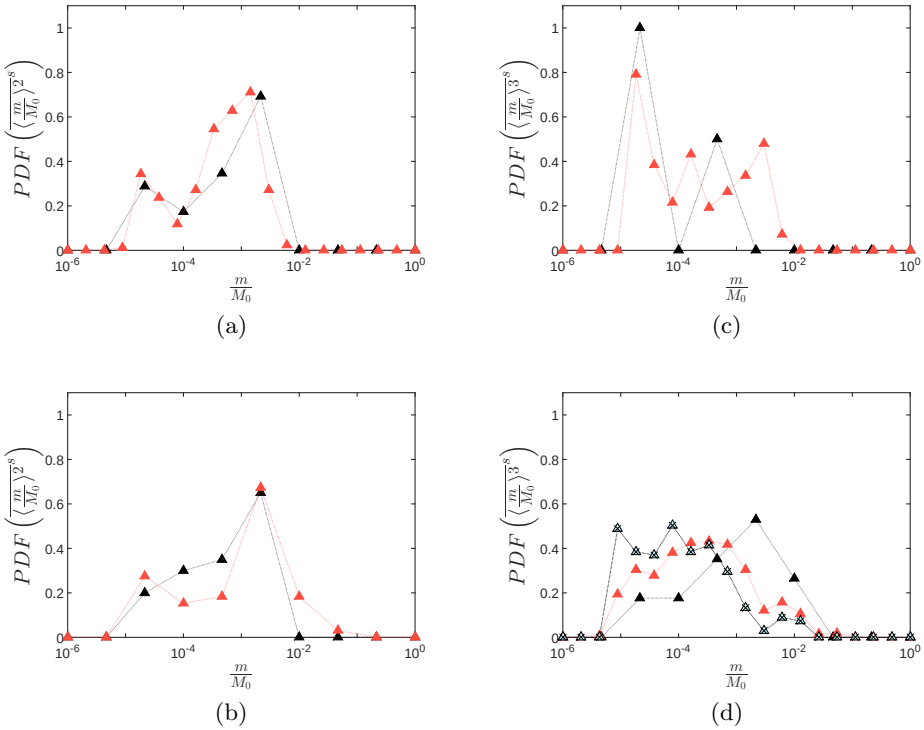


Figure A.2: Probability Distribution Function (PDF) of the droplet mass pooled by scenario (I - black, II - red, III blue) for three $\alpha$, from top to bottom: -20, and 40°. The left column corresponds to droplets ejected from the sheet maximum extension until its collapse along the edge. The right column corresponds to droplets ejected after the collapse along the edge. The Weber number is $We = 2000$. The 's' index of the y-coordinate indicates pooling by scenario. Symbols with a black cross correspond to a pooling with experiments where some final collapse droplets are missing.

# Appendix B

# Travelled distance: the aerodynamic wall

The ballistic trajectory $\mathbf{x}(t) = x(t)\mathbf{e}_x + z(t)\mathbf{e}_z$ of each ejected droplet can be computed from Newton's law, as a function of its mass $m$ and ejection speed $v$:

$$\begin{aligned} m\frac{d^2\mathbf{x}}{dt^2} &= -mg\mathbf{e}_z - 6\pi\mu_a r\frac{d\mathbf{x}}{dt}\left[1+\frac{c}{100}Re^{2/3}\right] \quad \text{for} \quad Re = \frac{2r\rho_a}{\mu_a}\left|\frac{d\mathbf{x}}{dt}\right| < 1000 \\ m\frac{d^2\mathbf{x}}{dt^2} &= -mg\mathbf{e}_z - \frac{3(1+c)}{125}\frac{\pi}{2}\rho_a r^2\frac{d\mathbf{x}}{dt}\left|\frac{d\mathbf{x}}{dt}\right| \quad \text{for} \quad Re > 1000 \end{aligned} \tag{B.1}$$

where $Re$ is the Reynolds number, $r = (3m/4\pi\rho)^{1/3}$ is the droplet radius, $c$ is a fitting parameter, and $\rho_a$ and $\mu_a$ are the density and dynamic viscosity of the air, respectively. We here consider $\mathbf{e}_x$ as the horizontal direction of ejection, and $x(t)$ is the distance travelled horizontally since ejection, no matter in which direction $\theta_v$. In Eq. (B.1), the air drag is calculated with an approximation valid for spherical objects in a large range of Reynolds number, from $10^-2$ to $10^5$ (cf. similar models in Clift *et al.* (1978)). A fit on experimental data from Duan *et al.* (2015) yields $c \simeq 16$.

Owing to air drag, the horizontal speed decreases with time and $x(t)$ reaches an asymptotic value $\Psi = \lim_{t\to\infty} x$ called the aerodynamic wall (Cohen *et al.*, 2013).

First, Eq. (B.1) is non-dimensionalized with characteristic timescale $T$ and length scale $L$ defined in the limit of small Reynolds number, $T = 2\rho r^2/(9\mu_a)$, $L = gT^2$, $\mathbf{y} = \mathbf{x}/L$, $\tau = t/T$ from which we obtain:

$$\begin{aligned} \frac{d^2\mathbf{y}}{d\tau^2} &= -\mathbf{e}_z - \left[1+\frac{c}{100}\beta^{2/3}\left|\frac{d\mathbf{y}}{dt}\right|^{2/3}\right]\frac{d\mathbf{y}}{d\tau} \quad \text{if} \quad \beta\left|\frac{d\mathbf{y}}{dt}\right| < 1000 \\ \frac{d^2\mathbf{y}}{d\tau^2} &= -\mathbf{e}_z - \frac{1+c}{1000}\beta\left|\frac{d\mathbf{y}}{dt}\right|\frac{d\mathbf{y}}{d\tau} \quad \text{if} \quad \beta\left|\frac{d\mathbf{y}}{dt}\right| > 1000 \end{aligned} \tag{B.2}$$

where the dimensionless parameter $\beta$ is defined as

$$\beta = \frac{mg\rho_a}{3\pi\mu_a^2} = \frac{4\rho_a\rho g r^3}{9\mu_a^2}. \tag{B.3}$$

This differential equation can be integrated, with an initial horizontal dimensionless speed

$$\left.\frac{d\mathbf{y}}{d\tau}\right|_{\tau=0}\cdot\mathbf{e}_x = u_0 = \frac{9\mu_a}{2\rho g r^2}v_x$$

and initial vertical dimensionless speed

$$\left.\frac{d\mathbf{y}}{d\tau}\right|_{\tau=0}\cdot\mathbf{e}_z = u_z = \frac{9\mu_a}{2\rho g r^2}v_z.$$

We here consider $\mathbf{e}_x$ as the horizontal direction of ejection, and $x(t)$ is the distance travelled horizontally since ejection, no matter in which direction $\theta_v$ or inclination of the

substrate $\alpha$. At the moment of ejection, each droplet departs from $(x_0, z_0) = (0, 0)$ and the initial dimensional velocity express as

$$(v_x, \quad v_z) = \left(\sqrt{(v_n \cos\alpha)^2 + v_t^2}, \quad -v_n \sin\alpha\right), \tag{B.4}$$

where $v_n$ and $v_t$ are the speed of the ejected droplets in the direction normal and tangential to the edge respectively, in the plane of the substrate (Fig. 6.17). The cosine of $v_n$ is combined to $v_t$ to yield the horizontal component of the initial velocity $v_x = \sqrt{(v_n \cos\alpha)^2 + v_t^2}$. Only the component normal to the edge is projected according to the inclination. The sine of $v_n$ indeed gives the initial vertical speed $v_z = -v_n \sin\alpha$.

The Reynolds number is given by $\beta|d\mathbf{y}/d\tau|$.

### B.0.1 Exact solution at low Reynolds number

There is an exact solution to Eq. (B.2) at low Reynolds number, i.e., for droplets that are sufficiently small so $\beta \ll 1$. Equation B.2 then simplifies into:

$$\frac{d^2\mathbf{y}}{d\tau^2} + \frac{d\mathbf{y}}{d\tau} = -\mathbf{e}_z \tag{B.5}$$

Time-integration yields

$$\mathbf{y} = (1 - e^{-\tau})\,(u_0\mathbf{e}_x + u_z\mathbf{e}_z) - \tau\mathbf{e}_z.$$

The maximum horizontal distance travelled is then

$$y_\infty = \lim_{\tau\to\infty} \mathbf{y}\cdot\mathbf{e}_x = u_0$$

or, in dimensional form

$$\Psi_0 = \Psi(\beta \ll 1) = y_\infty L = \frac{2\rho r^2 v_x}{9\mu_a}$$

The condition $Re < 1$ yields

$$\frac{2r\rho_a L}{\mu_a T} < 1 \Rightarrow \beta < 1 \tag{B.6}$$

One can now analyse the effect of the inclination of the substrate $\alpha$ for these low Reynolds numbers but also of the ratio of the speeds $v_n/v_t$. This ratio is linked to the angle $\theta_v$ that measures the direction of ejection from the impact point. Since we have

$$v = \sqrt{v_n^2 + v_t^2}, \quad v_n = v\cos\theta_v \quad \text{and} \quad \mathrm{v_t} = \mathrm{v}\sin\theta_\mathrm{v},$$

The maximum distance travelled is thus proportional to

$$\Psi_0 \propto v\sqrt{\cos^2\theta_v \sin^2\alpha + \sin^2\theta_v}. \tag{B.7}$$

This function is plotted over a range of $\alpha$ and $\theta_v$ values in Fig. B.1a. The inclination reduces the distance travelled for given mass and initial speed, and it is the horizontal substrate that yields the maximum distance for a given $\theta_v$. This can be also be deduced from Eq. (B.7) since the square root is here an even function of $\alpha$. However at a given $\alpha$ (significantly different from 0°), the ratio $v_n/v_t$ can affect the distance travelled, especially for large $\theta_v$. Indeed, in the extreme configuration, if $\theta_v$ is 90°, the droplet is ejected tangentially to the edge and as a result, its distance travelled is not affected by the inclination of the substrate. $\Psi_0$ is then maximal for large values of $\theta_v$.

In our experiments, we observe that the probability distribution function of the ejection angle $\theta_v$ of the droplets ejected before the collapse of the liquid sheet is shaped as a Gaussian of mean value close to zero and standard deviation that goes from 66° for $\alpha$ = -40° to 17° for $\alpha = 60°$. When computing the maximum distance travelled using a theoretical norm as entry parameter, we chose to set $\theta_v$ = 0°. This value does not always maximizes the distance travelled but we believe it to be a reasonable assumption considering the arguments developed in section 6.5.

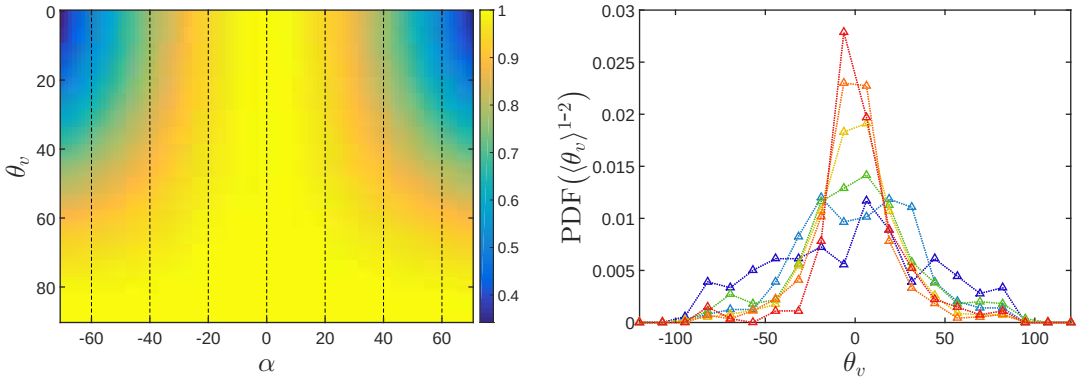


(a) (b)

Figure B.1: (a) Evaluation in $\theta_v$ and $\alpha$ of the normalized Eq. (B.7) with the colormap indicating the percentage to maximum distance. (b) Probability distribution function (PDF) of the droplet ejection angle $\theta_v$ ejected before the collapse of the sheet ($\tau_n < \tau_r$) per inclination $\alpha$ with values in colour: -40° (dark blue) -20° (light blue), 0° (green), 20° (yellow), 40° (orange) and 60° (red). $We = 2000$. Average values and standard deviations of the best Gaussian fit are, from -40° to 60°, [1.3° 2.6° 1.2° 0.5° -0.9° -1.6°] and [66° 47° 36° 27° 20° 17°] respectively.

### B.0.2 Numerical solution for any Reynolds number

The droplets ejected during the sheet fragmentation are in the range $m/M_0 \in [3\times10^{-6}, 3\times10^{-2}]$ (Fig. 6.13a), which corresponds to $r \in [0.035, 0.75]$ mm and $\beta \in [0.67, 6700]$. The ejection speed can reach 10 m/s, so the Reynolds number at ejection can be as high as 1000. Therefore we need to solve Eq. (B.2) numerically.

The solution is represented for dimensionless size $\beta \in [10^{-4}, 10^{7}]$, ejection speed $v \in [10^{-3}, 10]$ m/s and $\alpha \in 0°; 40°; 80°$ in Fig. B.2. Once normalized by $\Psi_0$, the aerodynamic wall $\Psi$ does not depend on ejection speed $v$ anymore, except for very large speed (here $v = 10$ m/s) where $\Psi/\Psi_0$ can be twice smaller than at moderate speed. So in first approximation,

$$\frac{\Psi}{\Psi_0} = F(\beta) \tag{B.8}$$

where $F(\beta) \to 1$ for $\beta \to 0$ and $F(\beta) \to 12/\sqrt{\beta}$ when $\beta \to \infty$.

The function $F(\beta)$ satisfies $F(0) = 1$ (low Reynolds limit), and it scales as $F \sim \beta^{-1/2}$ for $\beta \gg 1$ (high Reynolds limit). Since $\beta$ is only dependent on droplet size $r$ and not on speed $v_x$, the aerodynamic wall at a distance $\Psi$ is always approximately proportional to the ejection speed $v$. Figure B.2 also confirms the relative small influence of the inclination of the substrate on the distance travelled by the droplets.

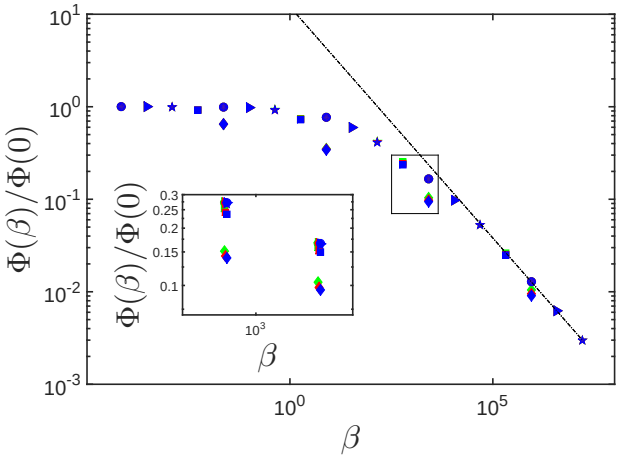


Figure B.2: Maximum travelled horizontal distance $\Psi$, as a function of the dimensionless droplet size $\beta$. Each symbol corresponds to a different ejection speed $v$: ($\bigcirc$) $v = 10^{-3}$ m/s, ($\triangleright$) $v = 10^{-2}$ m/s, ($\bigstar$) $v = 10^{-1}$ m/s, ($\square$) $v = 1$ m/s, ($\diamond$) $v = 10$ m/s. The solid line corresponds to $\Psi(\beta)/\Psi(0) \simeq 12\beta^{-1/2}$. The inclination of the substrate is varied with $\alpha = 0°$ (green) $40°$ (red) and $80°$ (blue). Inset: zoomed view of the framed portion.

# References


Adam, C. 2012. Fundamental studies of bloodstain formation and characteristics. *Forensic Science International*, **219**, 76–87.

Almohammadi, H., & Amirfazli, A. 2017a. Asymmetric Spreading of a Drop upon Impact onto a Surface. *Langmuir*, **33**(23), 5957–5964.

Almohammadi, H., & Amirfazli, A. 2017b. Understanding the drop impact on moving hydrophilic and hydrophobic surfaces. *Soft Matter*, **13**(10), 2040–2053.

Alt, S., & Kollar, A. 2010. Hydrodynamics of raindrop impact stimulate ascospore discharge of Venturia inaequalis. *Fungal Biology*, **114**(4), 320–324.

Andrew, M., Yeomans, J. M., & Pushkin, D. O. 2017. A solvable model of axisymmetric and non-axisymmetric droplet bouncing. *Soft Matter*, **13**(5), 985–994.

Antonini, C., Innocenti, M., Horn, T., Marengo, M., & Amirfazli, A. 2011. Understanding the effect of superhydrophobic coatings on energy reduction in anti-icing systems. *Cold Regions Science and Technology*, **67**(1-2), 58–67.

Antonini, C., Amirfazli, A., & Marengo, M. 2012. Drop impact and wettability: From hydrophilic to superhydrophobic surfaces. *Physics of Fluids*, **24**(10), 102104.

Antonini, C., Villa, F., & Marengo, M. 2014. Oblique impacts of water drops onto hydrophobic and superhydrophobic surfaces: Outcomes, timing, and rebound maps. *Experiments in Fluids*, **55**(4), 1713.

Arora, S., Ligoure, C., & Ramos, L. 2016. Interplay between viscosity and elasticity in freely expanding liquid sheets. *Physical Review Fluids*, **1**(8), 083302.

Baccar, R., Fournier, C., Dornbusch, T., Andrieu, B., Gouache, D., & Robert, C. 2011. Modelling the effect of wheat canopy architecture as affected by sowing density on Septoria tritici epidemics using a coupled epidemicvirtual plant model. *Annals of Botany*, **108**(6), 1179–1194.

Bakshi, S., Roisman, I.V., & Tropea, C. 2007. Investigations on the impact of a drop onto a small spherical target. *Physics of Fluids*, **19**(3), 032102–1–12.

Bartolo, D., Josserand, C., & Bonn, D. 2005. Retraction dynamics of aqueous drops upon impact on non-wetting surfaces. *Journal of Fluid Mechanics*, **545**, 329–338.

Biance, A.-L., Chevy, F., Clanet, C., Lagubeau, G., & Quéré, D. 2006. On the elasticity of an inertial liquid shock. *Journal of Fluid Mechanics*, **554**(May), 47–66.

Bird, J. C., Tsai, S. H., & Stone, H. A. 2009. Inclined to splash: Triggering and inhibiting a splash with tangential velocity. *New Journal of Physics*, **11**, 063017.

Bird, J. C., Dhiman, R., Kwon, H.-M., & Varanasi, K. K. 2013. Reducing the contact time of a bouncing drop. *Nature*, **503**(7476), 385–388.

Blanchette, F., & Bigioni, T. P. 2006. Partial coalescence of drops at liquid interfaces. *Nature Physics*, **2**(4), 254–257.

Boyer, F., Sandoval-Nava, E., Snoeijer, J. H., Dijksman, J. F., & Lohse, D. 2016. Drop impact of shear thickening liquids. *Physical review fluids*, **1**(1), 013901.

Breitenbach, J., Roisman, I.V., & Tropea, C. 2018. From drop impact physics to spray cooling models: a critical review. *Experiments in Fluids*, **59**(3), 55.

Bremond, N., & Villermaux, E. 2006. Atomization by jet impact. *Journal of Fluid Mechanics*, **549**, 273–306.

Calonnec, A., Burie, J.-B., Langlais, M., Guyader, S., Saint-Jean, S., Sache, I., & Tivoli, B. 2013. Impacts of plant growth and architecture on pathogen processes and their consequences for epidemic behaviour. *European Journal of Plant Pathology*, **135**(3), 479–497.

Castilla, N. P., Leaño, R. M., Elazegui, F. A., Teng, P. S., & Savary, S. 1996. Effects of plant contact, inoculation pattern, leaf wetness regime, and nitrogen supply on inoculum efficiency in rice sheath blight. *Journal of Phytopathology*, **144**(4), 187–192.

Chakraborty, S., & Newton, A. C. 2011. Climate change, plant diseases and food security: An overview. *Plant Pathology*, **60**(1), 2–14.

Chandra, S., & Avedisian, C.T. 1991. On the collision of a droplet with a solid surface. *Proceedings of the Royal Society A: Mathematical, Physical and Engineering Sciences*, **432**(1884), 13–41.

Clanet, C., & Villermaux, E. 2002. Life of a smooth liquid sheet. *Journal of Fluid Mechanics*, **462**, 307–340.

Clanet, C., Béguin, C., Richard, D., & Quéré, D. 2004. Maximal deformation of an impacting drop. *Journal of Fluid Mechanics*, **517**, 199–208.

Clift, R., Grace, J. R., & Weber, M. 1978. *Bubbles, drops, and particles*. London: Academic Press.

Cohen, C., Darbois-Texier, B., Dupeux, G., Brunel, E., Quéré, D., & Clanet, C. 2013. The aerodynamic wall. *Proceedings of the Royal Society A: Mathematical, Physical and Engineering Sciences*, **470**(2161), 20130497. cited By 9.

Cook, R. J. 2000. Advances in plant health management in the twentieth century. *Annual Review of Phytopathology*, **38**, 95–116.

de Ruiter, J., Pepper, R. E., & Stone, H. A. 2010. Thickness of the rim of an expanding lamella near the splash threshold. *Physics of Fluids*, **22**(2), 022104.

Derby, B. 2010. Inkjet printing of functional and structural materials: fluid property requirements, feature stability, and resolution. *Annual Review of Materials Research*, **40**, 395–414.

Derksen, R. C., Paul, P. A., Ozkan, H. E., & Zhu, H. 2012. Field evaluations of application techniques for fungicide spray deposition on wheat and artificial targets. *Applied Engineering in Agriculture*, **28**(3), 325–331.

Dhiman, R., & Chandra, S. 2010. Rupture of thin films formed during droplet impact. *Proceedings of the Royal Society A: Mathematical, Physical and Engineering Sciences*, **466**(2116), 1229–1245.

Duan, Z., He, B., & Duan, Y. 2015. Sphere drag and heat transfer. *Scientific reports*, **5**, 12304.

Duez, C., Ybert, C., Clanet, C., & Bocquet, L. 2010. Wetting controls separation of inertial flows from solid surfaces. *Physical Review Letters*, **104**(8), 084503.

Eggers, J., Fontelos, M. A., Josserand, C., & Zaleski, S. 2010. Drop dynamics after impact on a solid wall: Theory and simulations. *Physics of Fluids*, **22**(6), 062101.

Enserink, M., Hines, P. J., Vignieri, S. N., Wigginton, N. S., & Yeston, J. S. 2013. Smarter pest control. The pesticide paradox. Introduction. *Science (New York, N.Y.)*, **341**(6147), 728–729.

Eyal, Z. 1987. *The Septoria diseases of wheat: concepts and methods of disease management.* CIMMyT.

Fitt, B. D. L., Gregory, P. H., Todd, A. D., McCartney, H. A., & Macdonald, O. C. 1987. Spore Dispersal and Plant Disease Gradients; a Comparison between two Empirical Models. *Journal of Phytopathology*, **118**(3), 227–242.

Fitt, B. D. L., McCartney, H. A., & Walklate, P. J. 1989. The role of rain in dispersal of pathogen inoculum. *Annual review of phytopathology.*, **27**, 241–270.

Fitt, B. D. L., Inman, A. L., Lacey, M. E., & McCartney, H. A. 1992. Splash dispersal of spores of Pseudocercosporella capsellae (white leaf spot) from oilseed rape leaves of different inclination, flexibility and age. *Zeitschrift für Pflanzenkrankheiten und Pflanzenschutz/Journal of Plant Diseases and Protection*, 234–244.

Fones, H., & Gurr, S. 2015. The impact of Septoria tritici Blotch disease on wheat: An EU perspective. *Fungal Genetics and Biology*, **79**, 3–7.

Fournet, J. 1969. Propriétés et rôle du cirrhe du Septoria nodorum Berk. *Pages 87–94 of: Annales de Phytopathologie*, vol. 1.

Fujimoto, H., Yoshimoto, S., Takahashi, K., Hama, T., & Takuda, H. 2017. Deformation behavior of two droplets successively impinging obliquely on hot solid surface. *Experimental Thermal and Fluid Science*, **81**, 136–146.

Furbish, D. J., Hammer, K. K., Schmeeckle, M., Borosund, M. N., & Mudd, S. M. 2007. Rain splash of dry sand revealed by high-speed imaging and sticky paper splash targets. *Journal of Geophysical Research: Earth Surface*, **112**(1), 1–9.

Garin, G., Fournier, C., Andrieu, B., Houlès, V., Robert, C., & Pradal, C. 2014. A modelling framework to simulate foliar fungal epidemics using functional-structural plant models. *Annals of Botany*, **114**(4), 795–812.

Gigot, C. 2013. *Potentialités des associations de variétés pour limiter la progression épidémique de la septoriose du blé : rôle des mécanismes de dispersion des spores par la pluie dans un couvert végétal hétérogène.* Ph.D. thesis, Sciences agricoles. AgroParisTech.

Gigot, C., Saint-Jean, S., Huber, L., Maumené, C., Leconte, M., Kerhornou, B., & de Vallavieille-Pope, C. 2013. Protective effects of a wheat cultivar mixture against splash-dispersed septoria tritici blotch epidemics. *Plant Pathology*, **62**(5), 1011–1019.

Gigot, C., De Vallavieille-Pope, C., Huber, L., & Saint-Jean, S. 2014. Using virtual 3-D plant architecture to assess fungal pathogen splash dispersal in heterogeneous canopies: A case study with cultivar mixtures and a non-specialized disease causal agent. *Annals of Botany*, **114**(4), 863–875.

Gilet, T., & Bourouiba, L. 2014. Rain-induced ejection of pathogens from leaves: Revisiting the hypothesis of splash-on-film using high-speed visualization. *Integrative and Comparative Biology*, **54**(6), 974–984.

Gilet, T., & Bourouiba, L. 2015. Fluid fragmentation shapes rain-induced foliar disease transmission. *Journal of the Royal Society Interface*, **12**(March), 20141092.

Gilet, T., & Bush, J.W.M. 2012. Droplets bouncing on a wet, inclined surface. *Physics of Fluids*, **24**(12), 122103.

Gilet, T., Mulleners, K., Lecomte, J. P., Vandewalle, N., & Dorbolo, S. 2007. Critical parameters for the partial coalescence of a droplet. *Physical Review E - Statistical, Nonlinear, and Soft Matter Physics*, **75**(3), 036303.

González-Domínguez, E., Rossi, V., Michereff, S.J., García-Jiménez, J., & Armengol, J. 2014. Dispersal of conidia of Fusicladium eriobotryae and spatial patterns of scab in loquat orchards in Spain. *European Journal of Plant Pathology*, **139**(4), 849–861.

Gordillo, J. M., Lhuissier, H., & Villermaux, E. 2014. On the cusps bordering liquid sheets. *Journal of Fluid Mechanics*, **754**, R11–R111.

Gregory, P. H. 1968. Interpreting plant disease dispersal gradients. *Annual Review of Phytopathology*, **6**(1), 189–212.

Grishaev, V., Iorio, C. S., Dubois, F., & Amirfazli, A. 2015. Complex Drop Impact Morphology. *Langmuir*, **31**(36), 9833–9844.

Grishaev, V., Iorio, C. S., Dubois, F., & Amirfazli, A. 2017. Impact of particle-laden drops: Particle distribution on the substrate. *Journal of Colloid and Interface Science*, **490**, 108–118.

Howland, C. J., Antkowiak, A., Castrejón-Pita, J. R., Howison, S. D., Oliver, J. M., Style, R. W., & Castrejón-Pita, A. A. 2016. It's Harder to Splash on Soft Solids. *Physical Review Letters*, **117**(18), 184502.

Huber, L., Madden, L. V., & Fitt, B. D. L. 2006. Environmental biophysics applied to the dispersal of fungal spores by rain-splash. *Pages 417–444 of: The epidemiology of plant diseases*. Springer.

Hulse-Smith, L., Mehdizadeh, N. Z., & Chandra, S. 2005. Deducing drop size and impact velocity from circular bloodstains. *Journal of Forensic Sciences*, **50**(1), 54–63.

Jin, Z., Sui, D., & Yang, Z. 2015. The impact, freezing, and melting processes of a water droplet on an inclined cold surface. *International Journal of Heat and Mass Transfer*, **90**, 439–453.

Jorgensen, L. N., Van Den Bosch, F., Oliver, R. P., Heick, T. M., & Paveley, N. D. 2017. Targeting Fungicide Inputs According to Need. *Annual Review of Phytopathology*, **55**, 181–203.

Josserand, C., & Thoroddsen, S. T. 2016. Drop Impact on a Solid Surface. *Annual Review of Fluid Mechanics*, **48**, 365–391.

Juarez, G., Gastopoulos, T., Zhang, Y., Siegel, M. L., & Arratia, P. E. 2012. Splash control of drop impacts with geometric targets. *Physical Review E - Statistical, Nonlinear, and Soft Matter Physics*, **85**(2), 026319.

Kang, B. S., & Lee, D. H. 2000. On the dynamic behavior of a liquid droplet impacting upon an inclined heated surface. *Experiments in Fluids*, **29**(4), 380–387.

Kang, C. W., & Ng, H. W. 2006. Splat morphology and spreading behavior due to oblique impact of droplets onto substrates in plasma spray coating process. *Surface and Coatings Technology*, **200**(18-19), 5462–5477.

Kema, G. H. J., Yu, D., Rijkenberg, F. H. J., Shaw, M. W., & Baayen, R. P. 1996. Histology of the pathogenesis of Mycosphaerella graminicola in wheat. *Phytopathology*, **86**(7), 777–786.

Kim, H., Park, U., Lee, C., Kim, H., Hwan Kim, M., & Kim, J. 2014. Drop splashing on a rough surface: How surface morphology affects splashing threshold. *Applied Physics Letters*, **104**(16), 161608.

Kwon, D. H., Huh, H. K., & Lee, S. J. 2014. Wettability and impact dynamics of water droplets on rice (Oryza sativa L.) leaves. *Experiments in Fluids*, **55**, 1691.

Laan, N., de Bruin, K. G., Bartolo, D., Josserand, C., & Bonn, D. 2014. Maximum diameter of impacting liquid droplets. *Physical Review Applied*, **2**(4), 044018.

Laan, N., de Bruin, K. G., Slenter, D., Wilhelm, J., Jermy, M., & Bonn, D. 2015. Bloodstain Pattern Analysis: Implementation of a fluid dynamic model for position determination of victims. *Scientific Reports*, **5**(11461), 1–8.

Lagubeau, G., Fontelos, M. A., Josserand, C., Maurel, A., Pagneux, V., & Petitjeans, P. 2012. Spreading dynamics of drop impacts. *Journal of Fluid Mechanics*, **713**, 50–60.

Lastakowski, H., Boyer, F., Biance, A.-L., Pirat, C., & Ybert, C. 2014. Bridging local to global dynamics of drop impact onto solid substrates. *Journal of Fluid Mechanics*, **747**, 103–118.

Lejeune, S., Gilet, T., & Bourouiba, L. 2018. Edge effect: Liquid sheet and droplets formed by drop impact close to an edge. *Physical Review Fluids*, **3**(8), 083601.

Leroux, P, Walker, AS, Couleaud, G, Maumené, C, Henaff, G le, *et al.* 2008. Field strategies to manage fungicide resistance in Mycosphaerella graminicola, the causal agent of wheat leaf blotch. *Pages 143–149 of: Modern fungicides and antifungal compounds V: 15th International Reinhardsbrunn Symposium, Friedrichroda, Germany, May 6-10, 2007.* Deutsche Phytomedizinische Gesellschaft eV Verlag.

Li, E. Q., & Thoroddsen, S. T. 2015. Time-resolved imaging of a compressible air disc under a drop impacting on a solid surface. *Journal of Fluid Mechanics*, **780**, 636–648.

Liang, G., & Mudawar, I. 2017. Review of drop impact on heated walls. *International Journal of Heat and Mass Transfer*, **106**, 103–126.

Liu, Y., Tan, P., & Xu, L. 2013. Compressible air entrapment in high-speed drop impacts on solid surfaces. *Journal of Fluid Mechanics*, **716**, R91–R912.

Liu, Y., Moevius, L., Xu, X., Qian, T., Yeomans, J.M., & Wang, Z. 2014. Pancake bouncing on superhydrophobic surfaces. *Nature Physics*, **10**(7), 515–519.

Liu, Y., Andrew, M., Li, J., Yeomans, J. M., & Wang, Z. 2015. Symmetry breaking in drop bouncing on curved surfaces. *Nature Communications*, **6**, 10034.

Lovell, D. J., Hunter, T., Powers, S. J., Parker, S. R., & Van Den Bosch, F. 2004. Effect of temperature on latent period of septoria leaf blotch on winter wheat under outdoor conditions. *Plant Pathology*, **53**(2), 170–181.

Malouin, B. A., Koratkar, N. A., Hirsa, A. H., & Wang, Z. 2010. Directed rebounding of droplets by microscale surface roughness gradients. *Applied Physics Letters*, **96**, 234103.

Marengo, M., Antonini, C., Roisman, I. V., & Tropea, C. 2011. Drop collisions with simple and complex surfaces. *Current Opinion in Colloid and Interface Science*, **16**(4), 292–302.

Martin, G. D., Hoath, S. D., & Hutchings, I. M. 2008. Inkjet printing - The physics of manipulating liquid jets and drops. *Journal of Physics: Conference Series*, **105**(1), 012001.

Metcalfe, R.J., Shaw, M.W., & Russell, P.E. 2000. The effect of dose and mobility on the strength of selection for DMI fungicide resistance in inoculated field experiments. *Plant Pathology*, **49**(5), 546–557. cited By 25.

Montavon, G., Sampath, S., Berndt, C. C., Herman, H., & Coddet, C. 1997. Effects of the spray angle on splat morphology during thermal spraying. *Surface and Coatings Technology*, **91**(1-2), 107–115.

Moreira, A. L. N., Moita, A. S., & Panao, M. R. 2010. Advances and challenges in explaining fuel spray impingement: How much of single droplet impact research is useful? *Progress in energy and combustion science*, **36**(5), 554–580.

Mundo, C., Sommerfeld, M., & Tropea, C. 1995. Droplet-wall collisions: Experimental studies of the deformation and breakup process. *International Journal of Multiphase Flow*, **21**(2), 151–173.

Newton, A. C., Gravouil, C., & Fountaine, J. M. 2010. Managing the ecology of foliar pathogens: Ecological tolerance in crops. *Annals of Applied Biology*, **157**(3), 343–359.

Ntahimpera, N., Ellis, M. A., Wilson, L. L., & Madden, L. V. 1998. Effects of a cover crop on splash dispersal of Colletotrichum acutatum conidia. *Phytopathology*, **88**(6), 536–543.

Ntahimpera, N., Wilson, L. L., Ellis, M. A., & Madden, L. V. 1999. Comparison of rain effects on splash dispersal of three Colletotrichum species infecting strawberry. *Phytopathology*, **89**(7), 555–563.

Oerke, E.-C. 2006. Crop losses to pests. *Journal of Agricultural Science*, **144**, 31–43.

Ojiambo, P. S., Gent, D. H., Mehra, L. K., Christie, D., & Magarey, R. 2017. Focus expansion and stability of the spread parameter estimate of the power law model for dispersal gradients. *PeerJ*, **2017**(6), e3465.

Palacios, J., Hernández, J., Gómez, P., Zanzi, C., & López, J. 2013. Experimental study of splashing patterns and the splashing/deposition threshold in drop impacts onto dry smooth solid surfaces. *Experimental Thermal and Fluid Science*, **44**, 571–582.

Pangga, I. B., Hanan, J., & Chakraborty, S. 2011. Pathogen dynamics in a crop canopy and their evolution under changing climate. *Plant Pathology*, **60**, 70–81.

Pasandideh-Fard, M., Qiao, Y. M., Chandra, S., & Mostaghimi, J. 1996. Capillary effects during droplet impact on a solid surface. *Physics of Fluids*, **8**(3), 650–659.

Paul, P. A., El-Allaf, S. M., Lipps, P. E., & Madden, L. V. 2004. Rain splash dispersal of Gibberella zeae within wheat canopies in Ohio. *Phytopathology*, **94**(12), 1342–1349.

Perryman, S. A. M., Clark, S. J., & West, J. S. 2014. Splash dispersal of Phyllosticta citricarpa conidia from infected citrus fruit. *Scientific Reports*, **4**(6568), 1–8.

Pertot, I., Caffi, T., Rossi, V., Mugnai, L., Hoffmann, C., Grando, M. S., Gary, C., Lafond, D., Duso, C., Thiery, D., Mazzoni, V., & Anfora, G. 2017. A critical review of plant protection tools for reducing pesticide use on grapevine and new perspectives for the implementation of IPM in viticulture. *Crop Protection*, **97**, 70–84.

Philippi, J., Lagrée, P.-Y., & Antkowiak, A. 2016. Drop impact on a solid surface: Short-time self-similarity. *Journal of Fluid Mechanics*, **795**, 96–135.

Pietravalle, S., Van Den Bosch, F., Welham, S. J., Parker, S. R., & Lovell, D. J. 2001. Modelling of rain splash trajectories and prediction of rain splash height. *Agricultural and Forest Meteorology*, **109**(3), 171–185.

Ponomarenko, A., Goodwin, S.B., & Kema, G.H.J. 2011. *Septoria tritici blotch (STB) of wheat.*

Range, K., & Feuillebois, F. 1998. Influence of surface roughness on liquid drop impact. *Journal of Colloid and Interface Science*, **203**, 16–30.

Rapilly, F., & Jolivet, E. 1976. Construction d'un modèle (episept) permettant la simulation d'une épidémie de Septoria nodorum BERK. sur blé. *Revue de statistique appliquée*, **24**(3), 31–60.

Rein, M. 1993. Phenomena of liquid drop impact on solid and liquid surfaces. *Fluid Dynamics Research*, **12**(2), 61–93.

Reynolds, K. M., Bulger, M. A., Madden, L. V., & Ellis, M. A. 1987. New methods using simulated rain to study the splash dispersal of plant pathogens. *Phytopathology (USA)*, **77**(6), 921–926.

Reyssat, É., Chevy, F., Biance, A.-L., Petitjean, L., & Quéré, D. 2007. Shape and instability of free-falling liquid globules. *EPL*, **80**, 34005.

Reyssat, M., Pépin, A., Marty, F., Chen, Y., & Quéré, D. 2006. Bouncing transitions on microtextured materials. *Europhysics Letters*, **74**(2), 306–312.

Reyssat, M., Pardo, F., & Quéré, D. 2009. Drops onto gradients of texture. *EPL*, **87**, 36003.

Riboux, G., & Gordillo, J. M. 2014. Experiments of drops impacting a smooth solid surface: A model of the critical impact speed for drop splashing. *Physical Review Letters*, **113**(2), 024507.

Riboux, G., & Gordillo, J. M. 2015. The diameters and velocities of the droplets ejected after splashing. *Journal of Fluid Mechanics*, **772**, 630–648.

Rioboo, R., Tropea, C., & Marengo, M. 2001. Outcomes from a drop impact on solid surfaces. *Atomization and Sprays*, **11**(2), 155–165.

Rioboo, R., Marengo, M., & Tropea, C. 2002. Time evolution of liquid drop impact onto solid, dry surfaces. *Experiments in Fluids*, **33**, 112–124.

Robert, C., Fournier, C., Andrieu, B., & Ney, B. 2008. Coupling a 3D virtual wheat (Triticum aestivum) plant model with a Septoria tritici epidemic model (Septo3D): A new approach to investigate plant-pathogen interactions linked to canopy architecture. *Functional Plant Biology*, **35**(10), 997–1013.

Roisman, I. V. 2009. Inertia dominated drop collisions. II. An analytical solution of the Navier-Stokes equations for a spreading viscous film. *Physics of Fluids*, **21**(5), 052104.

Roisman, I. V., Rioboo, R., & Tropea, C. 2002. Normal impact of a liquid drop on a dry surface: Model for spreading and receding. *Proceedings of the Royal Society A: Mathematical, Physical and Engineering Sciences*, **458**(2022), 1411–1430.

Roisman, I. V., Berberović, E., & Tropea, C. 2009. Inertia dominated drop collisions. I. On the universal flow in the lamella. *Physics of Fluids*, **21**(5), 052103.

Roisman, I. V., Weickgenannt, C. M., Lembach, A. N., & Tropea, C. 2010. Drop impact close to a pore: experimental and numerical investigations. *In: Proceedings of the 23rd Annual Conference on Liquid Atomization and Spray Systems, ILASS-Europe*.

Roisman, I.V., Horvat, K., & Tropea, C. 2006. Spray impact: Rim transverse instability initiating fingering and splash, and description of a secondary spray. *Physics of Fluids*, **18**(10), 102104.

Rozhkov, A., Prunet-Foch, B., & Vignes-Adler, M. 2002. Impact of water drops on small targets. *Physics of Fluids*, **14**(10), 3485–3501.

Rozhkov, A., Prunet-Foch, B., & Vignes-Adler, M. 2004. Dynamics of a liquid lamella resulting from the impact of a water drop on a small target. *Proceedings of the Royal Society A: Mathematical, Physical and Engineering Sciences*, **460**(2049), 2681–2704.

Sache, I. 2000. Short-distance dispersal of wheat rust spores by wind and rain. *Agronomie*, **20**(7), 757–767.

Saint-Jean, S., Chelle, M., & Huber, L. 2004. Modelling water transfer by rain-splash in a 3D canopy using Monte Carlo integration. *Agricultural and Forest Meteorology*, **121**(3-4), 183–196.

Sauret, A., Troger, A., & Jop, P. 2017. An experimental study on particle effects in liquid sheets. *EPJ Web of Conferences*, **140**, 09012.

Schroll, R. D., Josserand, C., Zaleski, S., & Zhang, W. W. 2010. Impact of a viscous liquid drop. *Physical Review Letters*, **104**(3), 034504.

Shaw, M. W., & Royle, D. J. 1989. Airborne inoculum as a major source of Septoria tritici (Mycosphaerella graminicola) infections in winter wheat crops in the UK. *Plant Pathology*, **38**(1), 35–43.

Sherman, J., & Gent, D. H. 2014. Concepts of sustainability, motivations for pest management approaches, and implications for communicating change. *Plant Disease*, **98**(8), 1024–1035.

Steinberg, G. 2015. Cell biology of Zymoseptoria tritici: Pathogen cell organization and wheat infection. *Fungal Genetics and Biology*, **79**, 17–23.

Stone, H. A. 1994. Dynamics of drop deformation and breakup in viscous fluids. *Annual Review of Fluid Mechanics*, **26**(1), 65–102.

Stow, C. D., & Hadfield, M. G. 1980. An investigation of the conditions for splashing of water drops on solid, dry surfaces. *Journal of the Meteorological Society of Japan*, **58**(1), 59–67.

Stow, C. D., & Stainer, R. D. 1977. The physical products of a splashing water drop. *Journal of the Meteorological Society of Japan*, **55**(5), 518–531.

Strange, R. N., & Scott, P. R. 2005. Plant disease: A threat to global food security. *Annual Review of Phytopathology*, **43**, 83–116.

Suffert, F., Sache, I., & Lannou, C. 2011. Early stages of septoria tritici blotch epidemics of winter wheat: Build-up, overseasoning, and release of primary inoculum. *Plant Pathology*, **60**(2), 166–177.

Thoroddsen, S., Etoh, T. G., Takehara, K., Ootsuka, N., & Hatsuki, Y. 2005. The air bubble entrapped under a drop impacting on a solid surface. *Journal of Fluid Mechanics*, **545**, 203–212.

Thoroddsen, S. T., & Sakakibara, J. 1998. Evolution of the fingering pattern of an impacting drop. *Physics of Fluids*, **10**(6), 1359–1374.

Thoroddsen, S. T., Etoh, T. G., & Takehara, K. 2008. High-speed imaging of drops and bubbles. *Annual Review of Fluid Mechanics*, **40**, 257–285.

Thoroddsen, S. T., Takehara, K., & Etoh, T. G. 2012. Micro-splashing by drop impacts. *Journal of Fluid Mechanics*, **706**, 560–570.

Vaikuntanathan, V., Kannan, R., & Sivakumar, D. 2010. Impact of water drops onto the junction of a hydrophobic texture and a hydrophilic smooth surface. *Colloids and Surfaces A: Physicochemical and Engineering Aspects*, **369**, 65–74.

Vernay, C., Ramos, L., & Ligoure, C. 2015. Free radially expanding liquid sheet in air: Time-and space-resolved measurement of the thickness field. *Journal of Fluid Mechanics*, **764**, 428–444.

Vidal, T., Boixel, A.-L., Durand, B., de Vallavieille-Pope, C., Huber, L., & Saint-Jean, S. 2017. Reduction of fungal disease spread in cultivar mixtures: Impact of canopy architecture on rain-splash dispersal and on crop microclimate. *Agricultural and Forest Meteorology*, **246**, 154–161.

Vidal, T., Gigot, C., De Vallavieille-Pope, C., Huber, L., & Saint-Jean, S. 2018. Contrasting plant height can improve the control of rain-borne diseases in wheat cultivar mixture: Modelling splash dispersal in 3-D canopies. *Annals of Botany*, **121**(7), 1299–1308.

Villermaux, E. 2007. Fragmentation. *Annual Review of Fluid Mechanics*, **39**, 419–446.

Villermaux, E., & Bossa, B. 2009. Single-drop fragmentation determines size distribution of raindrops. *Nature Physics*, **5**(9), 697–702.

Villermaux, E., & Bossa, B. 2011. Drop fragmentation on impact. *Journal of Fluid Mechanics*, **668**(February), 412– 435.

Villermaux, E., Marmottant, P., & Duplat, J. 2004. Ligament-Mediated Spray Formation. *Physical Review Letters*, **92**(7), 074501.

Visser, C. W., Frommhold, P. E., Wildeman, S., Mettin, R., Lohse, D., & Sun, C. 2015. Dynamics of high-speed micro-drop impact: Numerical simulations and experiments at frame-to-frame times below 100 ns. *Soft Matter*, **11**(9), 1708–1722.

Šikalo, Š., Tropea, C., & GaniÄ, E. N. 2005. Impact of droplets onto inclined surfaces. *Journal of Colloid and Interface Science*, **286**(2), 661–669.

Walklate, P. J. 1989. Vertical dispersal of plant pathogens by splashing. Part I: the theoretical relationship between rainfall and upward rain splash. *Plant Pathology*, **38**, 56–63.

Walklate, P. J., McCartney, H. A., & Fitt, B. D. L. 1989. Vertical dispersal of plant pathogens by splashing. Part II: experimental study of the relationship between raindrop size and the maximum splash height. *Plant Pathology*, **38**(1), 64–70.

Wang, Y., & Bourouiba, L. 2017. Drop impact on small surfaces: Thickness and velocity profiles of the expanding sheet in the air. *Journal of Fluid Mechanics*, **814**, 510–534.

Wirth, W., Storp, S., & Jacobsen, W. 1991. Mechanisms controlling leaf retention of agricultural spray solutions. *Pesticide Science*, **33**(4), 411–420.

Wolfe, M. S. 2000. Crop strength through diversity. *Nature*, **406**(August), 681–682.

Worthington, A. M. 1877. On the forms assumed by drops of liquids falling vertically on a horizontal plate. *Proceedings of the royal society of London*, **25**(171-178), 261–272.

Xu, L., Barcos, L., & Nagel, S. R. 2007. Splashing of liquids: Interplay of surface roughness with surrounding gas. *Physical Review E*, **76**(6), 066311.

Yang, X., Madden, L. V., & Brazee, R. D. 1991a. Application of the diffusion equation for modelling splash dispersal of point-source pathogens. *New Phytologist*, **118**(2), 295–301.

Yang, X., Madden, L. V., Reichard, D. L., Fox, R.D., & Ellis, M. A. 1991b. Motion analysis of drop impaction on a strawberry surface. *Agricultural and Forest Meteorology*, **56**, 67–92.

Yarin, A. L. 2006. Drop impact dynamics: Splashing, spreading, receding, bouncing. *Annual Review of Fluid Mechanics*, **38**, 159–192.

Yarin, A. L., & Weiss, D. A. 1995. Impact of Drops on Solid Surfaces: Self-Similar Capillary Waves, and Splashing as a New Type of Kinematic Discontinuity. *Journal of Fluid Mechanics*, **283**, 141–173.

Yeong, Y. H., Burton, J., Loth, E., & Bayer, I. S. 2014. Drop Impact and Rebound Dynamics on an Inclined Superhydrophobic Surface. *Langmuir*, **30**, 12027–12038.

Zhang, R., Hao, P., & He, F. 2017. Drop Impact on Oblique Superhydrophobic Surfaces with Two-Tier Roughness. *Langmuir*, **33**, 3556–3567.

Zou, X., Mõttus, M., Tammeorg, P., Torres, C. L., Takala, T., Pisek, J., Mäkelä, P., Stoddard, F.L., & Pellikka, P. 2014. Photographic measurement of leaf angles in field crops. *Agricultural and Forest Meteorology*, **184**, 137–146.